ISSN 2500-316X (Online)

RUSSIAN TECHNOLOGICAL JOURNAL

РОССИЙСКИЙ
ТЕХНОЛОГИЧЕСКИЙ
ЖУРНАЛ

Information systems.
Computer sciences.
Issues of information security

Multiple robots (robotic centers) and systems.
Remote sensing and non-destructive testing

Modern radio engineering and telecommunication systems

Micro- and nanoelectronics.
Condensed matter physics

Analytical instrument engineering and technology

Mathematical modeling

Economics of knowledge-intensive and high-tech enterprises and industries.
Management in organizational systems

Product quality management. Standardization

Philosophical foundations of technology and society

12+
www.rtj-mirea.ru

12(1) 2024

ISSN 2500-316X (Online)

RUSSIAN TECHNOLOGICAL JOURNAL

РОССИЙСКИЙ ТЕХНОЛОГИЧЕСКИЙ ЖУРНАЛ

- Information systems. Computer sciences. Issues of information security
- Multiple robots (robotic centers) and systems. Remote sensing and non-destructive testing
- Modern radio engineering and telecommunication systems
- Micro- and nanoelectronics. Condensed matter physics
- Analytical instrument engineering and technology
- Mathematical modeling
- Economics of knowledge-intensive and high-tech enterprises and industries. Management in organizational systems
- Product quality management. Standardization
- Philosophical foundations of technology and society

- Информационные системы. Информатика. Проблемы информационной безопасности
- Роботизированные комплексы и системы. Технологии дистанционного зондирования и неразрушающего контроля
- Современные радиотехнические и телекоммуникационные системы
- Микро- и наноэлектроника. Физика конденсированного состояния
- Аналитическое приборостроение и технологии
- Математическое моделирование
- Экономика наукоемких и высокотехнологичных предприятий и производств. Управление в организационных системах
- Управление качеством продукции. Стандартизация
- Мировоззренческие основы технологии и общества

Russian Technological Journal
2024, Vol. 12, No. 1

Russian Technological Journal
2024, том 12, № 1

https://www.rtj-mirea.ru

https://doi.org/10.32362/2500-316X

ISSN 2500-316X (Online)

Russian Technological Journal
2024, Vol. 12, No. 1

Publication date January 31, 2024.

The peer-reviewed scientific and technical journal highlights the issues of complex development of radio engineering, telecommunication and information systems, electronics and informatics, as well as the results of fundamental and applied interdisciplinary researches, technological and economical developments aimed at the development and improvement of the modern technological base.

Periodicity: bimonthly.
The journal was founded in December 2013. The titles were «Herald of MSTU MIREA» until 2016 (ISSN 2313-5026) and «Rossiiskii tekhnologicheskii zhurnal» from January 2016 until July 2021 (ISSN 2500-316X).

Founder and Publisher:
Federal State Budget
Educational Institution of Higher Education
«MIREA – Russian Technological University»
78, Vernadskogo pr., Moscow, 119454 Russia.

The journal is included into the List of peer-reviewed science press of the State Commission for Academic Degrees and Titles of Russian Federation. The Journal is included in Russian State Library (RSL), Russian Science Citation Index, eLibrary, Socionet, Directory of Open Access Journals (DOAJ), Directory of Open Access Scholarly Resources (ROAD), Google Scholar, Ulrich's International Periodicals Directory.

The registration number ПИ № ФС 77 - 81733 was issued in August 19, 2021 by the Federal Service for Supervision of Communications, Information Technology, and Mass Media of Russia.

The subscription index of *Pressa Rossii*: **79641**.

Russian Technological Journal
2024, том 12, № 1

Дата опубликования 31 января 2024 г.

Научно-технический рецензируемый журнал освещает вопросы комплексного развития радиотехнических, телекоммуникационных и информационных систем, электроники и информатики, а также результаты фундаментальных и прикладных междисциплинарных исследований, технологических и организационно-экономических разработок, направленных на развитие и совершенствование современной технологической базы.

Периодичность: один раз в два месяца.
Журнал основан в декабре 2013 года. До 2016 г. издавался под названием «Вестник МГТУ МИРЭА» (ISSN 2313-5026), а с января 2016 г. по июль 2021 г. под названием «Российский технологический журнал» (ISSN 2500-316X).

Учредитель и издатель:
федеральное государственное бюджетное образовательное учреждение высшего образования «МИРЭА – Российский технологический университет»
119454, РФ, г. Москва, пр-т Вернадского, д. 78.

Журнал входит в Перечень ведущих рецензируемых научных журналов ВАК РФ, в которых должны быть опубликованы основные научные результаты диссертаций на соискание ученой степени кандидата наук и доктора наук, индексируется в РГБ, РИНЦ, eLibrary, Соционет, Directory of Open Access Journals (DOAJ), Directory of Open Access Scholarly Resources (ROAD), Google Scholar, Ulrich's International Periodicals Directory.

Регистрационный номер и дата принятия решения о регистрации СМИ ПИ № ФС 77 - 81733 от 19.08.2021 г.
СМИ зарегистрировано Федеральной службой по надзору в сфере связи, информационных технологий и массовых коммуникаций (Роскомнадзор).

Индекс по объединенному каталогу «Пресса России» **79641**.

https://www.rtj-mirea.ru

Editorial Board

Редакционная коллегия

Contents

Содержание

Multiple robots (robotic centers) and systems. Remote sensing and non-destructive testing

Роботизированные комплексы и системы. Технологии дистанционного зондирования неразрушающего контроля

UDC 007.52; 629.3.05; 004.021
https://doi.org/10.32362/2500-316X-2024-12-1-7-14

RESEARCH ARTICLE

Automation of autonomous mobile robot docking based on the counter growth rapidly exploring random tree method

Vladimir V. Golubov @,
Sergey V. Manko

MIREA – Russian Technological University, Moscow, 119454 Russia
@ Corresponding author, e-mail: golubov@mirea.ru

Abstract
Objectives. The article substantiates the relevance of automatic docking of autonomous mobile robots. Specific examples show that the implementation of the automatic docking functions of autonomous robots reveals the potential for creating multi-agent systems with a transformable structure. The aim of the work is to develop means for automatic docking of autonomous mobile robots in complex scenarios and an uncertain environment.
Methods. The proposed approach to automating autonomous mobile robot docking is reduced to a modification of the counter-growth rapidly-exploring random tree (RRT) method. It is based on the parallel execution of a decentralized route planning algorithm with mutual coordination of distributed computing processes. The effectiveness of the complex of algorithmic and software tools developed was evaluated using computer and natural simulation methods. The final series of full-scale experiments was carried out on the example of JetBot AI kit Nvidia platforms for automatic docking of autonomous robots. This was performed using the means and methods of intelligent control, visual navigation, technical vision and wireless network communication.
Results. The study analyzed the features of automatic docking as one of the tasks of group control of autonomous robots. This is part of multi-agent systems, capable of reconfiguring structures for purposeful changes to the existing set of functional properties and application possibilities. The study also proposes a decentralized modification of the counter-growth RRT method. This allows the movements of autonomous mobile robots in the course of their mutual approach and subsequent docking to be planned. A set of software-algorithmic tools was developed to automate the docking of autonomous robots. A series of model and full-scale experiments were carried out to confirm the effectiveness of the approach developed herein.
Conclusions. The modification presented herein of the counter-growth RRT method, traditionally used for planning the movements of manipulators and mobile platforms, is complementary to the tasks it resolves. This enables the docking of autonomous robots to be automated. The results obtained open up the potential for universal schedulers with extended functionality for autonomous robot control systems to be designed.

Keywords: autonomous robot, intelligent control, group control, multi-agent robotic system, automatic docking, counter-growth RRT method

• **Submitted:** 18.02.2023 • **Revised:** 13.06.2023 • **Accepted:** 04.12.2023

For citation: Golubov V.V., Manko S.V. Automation of autonomous mobile robot docking based on the counter growth rapidly exploring random tree method. *Russ. Technol. J.* 2024;12(1):7–14. https://doi.org/10.32362/2500-316X-2024-12-1-7-14

Financial disclosure: The authors have no a financial or property interest in any material or method mentioned.

The authors declare no conflicts of interest.

НАУЧНАЯ СТАТЬЯ

Автоматизация стыковки автономных мобильных роботов на основе развития метода поисковых случайных деревьев со встречным ростом

В.В. Голубов @**,**
С.В. Манько

МИРЭА – Российский технологический университет, Москва, 119454 Россия
@ *Автор для переписки, e-mail: golubov@mirea.ru*

Резюме
Цели. В статье обоснована актуальность задачи автоматической стыковки автономных мобильных роботов. На конкретных примерах показано, что реализация функций автоматической стыковки автономных роботов открывает перспективы создания многоагентных систем с трансформируемой структурой. Целью работы является разработка средств автоматической стыковки автономных мобильных роботов, функционирующих в условиях сложных сцен и неопределенности окружающей обстановки.
Методы. Предлагаемый подход к автоматизации стыковки автономных мобильных роботов сводится к модификации метода поисковых случайных деревьев со встречным ростом на основе параллельного выполнения децентрализованного алгоритма планирования маршрутов с взаимной координацией процессов распределенных вычислений. Оценка эффективности разработанного комплекса алгоритмических и программных средств осуществлялась с помощью методов компьютерного и натурного моделирования. Заключительная серия натурных экспериментов проводилась на примере автоматической стыковки автономных робототехнических платформ «JetBot AI kit Nvidia», выполняемой с привлечением средств и методов интеллектуального управления, визуальной навигации, технического зрения и беспроводной сетевой связи.
Результаты. Проведен анализ особенностей автоматической стыковки, как одной из задач группового управления автономными роботами в составе многоагентных систем, способных реконфигурировать свою структуру для целенаправленного изменения имеющегося набора функциональных свойств и возможностей прикладного применения. Предложена децентрализованная модификация метода поисковых случайных деревьев со встречным ростом, позволяющая обеспечить планирование перемещений автономных мобильных роботов по ходу их взаимного сближения и последующей стыковки. Разработан комплекс программно-алгоритмических средств автоматизации стыковки автономных роботов. Проведены серии модельных и натурных экспериментов, подтвердивших эффективность развиваемого подхода.
Выводы. Представленная модификация метода поисковых случайных деревьев со встречным ростом, традиционно применяемого для планирования перемещений манипуляторов и подвижных платформ, дополняет состав решаемых им задач, позволяя обеспечить автоматизацию стыковки автономных роботов. Полученные результаты открывают перспективы создания универсальных планировщиков с расширенным функционалом для систем управления автономными роботами.

Ключевые слова: автономный робот, интеллектуальное управление, групповое управление, многоагентная робототехническая система, автоматическая стыковка, метод поисковых случайных деревьев со встречным ростом

• **Поступила:** 18.02.2023 • **Доработана:** 13.06.2023 • **Принята к опубликованию:** 04.12.2023

Для цитирования: Голубов В.В., Манько С.В. Автоматизация стыковки автономных мобильных роботов на основе развития метода поисковых случайных деревьев со встречным ростом. *Russ. Technol. J.* 2024;12(1):7–14. https://doi.org/10.32362/2500-316X-2024-12-1-7-14

Прозрачность финансовой деятельности: Авторы не имеют финансовой заинтересованности в представленных материалах или методах.

Авторы заявляют об отсутствии конфликта интересов.

INTRODUCTION

Modern examples of semi-automatic and autonomous robots must have a set of capabilities consisting of: analyzing received information; evaluating the situation at the current moment of time; and planning actions with subsequent implementation in accordance with specified quality criteria.

The specific character of group control of robots within a joint grouping requires mutual coordination. This includes motion planning and routing. The analysis of the specific features of these tasks, taking into account admissible formulations, is an extremely important issue. It is this issue which largely predetermines the choice of suitable algorithmic solutions.

FEATURES OF AUTOMATIC DOCKING AS A TASK OF GROUP CONTROL OF AUTONOMOUS ROBOTS

In a wide range of tasks for group control of robots, automatic docking can also be considered typical for certain application domains [1]. An illustrative example of this can be seen in the high-precision movement of elements of large-sized structures using KUKAomniMove (KUKAAG, Germany) robotic transportation platforms (Fig. 1). Such platforms are used in the aviation and machine-building industries in the assembly of airplane bodies, high-speed trains, and other large-sized products. KUKAomniMove is a multi-wheeled robotic platform capable of operating in remote or semi-automatic control. When required, robotic transportation platforms of this type, equipped with special interface devices, can dock with each other under operator control to transport objects of the appropriate weight and size.

In the case of robots with a transformable structure, the automatic docking of mechatronic-modular elements with autonomous mobility is a composite step, resulting in the synthesis of a new configuration, as shown in Fig. 2 [2–6].

Automatic docking operations can in general be characterized in terms of the complexity of an a priori unknown environment. This environment is determined by the following factors: significant initial distance of robots from each other; lack of mutual visibility

Fig. 1. KUKAomniMove (KUKAAG, Germany) robotic transportation platform: general view of the platform and the manual remote control (a); docking facilities (b); robotic transportation platforms in the docked state (c); transportation of large-sized products (d)

(a) (b) (c)

Fig. 2. Reconfigurable mechatronic-modular robot SMORES (UPenn, USA): autonomous mechatronic module (a); automatic docking of modules (b); synthesized structure (c)

conditions; and the possible presence of obstacles. The detection range of obstacles is limited by the parameters of information-measuring devices. In cases when both robots play an active role in automatic docking, the formulation of the problem is also of special interest and complexity. One promising approach to the creation of special tools, designed to manage automatic docking functions of autonomous robots as part of the software and algorithmic support of their control systems, is the development and decentralization of the counter growth rapidly exploring random trees method: RRT-Connect.

DEVELOPMENT OF THE COUNTER GROWTH RAPIDLY EXPLORING RANDOM TREES (RRT) METHOD FOR THE AUTOMATION OF AUTONOMOUS MOBILE ROBOT DOCKING

The main feature of the RRT family methods is an original approach to the robot motion planning based on the construction of the tree-like models of changes in its admissible states [7, 8].

If in the classical version of the RRT method, the tree synthesis is performed from the point of the robot's initial state until reaching a given target state, then the RRT-Connect version assumes that both the initial and target points of the route are the root nodes of tree structures. The process of tree formation is thus completed at the moment of the first mutual interlocking of the generated branches [9]. The RRT-Connect counter growth (rapidly exploring random trees) method [10], focuses on resolving route construction between two points. It can thus serve as an effective tool for planning the movements of autonomous mobile robots of different structures [11] in the course of their mutual convergence and automatic docking [12–14].

The application of the RRT-Connect method in resolving the automation of docking of autonomous mobile robots requires its modification in accordance with requirements regulating the introduction of necessary changes and additions, as follows:

- decentralization of the computational procedure with division into parallel processes of tree generation with counter-growth according to a single algorithm for both participants of the docking operation;
- coordination of processes performed at the level of mutual exchange of data on the current configuration of formed trees and observed constraints;
- initialization of root nodes of synthesized trees at the points of initial location of the robots before the start of their docking operation with reference to a common coordinate system;
- simultaneous completion of tree generation processes at the first mutual interlocking of branches.

Figure 3 shows a generalized block diagram of the algorithm which implements a decentralized modification of the counter growth RRT-Connect method for robot motion planning during automatic docking. The software implementation of the algorithm must enable the constructed tree and the entire route network to be reinitialized for transformation when detecting obstacles as the robot moves along the previously laid path.

The basic ability of automatic docking of autonomous robots in an obstacle-laden environment based on the decentralized modification of the RRT-Connect method is confirmed by the results of complex computer simulation. Fragments are shown in Fig. 4.

EXPERIMENTAL TESTING OF SOFTWARE-ALGORITHMIC RESOURCES FOR AUTOMATION OF THE AUTONOMOUS MOBILE ROBOTS DOCKING BASED ON THE DECENTRALIZED MODIFICATION OF THE RRT-CONNECT METHOD

A series of *in situ* experiments at a specialized laboratory test site was carried out, in order to assess the practical feasibility of an approach based on the application of a decentralized modification of the counter growth RRT-Connect to automate the docking of the autonomous mobile robots. A general view of the research site is shown in Fig. 5a. It was designed to debug and verify the means and methods of intelligent and group control of autonomous mobile objects. It uses a large fleet of mobile robotic platforms such as Jetson

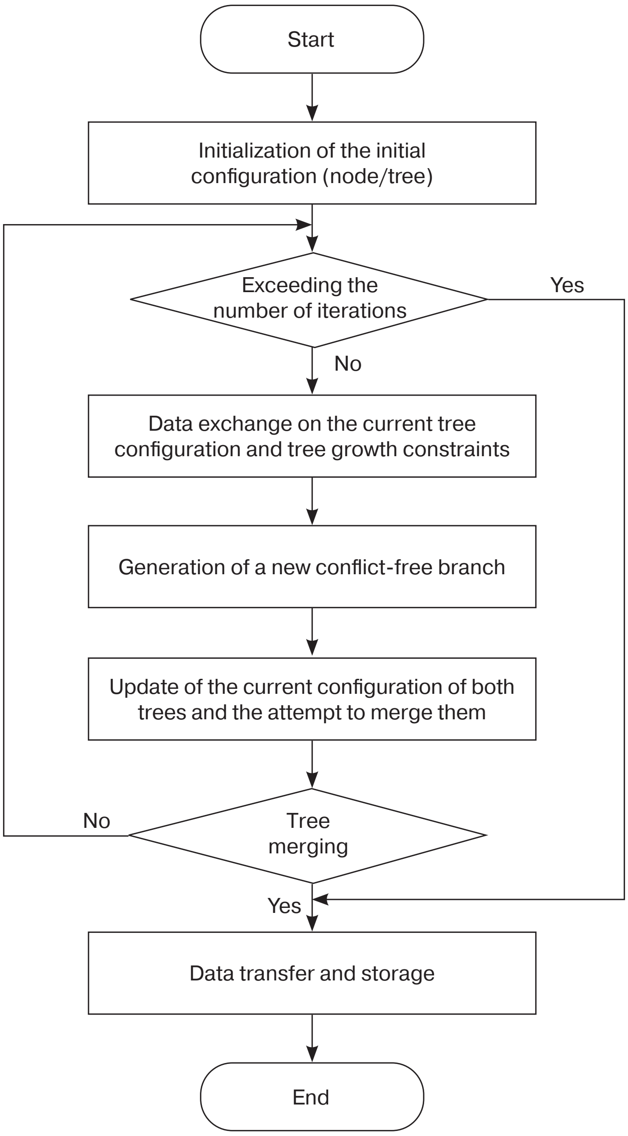

Fig. 3. Generalized block diagram of an algorithm implementing a decentralized modification of the RRT-Connect method for robot motion planning during automatic docking

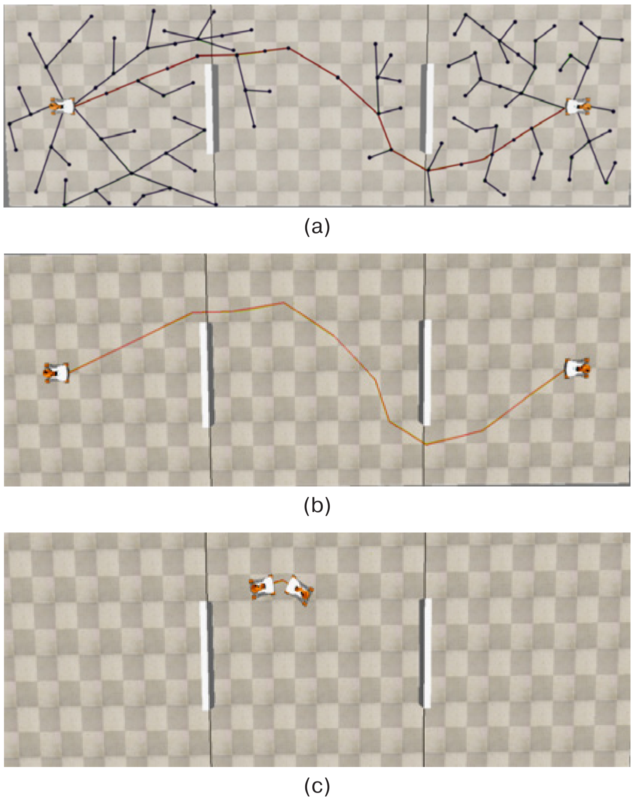

Fig. 4. Computer simulation of automatic docking of autonomous robots in an obstacle-ridden environment based on decentralized modification of the counter growth rapidly exploring random trees method RRT-Connect

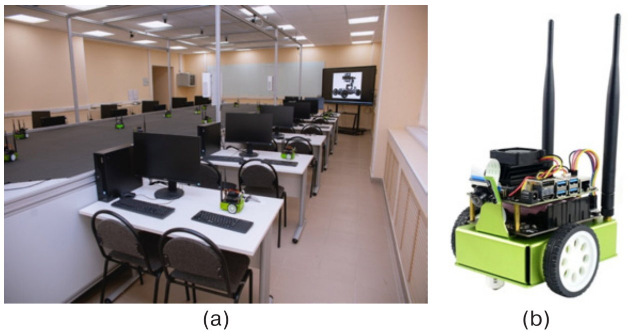

Fig. 5. Specialized laboratory testing site for debugging and verification of tools and methods of intellectual and group control of mobile objects (a) based on Jetson Nano JetBot AI kit Nvidia autonomous mobile robotics platforms (b)

Nano JetBot AI kit Nvidia (NVIDIA and Waveshare, USA)[1], network equipment for maintaining wireless communication channels and external surveillance cameras for monitoring the working environment and resolving visual navigation tasks.

The JetBot AI kit Nvidia Mobile robotics platform is shown in Fig. 5b). It has a wide range of potential capabilities and is equipped with a Jetson Nano (NVIDIA, Waveshare, USA) high-performance microcomputer, a small video camera (and, if necessary, other information-measuring means), a wireless network communication device, and an autonomous power supply based on rechargeable batteries.

The generalized structure of the set of software-algorithmic tools for automatic docking of the autonomous robots is shown in Fig. 6 and includes:

- motion planning subsystem based on a decentralized version of the RRT-Connect method;
- navigation subsystem to determine the current coordinates and orientation of the robot;
- sub-system for obstacle detection and mapping subsystem based on on-board camera image processing;

[1] https://www.waveshare.com/jetbot-ai-kit.htm. Accessed January 15, 2022.

- wireless network communication subsystem for mutual data exchange with the second docking participant;
- motion control subsystem, which ensures movement of the robot along the formed route.

The principles of the navigation subsystem construction are based on the image processing from external surveillance cameras with recognition and localization of ArUco-labels [15] used for robot marking, as shown in Fig. 7.

The requisite information interaction of autonomous robots at all stages of planning and implementation of their automatic docking is achieved in accordance with the standards of Wi-Fi-technology of wireless network communication using the user datagram protocol.

The motion planning subsystem is based on the decentralized version of the counter growth rapidly exploring random trees method RRT-Connect. It forms a route network for building the trajectory of the robot's convergence with the second docking participant. Mutually directed tree growth, simultaneously generated by the planners of both robots, is coordinated through wireless network communication channels with the exchange of necessary data sets.

The composition of the information transmitted reflects the current configuration of trees, as well as the location of obstacles observed by the subsystem for their detection and mapping. At the same time, the areas outside the coverage area of the external situation sensory control means are considered free of obstacles.

The end of the planning stage at the moment of the first interlocking of the branches of the synthesized trees determines the transition to the next stage of the automatic docking of the autonomous robots. This is associated with the control of their movement along the routes formed towards the proposed meeting point.

When previously unobserved obstacles are detected, the robot movement is suspended. The resumption of schedulers and restart of route construction procedures are based on a decentralized modification of the counter growth RRT-Connect method.

Secondary initialization of the scheduler requires the iterative implementation of the following actions:

- re-initialization of the route tree, checking the conditions of compliance with new constraints for

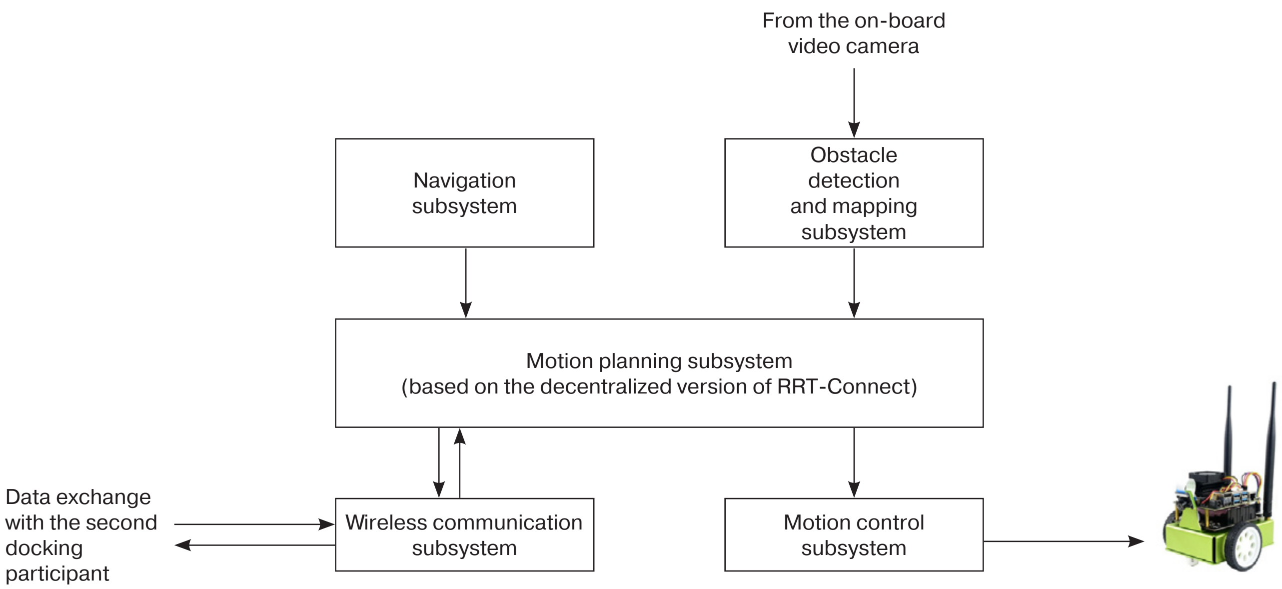

Fig. 6. Generalized structure of the on-board set of software-algorithmic means for the automatic docking of autonomous mobile robots

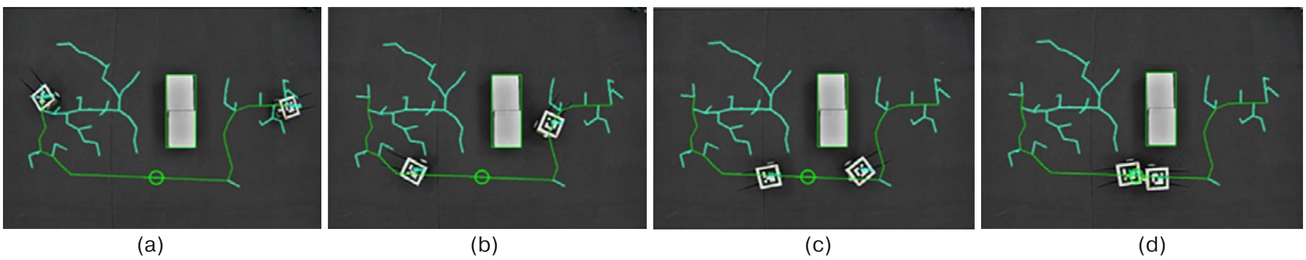

Fig. 7. Fragments of a full-scale experiment on emulation of automatic docking of the autonomous mobile robots

intersection of its branches with the boundaries of detected obstacles;
- removing all branches of the tree which do not satisfy the check conditions;
- removing branches that have lost connection with the root vertex as a result of the previous step;
- if the integrity of the path to the rendezvous point with the second robot is broken, the process of generating the reconstructed tree is resumed before the route to the new meeting point is established;
- transition to the motion continuation phase.

The workability and efficiency of autonomous robots automatic docking based on the decentralized modification of the counter growth RRT-Connect method are confirmed by the results of full-scale experiments, fragments of which are presented in Fig. 7.

CONCLUSIONS

An analysis of Russian and foreign literature shows that the emphasis placed on the development of the rapidly exploring random trees method is due to the wide possibilities of its application in resolving motion planning problems of both mobile and manipulation robots. These include robotic systems with an onboard manipulator (including those with a redundant or reconfigurable structure) on a transport platform. The modification presented herein of the method complements the composition of problems resolved by it. It also allows us to enable the automation of docking of autonomous robots. The results obtained open potential for the creation of universal schedulers with extended functionality for control systems of autonomous robots.

Authors' contribution. All authors equally contributed to the research work.

REFERENCES

1. Wang Y., Shan M., Yue Y., Wang D. Autonomous Target Docking of Nonholonomic Mobile Robots Using Relative Pose Measurements. *IEEE Trans. Ind. Electron*. 2021;68(8):7233–7243. https://doi.org/10.1109/TIE.2020.3001805
2. Davey J., Kwok N., Yim M. Emulating self-reconfigurable robots – design of the SMORES system. In: *2012 IEEE/RSJ International Conference on Intelligent Robots and Systems*. 2012. P. 4464–4469. https://doi.org/10.1109/IROS.2012.6385845
3. Tosun T., Daudelin J., Jing G., Kress-Gazit H., Campbell M., Yim M. Perception-informed autonomous environment augmentation with modular robots. In: *2018 IEEE International Conference on Robotics and Automation*. 2018. P. 6818–6824. https://doi.org/10.1109/ICRA.2018.8463155
4. Liu C., Lin Q., Kim H., Yim M. *SMORES-EP, a Modular Robot with Parallel Self-assembly*. arXiv preprint or arXiv:2014.00800v2. https://doi.org/10.48550/arXiv.2104.00800
5. Knizhnik G., Yim M. Docking and Undocking a Modular Underactuated Oscillating Swimming Robot. In: *2021 IEEE International Conference on Robotics and Automation*. 2021. P. 6754–6760. https://doi.org/10.1109/ICRA48506.2021.9562033
6. Sohal S.S., Sebastian B., Ben-Tzvi P. Autonomous Docking of Hybrid-Wheeled Modular Robots with an Integrated Active Genderless Docking Mechanism. *J. Mechanisms Robotics.* 2021;14(1):011010. https://doi.org/10.1115/1.4051519
7. LaValle S.M., Kuffner J. Rapidly-Exploring Random Trees: Progress and Prospects. In: Donald B., Lynch K., Rus D. (Eds.). *Algorithmic and Computational Robotics*. NY: CRC Press; 2001. P. 293–308. https://doi.org/10.1201/9781439864135
8. Голубов В.В., Манько С.В. Особенности и перспективы применения метода поисковых случайных деревьев для планирования перемещений автономных роботов. *Russ. Technol. J.* 2023;11(6):16–27. https://doi.org/10.32362/2500-316X-2023-11-6-16-27
[Golubov V.V., Manko S.V. Features and perspectives of application of the search random trees method for movement planning of autonomous robots. *Russ. Technol. J.* 2023;11(6):16–27 (in Russ.). https://doi.org/10.32362/2500-316X-2023-11-6-16-27]
9. Kuffner J., LaValle S.M. RRT-Connect: An Efficient Approach to Single-Query Path Planning. In: *2000 IEEE International Conference on Robotics and Automation*. 2000. P. 995–1001. https://doi.org/10.1109/ROBOT.2000.844730
10. Kang J.G., Lim D.W., Choi Y.S., Jang W.J., Jung J.W. Improved RRT-Connect Algorithm Based on Triangular Inequality for Robot Path Planning. *Sensors*. 2021;21(2):333. https://doi.org/10.3390/s21020333
11. Gravot F., Haneda A., Okada K., Inaba N. Cooking for humanoid robot, a task that needs symbolic and geometric reasonings. In: *2006 IEEE International Conference on Robotics and Automation*. 2006. P. 462–467. https://doi.org/10.1109/ROBOT.2006.1641754
12. Zahroof T., Bylard A., Shageer H., Pavone M. Perception-Constrained Robot Manipulator Planning for Satellite Servicing. In: *2019 IEEE Aerospace Conference*. 2019. P. 1–10. https://doi.org/10.1109/AERO.2019.8741569
13. Klemm S., Essinger M., Oberländer J., Zofka M.R., Kuhnt F., Weber M., Kohlhaas R., Kohs A., Roennau A., Schamm T., Zöllner J.M. Autonomous multi-story navigation for valet parking. In: *2016 IEEE 19th International Conference on Intelligent Transportation Systems*. 2016. P. 1126–1133. https://doi.org/10.1109/ITSC.2016.7795698
14. Han P., Li G., Zhang H. Leveraging Past Experience for Path planning of Marine Vessel: A Docking Example. *Modeling, Identification and Control*. 2022;43(3):101–109. http://doi.org/10.4173/mic.2022.3.2
15. Garrido-Jurado S., Muñoz-Salinas R., Madrid-Cuevas F.J., Marin-Jiménez M.J. Automatic generation and detection of highly reliable fiducial markers under occlusion. *Pattern Recognition*. 2014;47(6):2280–2292. https://doi.org/10.1016/j.patcog.2014.01.005

About the authors

Vladimir V. Golubov, Postgraduate Student, Department of Problems Control, Institute of Artificial Intelligence, MIREA – Russian Technological University (78, Vernadskogo pr., Moscow, 119454 Russia). E-mail: golubov@mirea.ru. https://orcid.org/0009-0007-9227-6184

Sergey V. Manko, Dr. Sci. (Eng.), Professor, Department of Problems Control, Institute of Artificial Intelligence, MIREA – Russian Technological University (78, Vernadskogo pr., Moscow, 119454 Russia). Laureate of the Government Prize of the Russian Federation in the field of education, Member of the Scientific Council on Robotics and Mechatronics of the Russian Academy of Sciences. E-mail: manko@mirea.ru. Scopus Author ID 55761014700, RSCI SPIN-code 2070-1592, https://orcid.org/0000-0002-6297-8894

Об авторах

Голубов Владимир Васильевич, аспирант, кафедра проблем управления Института искусственного интеллекта ФГБОУ ВО «МИРЭА – Российский технологический университет» (119454, Россия, Москва, пр-т Вернадского, д. 78). E-mail: golubov@mirea.ru. https://orcid.org/0009-0007-9227-6184

Манько Сергей Викторович, д.т.н., профессор, кафедра проблем управления Института искусственного интеллекта ФГБОУ ВО «МИРЭА – Российский технологический университет» (119454, Россия, Москва, пр-т Вернадского, д. 78). Лауреат премии Правительства Российской Федерации в области образования, Член научного Совета по робототехнике и мехатронике Российской академии наук. E-mail: manko@mirea.ru. Scopus Author ID 55761014700, SPIN-код РИНЦ 2070-1592, https://orcid.org/0000-0002-6297-8894

Translated from Russian into English by Lyudmila O. Bychkova
Edited for English language and spelling by Dr. David Mossop

Multiple robots (robotic centers) and systems. Remote sensing and non-destructive testing

Роботизированные комплексы и системы. Технологии дистанционного зондирования неразрушающего контроля

UDC 621.396.69
https://doi.org/10.32362/2500-316X-2024-12-1-15-29

RESEARCH ARTICLE

Detection of defects in printed circuit boards by the acoustic emission method

Saygid U. Uvaysov,
Ngoc T. Luu,
Cong D. Nguyen,
The H. Vo,
Aleksey V. Dolmatov @

MIREA – Russian Technological University, Moscow, 119454 Russia
@ *Corresponding author, e-mail: dolmatov@mirea.ru*

Abstract
Objectives. Defects in the form of layering may occur during lamination in the production of multilayer printed circuit boards (MPCB). These defects cannot be detected by optical and electrical methods of output control. However, they can lead to breaches of the mechanical mode of operation and failures while running radioelectronic devices. In order to detect such defects, the acoustic emission (AE) method is proposed. This is based on the occurrence and propagation of acoustic waves in MPCBs caused by the presence of defects. The aim of this study is to investigate the possibility of using the AE method to detect defects in multilayer printed circuit boards. These defects can occur, in particular, in the lamination process.
Methods. A mechanical processes modeling program (for research on the MPCB model) and various samples of two-layer printed circuit boards with pre-introduced defects (for experimental studies) were used to study the propagation of acoustic signals in the MPCB in the presence of defects. A solenoid mounted on the MPCB was used as a source of acoustic signals, while a piezoelectric sensor was used to receive signals. Data processing was carried out by comparing AE signals obtained for a serviceable MPCB sample and for MPCB samples with defects.
Results. Simulation of the acoustic signal propagation in MPCBs in serviceable and faulty (with a rectangular defect in the form of delamination) states was carried out to show the difference in the received signals at the sensor installation point. Experimental studies were also conducted to examine the AE method applicability for detecting defects of various sizes and quantities.
Conclusions. The studies demonstrated that the AE method allows the presence of defects in MPCB occurring during the lamination process to be detected effectively and reliably. This study proposes a new approach to non-destructive testing of MPCB using the AE method. This method significantly increases the reliability of MPCBs and the efficiency of their production processes.

Keywords: acoustic emission, multilayer printed circuit board, defect detection, delamination, non-destructive testing

• **Submitted:** 05.05.2023 • **Revised:** 03.07.2023 • **Accepted:** 12.12.2023

For citation: Uvaysov S.U., Luu N.T., Nguyen C.D., Vo Th.H., Dolmatov A.V. Detection of defects in printed circuit boards by the acoustic emission method. *Russ. Technol. J.* 2024;12(1):15–29. https://doi.org/10.32362/2500-316X-2024-12-1-15-29

Financial disclosure: The authors have no a financial or property interest in any material or method mentioned.

The authors declare no conflicts of interest.

НАУЧНАЯ СТАТЬЯ

Обнаружение дефектов в многослойной печатной плате методом акустической эмиссии

С.У. Увайсов,
Н.Т. Лыу,
К.Д. Нгуен,
Т.Х. Во,
А.В. Долматов @

МИРЭА – Российский технологический университет, Москва, 119454 Россия
@ *Автор для переписки, e-mail: dolmatov@mirea.ru*

Резюме

Цели. При производстве многослойных печатных плат (МПП) в процессе ламинирования в них могут возникать дефекты в виде расслоений. Они не обнаруживаются оптическими и электрическими методами выходного контроля, но в процессе эксплуатации радиоэлектронного средства могут вызвать нарушения механического режима работы и привести к отказам. Для обнаружения таких дефектов предлагается использовать метод акустической эмиссии (АЭ), основанный на возникновении и распространении акустических волн в МПП, вызванных наличием дефектов. Целью данного исследования является изучение возможности использования метода АЭ для обнаружения дефектов МПП, возникающих, в частности, в процессе ламинирования.

Методы. Для исследования распространения акустических сигналов в МПП при наличии дефектов использовались программа моделирования механических процессов (для исследования на модели МПП) и различные образцы двухслойных печатных плат с заранее внесенными дефектами (для экспериментальных исследований). В качестве источника акустических сигналов использовался соленоид, установленный на МПП, а для приема сигналов – пьезоэлектрический датчик. Обработка данных проводилась путем сравнения сигналов АЭ, полученных для исправного образца МПП и для образцов МПП с дефектами.

Результаты. Проведено моделирование распространения акустического сигнала в МПП в исправном и неисправном (с прямоугольным дефектом в виде расслоения) состояниях, которое показало различие полученных сигналов в точке установки датчика. Также были проведены экспериментальные исследования с целью изучения применимости метода АЭ для выявления дефектов различного размера и количества.

Выводы. Исследования показали, что метод АЭ позволяет достаточно эффективно и достоверно обнаруживать наличие дефектов в МПП, возникающих в процессе ламинирования. В данном исследовании предлагается новый подход к неразрушающему контролю МПП с использованием метода АЭ, который может значительно повысить надежность МПП и эффективность процессов их производства.

Ключевые слова: акустическая эмиссия, многослойная печатная плата, обнаружение дефектов, расслоение, неразрушающий контроль

• **Поступила:** 05.05.2023 • **Доработана:** 03.07.2023 • **Принята к опубликованию:** 12.12.2023

Для цитирования: Увайсов С.У., Лыу Н.Т., Нгуен К.Д., Во Т.Х., Долматов А.В. Обнаружение дефектов в многослойной печатной плате методом акустической эмиссии. *Russ. Technol. J.* 2024;12(1):15–29. https://doi.org/10.32362/2500-316X-2024-12-1-15-29

Прозрачность финансовой деятельности: Авторы не имеют финансовой заинтересованности в представленных материалах или методах.

Авторы заявляют об отсутствии конфликта интересов.

INTRODUCTION

Multilayer printed circuit boards (MPCBs) are an important component in many electronic devices. As such, their quality control is critical to ensure the reliability and functionality of the devices. One of the most important steps in MPCB production is the lamination process. This involves joining multiple layers of copper-clad dielectric material, in order to form a multilayer board[1]. Laminating is prone to defects such as delamination, cracks, and voids which can degrade the PCB electrical and mechanical properties.

A variety of non-destructive testing methods such as X-ray inspection, optical microscopy, and ultrasonic inspection have been developed to detect defects in MPCBs. However, these methods have limitations in terms of cost, time, and accuracy. The non-destructive acoustic emission (AE) method has attracted increasing attention in recent years due to its high sensitivity, real-time monitoring capability and non-contact defect detection capability[2].

Acoustic emission is a phenomenon associated with the generation of elastic waves as a result of a sudden and localized energy release within the material [1]. The AE waves can be captured and analyzed, in order to obtain information about the location, magnitude, and type of defect in MPCB material. Using the AE method for detecting defects in MPCB has been investigated by scientists and experts [2–4].

This study considers the possibility of applying the AE method to detect defects occurring in MPCB lamination process. A solenoid is used as a source for generating AE signals, and a piezoelectric plate is used as a sensor for capturing signals. The signals obtained for the defective and serviceable MPCBs are compared, in order to evaluate the efficiency of the AE method for detecting defects.

The aim of the study was to develop a non-destructive testing method for detecting defects in MPCB occurring during the lamination process. This can significantly improve the reliability and efficiency of MPCB production. The work investigates whether the AE method can effectively detect defects in MPCB which may be formed during the lamination process. If this is so, then what are the advantages and limitations of this method compared to other existing ones.

LITERATURE REVIEW

Several studies have investigated the use of AE method for detecting defects in PCBs. Zhao et al. (2015) used the AE method for detecting defects in PCB during the hole drilling process [5]. It was discovered that AE signals can be used to distinguish between different types of defects such as incomplete hole, burr, and breakthrough. Liu et al. (2018) developed a method for detecting delamination in MPCB using AE [6]. This method used a pencil lead breakage as an AE source and a piezoelectric transducer as a sensor for detecting AE signals. The result showed that AE signals can be used to detect the presence and location of delamination in MPCBs.

Chen et al. (2020) investigated the use of AE method for detecting defects in flexible PCB [7]. For this purpose, a piezoelectric sensor was used to detect AE signals generated by needle puncture of a flexible PCB. It was found that AE signals can be used to determine the location and severity of the defect and that this method is sensitive to defects as small as 0.5 mm.

Although previous studies have shown the potential of the AE method for detecting defects in PCB, there are still problems in its implementation in diagnostic practice. One of the problems is the need to use complex algorithms for processing and analyzing different types of signals and noise [8, 9]. Another problem is the selection and optimization of the AE source and AE sensor placement which can affect the sensitivity and accuracy of the method [10].

Despite these problems, the AE method for detecting defects in MPCBs has significant advantages. The AE method is a non-destructive and non-contact method which can be performed in real time without the need

[1] Pokrovskaya M.V., Popova T.A. *Materials and structural elements of the REM.* Textbook. Part 1: *Material science and structural materials.* Moscow: RTU MIREA; 2021. 200 p. (in Russ.).

[2] Nosov V.V., Yamilova A.R. *Acoustic emission method.* Textbook. St. Petersburg: Lan; 2022. 304 p. (in Russ.).

for expensive equipment[3] [11, 12]. The AE signals can provide information about the location and type of defect, allowing the root cause of the faulty state to be identified and the quality control of MPCB production to be improved [13–15].

MODELING OF ACOUSTIC SIGNAL PROPAGATION IN MPCB

Initial data for modeling

In order to verify the effectiveness of the analytical simulation, *ABAQUS*[4] software was used for the numerical analysis of the accuracy of the piezoelectric sensor response in the MPCB model. Plate modeling MPCB is made of FR 4 foil-coated fiberglass (WAVGAT authorization store, China) having 0.2 × 0.15 × 0.0015 m in size. The characteristics of FR 4 material are presented in Table 1.

Table 1. Material parameters of the studied MPCB

Material	Density, kg/m^3	Elastic modulus, hPa	Poisson ratio
FR 4	1850	24	0.136

Transient excitation is required to model the defect effect on the AE signal propagation. In this paper, AE signal is excited using the time dependence function for excitation force $F(t)$ (Fig. 1) [15] represented mathematically as follows:

$$F(t)=\begin{cases} F_{\max}\left(t/t_e\right), & t\le t_e,\\ F_{\max}(2-t_e t), & t_e\le t\le 2t_e,\\ 0, & t\ge 2t_e,\end{cases}$$

where t_e is the time of achieving the maximum value of excitation force $F_{\max}$.

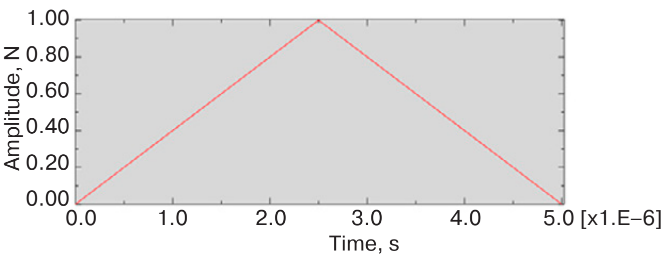

Fig. 1. Function *F*(*t*)

The schematic diagram of the sensor and AE signal source arrangement as well as the model in the *ABAQUS* software are shown in Fig. 2.

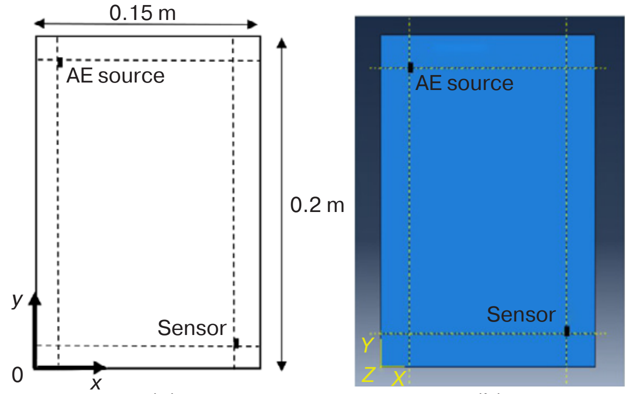

(a) (b)

Fig. 2. The schematic diagram of the sensor and AE signal source arrangement (a) and the model in the *ABAQUS* software (b)

In order to model the presence of a delamination defect in the MPCB sample, a rectangular area 3 × 3.7 cm was created in the *ABAQUS* software. The MPCB model with a rectangular defect is shown in Fig. 3.

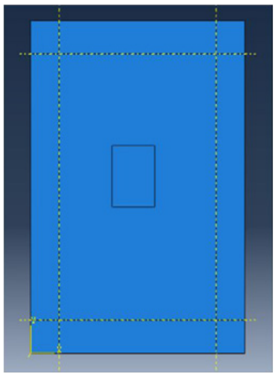

Fig. 3. The MPCB model with rectangular defect of 3 × 3.7 cm in size

The simulation studies wave propagation and piezo sensor response to AE signals generated by a virtual solenoid in the presence of a defect. The resulting signals are used for further analysis and comparison with the signals received from the MPCB sample without defect. The experimental results enable the possibility of using this approach for detecting defect in MPCB to be evaluated.

Modeling result

The acoustic wave propagation at certain time instants (0.12, 0.32, 0.64, 0.84, and 1.16 μs) in the absence of defect in MPCB is shown in Fig. 4.

The sensor signal received in modeling in the absence of a defect in MPCB is shown in Fig. 5.

---

[3] Sych T.V. *The perfection of the acoustic-emission control technology based on the finite-element analysis of the acoustic path.* Diss. Cand. Sci. (Eng.). Moscow: SGUPS; 2016. 149 p. (in Russ.).

[4] https://www.3ds.com/products-services/simulia/products/abaqus/. Accessed August 30, 2023.

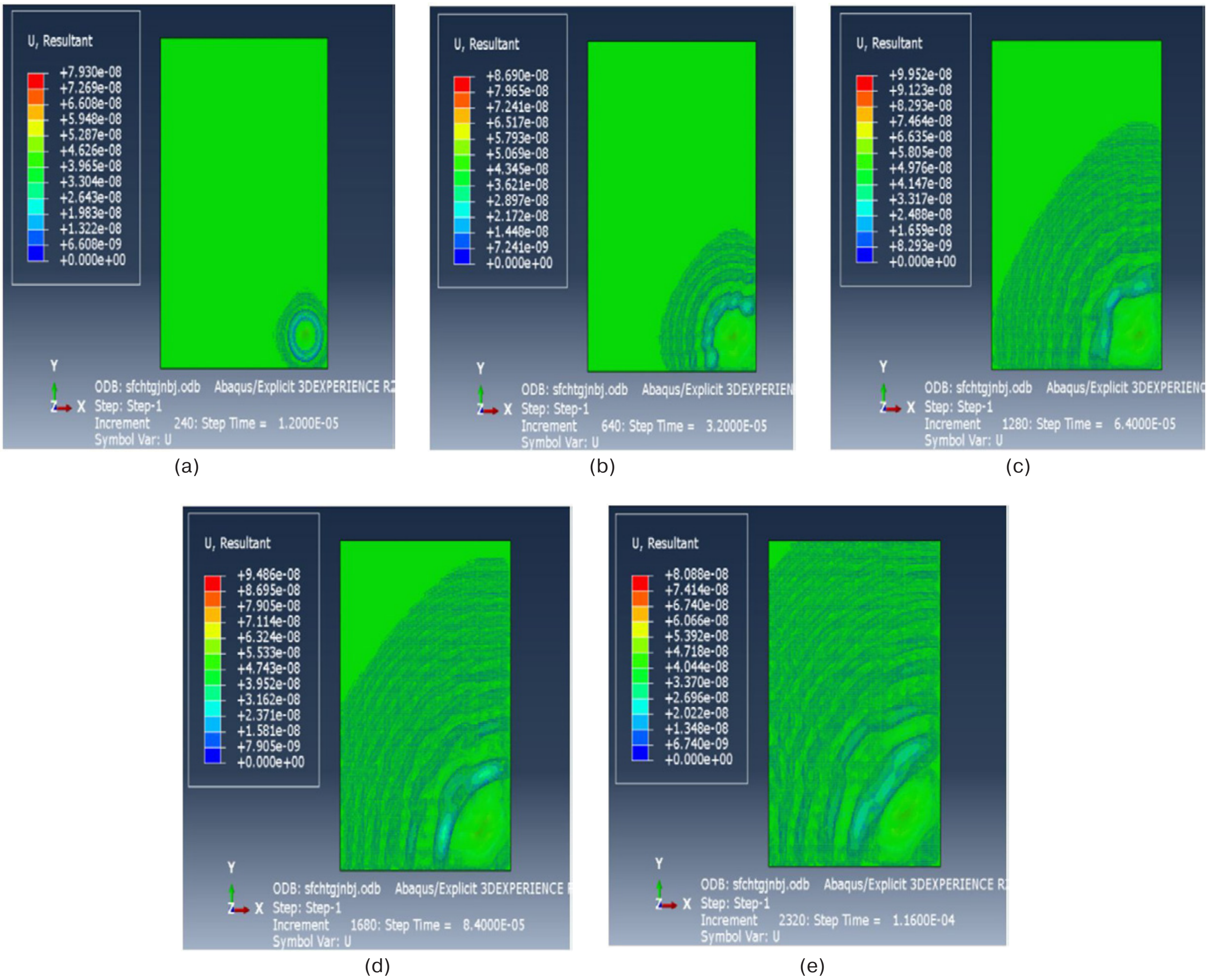

Fig. 4. Acoustic wave propagation in MPCB in the absence of a defect at time instants: (a) 0.12 µs, (b) 0.32 µs, (c) 0.64 µs, (d) 0.84 µs, and (e) 1.16 µs

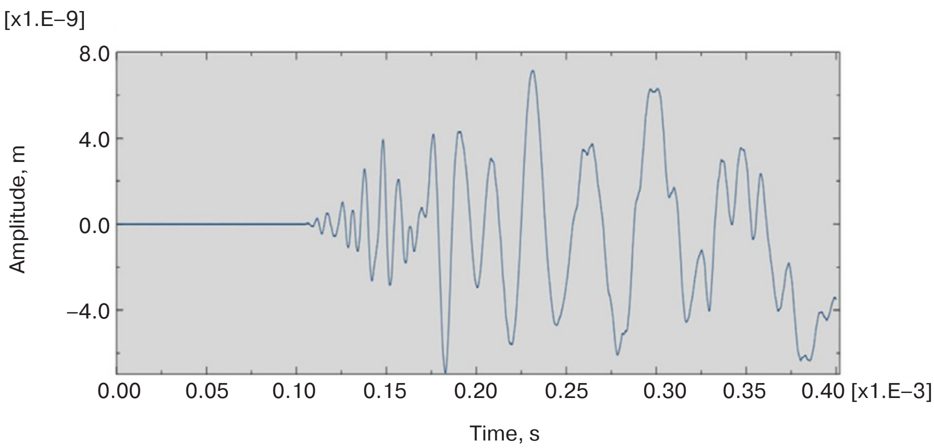

Fig. 5. Sensor signal in the absence of defect in MPCB

Similarly, in the presence of a defect in MPCB (defect in the form of the 3 × 3.7 cm rectangle), the process of acoustic wave propagation through MPCB at the same time instants (0.12, 0.32, 0.64, 0.84, and 1.16 µs) and the sensor signal are shown in Figs. 6. and 7, respectively.

Next, the sensor signals are compared for the absence and the presence of the defect (Fig. 8).

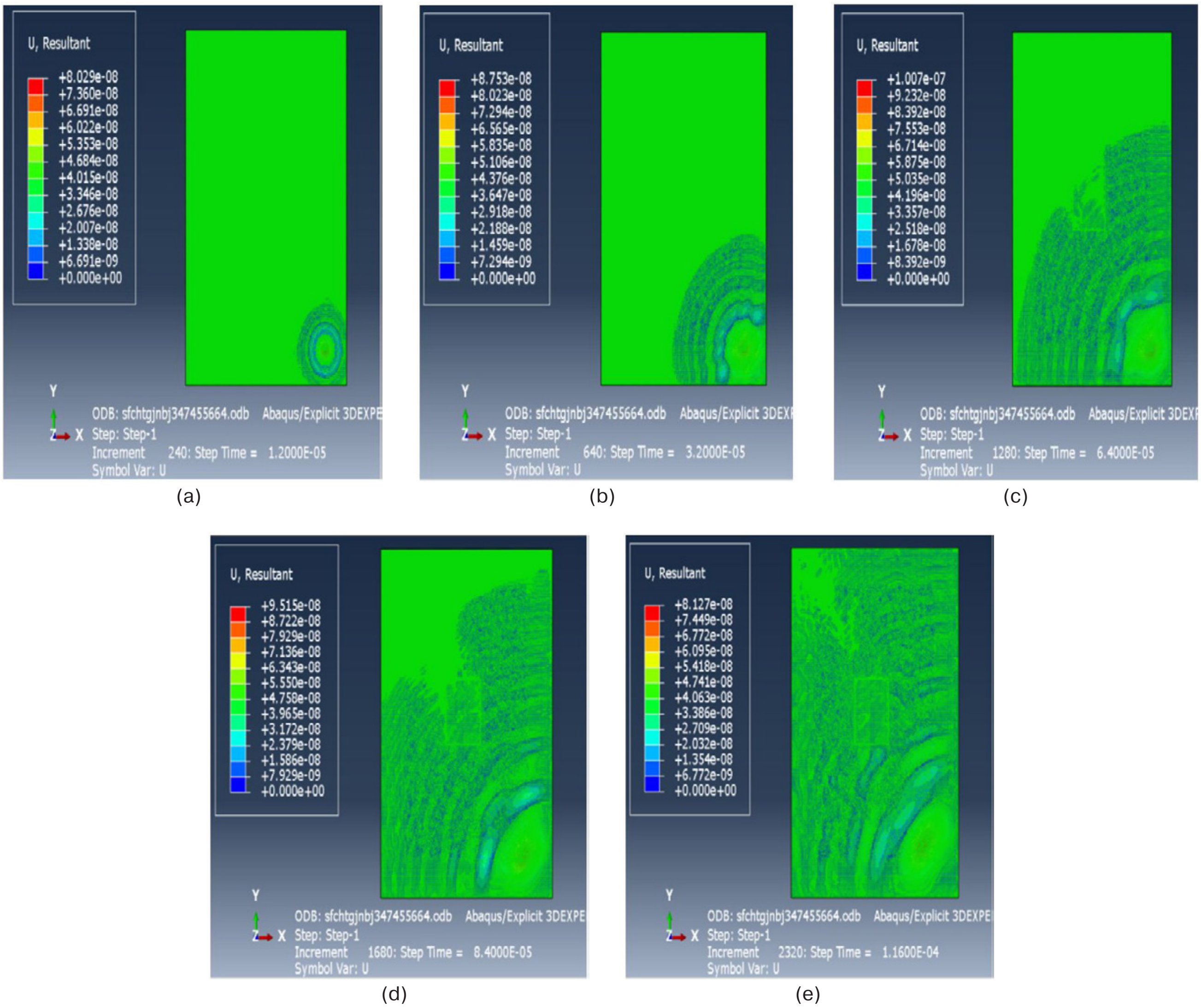

Fig. 6. Acoustic wave propagation in MPCB in the presence of the 3 × 3.7 cm defect at the following time instants: (a) 0.12 μs, (b) 0.32 μs, (c) 0.64 μs, (d) 0.84 μs, and (e) 1.16 μs

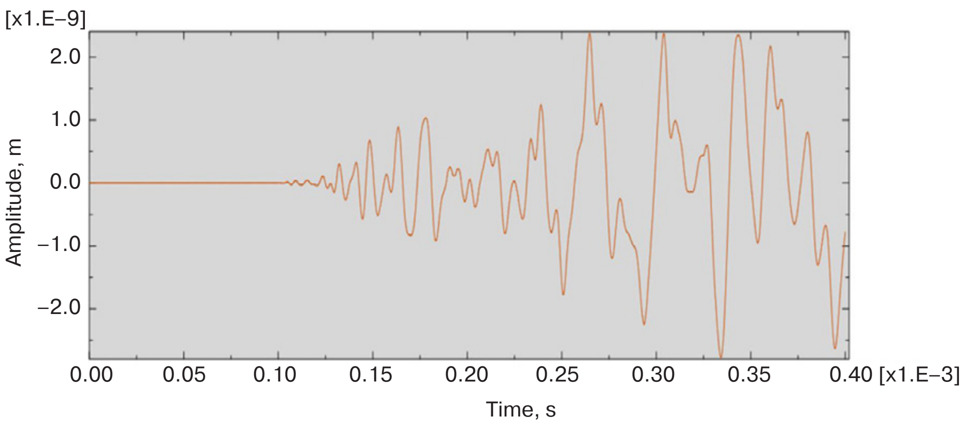

Fig. 7. Sensor signal in the presence of a defect in MPCB

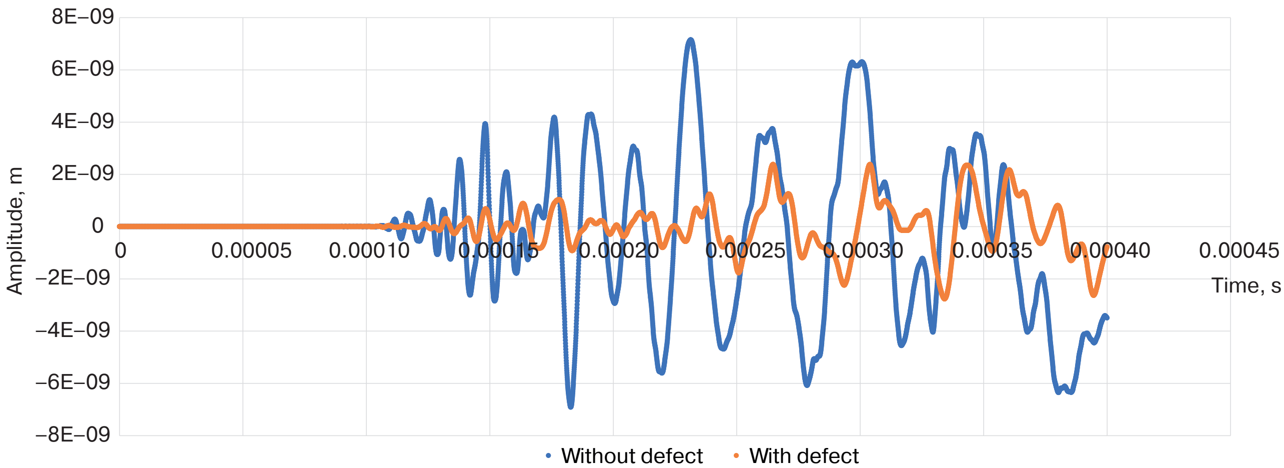

Fig. 8. Comparison of AE signals from the sensor with and without a defect in MPCB

The comparative results of the signals show that the presence of a defect causes distortion in the wave propagation process. This results in significant differences (several times) in the signal amplitude and signal arrival time compared to the case without a defect.

EXPERIMENTAL STUDIES ON A TWO-LAYER PRINTED CIRCUIT BOARD

Experimental setup description

An experimental setup was designed for this study (Fig. 9). It consists of: UNO R3 ATMEGA16U2 + MEGA328P chip for Arduino UNO R3 with breadboard and USB cable (1) (IGMOPNRQ module store, China); a piezoelectric plate of 27 mm in diameter (2) (KY WIN ROBOT store, China); V3 power key (3) (Amperka, Russia); 12 VAC source (4) (Teslocom, Russia); TAU-0520 solenoid tuned to 10 Hz frequency (5) (Amperka, Russia); two-layer printed circuit board (6) (WAVGAT authorization store, China); computer equipped with *Audacity* software[5] used for capturing and analyzing acoustic signals (7).

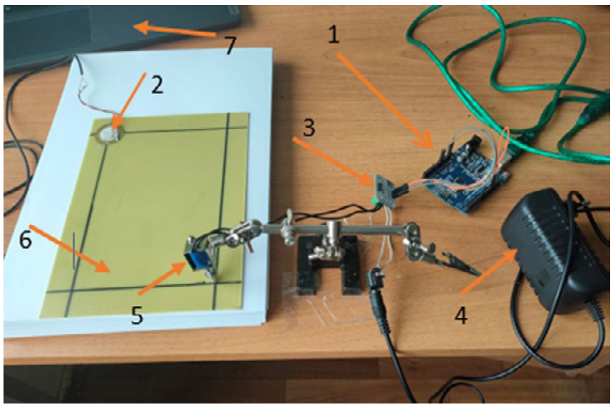

Fig. 9. The experimental setup

The technical characteristics of the acoustic signal sensor are given in Table 2. The image and view of the sensor are presented in Fig. 10.

[5] https://www.audacityteam.org/. Accessed August 30, 2023.

Table 2. Sensor parameters

No.	Parameter	Parameter value
1	Resonant frequency	3.5 ± 0.5 KHz
2	Resonant resistance	<300 Ohm
3	Static capacity	28000 pF ± 30%
4	Storage temperature	from −30 to +70°C
5	Plate material	copper
6	External diameter *D*	27 ± 0.1 mm
7	Internal diameter *d*	20 ± 0.2 mm
8	Thickness *t*	0.15 ± 0.05 mm
9	Thickness *T*	0.35 ± 0.05 mm

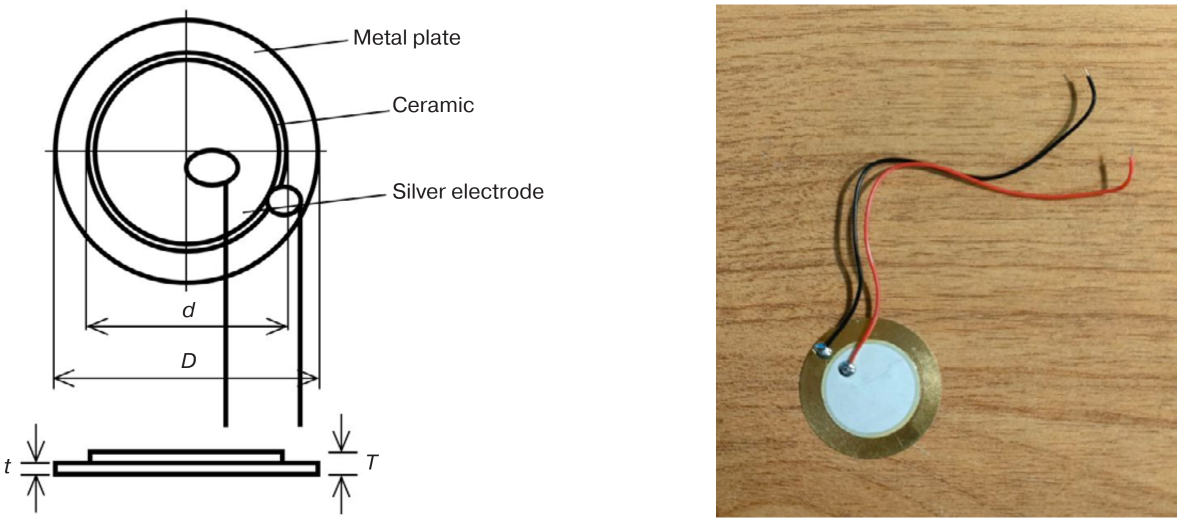

(a) (b)

Fig. 10. Drawing (a) and view (b) of the piezoelectric sensor of acoustic signals

In the experimental study, a piezoelectric plate was placed on the MPCB surface and was used to capture sound waves propagating after the solenoid impacts on the MPCB. The working mechanism of the piezoelectric sensor operates in the presence of mechanical motion in the solenoid only. In its absence, no electrical signal is generated. This approach allows the level of external noise to be significantly reduced, since the possibility of signal recording occurs only when the solenoid impacts on the MPCB.

Experimental results in the absence of a defect in PCB

Audacity software is used for acquiring and processing the signals. The software uses a normalized representation of acoustic signals as floating point numbers from −1 to +1; where −1 stands for the minimum possible sound level; while +1 represents the maximum one. This type of representation allows *Audacity* to accurately represent the full range of sound levels, while avoiding any potential loss of accuracy which might occur with integer-based representations. In addition, it simplifies mathematical operations on audio signals such as mixing and processing, since all signals are represented on the same scale.

Firstly, experimental studies are conducted on a two-layer PCB without defects. Three mechanical shocks were generated by the solenoid impacting PCB (with an interval of 3 s between shocks), and the acoustic signals were recorded by the piezoelectric sensor (Fig. 11). The comparison of the resulting signals is shown in Fig. 12. It was found that the signals received after three shocks are the same, thus indicating the PCB material uniformity.

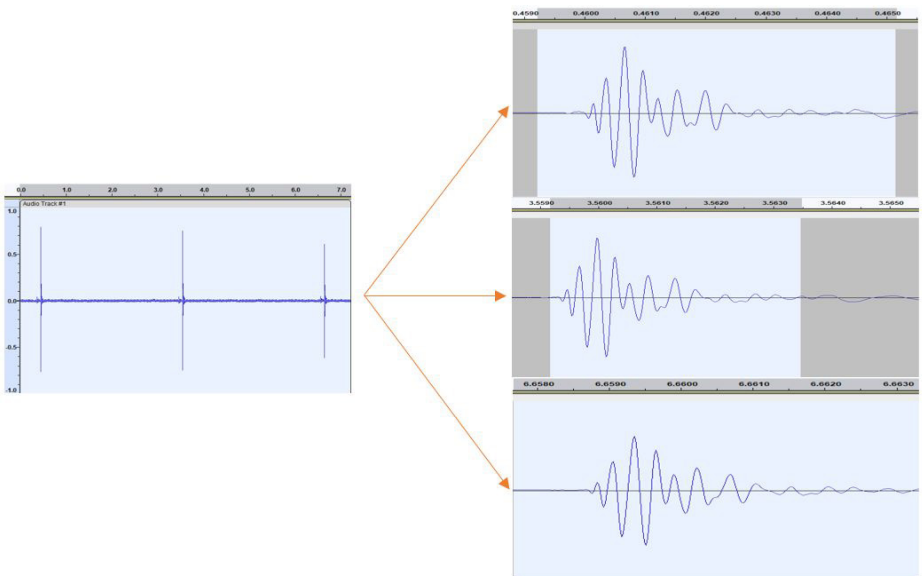

Fig. 11. The signal received from the sensor after 3 shocks in the absence of a defect

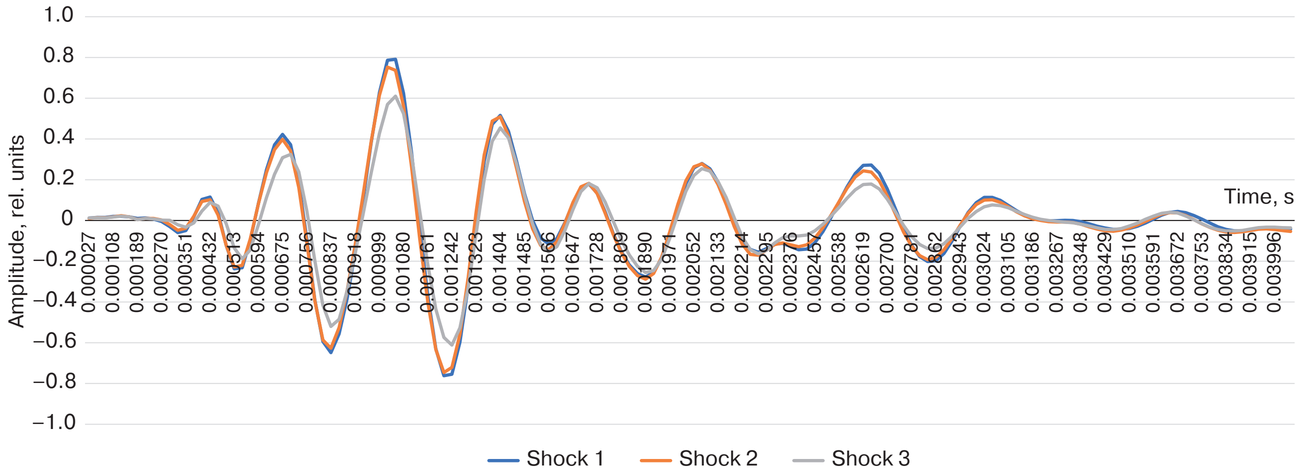

Fig. 12. Comparison of sensor signals after 3 solenoid shocks on PCB without a defect

Experimental results in the presence of a defect in PCB

Next, experiments were performed on a board with a rectangular defect of 3 × 3.7 cm shown in Fig. 13. Three mechanical solenoid shocks on PCB were recorded in the same way (Fig. 14), followed by the comparison of the resulting signals with the signal received in the absence of the defect.

The presence of a defect is detected by comparing the results with the result in the absence of a defect. The comparative result is shown in Fig. 15.

The comparative results show significant differences in signals in the presence and absence of a defect. This indicates that the defect affects the acoustic wave propagation and acoustic signals received by the sensor significantly.

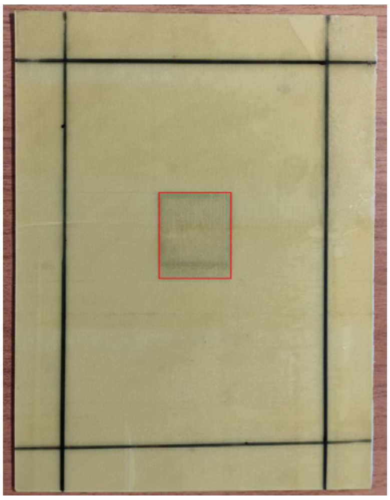

Fig. 13. PCB with a rectangular defect of 3 × 3.7 cm (the defect is marked with a red frame)

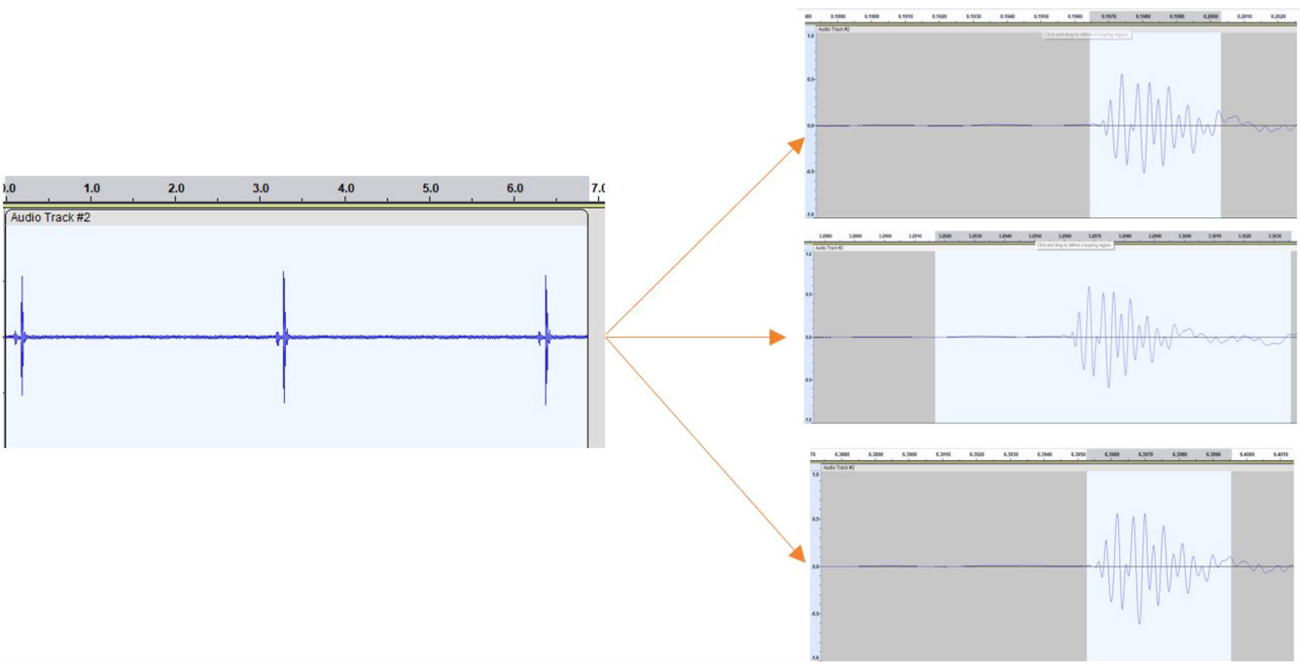

Fig. 14. The sensor signal after 3 shocks in the presence of a defect

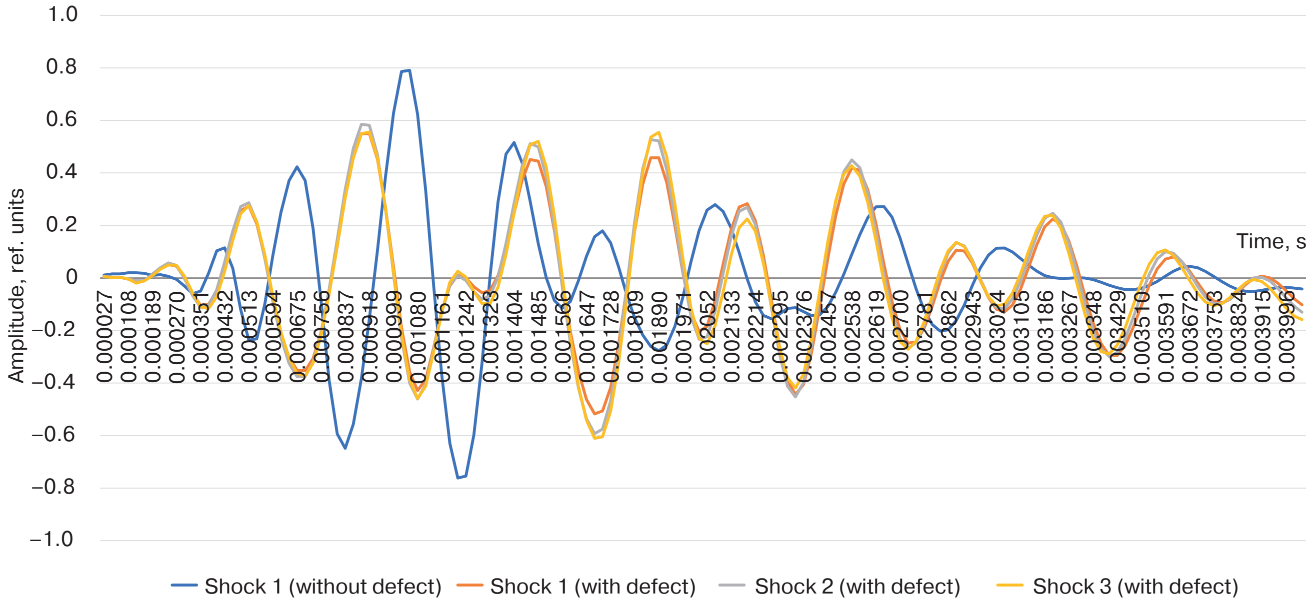

Fig. 15. Comparison of the sensor signals at 3 solenoid shocks on PCB having a 3 × 3.7 cm defect with the signal for PCB without defect

Research of the sensor sensitivity to defects of different sizes

In order to study sensor sensitivity to defect detection, two-layer PCB with defects in the form of squares with different side sizes: 4, 5, 6, and 7 mm were designed. Three mechanical shocks were applied sequentially to MPCB with a defect, while the signals from the sensor were compared with the signal for MPCB without a defect. The research results are shown in Figs. 16–19.

Signals relating to the 4 × 4 mm and 5 × 5 mm square defects were found to be similar to those for PCB without defects, thus indicating the sensor's inability to detect these types of defects. However, the signals for the 6 × 6 mm and 7 × 7 mm square defects show significant differences when compared to PCB without defects, thus indicating the capability of the sensor to detect these types of defects.

Next, the effect of the number of 5 × 5 mm square defects on the sensor's capability to detect defects was investigated. For this reason, PCBs with two (Fig. 20), three, and four 5 × 5 mm square defects were designed. Then three mechanical shocks were applied sequentially to the boards and the sensor signals were recorded (Figs. 21–23).

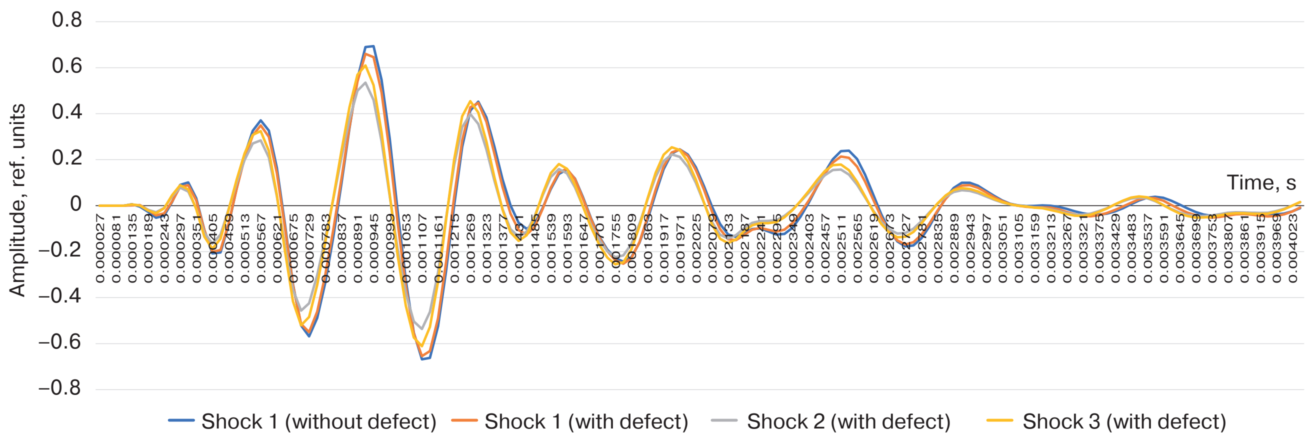

Fig. 16. Comparison of sensor signals for 3 solenoid shocks on PCB having a 4 × 4 mm defect with the signal for a serviceable PCB

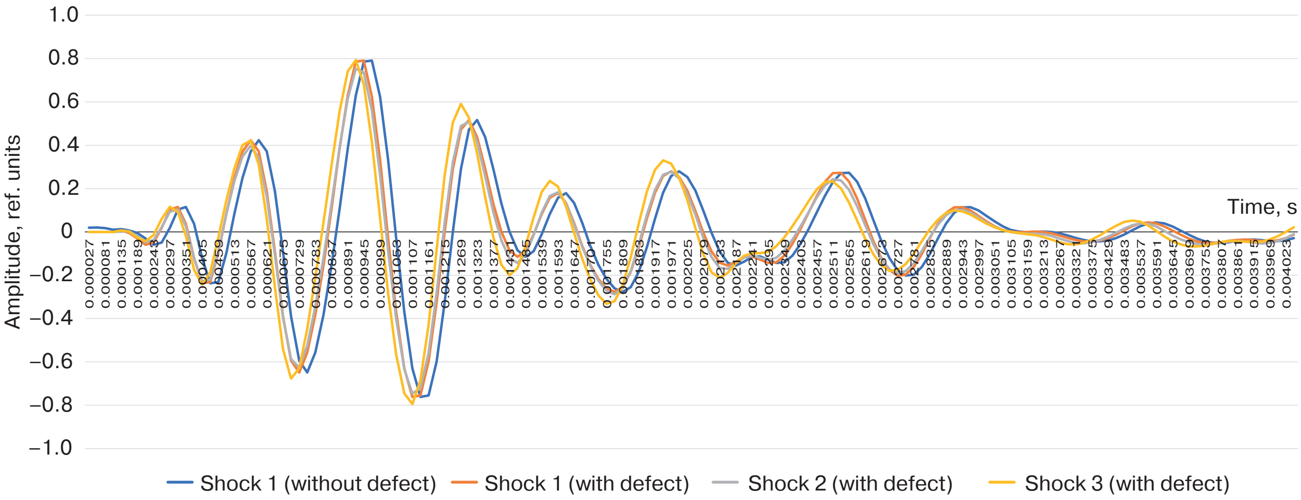

Fig. 17. Comparison of sensor signals for 3 solenoid shocks on PCB having a 5 × 5 mm defect with the signal for PCB without defects

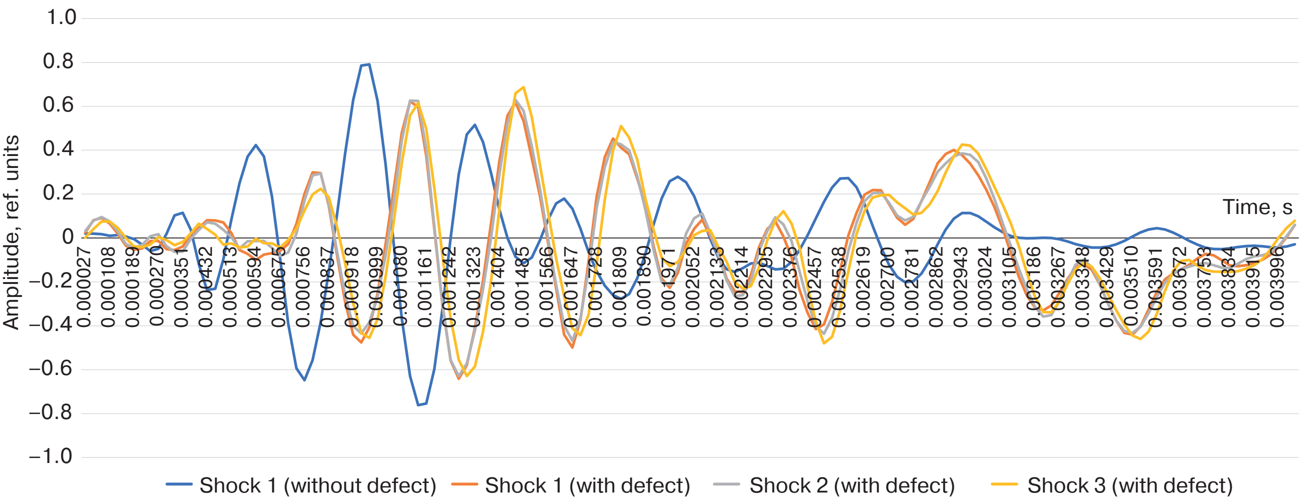

Fig. 18. Comparison of sensor signals for 3 solenoid shocks on PCB having a 6 × 6 mm defect with the signal for PCB without defects

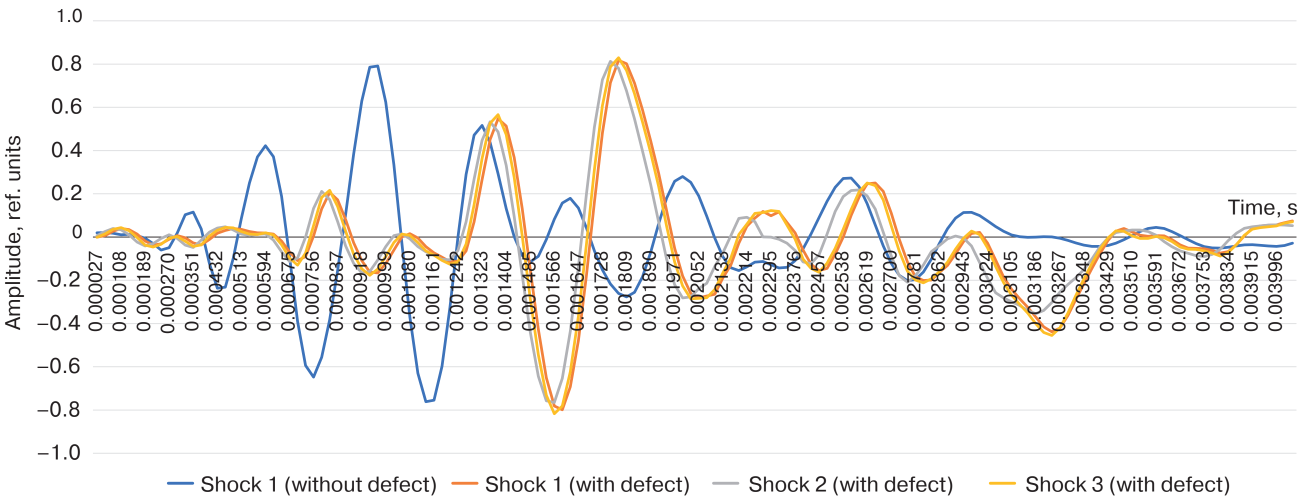

Fig. 19. Comparison of sensor signals for 3 solenoid shocks on PCB having a 7 × 7 mm defect with the signal for PCB without defects

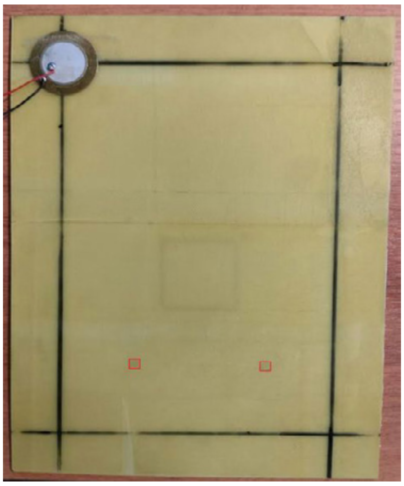

Fig. 20. PCB with two 5 × 5 mm square defects
(marked with a red frame)

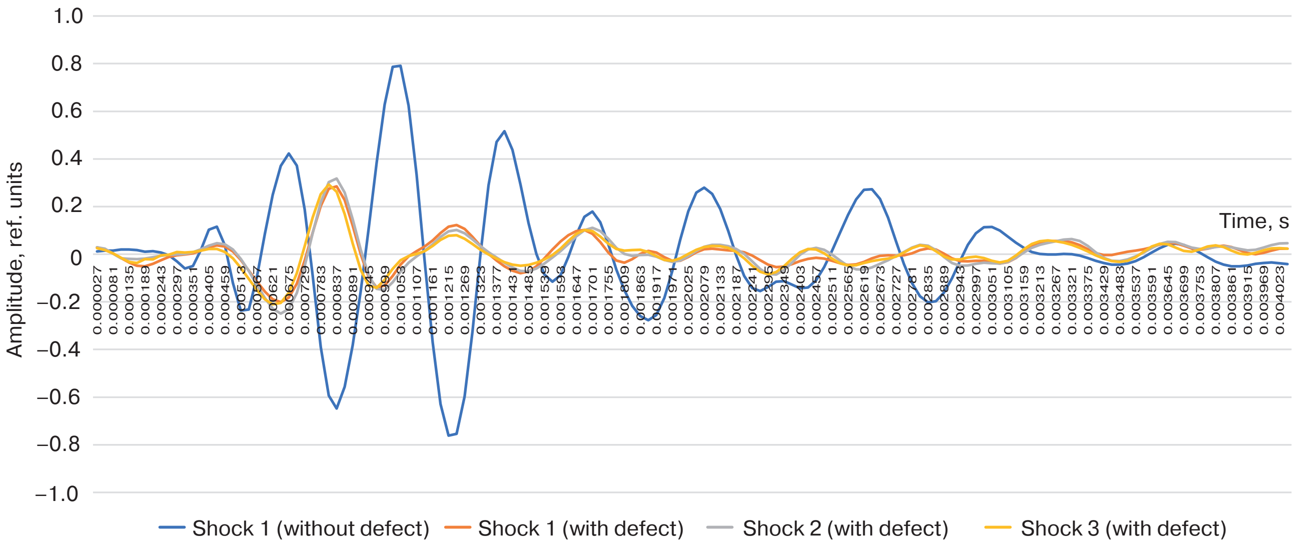

Fig. 21. Comparison of sensor signals for 3 solenoid shocks on PCB having two 5 × 5 mm defects
with the signal for PCB without defects

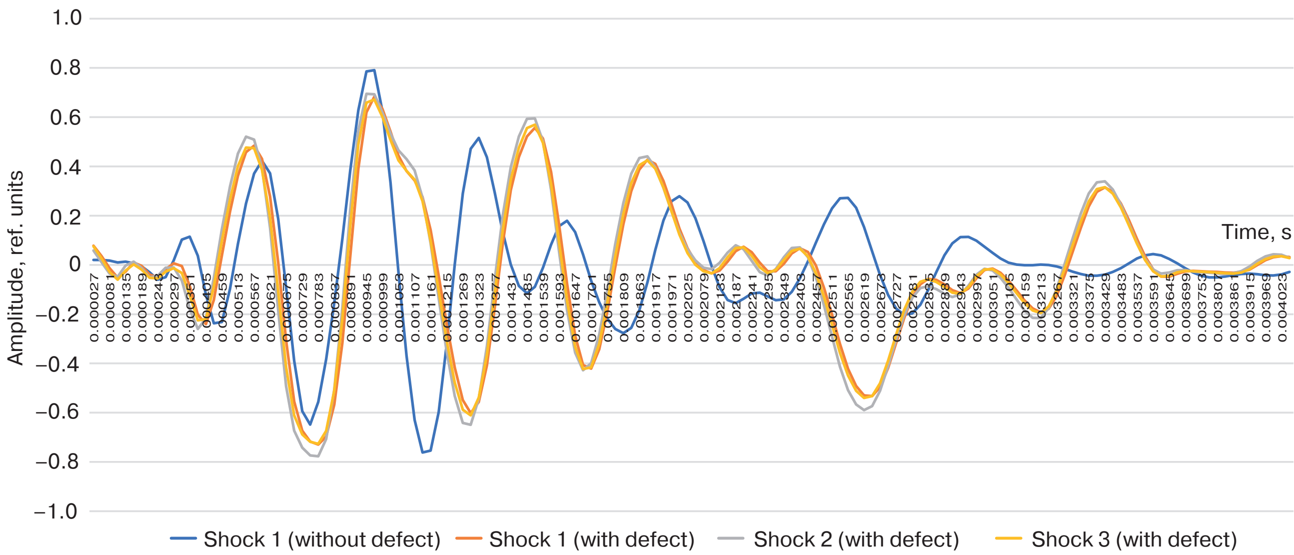

Fig. 22. Comparison of sensor signals for 3 solenoid shocks on PCB having three 5 × 5 mm defects
with the signal for PCB without defects

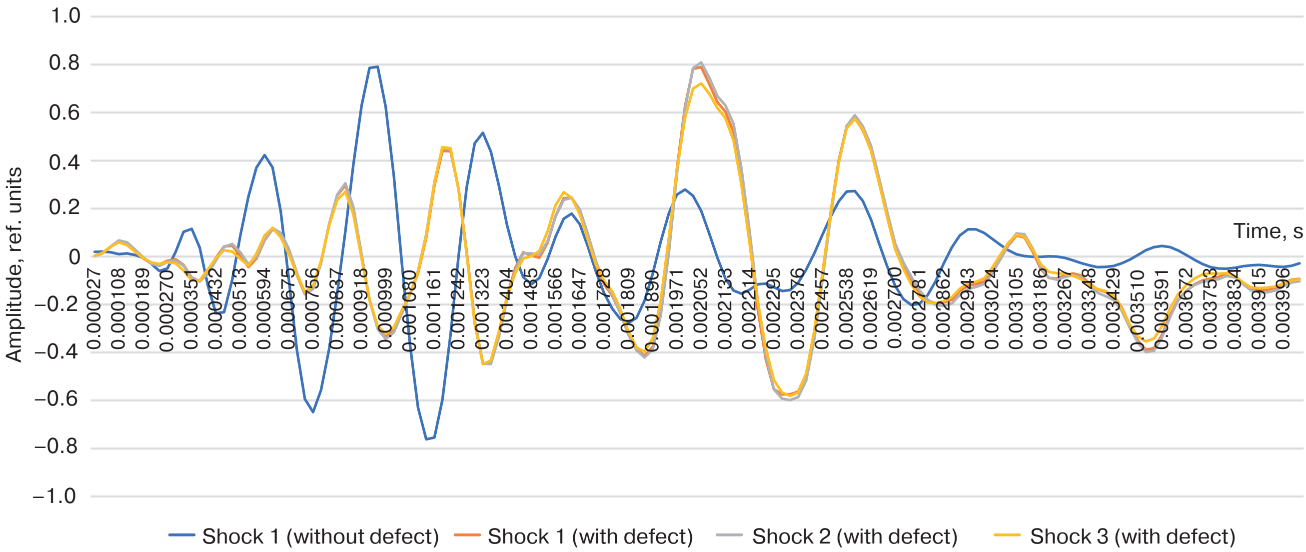

Fig. 23. Comparison of sensor signals for 3 solenoid shocks on PCB having four 5 × 5 mm defects with the signal for PCB without defects

Table 3. Studied defects and possibility of their recognition

Defect	Defect characterization (delamination)	Is it possible to use the AE method?
1	Rectangle 2 × 3 cm	Yes
2	Square 4 × 4 mm	No
3	Square 5 × 5 mm	No
4	Square 6 × 6 mm	Yes
5	Square 7 × 7 mm	Yes
6	Two squares 5 × 5 mm	Yes
7	Three squares 5 × 5 mm	Yes
8	Four squares 5 × 5 mm	Yes

The signals for each case were observed to be significantly different from those of PCB without defects. This suggests that the number of defects can affect the results obtained from the sensor.

The experiments showed the possibility of detecting defects in PCBs using the AE method. However, its sensitivity depends on the size and number of defects. The results also highlight the importance of analyzing the received signals to detect and localize defects in PCBs.

The final results on the possibility of recognizing the studied PCB defects using the AE method are shown in Table 3.

CONCLUSIONS

This paper examined the possibility of applying the AE method for detecting defects as delamination in MPCB. The modeling results for MPCB in serviceable and faulty states with a rectangular defect of 3 × 3.7 cm, as well as experimental studies for different sizes and number of defects were analyzed.

The approach developed herein allows for serviceable and faulty states of PCB to be recognized. It also helps determine the sensitivity of the AE method to the size of the defect being detected.

The research results permit the conclusion that the AE method can be applied in diagnosing the technical condition of MPCB, and that the results of physical tests are comparable to numerical experiments.

The authors continue to conduct further research towards developing a method for detecting defects in MPCB by using the AE method based on artificial neural networks. They also are working towards investigating the application of AE method in tests on the impact of harmonic vibration.

Authors' contribution. All authors equally contributed to the research work.

REFERENCES

1. Mashagulova D.A. Comparative analysis of acoustic methods for monitoring and diagnosing equipment. In: *Experience, Current Problems and Prospects for the Development of the Oil and Gas Complex: Materials of the X International Scientific and Practical Conference of Students, Postgraduates and Scientists.* Nizhnevartovsk: April 01–30, 2020. P. 59–63 (in Russ.).
2. Azin A.V., Ponomarev S.V., Rikkonen S.V., Maritskii N.N., Suntsov S.B. Review of methods for searching latent defects of printed circuit boards. In: *Reshetnev Readings: Materials of the 24th International Scientific and Practical Conference dedicated to the memory of the General Designer of Rocket and Space Systems Academician M.F. Reshetnev*. Krasnoyarsk: November 10–13. 2020;1:244–245 (in Russ.).
3. Azin A., Zhukov A., Narikovich A., Ponomarev S., Rikkonen S., Leitsin V. Nondestructive testing method for a new generation of electronics. *MATEC Web Conf.* 2018;143:04007. https://doi.org/10.1051/matecconf/201714304007
4. Luu N.T., Nguyen K.D., Demchenko S.K., Chernoverskaya V.V. Application of the acoustic emission method in the tasks of control and monitoring of the technical condition of the objects being diagnosed. In: *Proceedings of the International Symposium "Reliability and Quality*." 2021;2:77–82 (in Russ.).
5. Zhao W., Feng X., Xu B. Study on defect detection of PCB based on acoustic emission technology during the drilling process. *J. Electronic Measurement and Instrumentation*. 2015;29(10):1374–1380.
6. Li H., Dong Z., Yang Y., Liu B., Chen M., Jing W. Experimental Study of Damage Development in Salt Rock under Uniaxial Stress Using Ultrasonic Velocity and Acoustic Emissions. *Appl. Sci*. 2018;8(4):553. https://doi.org/10.3390/app8040553
7. Levikari S., Kärkkäinen T.J., Andersson C., Tammminen J., Silventoinen P. Acoustic Detection of Cracks and Delamination in Multilayer Ceramic Capacitors. *IEEE Transactions on Industry Applications*. 2019;55(2):1787–1794. https://doi.org/10.1109/TIA.2018.2873989
8. Altai E., Fedorov A.V., Stepanova K.A. Evaluation of the influence of filtration methods on the measurement error of acoustic emission signal parameters. In: *25th International Conference on Soft Computing and Measurements*: *collection of proceedings*. 2022;1:24–27 (in Russ.). Available from URL: https://scm.etu.ru/assets/files/2022/scm22/papers/stend01_024.pdf
9. Ovcharuk V.N., Chye E.U. The concept of the multichannel system of registration and analysis of acoustic emission signals. *Pribory = Instruments.* 2021;11(257):35–39 (in Russ.).
10. Matvienko Yu.G., Vasil'ev I.E., Chernov D.V., et al. Problems of locating acoustic emission sources. *Russ. J. Nondestruct. Test*. 2021;57(9):769–778. https://doi.org/10.1134/S1061830921090060
    [Original Russian Text: Matvienko Yu.G., Vasil'ev I.E., Chernov D.V., Ivanov V.I., Elizarov S.V. Problems of locating acoustic emission sources. *Defektoskopiya*. 2021;9:35–44 (in Russ.). https://doi.org/10.31857/S0130308221090049]
11. Aryan P., Sampath S., Sohn H. An Overview of Non-Destructive Testing Methods for Integrated Circuit Packaging Inspection. *Sensors*. 2018;18(7):1981. https://doi.org/10.3390/s18071981
12. Bourne K.A., Kapoor S.G. Process Monitoring During Micro-Drilling via Acoustic Emission, Ultrasonic Sound, and Spindle Load Sensors. In: *2012 International Manufacturing Science and Engineering Conference*. 2012;7341:781–790. https://doi.org/10.1115/MSEC2012-7341
13. Malikov V., Ananyev M., Ishkov A., Nikonov L. Experimental Studies of Conductive Paths of Printed Circuit Boards by Using Subminiature Eddy Current Transducers. *E3S Web of Conferences.* 2021;285(4):07037. https://doi.org/10.1051/e3sconf/202128507037
14. Huang M., Jiang L., Liaw P.K., Brooks C.R., Seeley R., Klarstrom D.L. Using Acoustic Emission in Fatigue and Fracture Materials Research. *JOM*. 1998;50(11). Available from URL: https://www.tms.org/pubs/journals/jom/9811/huang/huang-9811.html
15. Gao Y., Xiao D. Simulation and feature analysis of modal acoustic emission wave in planar C/SiC composite. *J. Vibroengineering*. 2018;20(1):748–761. https://doi.org/10.21595/jve.2017.18173

СПИСОК ЛИТЕРАТУРЫ

1. Машагулова Д.А. Сравнительный анализ акустических методов контроля и диагностирования оборудования. *Опыт, актуальные проблемы и перспективы развития нефтегазового комплекса: Материалы X Международной научно-практической конференции обучающихся, аспирантов и ученых.* Нижневартовск: 01–30 апреля 2020 г. С. 59–63.
2. Азин А.В., Пономарев С.В., Рикконен С.В., Марицкий Н.Н., Сунцов С.Б. Обзор методов поиска латентных дефектов печатных плат. *Решетневские чтения: Материалы XXIV Международной научно-практической конференции, посвященной памяти генерального конструктора ракетно-космических систем академика М.Ф. Решетнева.* Красноярск: 10–13 ноября 2020 г. 2020;1:244-245.
3. Azin A., Zhukov A., Narikovich A., Ponomarev S., Rikkonen S., Leitsin V. Nondestructive testing method for a new generation of electronics. *MATEC Web Conf.* 2018;143:04007. https://doi.org/10.1051/matecconf/201714304007
4. Лыу Н.Т., Нгуен К.Д., Демченко С.К., Черноверская В.В. Применение метода акустической эмиссии в задачах контроля и мониторинга технического состояния диагностируемых объектов. *Труды международного симпозиума «Надежность и качество»*. 2021;2:77–82.
5. Zhao W., Feng X., Xu B. Study on defect detection of PCB based on acoustic emission technology during the drilling process. *J. Electronic Measurement and Instrumentation*. 2015;29(10):1374–1380.
6. Li H., Dong Z., Yang Y., Liu B., Chen M., Jing W. Experimental Study of Damage Development in Salt Rock under Uniaxial Stress Using Ultrasonic Velocity and Acoustic Emissions. *Appl. Sci*. 2018;8(4):553. https://doi.org/10.3390/app8040553

7. Levikari S., Kärkkäinen T.J., Andersson C., Tammminen J., Silventoinen P. Acoustic Detection of Cracks and Delamination in Multilayer Ceramic Capacitors. *IEEE Transactions on Industry Applications*. 2019;55(2):1787–1794. https://doi.org/10.1109/TIA.2018.2873989
8. Алтай Е., Федоров А.В., Степанова К.А. Оценка влияния методов фильтрации на погрешность измерения параметров сигнала акустической эмиссии. *XXV Международная конференция по мягким вычислениям и измерениям: сборник трудов*. 2022;1:24–27. URL: https://scm.etu.ru/assets/files/2022/scm22/papers/stend01_024.pdf
9. Овчарук В.Н., Чье Е.У. Применение методов спектрального анализа в многоканальных системах регистрации сигналов акустической эмиссии. *Приборы*. 2021;11:35–39.
10. Матвиенко Ю.Г., Васильев И.Е., Чернов Д.В., Иванов В.И., Елизаров С.В. Проблемы локации источников акустической эмиссии. *Дефектоскопия.* 2021;9:35–44. https://doi.org/10.31857/S0130308221090049
11. Aryan P., Sampath S., Sohn H. An Overview of Non-Destructive Testing Methods for Integrated Circuit Packaging Inspection. *Sensors*. 2018;18(7):1981. https://doi.org/10.3390/s18071981
12. Bourne K.A., Kapoor S.G. Process Monitoring During Micro-Drilling via Acoustic Emission, Ultrasonic Sound, and Spindle Load Sensors. In: *2012 International Manufacturing Science and Engineering Conference*. 2012;7341:781–790. https://doi.org/10.1115/MSEC2012-7341
13. Malikov V., Ananyev M., Ishkov A., Nikonov L. Experimental Studies of Conductive Paths of Printed Circuit Boards by Using Subminiature Eddy Current Transducers. *E3S Web of Conferences.* 2021;285(4):07037. https://doi.org/10.1051/e3sconf/202128507037
14. Huang M., Jiang L., Liaw P.K., Brooks C.R., Seeley R., Klarstrom D.L. Using Acoustic Emission in Fatigue and Fracture Materials Research. *JOM*. 1998;50(11). URL: https://www.tms.org/pubs/journals/jom/9811/huang/huang-9811.html
15. Gao Y., Xiao D. Simulation and feature analysis of modal acoustic emission wave in planar C/SiC composite. *J. Vibroengineering*. 2018;20(1):748–761. https://doi.org/10.21595/jve.2017.18173

About the authors

Saygid U. Uvaysov, Dr. Sci. (Eng.), Professor, Head of the Department of Design and Production of Radioelectronic Devices, Institute of Radio Electronics and Informatics, MIREA – Russian Technological University (78, Vernadskogo pr., Moscow, 119454 Russia). E-mail: uvajsov@mirea.ru. Scopus Author ID 55931417100, ResearcherID H-6746-2015, RSCI SPIN-code 3801-4816, https://orcid.org/0000-0003-1943-6819

Ngoc T. Luu, Postgraduate Student, Department of Design and Production of Radioelectronic Devices, Institute of Radio Electronics and Informatics, MIREA – Russian Technological University (78, Vernadskogo pr., Moscow, 119454 Russia). E-mail: alex05vn@gmail.com. https://orcid.org/0009-0001-8779-7563

Cong D. Nguyen, Postgraduate Student, Department of Design and Production of Radioelectronic Devices, Institute of Radio Electronics and Informatics, MIREA – Russian Technological University (78, Vernadskogo pr., Moscow, 119454 Russia). E-mail: Ngcongduc9x@gmail.com. https://orcid.org/0009-0000-9237-156X

The H. Vo, Postgraduate Student, Department of Design and Production of Radioelectronic Devices, Institute of Radio Electronics and Informatics, MIREA – Russian Technological University (78, Vernadskogo pr., Moscow, 119454 Russia). E-mail: thehai.ttrd@gmail.com. https://orcid.org/0009-0009-7240-4374

Aleksey V. Dolmatov, Cand. Sci. (Eng.), Associate Professor, Department of Design and Production of Radioelectronic Devices, Institute of Radio Electronics and Informatics, MIREA – Russian Technological University (78, Vernadskogo pr., Moscow, 119454 Russia). E-mail: dolmatov@mirea.ru. RSCI SPIN-code 3887-2405, https://orcid.org/0000-0003-2969-2971

Об авторах

Увайсов Сайгид Увайсович, д.т.н., профессор, заведующий кафедрой конструирования и производства радиоэлектронных средств Института радиоэлектроники и информатики ФГБОУ ВО «МИРЭА – Российский технологический университет» (119454, Россия, Москва, пр-т Вернадского, д. 78). E-mail: uvajsov@mirea.ru. Scopus Author ID 55931417100, ResearcherID H-6746-2015, SPIN-код РИНЦ 3801-4816, https://orcid.org/0000-0003-1943-6819

Лыу Нгок Тиен, аспирант, кафедра конструирования и производства радиоэлектронных средств Института радиоэлектроники и информатики ФГБОУ ВО «МИРЭА – Российский технологический университет» (119454, Россия, Москва, пр-т Вернадского, д. 78). E-mail: alex05vn@gmail.com. https://orcid.org/0009-0001-8779-7563

Нгуен Конг Дык, аспирант, кафедра конструирования и производства радиоэлектронных средств Института радиоэлектроники и информатики ФГБОУ ВО «МИРЭА – Российский технологический университет» (119454, Россия, Москва, пр-т Вернадского, д. 78). E-mail: Ngcongduc9x@gmail.com. https://orcid.org/0009-0000-9237-156X

Во Тхе Хай, аспирант, кафедра конструирования и производства радиоэлектронных средств Института радиоэлектроники и информатики ФГБОУ ВО «МИРЭА – Российский технологический университет» (119454, Россия, Москва, пр-т Вернадского, д. 78). E-mail: thehai.ttrd@gmail.com. https://orcid.org/0009-0009-7240-4374

Долматов Алексей Вячеславович, к.т.н., доцент, кафедра конструирования и производства радиоэлектронных средств Института радиоэлектроники и информатики ФГБОУ ВО «МИРЭА – Российский технологический университет» (119454, Россия, Москва, пр-т Вернадского, д. 78). E-mail: dolmatov@mirea.ru. SPIN-код РИНЦ 3887-2405, https://orcid.org/0000-0003-2969-2971

Translated from Russian into English by Kirill V. Nazarov
Edited for English language and spelling by Dr. David Mossop

UDC 621.37 + 004.52
https://doi.org/10.32362/2500-316X-2024-12-1-30-58

RESEARCH ARTICLE

Software-architectural configuration of the multifunctional audio digital signal processor module for signal mediatesting of audio devices

Andrey V. Gevorsky [@],
Mikhail S. Kostin,
Konstantin A. Boikov

MIREA – Russian Technological University, Moscow, 119454 Russia
[@] *Corresponding author, e-mail: x33590@gmail.com*

Abstract
Objectives. The aim of this study is to develop and analyze parameters for a multifunctional audio module based on the ADAU1701 audio digital signal processor in the *SigmaStudio* environment. This will be used for testing audio devices in the following modes: routing of balanced and unbalanced audio channels according to the differential scheme Di-Box/R Di-Box; spatiotemporal and dynamic audio processing; three-band monochannel cross-separation with independent equalization; and correction of the frequency response of the audio channel with tracking notch auto-suppression of electro-acoustic positive feedback in a given spectral band.
Methods. Visual-graphical architectural programming of audio modules in the *SigmaStudio* and *Flowstone*, as well as algorithms for real-time signal audio measurements and analysis of experimental data in the *REW* and *Soundcard Oscilloscope* are used.
Results. The characteristics of the Di-Box/R Di-Box circuit were studied, in order to estimate the effect of differential signal conversion on the signal-to-noise ratio in the audio signal path. The characteristics of the reverberation and saturation submodules were established. Furthermore, the effect of equalization modes on the frequency response correction of a studio audio monitor was determined. The paper also studied the effect of an audio compressor on the dynamic range and the level of the output signal. The experimental results of the submodule for compensating the frequency response of an audio monitor using matched filtering were established, and the spectral characteristics of the submodule for automatic suppression of electro-acoustic positive feedback were obtained.
Conclusions. The software architecture of a multifunctional audio module based on the ADAU1701 audio digital signal processor for testing and debugging media devices in a given spectral-dynamic and spectral-temporal ranges was designed. Balanced routing allows the effect of noise induced into the audio channel to be reduced 20-fold, thus enabling calibration of pickup audio devices. The audio signal processing submodule provides: compression response in the dynamic range from −27 to 18.6 dB with the possibility of equalization parameterization in the range of 0.04–18 kHz; reverberation response in the range from 0.5–3000 ms; audio-channel cross-division into 3 with the ability to adjust the amplitude-frequency response in the dynamic range from −30 to 30 dB. The auto-correction submodule of the amplitude-frequency response allows the dynamic nonuniformity of the amplitude-frequency response to be reduced by 40 dB. The auto-suppression submodule of electro-acoustic positive feedback provides notch formant suppression up to −100 dB with an input dynamic range from −50 to 80 dB.

Keywords: audio module, ADSP, ADAU1701, visual-graphic programming, software-defined architecture, audio-visual signal processing, audio signal, media-testing

• **Submitted:** 13.03.2023 • **Revised:** 20.04.2023 • **Accepted:** 18.12.2023

For citation: Gevorsky A.V., Kostin M.S., Boikov K.A. Software-architectural configuration of the multifunctional audio digital signal processor module for signal mediatesting of audio devices. *Russ. Technol. J*. 2024;12(1):30–58. https://doi.org/10.32362/2500-316X-2024-12-1-30-58

Financial disclosure: The authors have no a financial or property interest in any material or method mentioned.

The authors declare no conflicts of interest.

НАУЧНАЯ СТАТЬЯ

Программно-архитектурная конфигурация многофункционального ADSP-модуля сигнального медиатестирования аудиоустройств

А.В. Геворский @,
М.С. Костин,
К.А. Бойков

МИРЭА – Российский технологический университет, Москва, 119454 Россия
@ Автор для переписки, e-mail: x33590@gmail.com

Резюме
Цели. Цель статьи – программно-архитектурная разработка и параметрический анализ многофункционального аудиомодуля на базе ADSP-процессора (audio digital signal processor) ADAU1701 в среде *SigmaStudio* для тестирования аудиоустройств в следующих режимах: маршрутизация балансных и небалансных аудиоканалов по дифференциальной схеме «Di-Box/R Di-Box»; пространственно-временная и динамическая аудиообработка; трехполосное моноканальное кросс-разделение с независимой эквализацией; коррекция амплитудно-частотной характеристики (АЧХ) аудиоканала со следящим режекторным автоподавлением электроакустической положительной обратной связи (ПОС) в заданной спектральной полосе.
Методы. Использованы методы визуально-графического архитектурного программирования аудиомодулей в программных средствах *SigmaStudio* и *Flowstone*, алгоритмы сигнальных аудиоизмерений и анализа экспериментальных данных в *REW* и *Soundcard Oscilloscope*.
Результаты. Исследованы характеристики схемы «Di-Box/R Di-Box» для оценки влияния дифференциального преобразования сигнала на отношение сигнал/шум в аудиоканале. Приведены характеристики субмодулей реверберации и сатурации. Показано влияние режимов эквализации на коррекцию АЧХ студийного аудиомонитора. Исследовано воздействие аудиокомпрессора на динамический диапазон и уровень выходного сигнала. Проведены результаты экспериментального исследования субмодуля компенсационной коррекции АЧХ аудиомонитора при помощи согласованной фильтрации, а также получены спектральные характеристики субмодуля автоподавления электроакустической ПОС.
Выводы. Разработана программная архитектура многофункционального аудиомодуля на ADSP-процессоре ADAU1701 для тестирования и отладки медиаустройств в заданном спектрально-динамическом диапазоне. Балансная маршрутизация в 20 раз снижает влияние наводимых на аудиоканал шумов, что позволяет калибровать звукоснимающие аудиоустройства. Субмодуль аудиообработки обеспечивает компрессионную характеристику с динамическим диапазоном от −27 до 18.6 дБ с возможностью эквализационной параметризации в диапазоне 0.04–18 кГц; реверберационную характеристику в диапазоне 0.5–3000 мс; аудиоканальное кросс-разделение на 3 частотных поддиапазона с регулировкой АЧХ в динамическом диапазоне от −30 до 30 дБ. Субмодуль автокоррекции АЧХ позволяет снизить на 40 дБ динамическую неравномерность АЧХ. Субмодуль автоподавления электроакустической ПОС обеспечивает режекторное формантоподавление до −100 дБ при входном динамическом диапазоне от −50 до 80 дБ.

Ключевые слова: аудиомодуль, ADSP, ADAU1701, визуально-графическое программирование, программно-конфигурируемая архитектура, аудиовизуальная обработка сигналов, аудиосигнал, медиатестирование

• **Поступила:** 13.03.2023 • **Доработана:** 20.04.2023 • **Принята к опубликованию:** 18.12.2023

Для цитирования: Геворский А.В., Костин М.С., Бойков К.А. Программно-архитектурная конфигурация многофункционального ADSP-модуля сигнального медиатестирования аудиоустройств. *Russ. Technol. J.* 2024;12(1):30–58. https://doi.org/10.32362/2500-316X-2024-12-1-30-58

Прозрачность финансовой деятельности: Авторы не имеют финансовой заинтересованности в представленных материалах или методах.

Авторы заявляют об отсутствии конфликта интересов.

INTRODUCTION

The development and operation of radio-electronic devices and device-applications for digital processing of audio signals based on the specialized architecture of ADAU audio processors (Analog Devices, Inc., USA)[1] using virtual studio technology (VST) are very relevant. They are widely used in producing mixing consoles, audio effects processors, and means of dynamic, frequency, spatial-temporal, and signal audio correction. The study covers the area of signal radio acoustics along with audio-visual systems and technologies including in-circuit media testing and studies the characteristics of audio paths of audio digital signal processors (ADSP) (Fig. 1) [1].

In this paper, we set out to create a digital architecture for the multifunctional laboratory audio module in the *SigmaStudio*[2] environment, and analyze its characteristics in the aims of resolving the specialized tasks of debugging and studying the multimedia devices and complexes [2]. These tasks include: switching and transformation of balanced and unbalanced audio paths; studying the parametric impact of dynamic and spatial-temporal processing effects on audio signal; creation of submodule architecture for automatic correction of the amplitude-frequency response (AFR) of audio monitors in diffuse sound field; creation of submodule architecture for the automatic (tracking) suppression of electroacoustic positive feedback; and creation of submodule architecture of the three-band crossover with independent graphic

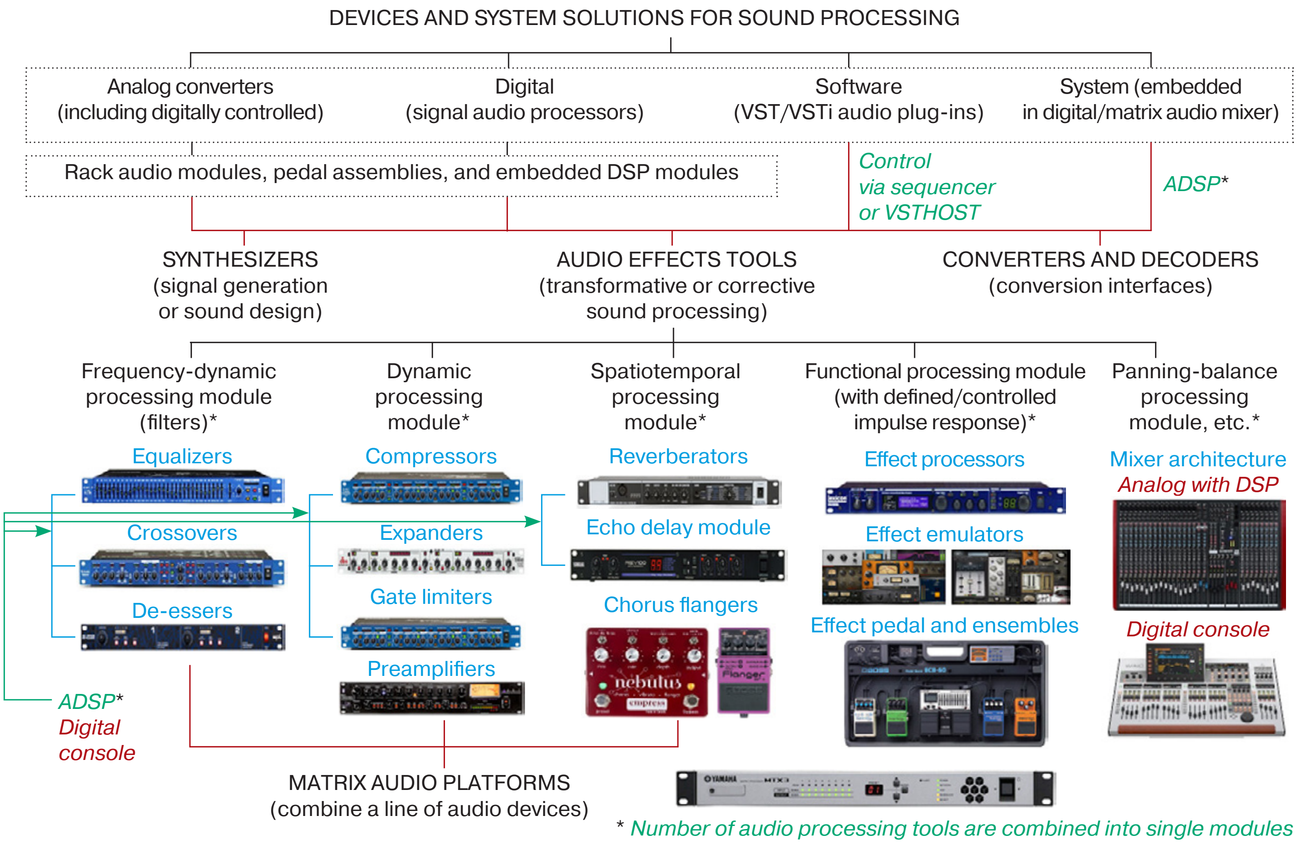

Fig. 1. ADSP classification

[1] https://www.analog.com/ADAU1701. Accessed November 10, 2022.
[2] https://wiki.analog.com/resources/tools-software/sigmastudio. Accessed February 20, 2023.

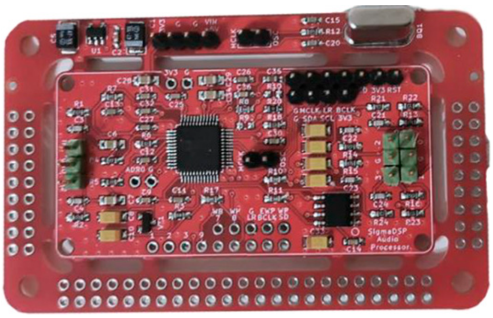

Fig. 2. ADAU1701 ADSP processor

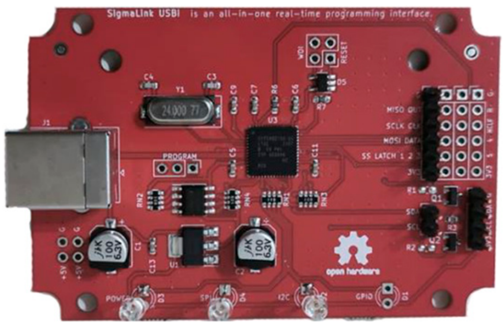

Fig. 3. SigmaLink-USBi programmer

equalization in low/mid/high-frequency (LF/MF/HF) audio ranges with specified parameterization of frequency spectrum and corresponding goodness and gain/attenuation coefficients.

The software architecture for the audio module is based on the *SigmaStudio* environment and uses the ADAU1701 audio processor (Fig. 2) encoded by the SigmaLink-USBi programmer (Analog Devices, Inc.) via I2C interface (Fig. 3). The audio module has a non-volatile EEPROM M24C64 memory manufactured by STMicroelectronics (France), 2 analog inputs with analog-to-digital converter (ADC) and 4 outputs with digital-to-analog converter (DAC) connected to JACK-Audio connectors of the stereo/mono configuration, respectively. The module is powered by a programmer with an output voltage of 3.3 V. The dynamic ranges and signal-to-noise ratio (SNR) of the 32-bit ADC/DAC are 100/104 dB, respectively. The signal audio processor is clocked by the external 12.288 MHz quartz resonator and is controlled (broadcasted) in real-time from the *SigmaStudio* visual-graphic design environment. The ADAU1701 is capable of operating with sampling frequency up to 192 kHz (with the specified clocking mode in the multifunctional audio module design being 48 kHz) [2].

The circuitry for the ADAU1701 processor of the signal audio module is shown in Fig. 4 [2]. On processor ports 2/4 (ADC inputs), there are resistor capacitor (RC) bandpass filters cutting constant and HF components out of the signal [3]. The circuit audio signal outputs correspond to ports 43–46 connected through RC bandpass filters.

The following pins and buses are brought out to the audio interface connector of the I2S serial bus (ensuring communication between the audio module and the programmer): G is GND, MCLK is 32 pin of the ADAU1701 chip, LR is MP4, BCLK is MP5, SDATA is MP0, 3V3 is 3.3 V power supply, and RST is RESET (Fig. 4).

The software and architectural configuration of the multifunctional ADSP-audio module consisting of 5 system switchable submodules is shown in Fig. 5. The signal audio module has 2 physical JACK-Audio inputs Input1 (Fig. 5, item *1*) connected via ADC to the first submodule. This is the R Di-Box reverse direct box (Fig. 5, item *2*) which performs switching of balanced (differential) and unbalanced lines. The protection of the audio system against input level overload is provided by the Limiter1 digital block (Fig. 5, item *3*) with a specified limitation from −24 up to +24 dB. The input level of the audio signal is controlled by the Single1 fader power controller within the range from −30 up to +30 dB. The selected audio module path is rooted on the '1 × N – 1' digital switch (Fig. 5, item *5*), as follows: the top position is adding the Effects audio submodule to the audio path (Fig. 5, item *6*); the second from top position is the audio signal pass-through mode (Fig. 5, item *7*); the third from top position is adding the AutoCorrection submodule to the audio path (Fig. 5, item *8*); and the fourth position is adding the Crossover submodule to the audio path (Fig. 5, item *9*). The first three cross-routes lead to S Mixer1 signal mixer (Fig. 5, item *10*) allowing controlling the dynamic level of the output signal within the range from −30 up to +6 dB. In this case, the audio signal from the Crossover submodule output is fed directly to DAC2 and DAC3 physical outputs and through the Add2 addition block to the DAC1 output (Fig. 5, item *14*).

The S Mixer1 signal mixer is connected to the switch '1 × N – 2' (Fig. 5, item *11*) which allows the routing of the output audio signal to be selected between balanced and unbalanced lines. In the upper position, the signal is switched to the Di-Box paraphase submodule (direct box) (Fig. 5, item *12*) from where the direct signal goes to the DAC0 physical output. The inverted signal (with a phase shift of 180°) goes to the DAC1 output. In the second case, the signal goes to the DAC0 physical output. Add1 and Add2 auxiliary addition blocks (Fig. 5, item *13*) allow the number of required pins of the audio module functional architecture circuit to be reduced.

The submodules (Fig. 5, items *2*, *6*, *8*, *9*, and *12*), the numerical analytics of which are outlined in [4], define the Box architecture of the multifunctional audio module and form an independent software-defined configuration.

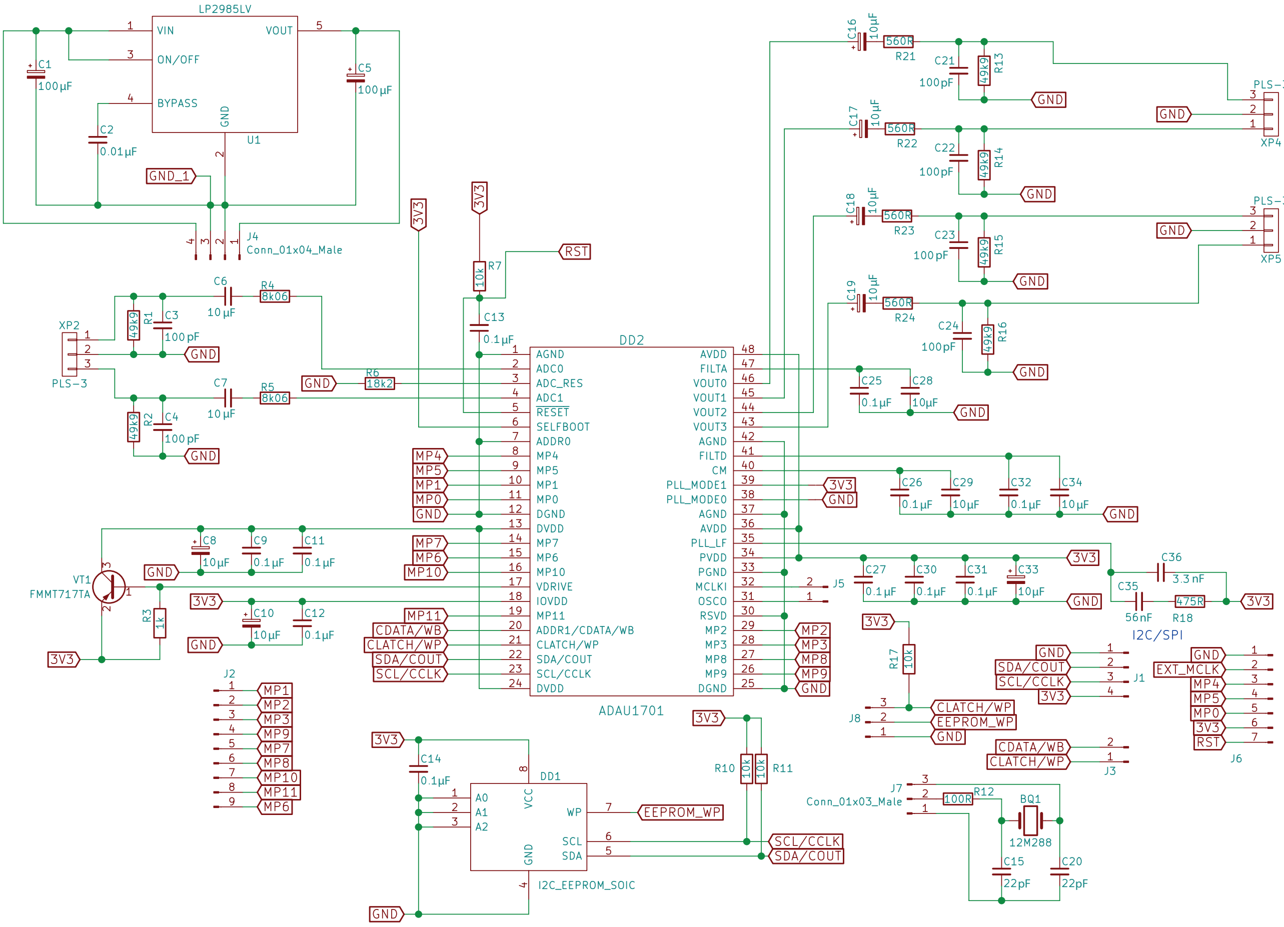

Fig. 4. Circuit architecture of the ADAU1701 audio processor[3]. The circuit element designations used here and in the following figures correspond to the designations adopted in GOST 2.710-81[4]

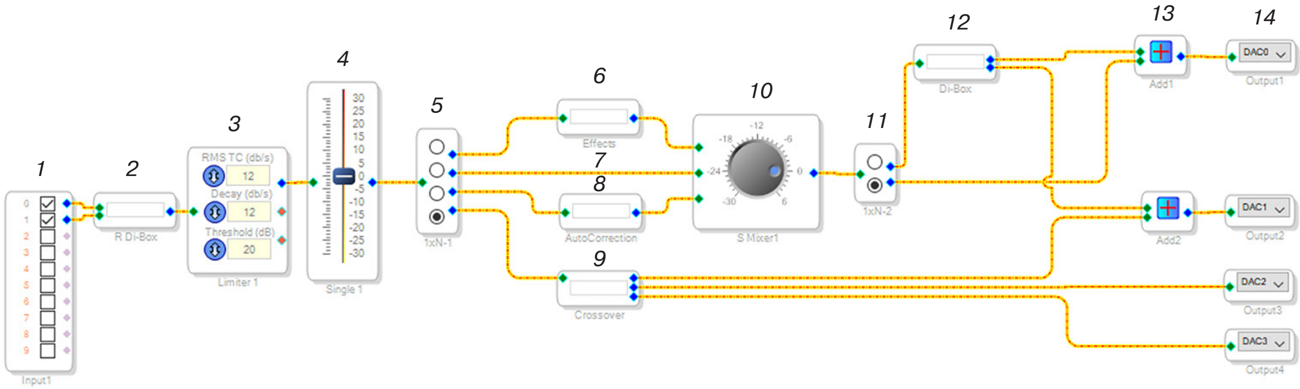

Fig. 5. Software-architectural configuration of ADSP module: *1* is Input1; *2* is R Di-Box submodule; *3* is Limiter1; *4* is Single1 input power controller; *5* is digital switch '1 × N – 1'; *6* is Effects audio submodule; *7* is audio through-pass mode; *8* is AutoCorrection submodule; *9* is Crossover submodule; *10* is S Mixer1 signal mixer; *11* is digital switch '1 × N – 2'; *12* is Di-Box submodule; *13* is Add1 and Add2 addition blocks; *14* is 'DAC0, 1, 2, 3' outputs

[3] Analog Devices. ADAU1701 Datasheet. 43 p. https://pdf1.alldatasheet.com/datasheet-pdf/view/159293/AD/ADAU1701.html. Accessed February 20, 2023.

[4] GOST 2.710-81. *Interstate Standard. Unified system for design documentation. Alpha-numerical designations in electrical diagrams*. Moscow: Izd. Standartov; 1985 (in Russ.).

1. STUDYING AND ANALYZING THE CHARACTERISTICS OF DI-BOX/R DI-BOX SUBMODULES

When an audio signal is transmitted over an unbalanced coaxial cable, the interference noise induced in the channel including interference from other audio lines of multicore switching can result in a significant decrease in SNR [4]. In this case, it would be sensible to use differential phase-symmetric lines with mono-balanced switching, for example, between an audio console and an audio device included in the line This would form a Di-Box circuit, as shown in Fig. 6, where switching is performed by means of TRS-TRS (tip, ring, sleeve) or TRS-XLR (external line return) connections.

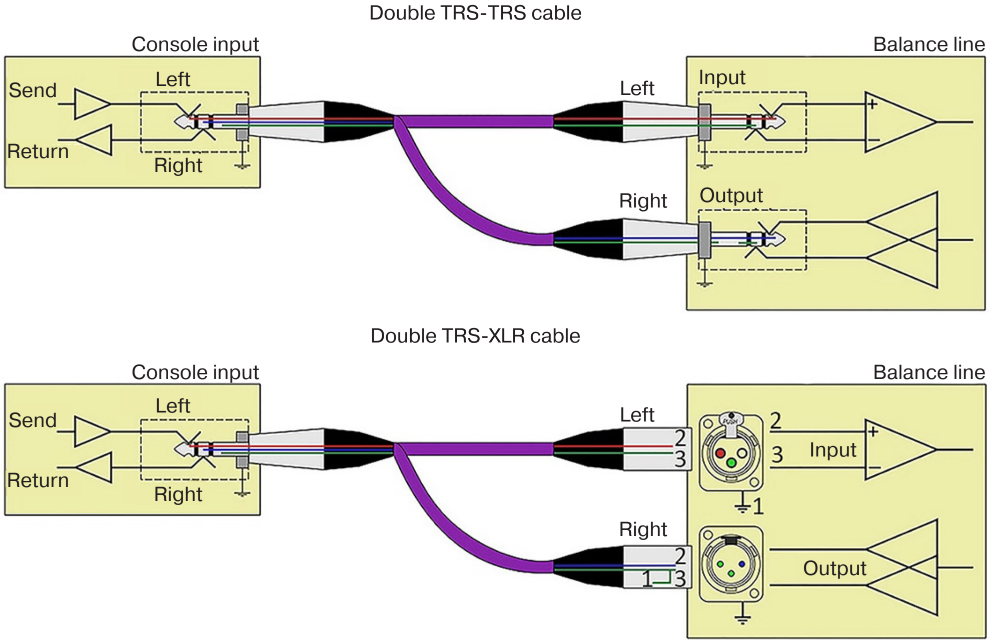

(a)

(b)

Fig. 6. Mono-balanced implementation of TRS-connector audio routing: (a) in-circuit return/send audio line (with built-in balanced audio device circuit at the input/output); (b) embedding an intermediate analog Di-Box transformer in the line with the ability to select (switch) the ground of the source (audio mixer) or receiver (audio monitor, etc.) [6]

Thus, the software-defined circuit of R Di-Box submodule is implemented at the input of the multifunctional audio module (Fig. 7a). This allows for the connection of a balanced line, for example, from an audio mixing console to a stage box [5]. One of the input channels passes through the submodule unchanged, while the second is phase inverted. Then at the receiver, the second channel signal is subtracted from the first channel signal, in order to compensate for in-phase interference swept into the differential line. In the case of an unbalanced connection, no audio signal is fed to the second channel.

The Di-Box submodule is installed at the ADSP module output (Fig. 7b). This allows the unbalanced mono signal to be converted into balanced–differential one necessary for compensation of additive noise induced on the audio path line. Using this submodule in the test mode is of practical interest when analyzing the effectiveness of noise immunity of audio systems upon the impact of external electromagnetic interference and noise exceeding −20 dB on the coaxial TRS audio line[5].

In order to study the time-response characteristics of the Di-Box submodule, a test sinusoidal signal with an amplitude of 35 mV at tone frequency of 1 kHz generated by a virtual signal generator equipped with the *Soundcard Oscilloscope* software [7] is fed to the input. Additive noise is added to this broadband with normal distribution. The experimental circuit (Fig. 8) uses the Xenyx X1622USB analog mixing console (Behringer, Germany) with mono channel panning capability as a SNR mixer. This is necessary because the two audio signals received from the stereo TRS output of the submodule (used in the balanced routing mode) require strictly separation with respect to panning. Interference located in the center of the stereo panning should be added for equal dynamic effect on both balanced channels.

The received differential signal goes through the coaxial line to R Di-Box submodule (second audio module implementing the circuit for balanced signal reception) based on the auxiliary ADSP audio module. Here it is converted into a single-channel signal and sent to the audio interface sound card. An oscillogram of the signal with compensated interference is recorded there (Fig. 9) using the *Soundcard Oscilloscope* software [5].

Analysis of the oscillograms depicted in Figs. 9c, 9d, and 9f shows that the balanced connection increases SNR by 26 dB. However, this scheme does not allow for compensation of the independent interferences induced on each channel separately.

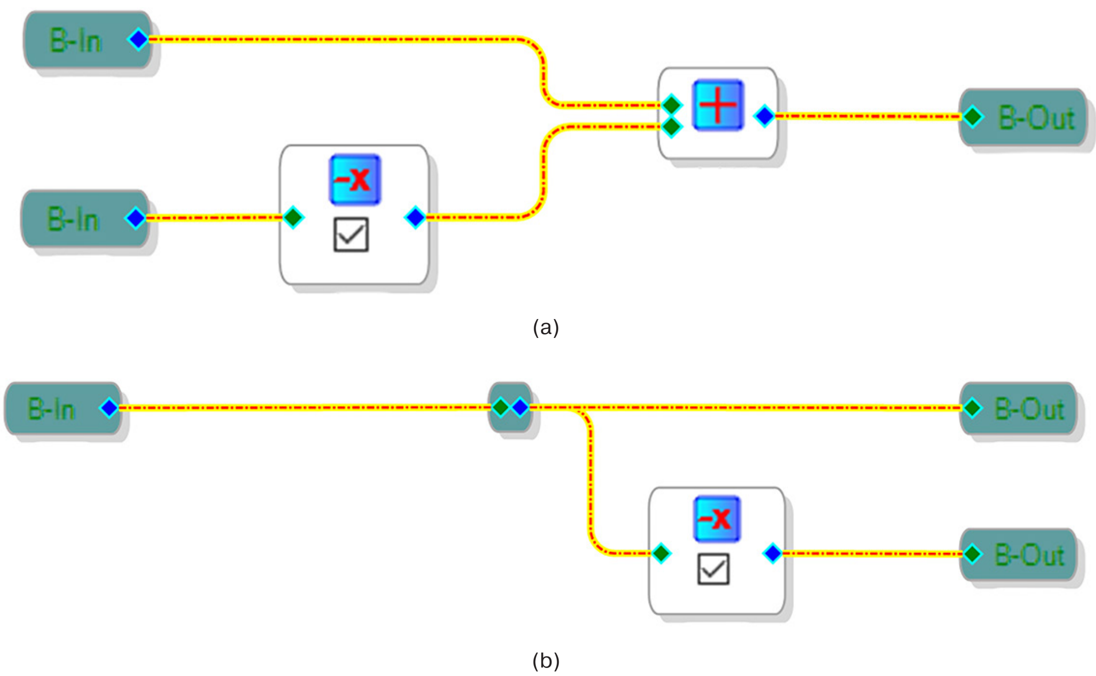

Fig. 7. Software-defined circuit of Di-Box/R Di-Box submodule combination based on ADAU1701: (a) R Di-Box module functional implementation; (b) Di-Box module functional implementation

[5] Applied Research and Technology (ART). dPDB Owner's Manual. 2 p. https://artproaudio.com/framework/uploads/2018/06/om_dpdb.pdf. Accessed February 20, 2023.

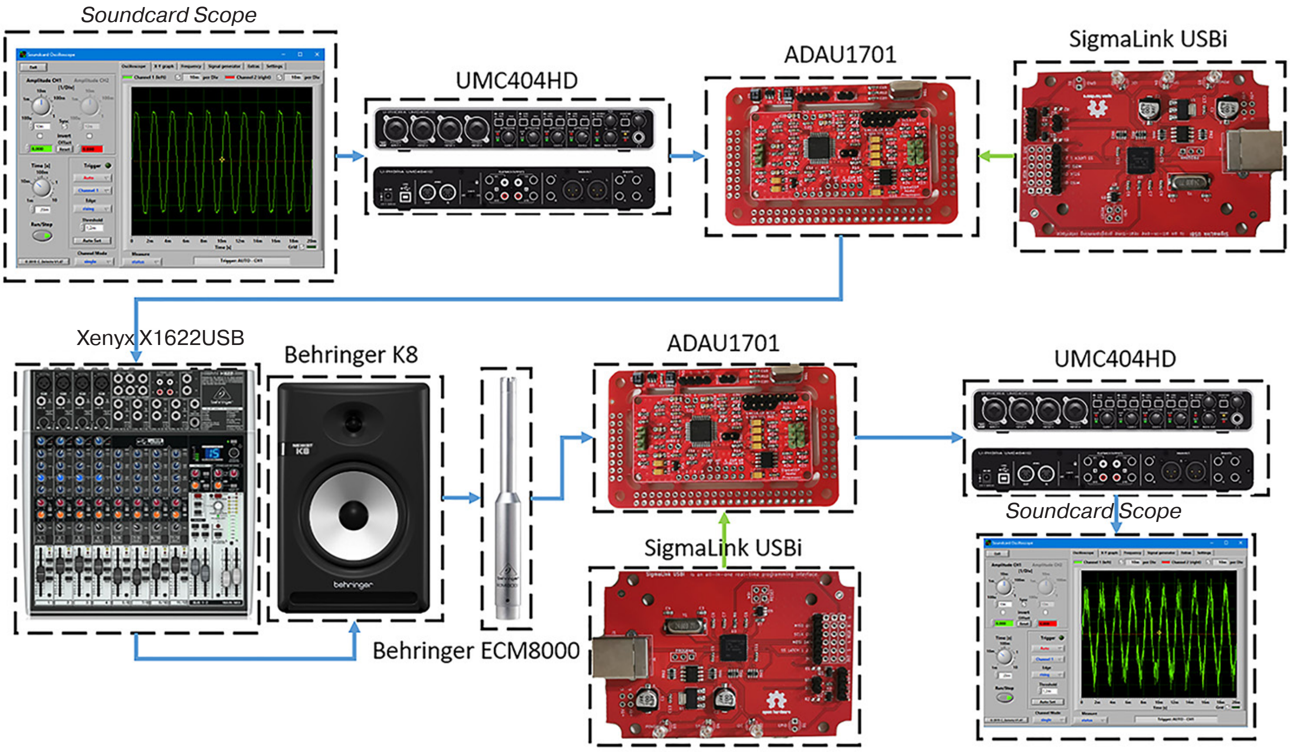

Fig. 8. Scheme of the experimental research on the balanced line submodule for suppressing broadband additive interference in TRS audio line. Behringer UMC404HD is audio interface; Behringer K8 is studio audio monitor; and Behringer ECM8000 is measuring microphone

2. DEVELOPING, ANALYZING, AND PARAMETERIZING THE CHARACTERISTICS OF SUBMODULE OF THE THREE-BAND CROSSOVER WITH INDEPENDENT GRAPHIC EQUALIZATION

The signal crossover is a multiband filter which divides audio signal into two or more frequency sub-bands adapted to the effective operation of electrodynamic cones designed for operation in different frequency bands [8]. The architecture of the circuit for the Crossover digital submodule implemented in the project allows the audio signal to be divided into three bandwidth channels of audio frequencies: low (40–250 Hz); middle (0.25–3 kHz); and high (3–18 kHz).

The three-band crossover submodule consists of a Crossover1 pre-equalization block (Fig. 10a, item *1*) which divides the audio signal into three sub-bands directly, a set of filters (paragraphic equalization line) in each channel with dynamic adjustment of amplification/attenuation (AMP/ATT) of 10 dB (Fig. 10a, items *2–4*), and volume faders for each individual channel (Fig. 10a, item *5*). These are adjustable within the dynamic range from −30 to +30 dB.

The configurable architecture of the pre-equalizer (cross-filter, Fig. 10, item *1*) the AFR of which is shown in Fig. 11 allows the separation boundaries of bandpass channels to be adjusted. It also enables the signal in a given band to be amplified or attenuated, the filter type selected, and a rigid connection to be created between their boundaries. It also inverts channel polarities, thus resulting in attenuation of the signal in the intersection of frequency bands [9]. Paragraphic equalization blocks formed from a discrete set of bandpass filters perform an independent equalization in LF/MF/HF channels according to fader presets shown in Fig. 10a.

The laboratory application of the three-band crossover submodule in the media test mode is actually of practical interest when processing audio signals within specified frequency bands, its spectral routing, as well as when testing, calibrating, and correcting AFR of audio monitors [8].

In the case of the experimental electroacoustic analysis of signal shaping and correction of frequency-dynamic characteristics of audio channels at the output of the digital crossover submodule, the AFR of each equalization line filter is recorded (Fig. 10). Electroacoustic measurements are carried out on the basis of the automated laboratory bench (Fig. 12) controlled by the *RoomEQWizard* (*REW*)[6] software package consisting of the Behringer UMC404HD audio interface (with calibration script), the Behringer ECM8000 measuring microphone (with calibration file), and the Behringer K8 studio audio monitor.

[6] https://www.roomeqwizard.com/. Accessed December 02, 2022.

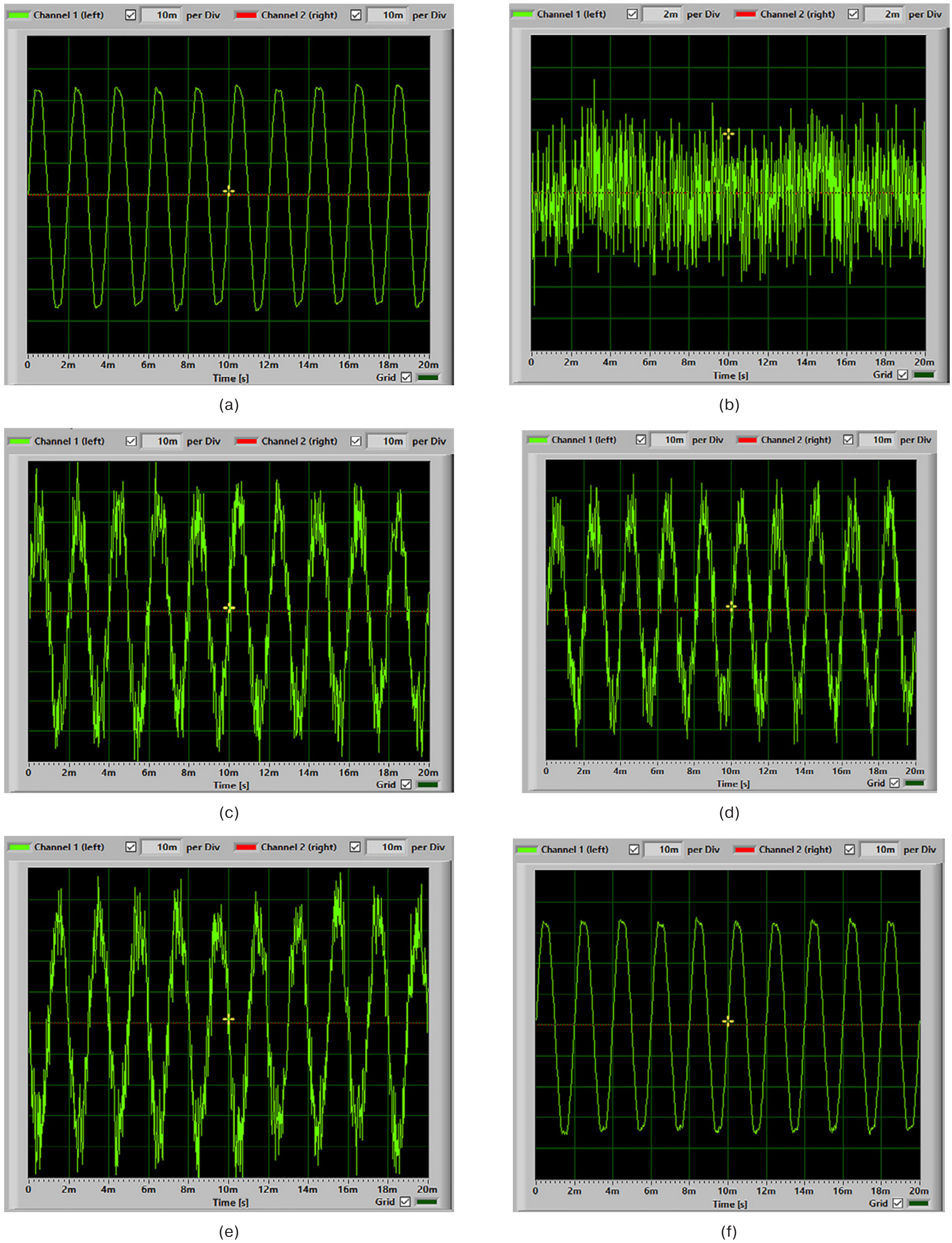

Fig. 9. Timing diagrams of the characteristics of the balanced audio path arranged according to the Di-Box/R Di-Box scheme:
(a) signal at balanced connection without induced noise; (b) additive noise; (c) signal at balanced connection with noise induced in the direct channel, SNR = 9 dB; (d) signal at balanced connection with noise induced in the inverted channel, SNR = 9 dB; (e) signal at unbalanced audio path connection and additive noise; (f) sum of direct and inverse (backward inverted) signal at R Di-Box, SNR = 35 dB

For reason of the purity of AFR measurements, the hardware presets of audio devices, architectural acoustics of the studio laboratory, as well as mutual positions between the measuring condenser microphone and audio monitor are not changed. Figure 13 shows the results of electroacoustic measurements of bandpass components at preset leveled value 0 dB for equalization crossover line filters, as well as at some fader position set arbitrarily (Fig. 10a, items *2*–*4*).

Controlling the presets of the equalization line allows the AFR of the audio monitor to be adjusted for specified characteristics of the frequency-dynamic balance at bandpass separation and audio signal panning (Fig. 14) [1]. In Figs. 13a and 13b, the AFR dynamic increase by 6 dB preset by the crossover is observed in the vicinity of 125 Hz frequency. A dynamic drop of 18 dB is observed in the region of 64 Hz. The dynamic increase in AFR by 12 dB at 800 Hz and the decrease in amplitude by 16 dB and 18 dB at 500 Hz and 1200 Hz, respectively, can be seen in Fig. 13d, as opposed to Fig. 13c. In the vicinity of 8 kHz frequency (Figs. 13d and 13e), a decrease in amplitude of 14 dB appears; while in the vicinity of 5 and 16 kHz, an increase of 16 dB occurs.

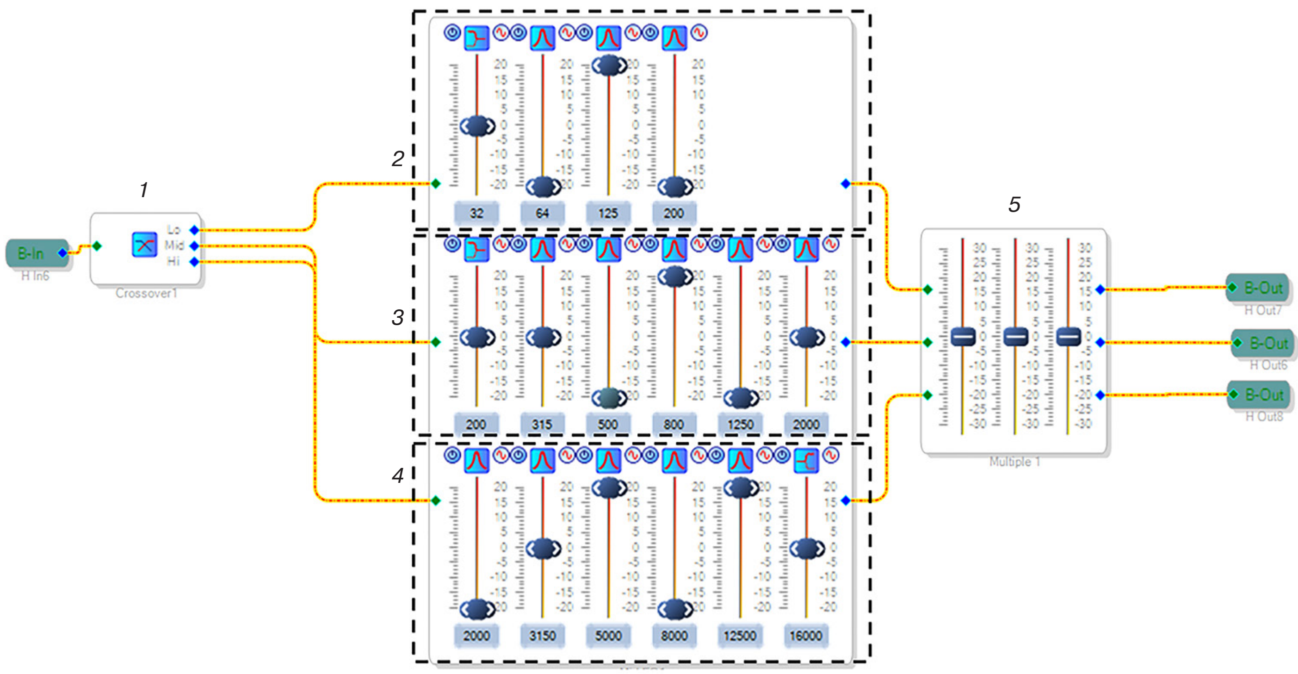

(a)

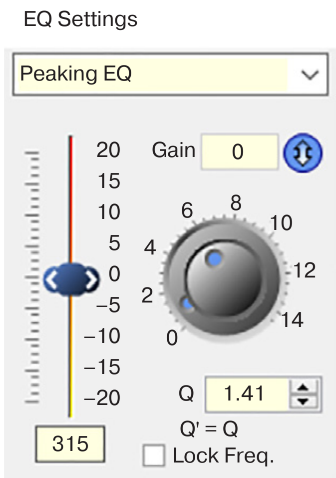

(b)

Fig. 10. Software-defined architecture of the three-band crossover submodule circuit:
(a) functional blocks:
1 is graphic pre-filtering equalizer;
2 is paragraphic LF equalizer;
3 is paragraphic MF equalizer;
4 is paragraphic HF equalizer;
5 is fader block for output volume control;
(b) parameterization of bandpass filter settings of the equalization block (frequency, goodness, limiting dynamic level of bandpass/notch AFR, AMP/ATT coefficient)

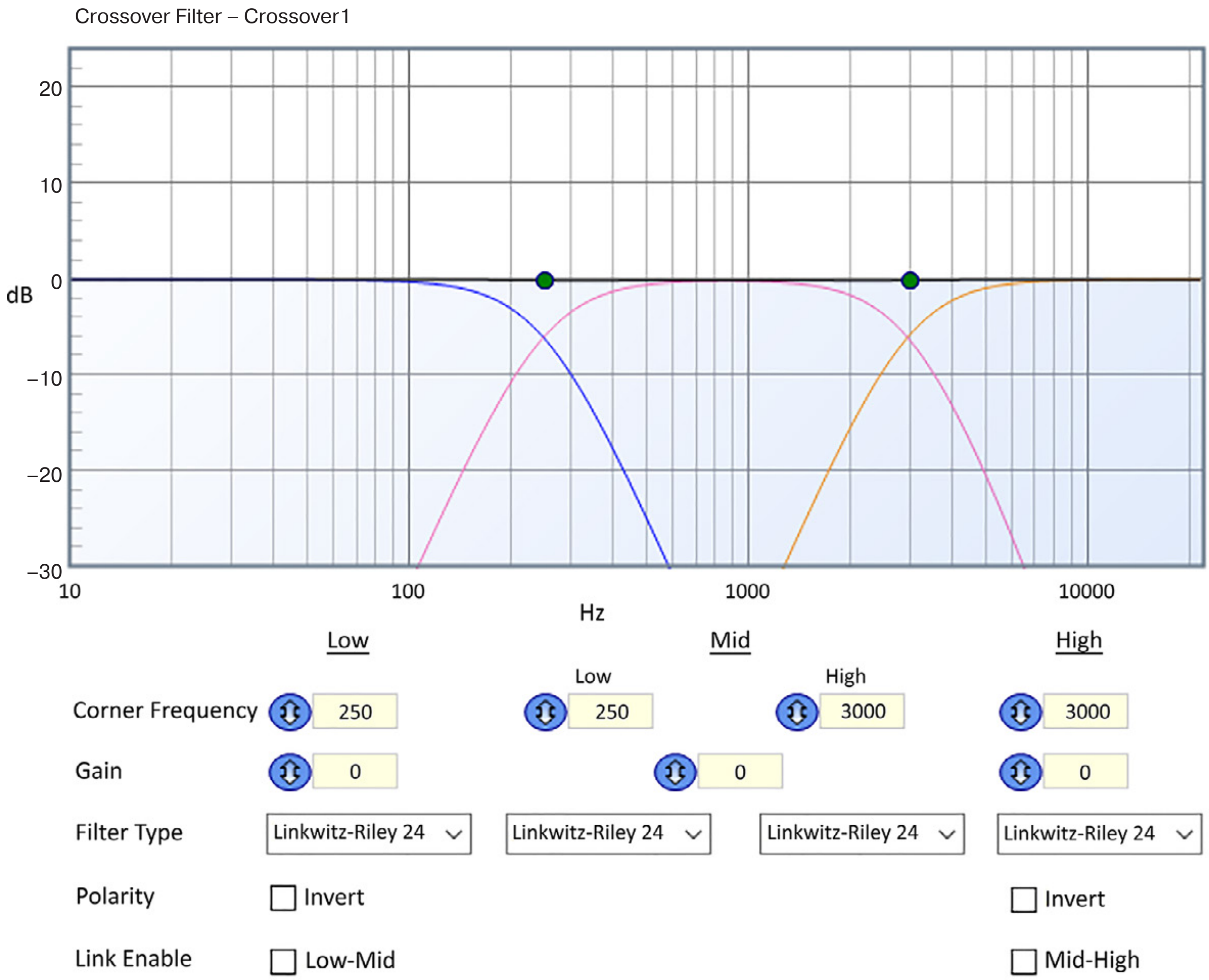

Fig. 11. Controlling the submodule settings of the digital three-band crossover digital crossover

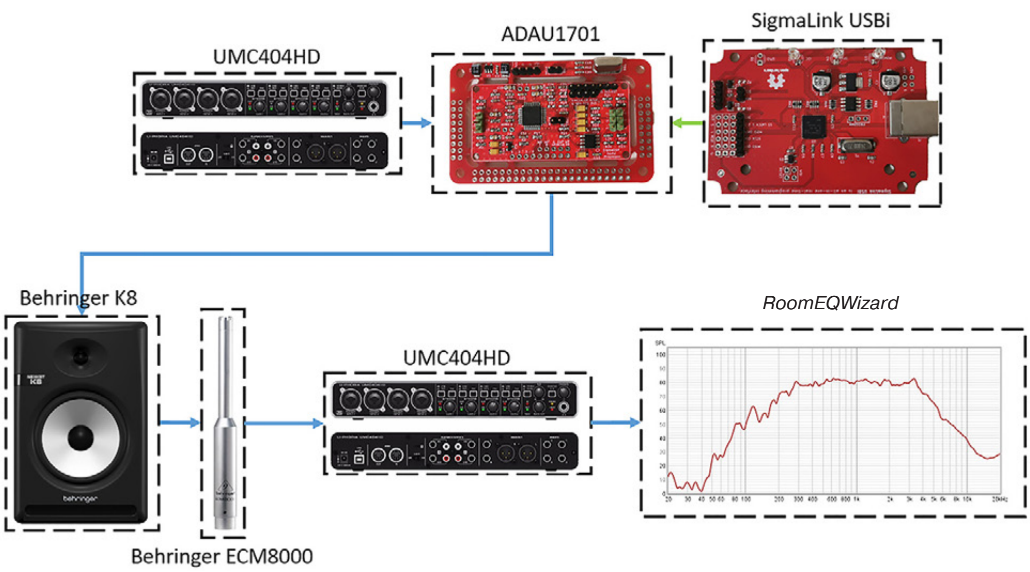

Fig. 12. Scheme of experimental research on controlling the AFR settings of a studio audio monitor using a digital crossover submodule

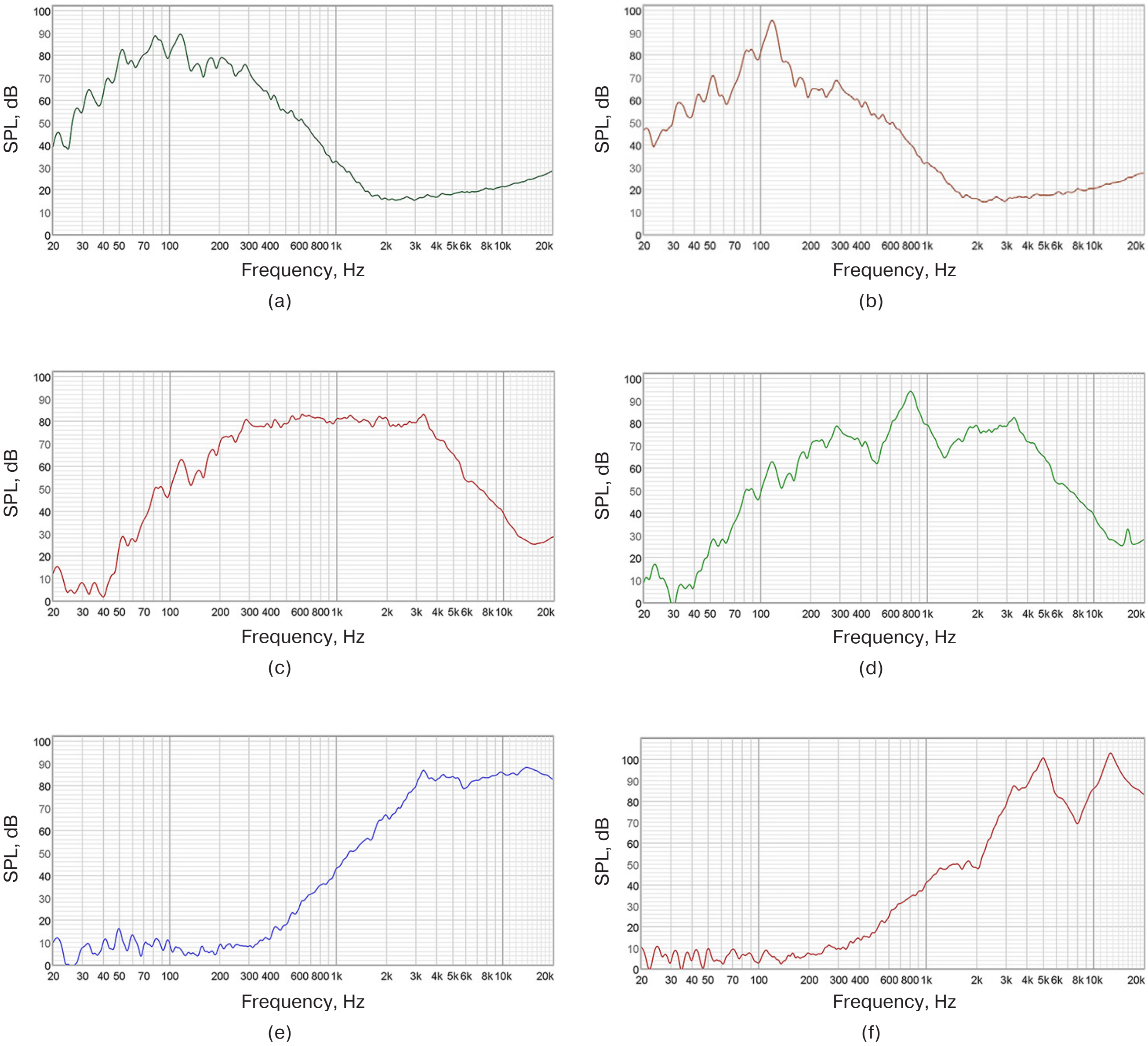

Fig. 13. AFR of the studio audio monitor formed by a digital crossover submodule in a given spectral region at preset leveled position 0 dB for filters (left) and arbitrary parameterization of the equalization line (right): (a), (b) LF audio channel; (c), (d) MF audio channel; (e), (f) HF audio channel

The measurements show that the three-way crossover submodule divides the audio signal into three audio-frequency channels: 20–250 Hz, 0.25–3 kHz, and 3–18 kHz. It also allows for repeatable AFR adjustment in each of them within the range from −30 dB up to 30 dB with the possibility of parametric correction. This allows this submodule to be used for audio signal routing in three-way loudspeaker systems, enabling independent research of each channel and panning the power spectral density function (PSDF) of the acoustic signal by frequency (Fig. 14).

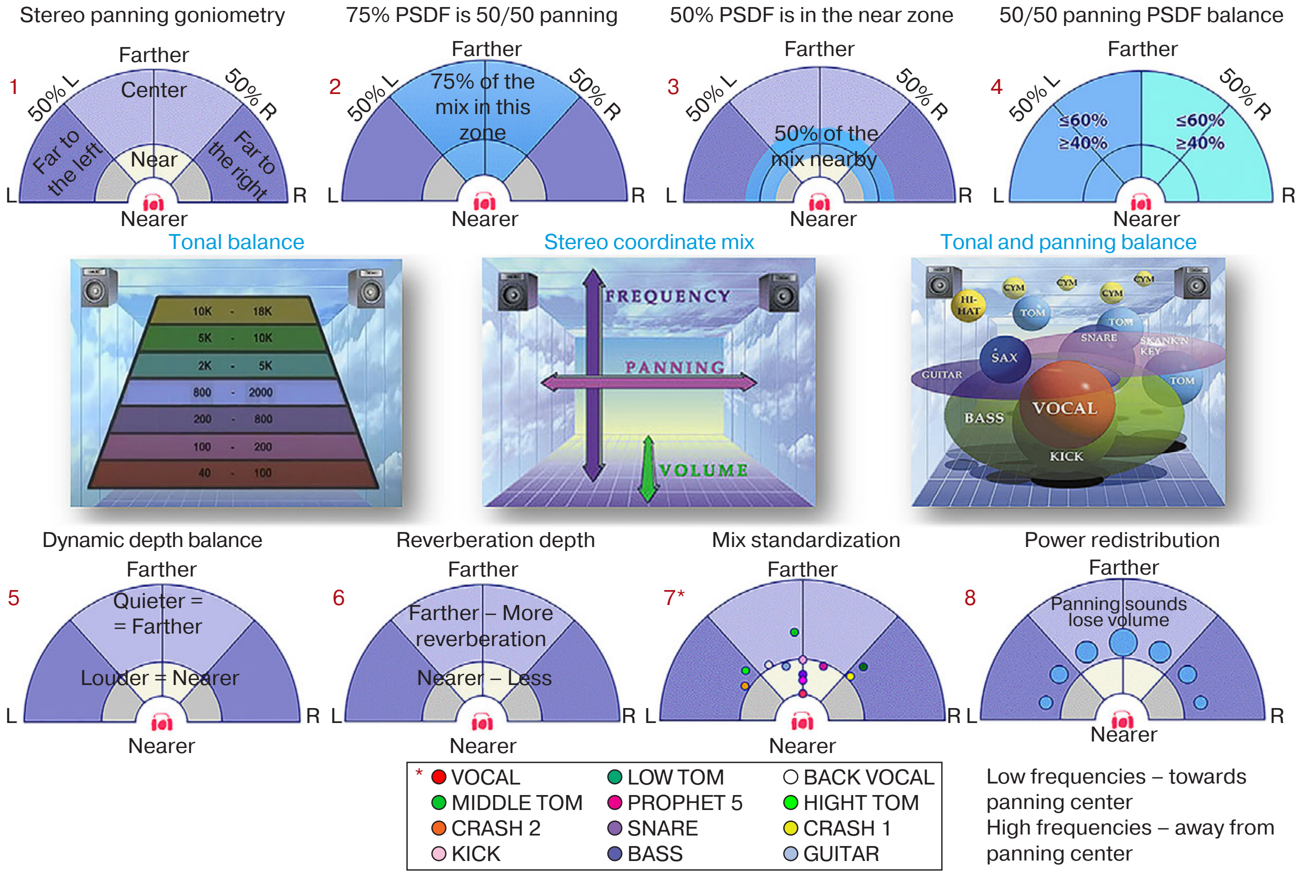

Fig. 14. PSDF panning by frequency (pitch) and sound intensity (depth)

3. ANALYZING THE COMPOSITE ARCHITECTURE CHARACTERISTICS FOR THE AUDIO EFFECTS SUBMODULE

The Effects audio effect submodule (Fig. 15) includes equalization, reverb, compression, and saturation blocks which form an insert line for audio signal processing. The audio mixer which admixes signals of the reverberator and saturator effects to the original audio signal (soundcheck) is installed at the submodule output with the ability to adjust the output levels of each of them. The digital architectural elements of the Effects submodule and its functional-graphical topology are shown in Fig. 15.

3.1. Analyzing and parameterizing the audio compressor characteristics

When analyzing the dynamic characteristics of the compressor which provides automated gain control in

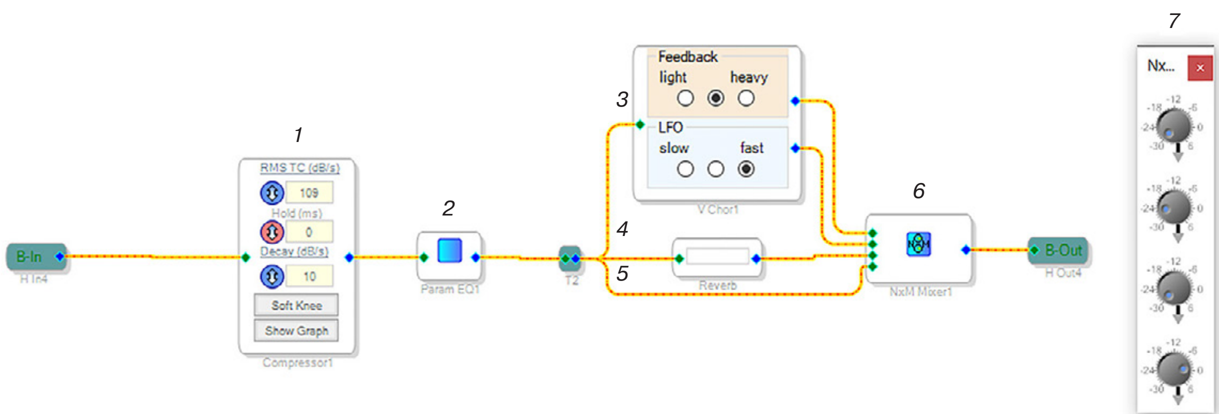

Fig. 15. Software-defined Box architecture of the audio effects submodule circuit: *1* is Compressor1; *2* is Param EQ1 parametric equalizer; *3* is V Chor1 saturation block; *4* is Reverb submodule; *5* is soundcheck signal route; *6* is 'N × M Mixer1' audio mixer; and *7* is 'N × M Mixer1' audio mixer adjustment window

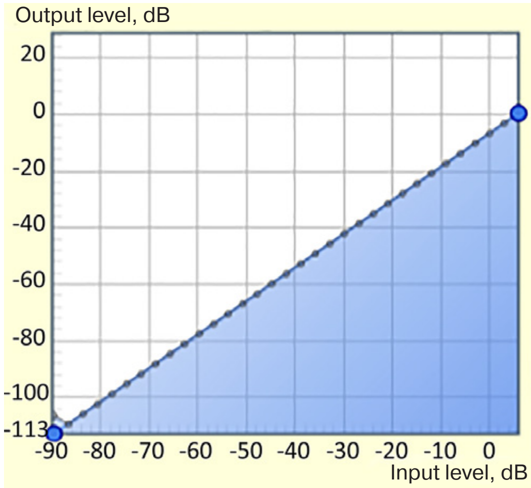

(a)

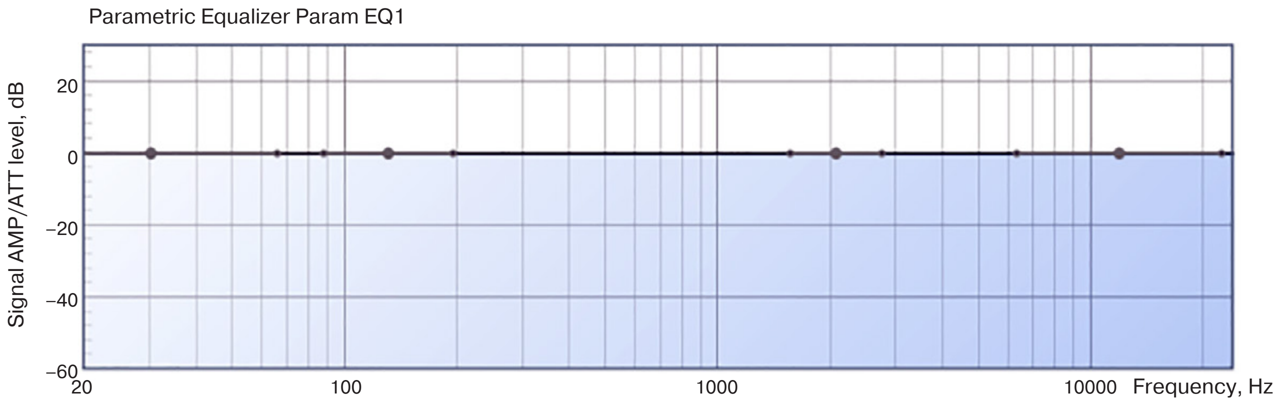

(b)

Fig. 16. Audio effects submodule presets: (a) initial amplitude response of the audio compressor (this mode does not affect the character of the test LFM signal passing); ▶ (b) equalization response of the submodule leveled at 0 dB ▼

the mode of equalizing the dynamic range of the digital submodule input signal, the level 0 dB needs to be set on the mixer for the channel with the signal bypassing the reverberator and saturator and minimum values for the rest. Figure 12 shows the experimental electroacoustic laboratory bench. It corresponds to the program switching of the audio module to the Effects submodule mode. Equalizer (Fig. 15, item *2*) is not involved, i.e. its AFR has a leveled zero dynamic value over the entire spectral band (Fig. 16). The submodule is tested using a monotonic linear-frequency modulated (LFM) signal of Sweep type within the range of 0.02–20 kHz and amplitude of 63 dB specified in the *RoomEQWizard* package.

The AFR of the audio monitor with free compression response is shown in Fig. 17. The signal level is −38.2 dB relative to full scale (dBFS). The AFR dynamic range is about 96 dB due to the roll-off in the LF region.

In order to evaluate the impact of the submodule compression response on the audio channel AFR, the graphic compressor presets may be changed by shifting the position of the compression response by 20 dB (Fig. 18).

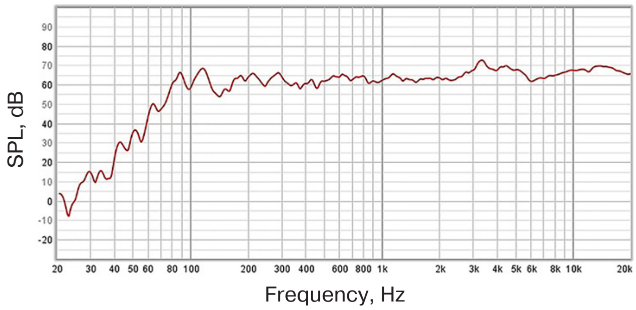

(a)

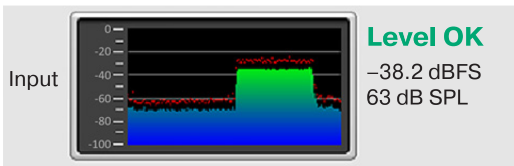

(b)

Fig. 17. Testing results for LFM signal of the audio path without compressor (reference AFR formation): (a) AFR of the audio monitor with free compression response (not subjected to the Effects submodule and compressor presets); (b) signal parameterization of *RoomEQWizard* presets (peak audio signal level relative to full scale in dBFS at the microphone)

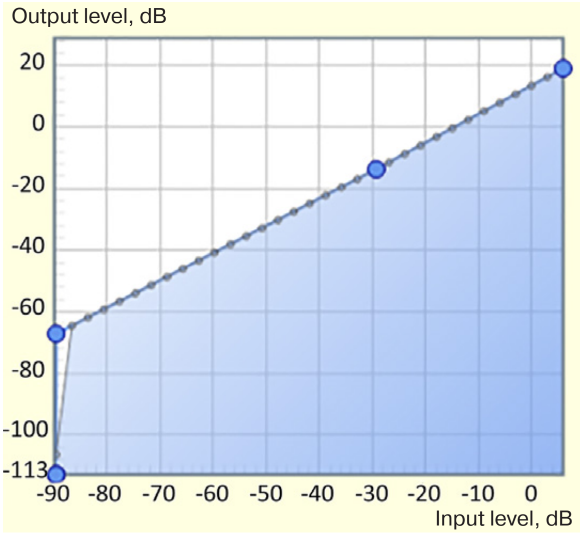

Fig. 18. Audio effects submodule presets: specified compression response with comparator threshold value of 20 dB (compander mode)

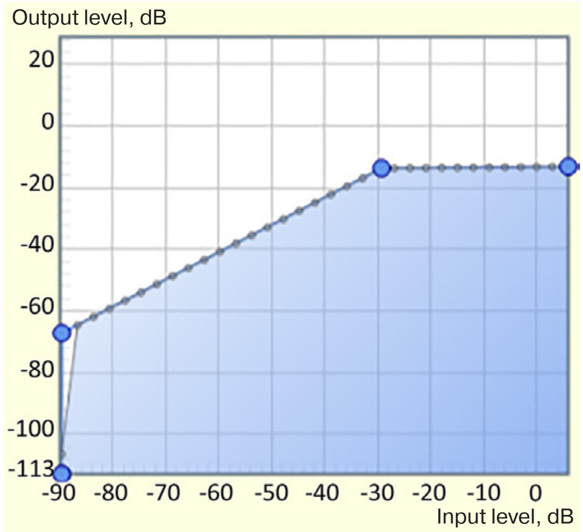

Fig. 20. Audio effects submodule presets: specified compression response with comparator triggering threshold −18 dB

Figure 19 shows that the AFR level is increased by 25.7 dB including 5.7 dB of inherent noise in the audio channel. The AFR dynamic range of the audio monitors is 85 dB: i.e., 11 dB less than in the absence of any changes in the dynamic balance adjustment threshold.

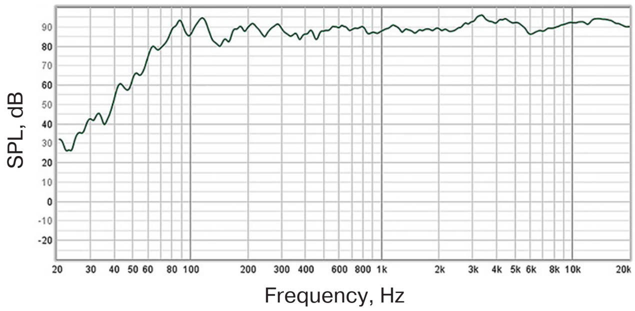

(a)

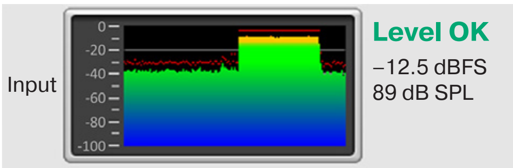

(b)

Fig. 19. Testing results for LFM signal of audio path with compressor at 20 dB threshold: (a) AFR of audio monitor with specified compression response; (b) signal parameterization of *RoomEQWizard* presets (peak audio signal level relative to full scale in dBFS at the microphone)

Next, in order to analyze the impact of the compressor on compressing the dynamic range of the audio channel, the output AFR level of the submodule is measured while setting the compressor response, in order to reduce the dynamic range of the input LFM signal to −18 dB as shown in Fig. 20.

The AFR shown in Fig. 21 indicates that the signal level has changed and is now −19.6 dBFS, i.e., increased by 18.6 dB relative to the uncompressed signal. The AFR dynamic range of audio monitors is 69 dB, i.e., 27 dB less than in the absence of any changes in the attenuation threshold.

Based on the electroacoustic measurement results, it can be concluded that the compressor allows the dynamic range of the signal to be compresses and its level increased over the whole frequency range according to the graphically defined compression response. It this way it stabilizes the dynamic range of the audio signal without distortion and overload of the tested audio device, and provides dynamic balance stabilization in the compander mode [10].

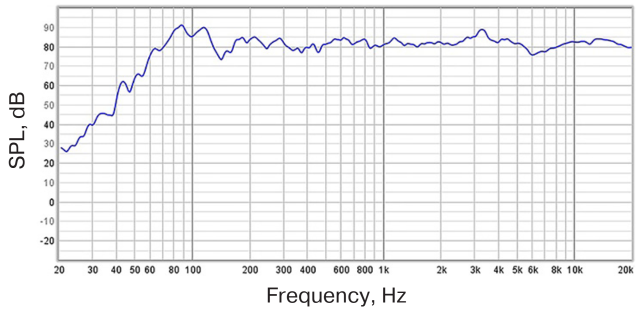

(a)

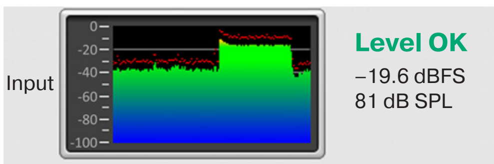

(b)

Fig. 21. Testing results for LFM signal of audio path with compressor at −18 dB threshold: (a) AFR of audio monitor with specified compression response; (b) signal parameterization of *RoomEQWizard* presets (peak audio signal level relative to full scale in dBFS at the microphone)

3.2. Analyzing and parameterizing equalizer characteristics

For the independent analysis of the equalization response of the Effects submodule, the compressor must be switched into bypass mode and the specified presets of the equalization filters (frequency, quality factor, and AMP/ATT) be set for the two options of forming the configuration of the acoustic signal AFR of the (Fig. 22). The paragraphic equalizer block of the multifunctional audio module allows up to 15 audio filtering elements to be set.

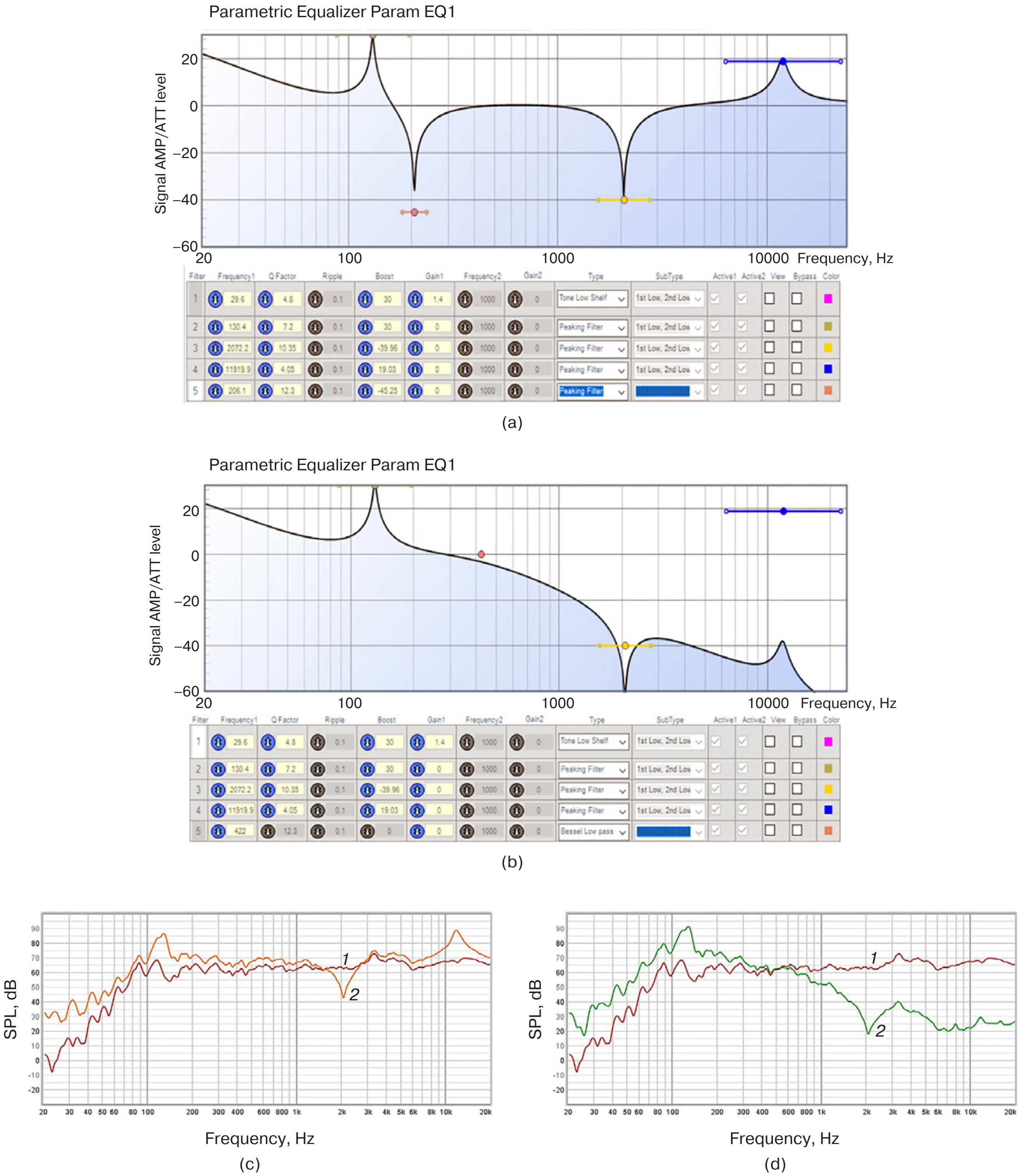

Fig. 22. Parameterization of the submodule equalization response for two options of filter configuration (a), (b) and corresponding electroacoustic AFR (c), (d) measured by microphone at the output of audio monitor (curves *1* are AFR without equalization, curves *2* are AFR after equalization)

As can be seen in Figs. 22b and 22d, the audio monitor AFRs repeat the preset equalization configurations (Figs. 22a and 22c) with a repeatability correlation of 0.85. This is due to the non-uniformity of the audio monitor AFR. In the section of the spectrum corresponding to the filter (Fig. 22a) at 130 Hz with 30 dB amplification, the amplitude is increased by about 20 dB, when compared to the amplitude of the same spectral band without processing. A similar situation can be observed for the filter at 2.072 kHz, with attenuation at −39.96 dB. Thus, the amplitude of the spectral band at this point is approximately 30 dB lower when compared to that of the original spectrum. A general dynamic rise can also be noted in the amplitude of the lower formants by an average of 20 dB, as set for the low-pass filter. Figure 22c shows that for the second option of equalization configuration, AFR with processing repeats the shape of the spectrum set on the equalizer (Fig. 22d). This can be established by an amplitude increase of 20 dB on average for frequencies in the range up to 100 Hz (in this case, the dynamic levels at frequencies "rolled-off" by physical parameters of the audio monitor are stretched), as well as by attenuation of high frequencies by about −35 dB.

Based on an analysis of the experimental characteristics, it can be concluded that the electro-acoustic AFR changes significantly depending on the equalizer settings, actually repeating the shape of the amplitude spectrum specified therein. This may be of practical interest when designing laboratory audio monitors with uniform AFR correction, as well as for testing media devices and acoustic systems when using a multifunctional module in this mode [11].

3.3. Developing and analyzing characteristics of a reverberator with timing architecture

Reverberation response is also analyzed in the independent activation of the graphic equalizer and the audio compressor submodule (Fig. 15, item *4*). A sequence of rectangular test pulses with an amplitude of 20 mV and controlled duty cycle generated by a specially developed VST plugin (synthesizer) in the visual-graphical system programming environment *Flowstone* (Fig. 23) is fed to the physical input of the ADAU1701 audio module through the UMC404HD audio interface [1]. The reverberator characteristics were analyzed on the basis of the electro-acoustic measurement laboratory bench as shown in Fig. 8.

In the proposed submodule architecture with timing reverberation [12] (Fig. 24), the signal passes through: the low-pass filter (item *5*) with a cutoff frequency of 6 kHz; the 21.25 ms digital delay block (item *6*) in 1020 samples; and the feedback loop (item *4*) providing control over 1–3 s timed reverberation. The feedback loop has two delay elements (item *6*) with a delay of 4 samples, and one with a delay of 12 samples with the ability to adjust the level of the passing signal. The delayed signal passes to the output in parallel with the original signal. This is reduced in frequency by a factor of 4 when compared to the sampling frequency of the system.

The results of the reverberation audio channel characteristic of the digital submodule with timing architecture are in the form of oscillograms recorded using the *Soundcard Oscilloscope* and the UMC404HD audio interface. This enables the impact of the specified time delays to be evaluated. The transfer factor and feedback

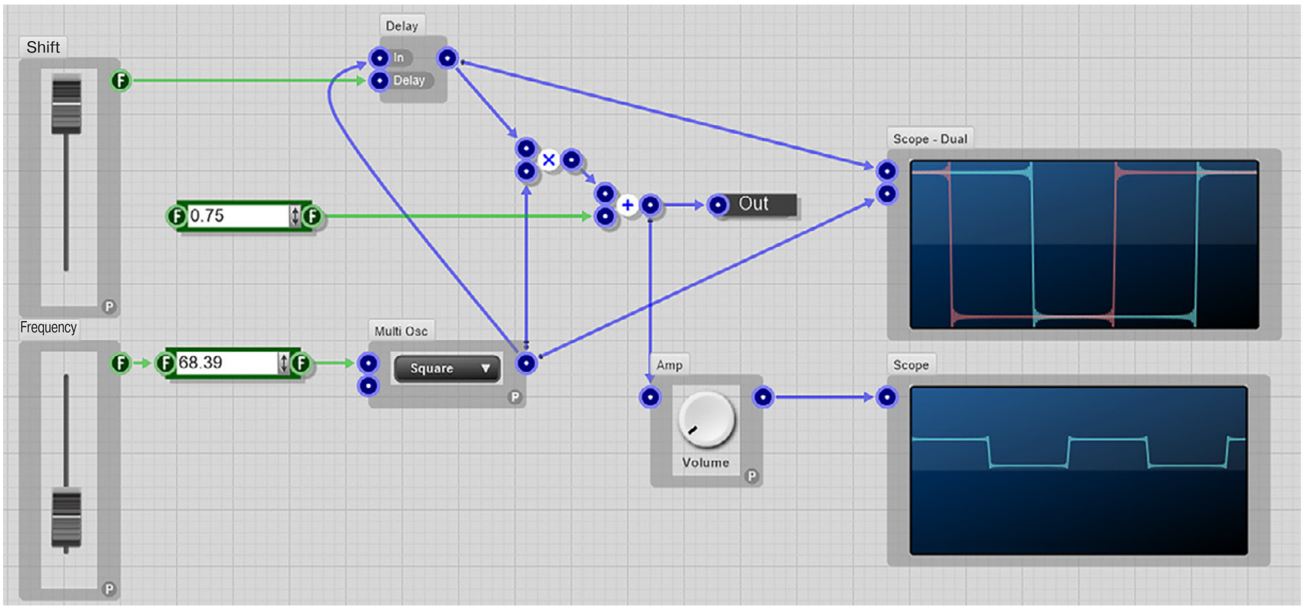

Fig. 23. VST synthesizer of test rectangular pulses

loop attenuation for generating echo reverberation signals are shown in Fig. 25.

Ananalysis of the characteristics obtained shows the amplitude instability of the test rectangular pulses: up to 5 mV due to the presence of a differential circuit at the UMC404HD audio interface output. In addition, the inherent noise of the sound card and ADSP module of about −40 dB is admixed to the signal. The oscillogram shown in Fig. 25b demonstrates that at given parameters of the reverberation limit level (0 dB for the delayed source signal, −8 dB for the feedback line (Fig. 24, item *2*), and −10 dB for the volume fader of the additional delay (Fig. 24, item *8*)), the main signal copies delayed by 500 ms and 1s with amplitudes of 3.5 mV and 1.0 mV, respectively, are added to the 12.5 mV main signal. When the signal is attenuated by −10 dB, the amplitude of the original signal (Fig. 25c) in the reverberation circuit is equal to 17 mV. Of the fragmentary components, only the first one with an amplitude equal to 2 mV remains. At the same time, at minimum parameters of feedback level (Fig. 25d) (−14 dB to the feedback circuit (Fig. 24, item *2*)), the amplitude of the original signal is equal to 17 mV. Of the additional components only the first one with an amplitude equal to 4 mV remains.

Thus, a timing-controlled digital reverb block adds delayed copies to the original audio signal. This submodule enables the feedback depth and its admixing degree to the original signal to be adjusted, i.e. used for simulating characteristics of the diffuse vector field of architectural acoustics. It is of interest in the creation of phantom reverberation effects, as well as when studying the properties of the audio signal and its qualitative reproduction under given conditions of the propagation environment [13].

3.4. Analyzing and parameterizing the signal saturator characteristics

The characteristics of V Chor1 saturation block of the Effects submodule (Fig. 15, item *3*) are analyzed and parameterized using a sinusoidal signal in the spectral region. The built-in low-frequency oscillation (LFO) add-on determines the delay time modulated by the low-frequency oscillator. It has three modes of operation: Slow (i.e., with the longest delay); Normal (medium); and Fast (i.e., with the shortest delay). The Feedback add-on defines the degree of mixing the delayed signal with the original one: Light (i.e., a small part is admixed); Normal (medium); and Heavy (oversaturated). The signal saturation mode in the Effects submodule is of practical interest in developing and testing digital media devices which enable the original signal (soundcheck) to be saturated with odd formants simulating the nonlinear distortion effect of transistor stages of analog audio tracts [4]. The saturation block consists of the positive feedback circuit and a low-frequency delay time modulator. The mode settings in the circuit are controlled by the 'N × M Mixer1' volume mixer at the submodule output (Fig. 15, item *7*).

The spectral response characteristics shown in Fig. 26 indicate that saturation adds multiple odd subharmonics to the spectrum of the test (original) signal with a frequency of 1 kHz. The spectrum analyzer has the maximum value hold mode enabled. In this way, the spectrum snapshot is taken one minute after the submodule starts operating. The results of analyzing the saturator response are given in the table.

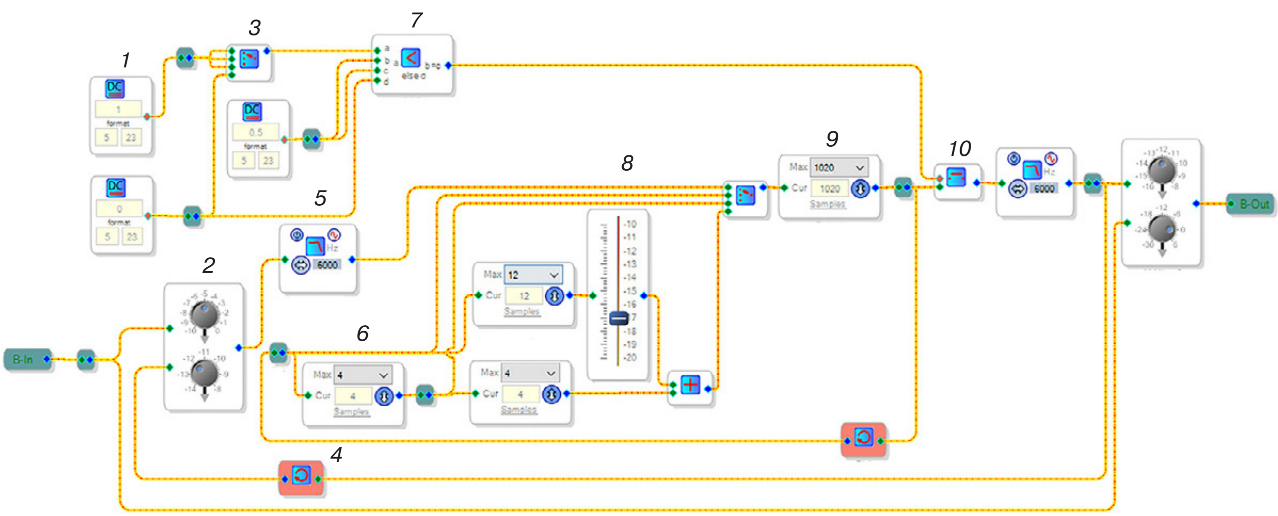

Fig. 24. Software-defined architecture of the 4th order timing reverberator submodule circuit: *1* is constant value generation blocks; *2* is mixer determining the feedback depth; *3* is synchronous multiplexer; *4* is feedback creation block; *5* is low-pass filter; *6* is signal delay block; *7* is comparator; *8* is additional delay fader; *9* is main signal delay block; *10* is digital key

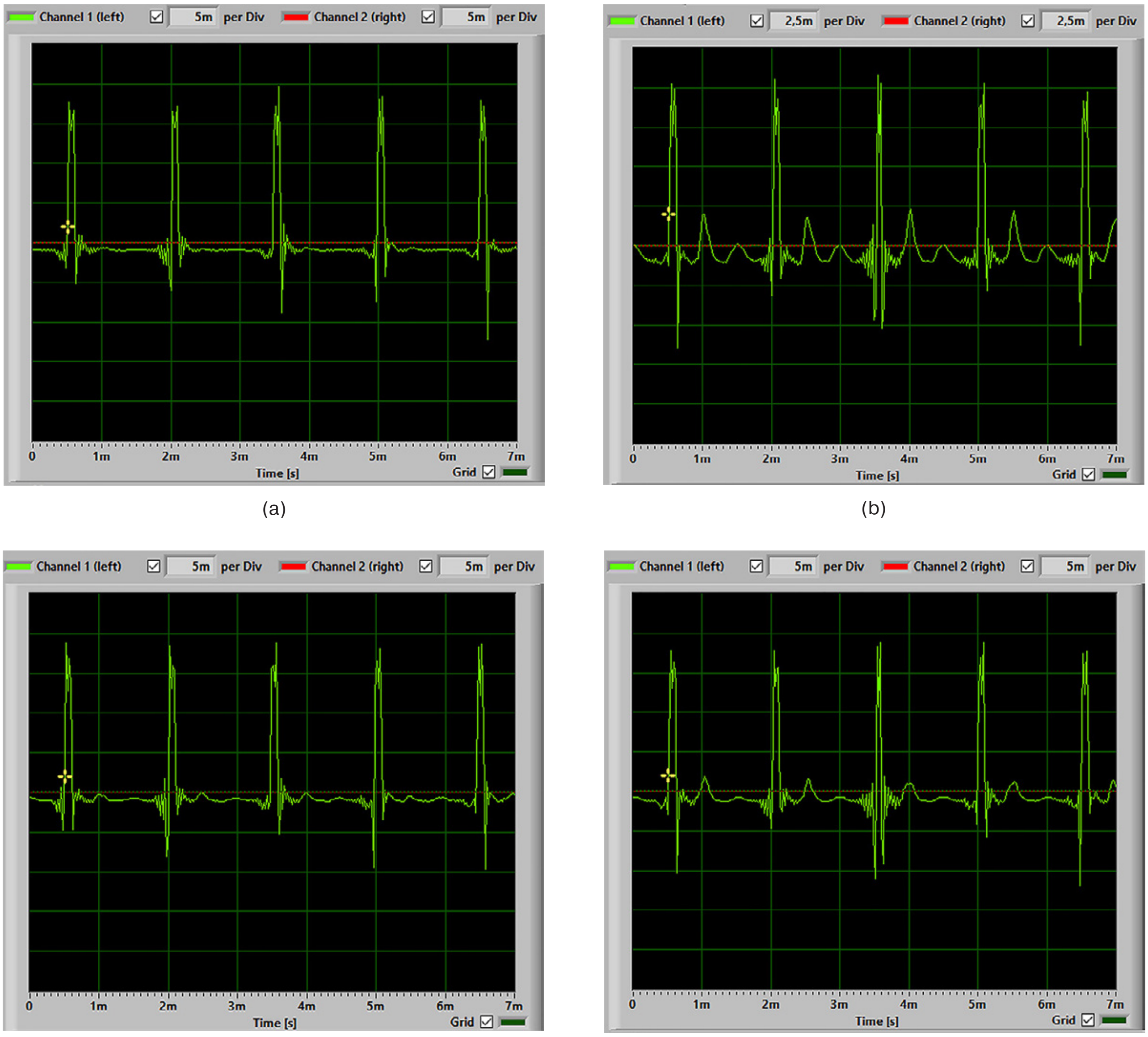

Fig. 25. Oscillograms of studying reverberation audio channel response: (a) test pulse signal; (b) audio signal with the limiting reverberation level corresponding to the circuit presets (Fig. 24); (c) audio signal attenuated by −10 dB in the reverberation circuit; (d) signal with the minimum feedback level corresponding to the circuit presets (Fig. 24)

Table. Experimental characteristics of the saturator at given add-ons

Saturator add-on (operation mode)	Feedback–Light	Feedback–Heavy	LFO–Slow	LFO–Fast	Feedback–Light, LFO–Slow	Feedback–Heavy, LFO–Fast
Amplitude of test signal with frequency 1 kHz, mV	60	60	60	60	60	60
Amplitude of the 1st subharmonic, mV	15	15	15	18	17	20
Amplitude of the 2nd subharmonic, mV	7	5	6	8	9	11
Frequency bandwidth carrier at 5 mV level, Hz	200	100	100	50	200	50
Number of subharmonics with a level of at least 1 mV	6	5	5	5	9	8

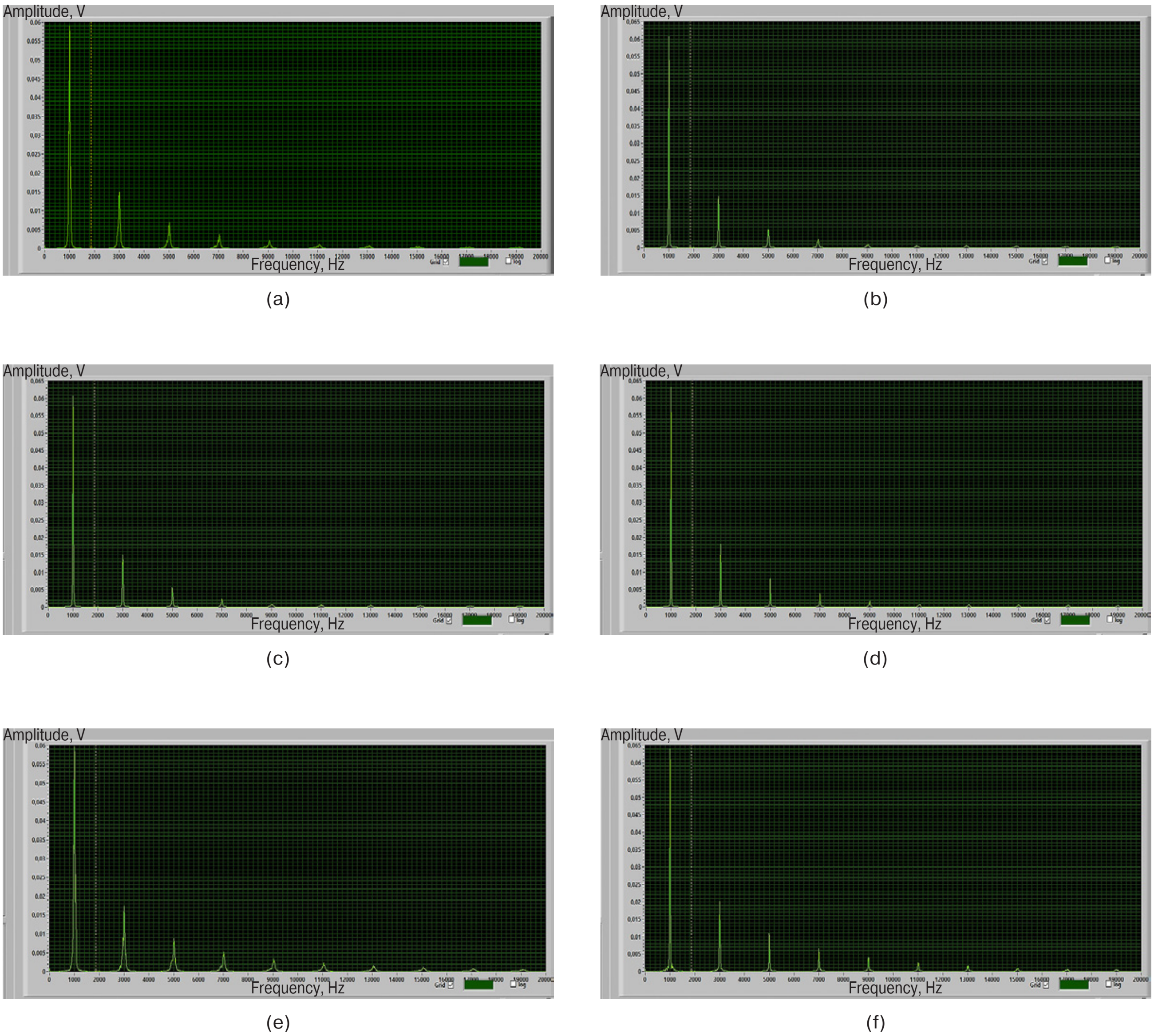

Fig. 26. Spectrograms of the signal saturation mode:
(a) output signal with the Feedback–Light add-on set;
(b) output signal with the Feedback–Heavy add-on set;
(c) output signal with the LFO–Slow add-on set;
(d) output signal with the LFO–Fast add-on set;
(e) output signal with the Feedback–Light and LFO–Slow add-ons;
and (f) output signal with the Feedback–Heavy and LFO–Fast add-ons

The data in the table indicates that the saturator operation in the Feedback–Light and LFO–Slow combined mode produces the largest number of subharmonics and the largest bandwidth of the original signal. The Feedback–Heavy and LFO–Fast mode yields the largest amplitude of the carrier and the first two subharmonics, and the smallest generated frequency bandwidth at 5 mV. Thus, the saturation block adds odd harmonics to the spectrum of the original signal, thus widening the formant band and increasing the spectral power density of the signal. Additionally, the number of subharmonics and their amplitude can be adjusted. The signal saturation mode enables effects of phono-tertial/phono-octave polyphony to be created. These are often used in processing real-time audio signals including electroacoustic measurements when analyzing the intensity distribution of spectrally saturated diffuse sound field [14].

4. DEVELOPING, ANALYZING AND EVALUATING THE EFFICIENCY OF THE AFR AUTOCORRECTION SUBMODULE

Due to their nonuniformity, the phase-dynamic responses of audio monitors, as well as AFR of the diffuse space of sound field propagation (including those caused by wave dispersion) are usually corrected by applying compensation filters to the distorted parts of AFR [4]. AFR uniformity is extremely important for correct audio signal processing and electroacoustic measurements. The architecture for the AFR autocorrection circuit, as proposed in this paper, enables the frequency-dynamic and phase balance of the speakers to be equalized. This is due to the specific features of AFR nonuniformity of the diffuse space, for example, a recording studio [12]. In order to create an adaptive filter in the circuit of the AFR autocorrection submodule, the AutoEQ developed block is used. This enables a corrective chain of matched filters to be automatically built, according to the AFR numerical values loaded into it.

Figure 27 shows an experimental scheme for synthesizing the adaptive parameterization and measurement of multifunctional audio module characteristics in the AFR autocorrection mode. The Behringer ECM8000 measuring microphone is installed opposite the center of the audio monitor speaker at an axial distance at the specified recording point. This is so that the sound pressure level (SPL) is no lower than 75 dB, while the audio module is included in the audio path between the output of the audio interface and the input of the active studio monitor.

The procedure for AFR monitor autocorrection consists in measuring the diffuse space AFR and creating a counterbalanced adaptive AFR of the correction filter. This enables the dynamic range of the electroacoustic path to be leveled within the limit range of ±10–15 dB due to phase-dynamic compensation in a given volume of the sound field [8]. In the *RoomEQWizard* package, a test LFM signal of the Sweep type in the 0.02–20 kHz bandwidth is generated at the audio interface output. Based on the data obtained by the program from the Behringer ECM8000 measuring microphone (AFR of the microphone and the audio interface is compensated by a calibration file), the acoustic AFR/PFR (phase-frequency response) of the room is created. This integrates the AFR/PFR of the signal audio path including studio audio monitors (Fig. 28a) which can then be exported from the program as a data array (frequency, amplitude, and phase) in ".txt" format (Fig. 28b).

Loading this file into *SigmaStudio* requires the header inside the export file to be changed, as shown in Fig. 28c. Next, the export file is loaded into the AutoEQ block of the AutoCorrection submodule. The AFR for the adaptive filtering system is automatically calculated and plotted (Fig. 29a).

The block interface enables the number of filters (up to 15) to be selected, along with the manual preset/adjustment of their parameters. The experimental curves of AFR autocorrection results generated by the AutoCorrection submodule are shown in Fig. 29b. The limit deviation of the dynamic range after autocorrection is within ±10 dB in the region up to 100 Hz and ±5 dB in the 0.1–20 kHz band. Auto-measurement mode and data file loading into ADAU1701 audio processor is provided for the different conditions of auto-compensation for AFR nonuniformity of the diffuse space due to correction of AFR of audio monitors.

The curves shown in Fig. 29b indicate that autocorrection allows the dynamic level "roll-off" in the band below 80 Hz to be raised by almost 40 dB. It also enables the average signal level in the dip region to be raised, e.g., by about 7 dB at 1 kHz without affecting peak values, e.g., at 80 Hz and 3.3 kHz. AFR non-uniformity in the measurements presented herein is ±10 dB in the region up to 100 Hz and ±5 dB in the 0.1–20 kHz band. This makes the AFR of the diffuse space in some volume of the sound field relatively uniform during electroacoustic tuning of studios and halls. This enables media systems to be tested, and audio equipment to be tuned and adjusted without introducing distortion [12].

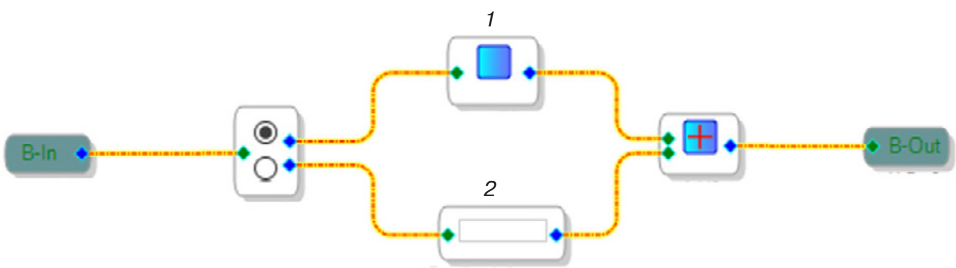

Fig. 27. Software-defined architecture of the AFR autocorrection submodule circuit: *1* is AFR autocorrection block Auto EQ1; *2* is Feedback Attenuator submodule for suppressing positive feedback automatically

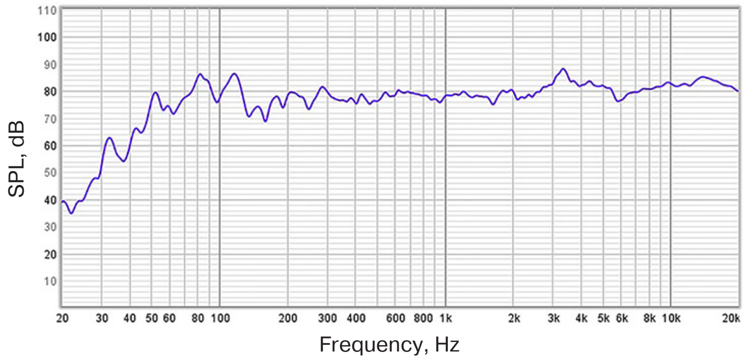

(a)

```
* Measurement data measured by REW V5.20.9
* Source: ASIO UMC ASIO Driver, In 1
* Format: 256k Log Swept Sine, 1 sweep at -12,0 dBFS with no timing reference
* Dated: 07.12.2022 15:57:29
* REW Settings:
*  C-weighting compensation: Off
*  Target level: 75.0 dB
* Note:
* Measurement: Dec 7
* Smoothing: None
* Frequency Step: 1/24 octave
* Start Frequency: 1.000 Hz
*
* Freq(Hz), SPL(dB), Phase(degrees)
1.000000, 34.963, -124.7207
1.030000, 34.536, -124.7025
...
...
...
19000.000000, 81.612, 19.5586
19500.000000, 80.173, 22.6615
```

(b)

```
"Sensitivity Excess Phase - dB SPL/watt (8 ohms, @0.50 meters) (High)"
        "Hz"   "Mag (dB)"       "deg"
1.000000, 34.963, -124.7207
1.030000, 34.536, -124.7025
...
...
...
19000.000000, 81.612, 19.5586
19500.000000, 80.173, 22.6615
```

(c)

Fig. 28. AFR of diffuse space:
(a) at an arbitrary point of sound field distribution of the laboratory studio for signal radioacoustics, audiovisual systems, and technologies of the Department of Radio Wave Processes and Technologies at MIREA – Russian Technological University (RTU MIREA);
(b) exported AFR/PFD data array corresponding to the curve in (a); and
(c) correction of the data export format from the *RoomEQWizard* package to the *SigmaStudio* environment

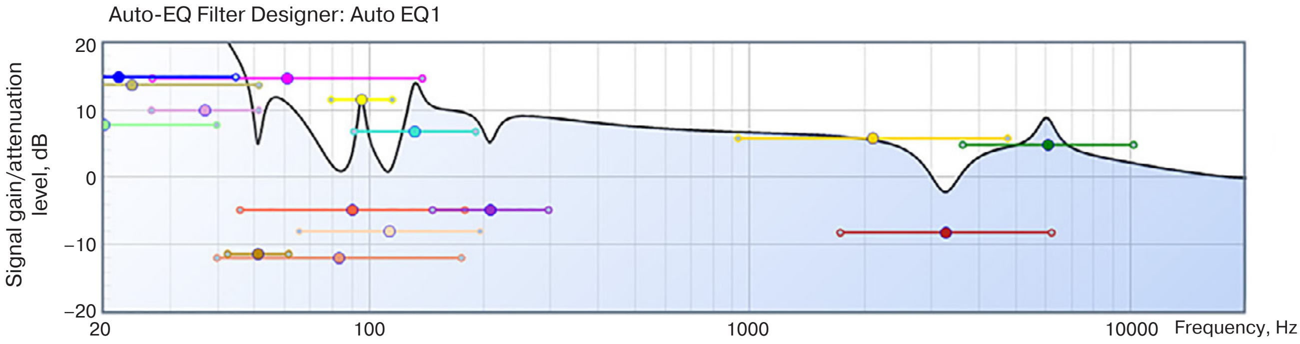

(a)

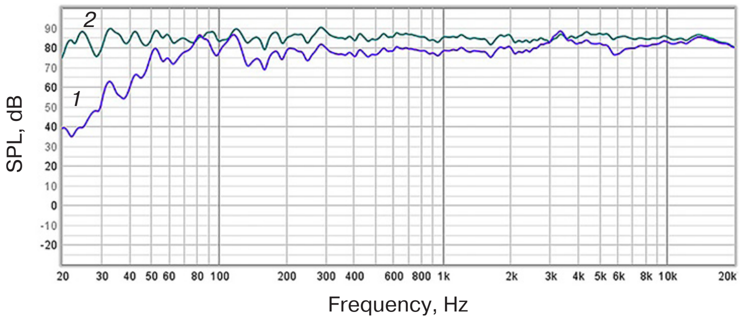

(b)

Fig. 29. Experimental results of the AFR autocorrection in an arbitrary coordinate volume of the diffuse space of the studio laboratory: (a) plotting the compensatory AFR/PFR of the adaptive filter based on the AutoEQ block; ▲ (b) AFR before (curve *1*) and after (curve *2*) autocorrection ▶

5. DEVELOPMENT AND SIGNAL-PARAMETRIC ANALYSIS OF THE AUTO-COMPENSATION SUBMODULE OF ELECTROACOUSTIC POSITIVE FEEDBACK

Electroacoustic positive feedback phenomenon is known to result in autogeneration, caused by the formation of a mode of sharply increasing phase-amplitude balance between the microphone and the audio monitor speaker. This is in the strict sense, determined by conditions of the sound propagation medium, the distance between the sound source and receiver, as well as their resonant frequencies and directional diagrams. The source thereof is the inherent noise of the electroacoustic channel [5]. Electroacoustic positive feedback is suppressed by disturbing the phase-dynamic balance of the system by means of initiating the selective phase drift (rendered phase shifting of the signal at critical resonant frequencies) or creating narrow-band notch filtering (dynamic suppression of the signal at critical frequencies) [15]. Figure 30 shows the submodule connection circuit for auto-compensating the electroacoustic positive feedback. In this case, the low position should be selected on the ‘1 × N − 3’ switch in the auto-correction submodule, corresponding to the mode of auto suppression of acoustic positive feedback in the Auto EQ1 Box submodule.

As shown in Fig. 31, the experimental scheme of the laboratory research of the audio module in the positive feedback auto-compensation mode requires the following audio channel routing: the audio signal induced into the diffuse space by the audio path inherent noise within the range from −50 to −40 dB from the monitor goes from the Behringer ECM8000 measuring microphone to the ADAU1701 input. From here it passes through the Auto EQ1 positive feedback auto-compensation submodule scheme. The signal is then routed to the input of the UMC404HD audio interface. From the output it goes to the Behringer K8 audio monitor. The microphone is located in the main line of the directional pattern of the audio monitor speaker at a distance of 1m. The audio interface input is set to sensitivity of 10 dB, in order to ensure the microphone picks up the inherent noise of the electroacoustic channel.

The initiated frequency resonances are compensated (notched) using the Auto EQ1 submodule included in the audio path. Then the selectively attenuated signals are fed to the audio interface input, where the oscillogram is recorded using the *Soundcard Oscilloscope*.

The software-defined circuit configuration of the positive feedback auto-compensation notch submodule (Fig. 32) is a system consisting of 18 auto-filtering blocks connected in series. This system enables selection at a nominally specified frequency combination of 31, 63, 87, 125, 175, 250, 350, 500, 700 Hz and 1, 1.4, 2, 2.8, 4, 5.6, 8, 11.2, 16 kHz with controllable bands providing an overlapping frequency range of 0.02–18 kHz [15].

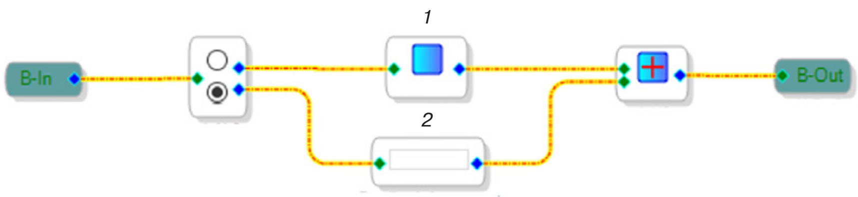

Fig. 30. Software-defined architecture of the submodule connection circuit for auto suppression of acoustic positive feedback: *1* is the AFR auto correction block Auto EQ1; *2* is the Feedback Attenuator submodule of automatic positive feedback suppression

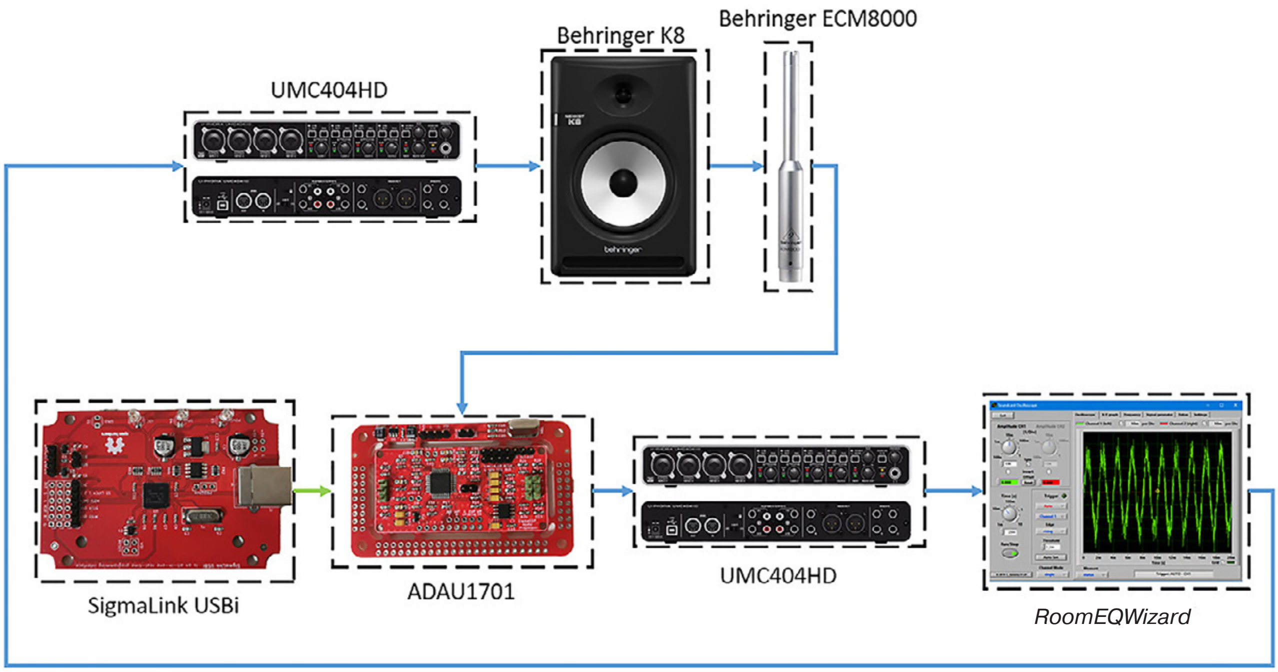

Fig. 31. Scheme of the experimental research of the multifunctional ADSP module in the mode of switching the submodule of electroacoustic positive feedback auto-compensation on

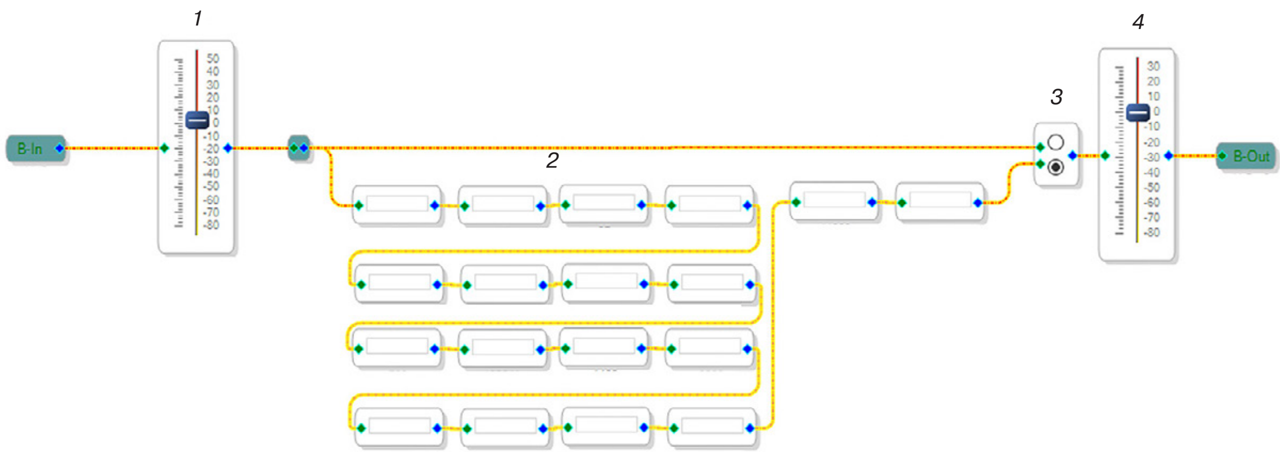

Fig. 32. Software-defined architecture of the circuit for positive feedback auto-compensation submodule: *1* is Single 1_2 input volume fader; *2* is the line of notch filters; *3* is 'N × 1 – 1_2' digital switch; *4* is the Single 2_2 output volume fader

frequency at the adjustable level of notch attenuation of the signal within the range from 0 dB to −100 dB.

In this method of positive feedback notch auto-compensation, notch filters are triggered only when resonance occurs and after the user-defined time of 0–10 s. Then they are reset, thus preventing the system from significantly impacting the AFR of the speaker. The filter frequencies and goodness (Fig. 33, item *6* and *7*) fully overlap the entire operating frequency range of 0.02–20 kHz at the input dynamic range from −50 to 80 dB.

When examining the Auto EQ1 submodule, a test signal in the form of the audio channel inherent noise with the level from −50 to −40 dB is formed at the circuit input. Figure 34 shows the experimental spectral-time characteristics of the signal auto-compensation of the electroacoustic positive feedback. This illustrates the mode of selective suppression of the initiated frequency-resonance spikes up to the level of 2.75 mV (below the dynamic level of the audio path inherent noise). The microphone continues to pick up the useful audio signal and noise at any other frequencies, including spectral formants which do not fall into the unstable mode region of the system. If the resonance does not occur within 10 s, the notch filter is switched off, thus preventing AFR notch distortion caused by random (simultaneous) resonances. The submodule of the electroacoustic positive feedback notch auto-compensation is of practical interest when testing studio media systems for stability according to the Nyquist criterion [4]. It also prevents overloading of audio monitors due to the electroacoustic positive feedback effect. When analyzing the frequency-time characteristics shown in Figs. 34a and 34b, special attention should be paid to the presence of a periodic signal with an amplitude of 240 mV consisting of 7 harmonic components with a level higher than 10 mV. The characteristics shown in Figs. 34c and 34d demonstrate the presence only of a noise signal with an amplitude of 2.75 mV without pronounced frequency components.

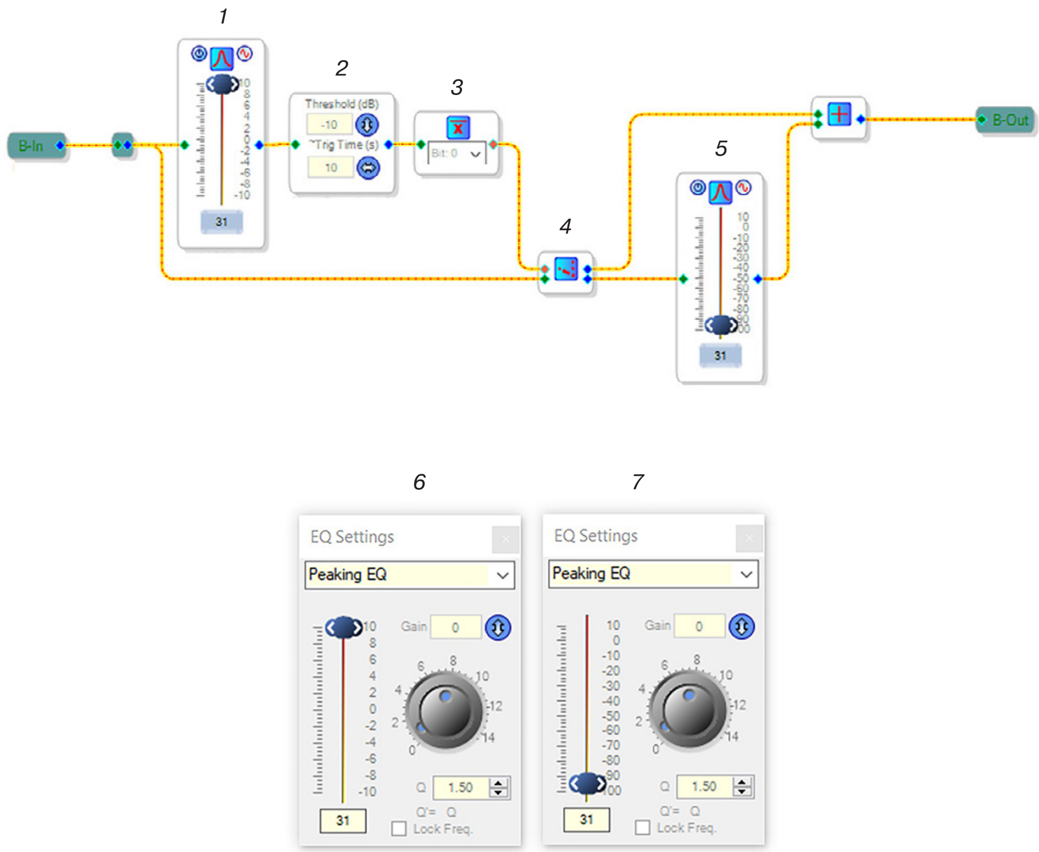

Fig. 33. Scheme of the block of bandpass auto-tracking the acoustic positive feedback: *1* is Mid EQ3_19 BF; *2* is Signal Detection1_21 block; *3* is ZeroComp1_21 zero-comparison block; *4* is DmX2_19 demultiplexer; *5* is Mid EQ2_21 NF; *6* is Mid EQ3_19 BF adjustment window; and *7* is Mid EQ2_21 NF adjustment window

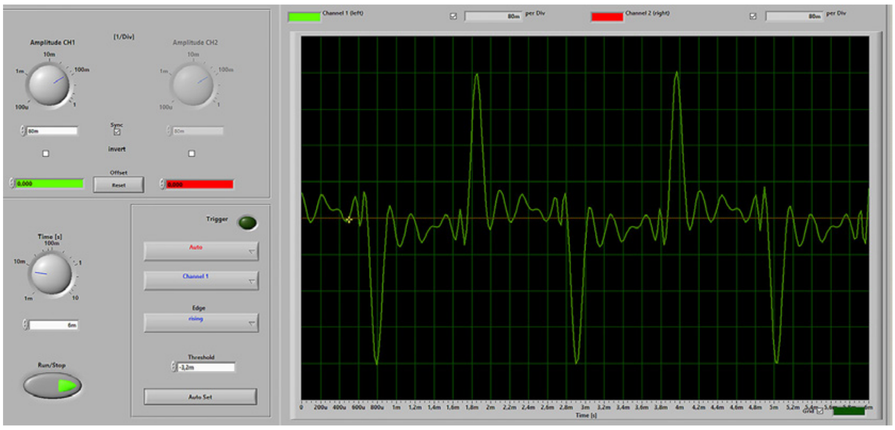

(a)

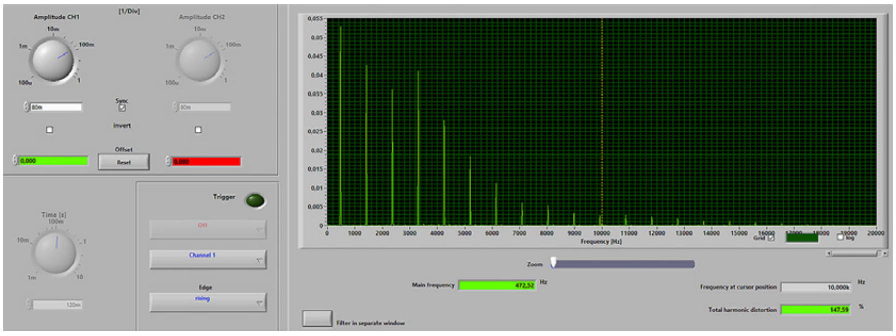

(b)

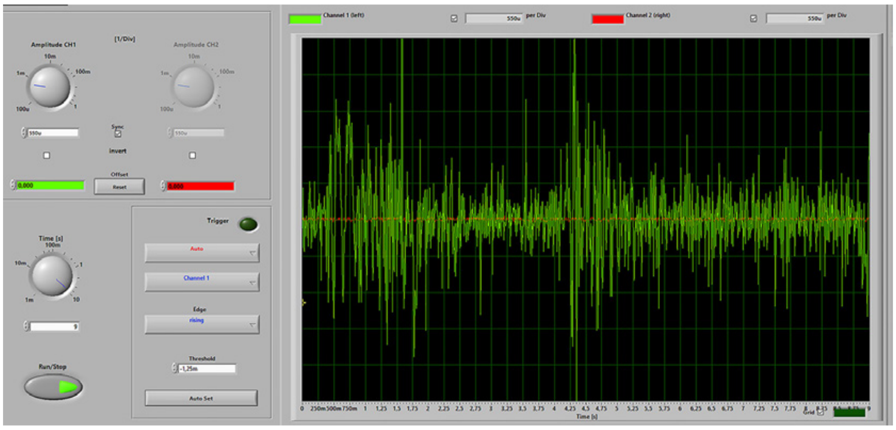

(c)

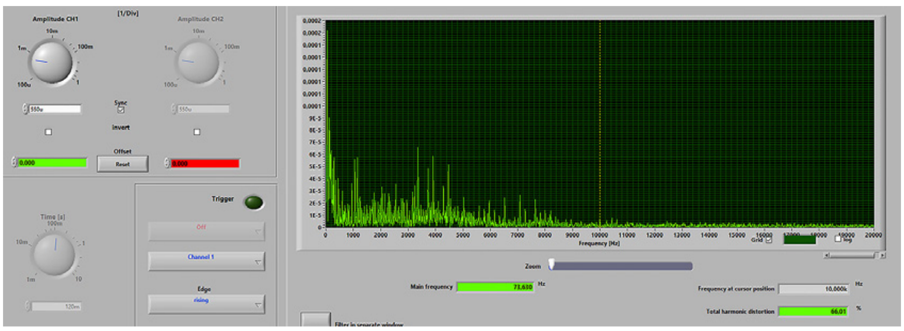

(d)

Fig. 34. Frequency-time characteristics of the research results for the positive feedback auto-compensation submodule: (a) oscillogram of the stable mode of acoustic positive feedback formation (without auto-compensation); (b) amplitude spectrum corresponding to oscillogram (a); (c) oscillogram of the stable mode of the positive feedback auto-compensation; (d) amplitude spectrum corresponding to oscillogram (c)

Fig. 35. Educational and scientific laboratory of signal radioacoustics, audiovisual systems, and technologies of RTU MIREA and VGTRK

CONCLUSIONS

The multifunctional audio signal processing module based on the ADAU1701 processor was designed and investigated in the *SigmaStudio* visual-graphical software-architectural ADSP design environment. This allowed for media systems to be tested, and the characteristics of sound processing devices to be investigated. It also enabled the debugging and correcting AFR of audio monitors, as well as the processing of audio signals and simulation of conditions of the diffuse environment of sound field propagation in a limited space. The electro-acoustic and in-channel audio measurements of the audio module were performed using specially constructed experimental benches and *RoomEQWizard* and *Soundcard Oscilloscope* automated measurement software. This was carried out using the facilities of the studio laboratory of signal radio-acoustics, audio-visual systems, and technologies at the Institute of Radio-electronics and Informatics at RTU MIREA and VGTRK[7] (Fig. 35).

The software architecture for the multifunctional audio module for media testing and debugging of audio signal systems and devices was designed on the basis of ADAU1701 ADSP processor. The experimental characteristics of submodules of the multifunctional device were obtained on the basis of bench laboratory studies which enabled the media devices to be tested in the specified spectral-dynamic and spatial-temporal ranges:

- the balance routing submodule allows the impact of noise induced on the audio channel to be reduced 20-fold, thus enabling calibration of pickup audio devices;
- the audio signal processing submodule provides compression response with dynamic range from −27 up to 18.6 dB with the possibility of equalization parameterization within the range of 0.04–18 kHz at the specified goodness and AMP/ATT levels of filters. It also provides reverberation response within the range of 0.5–3000 ms, as well as audio channel cross-division into sub-bands of 20–250 Hz, 0.25–3 kHz, and 3–20 kHz with the ability to adjust AFR within the dynamic range from −30 up to 30 dB. These elements are of particular interest for panoramic and frequency balancing of audio systems;
- the submodule of AFR/PFR auto-correction of audio monitors allows the AFR dynamic nonuniformity be reduced by 40 dB. The submodule of the electro-acoustic positive feedback auto-suppression provides notch formant suppression to −100 dB at the input dynamic range of −50 up to 80 dB without impacting AFR, since each filter of the system operates independently.

ACKNOWLEDGMENTS

The study was carried out within the framework of the research on “Radio-information systems and radio-electronic technologies” (code 170-IRI).

Authors’ contributions

A.V. Gevorsky—parametric analysis and research of a multifunctional audio module based on an ADSP processor.

M.S. Kostin—development of an architectural configuration of a multifunctional ADSP module.

K.A. Boikov—development of a test program for media testing of signal audio devices.

[7] Federal State Unitary Enterprise “All-Russia State Television and Radio Broadcasting Company” (in Russ.). https://vgtrk.ru/. Accessed February 20, 2023.

REFERENCES

1. Kostin M.S. Signal radio acoustics, audiovisual systems and technologies. In: *Science of RTU MIREA at the Present Stage: Collection of Scientific Papers of the Anniversary Scientific and Technical Conference Dedicated to the 75th Anniversary of RTU MIREA.* Moscow: RTU MIREA; 2022. P. 325–328 (in Russ.).
2. Afanas'ev A.A., Rybolovlev A.A., Ryzhkov A.P. *Tsifrovaya obrabotka signalov* (*Digital Signal Processing*). Moscow: Goryachaya liniya – Telekom; 2019. 356 p. (in Russ.).
3. Steiglitz K. *A Digital Signal Processing Primer: with Applications to Digital Audio and Computer Music.* NY, USA: Dover Publications Inc.; 2020. 320 p.
4. Pirkle W.C. *Designing Audio Effect Plugins in C++: for AAX, AU, and VST3 with DSP Theory*. 2nd ed. NY, USA: Routledge; 2019. 704 p.
5. Kovalgin Yu.A., Vologdin E.I. *Audiotekhnika* (*Audio Engineering*). Moscow: Goryachaya liniya – Telekom; 2013. 742 p. (in Russ.).
6. Petlenko D.B., Yarlykov A.D., Boikov K.A. *Analogo-tsifrovye preobrazovateli signal'nykh audiointerfeisov* (*Analog-to-Digital Converters of Signal Audio Interfaces*). Moscow: Reglet; 2023. 65 p. (in Russ.).
7. Popov O.B., Rikhter S.G. *Tsifrovaya obrabotka signalov v traktakh zvukovogo veshchaniya* (*Digital Signal Processing in Audio Broadcasting Paths*). Moscow: Goryachaya liniya – Telekom; 2012. 342 p. (in Russ.).
8. Kovalgin Yu.A., Vakhitov Sh.Ya. *Akustika* (*Acoustics*). Moscow: Goryachaya liniya – Telekom; 2022. 660 p. (in Russ.).
9. Zölzer U. *Digital Audio Signal Processing.* 2nd ed. Chippenham, England: Wiley; 2008. 340 p.
10. Self D. *Small Signal Audio Design.* 3rd ed. NY, USA: CRC Press; 2020. 784 p.
11. Cipriani A., Giri M. *Electronic Music and Sound Design: Theory and Practice with Max 8*. V. 2. 3rd ed. Rome, Italy: ConTempoNet; 2020. 748 p.
12. Kamenov A. *Digital Signal Processing for Audio Applications*. 2nd ed. Amazon. Kindle edition. RecordingBlogs; 2014. 348 p.
13. Collins K. *Studying Sound: A Theory and Practice of Sound Design Hardcover*. London, England: The MIT Press; 2020. 248 p.
14. Reiss J.D., McPherson A. *Audio Effects. Theory, Implementation and Application*. Boca Raton, USA: CRC Press; 2008. 368 p.
15. Petlenko D.B., Yarlykov A.D., Boikov K.A. *Tsifrovye metody sekvensornoi ekvalizatsii audiosignalov radioakusticheskikh system* (*Digital Methods of Sequencer Equalization of Audio Signals of Radioacoustic Systems*). Moscow: Reglet; 2023. 109 p. (in Russ.).

СПИСОК ЛИТЕРАТУРЫ

1. Костин М.С. Сигнальная радиоакустика, аудиовизуальные системы и технологии. В сб.: *Наука РТУ МИРЭА на современном этапе: сборник научных трудов Юбилейной научно-технической конференции, посвященной 75-летию РТУ МИРЭА*. М.: РТУ МИРЭА; 2022. С. 325–328.
2. Афанасьев А.А., Рыболовлев А.А., Рыжков А.П. *Цифровая обработка сигналов*. М.: Горячая линия – Телеком; 2019. 356 с.
3. Steiglitz K. *A Digital Signal Processing Primer: with Applications to Digital Audio and Computer Music.* NY, USA: Dover Publications Inc.; 2020. 320 p.
4. Pirkle W.C. *Designing Audio Effect Plugins in C++: for AAX, AU, and VST3 with DSP Theory*. 2nd ed. NY, USA: Routledge; 2019. 704 p.
5. Ковалгин Ю.А., Вологдин Э.И. *Аудиотехника.* М.: Горячая линия – Телеком; 2013. 742 с.
6. Петленко Д.Б., Ярлыков А.Д., Бойков К.А. *Аналого-цифровые преобразователи сигнальных аудиоинтерфейсов.* М.: Реглет; 2023. 65 с.
7. Попов О.Б., Рихтер С.Г. *Цифровая обработка сигналов в трактах звукового вещания*. М.: Горячая линия – Телеком; 2012. 342 с.
8. Ковалгин Ю.А., Вахитов Ш.Я. *Акустика.* М.: Горячая линия – Телеком; 2022. 660 с.
9. Zölzer U. *Digital Audio Signal Processing.* 2nd ed. Chippenham, England: Wiley; 2008. 340 p.
10. Self D. *Small Signal Audio Design.* 3rd ed. NY, USA: CRC Press; 2020. 784 p.
11. Cipriani A., Giri M. *Electronic Music and Sound Design: Theory and Practice with Max 8*. V. 2. 3rd ed. Rome, Italy: ConTempoNet; 2020. 748 p.
12. Kamenov A. *Digital Signal Processing for Audio Applications*. 2nd ed. Amazon. Kindle edition. RecordingBlogs; 2014. 348 p.
13. Collins K. *Studying Sound: A Theory and Practice of Sound Design Hardcover*. London, England: The MIT Press; 2020. 248 p.
14. Reiss J.D., McPherson A. *Audio Effects. Theory, Implementation and Application*. Boca Raton, USA: CRC Press; 2008. 368 p.
15. Петленко Д.Б., Ярлыков А.Д., Бойков К.А. *Цифровые методы секвенсорной эквализации аудиосигналов радиоакустических систем*. М.: Реглет; 2023. 109 с.

About the authors

Andrey V. Gevorsky, Student, MIREA – Russian Technological University (78, Vernadskogo pr., Moscow, 119454 Russia). E-mail: x33590@gmail.com. http://orcid.org/0009-0001-9734-7515

Mikhail S. Kostin, Dr. Sci. (Eng.), Associate Professor, Head of the Department of Radio Wave Processes and Technologies, Deputy Director, Institute of Radio Electronics and Informatics, MIREA – Russian Technological University (78, Vernadskogo pr., Moscow, 119454 Russia). E-mail: kostin_m@mirea.ru. Scopus Author ID 57208434671, RSCI SPIN-code 5819-2178, http://orcid.org/0000-0002-5232-5478

Konstantin A. Boikov, Cand. Sci. (Eng.), Associate Professor, Department of Radio Wave Processes and Technologies, Institute of Radio Electronics and Informatics, MIREA – Russian Technological University (78, Vernadskogo pr., Moscow, 119454 Russia). E-mail: bojkov_k@mirea.ru. Scopus Author ID 57208926258, RSCI SPIN-code 2014-6951, http://orcid.org/0000-0003-0213-7337

Об авторах

Геворский Андрей Владимирович, студент, ФГБОУ ВО «МИРЭА – Российский технологический университет» (119454, Россия, Москва, пр-т Вернадского, д. 78). E-mail: x33590@gmail.com. http://orcid.org/0009-0001-9734-7515

Костин Михаил Сергеевич, д.т.н., доцент, заведующий кафедрой радиоволновых процессов и технологий, заместитель директора Института радиоэлектроники и информатики ФГБОУ ВО «МИРЭА – Российский технологический университет» (119454, Россия, Москва, пр-т Вернадского, д. 78). E-mail: kostin_m@mirea.ru. Scopus Author ID 57208434671, SPIN-код РИНЦ 5819-2178, http://orcid.org/0000-0002-5232-5478

Бойков Константин Анатольевич, к.т.н., доцент, кафедра радиоволновых процессов и технологий Института радиоэлектроники и информатики ФГБОУ ВО «МИРЭА – Российский технологический университет» (119454, Россия, Москва, пр-т Вернадского, д. 78). E-mail: bojkov_k@mirea.ru. Scopus Author ID 57208926258, SPIN-код РИНЦ 2014-6951, http://orcid.org/0000-0003-0213-7337

Translated from Russian into English by Kirill V. Nazarov
Edited for English language and spelling by Dr. David Mossop

Modern radio engineering and telecommunication systems

Современные радиотехнические и телекоммуникационные системы

UDC 621.391.072
https://doi.org/10.32362/2500-316X-2024-12-1-59-68

RESEARCH ARTICLE

Influence of quadrature transformation imbalance on the noise immunity of signal reception with amplitude-phase shift keying

Gennady V. Kulikov @,
Xuan Kh. Dang

MIREA – Russian Technological University, Moscow, 119454 Russia
@ Corresponding author, e-mail: kulikov@mirea.ru

Abstract
Objectives. At the present time, amplitude-phase shift keyed (APSK) signals are actively used in satellite communication systems. In particular, they are applied in systems which operate in a limited radio frequency spectrum with increased data transmission quality requirements. Such systems use multi-channel type receivers with maximum likelihood decision on the received symbol (correlation receiver) or quadrature type receivers. The noise immunity of these receivers is directly dependent on the quality of the formation of reference oscillations. These oscillations are reference signals for correlation receivers and in-phase and quadrature components for quadrature receivers. The aim of the work is to analyze the influence of the amplitude and phase parameter spread of the in-phase and quadrature channels on the noise immunity of receiving APSK signals with a circular shape of the signal constellation.
Methods. Methods of statistical radio engineering, theory of optimal signal reception, and computer simulation are used.
Results. The study established the characteristics of noise immunity of the APSK signal reception depending on the spread of parameters of the quadrature converter. The theoretical calculations were confirmed by the results of modeling the transmission of APSK signals in a Gaussian communication channel. A comparison with systems using quadrature amplitude modulation (QAM) was carried out, in order to assess system stability in the presence of spread parameters among other similar systems.
Conclusions. The studies enabled us to conclude that an imbalance of the quadrature reference oscillations can lead to a significant decrease in the noise immunity of radio systems using APSK signals. The minimum energy loss due to imbalance of quadrature reference oscillations is achieved when the imbalance value is less than 10% in amplitude and 2°–3° in phase. The amplitude imbalance of quadrature reference oscillations when receiving QAM signals is more pronounced than in the case of APSK signals. The phase imbalance affects approximately the same.

Keywords: amplitude-phase shift keying, quadrature channels, amplitude imbalance, phase imbalance, bit error probability

• **Submitted:** 27.01.2023 • **Revised:** 07.05.2023 • **Accepted:** 13.07.2023

For citation: Kulikov G.V., Dang X.Kh. Influence of quadrature transformation imbalance on the noise immunity of signal reception with amplitude-phase shift keying. *Russ. Technol. J.* 2024;12(1):59–68. https://doi.org/10.32362/2500-316X-2024-12-1-59-68

Financial disclosure: The authors have no a financial or property interest in any material or method mentioned.

The authors declare no conflicts of interest.

НАУЧНАЯ СТАТЬЯ

Влияние разбаланса квадратурного преобразования на помехоустойчивость приема сигналов с амплитудно-фазовой манипуляцией

Г.В. Куликов @,
С.Х. Данг

МИРЭА – Российский технологический университет, Москва, 119454 Россия
@ Автор для переписки, e-mail: kulikov@mirea.ru

Резюме
Цели. В настоящее время сигналы с амплитудно-фазовой манипуляцией (АФМ) активно используются в системах спутниковой связи и, особенно, в системах, работающих в условиях ограниченности спектра радиочастот с повышенными требованиями к качеству передачи данных. В этих системах применяются приемники многоканального типа с принятием решения о принимаемом символе по максимуму правдоподобия (корреляционный приемник) или приемники квадратурного типа. Помехоустойчивость этих приемников напрямую зависит от качества формирования опорных колебаний: для корреляционных приемников – эталонных сигналов, а для квадратурных приемников – синфазной и квадратурной составляющих. Цель работы – анализ влияния разброса амплитудных и фазовых параметров синфазного и квадратурного канала на помехоустойчивость приема сигналов АФМ с круговой формой сигнального созвездия.
Методы. Использованы методы статистической радиотехники, теории оптимального приема сигналов и компьютерного моделирования.
Результаты. Получены характеристики помехоустойчивости приема сигналов АФМ в зависимости от разброса параметров квадратурного преобразователя. Теоретические расчеты подтверждены результатами имитационного моделирования при передаче АФМ-сигналов в гауссовском канале связи. Проведено сравнение с системами, использующими сигналы с квадратурной амплитудной модуляцией (КАМ).
Выводы. Проведенные исследования показали, что разбаланс квадратурных опорных колебаний может привести к существенному снижению помехоустойчивости радиосистем, использующих АФМ-сигналы. Минимальные энергетические потери из-за разбаланса квадратурных опорных колебаний достигаются при значении разбаланса менее 10% по амплитуде и 2°–3° по фазе. Амплитудный разбаланс квадратурных опорных колебаний при приеме сигналов КАМ сказывается сильнее, чем при приеме сигналов АФМ. Фазовый разбаланс сказывается приблизительно одинаково.

Ключевые слова: амплитудно-фазовая манипуляция, квадратурные каналы, амплитудный разбаланс, фазовый разбаланс, вероятность битовой ошибки

• **Поступила:** 27.01.2023 • **Доработана:** 07.05.2023 • **Принята к опубликованию:** 13.07.2023

Для цитирования: Куликов Г.В., Данг С.Х. Влияние разбаланса квадратурного преобразования на помехоустойчивость приема сигналов с амплитудно-фазовой манипуляцией. *Russ. Technol. J.* 2024;12(1):59–68. https://doi.org/10.32362/2500-316X-2024-12-1-59-68

Прозрачность финансовой деятельности: Авторы не имеют финансовой заинтересованности в представленных материалах или методах.

Авторы заявляют об отсутствии конфликта интересов.

INTRODUCTION

Many external and internal factors are used to determine the noise immunity of radio information transmission systems. External factors include radio wave propagation conditions and interference of various origins. Internal factors are operation validity and the stability of technical characteristics of devices included in the system.

In [1–4], the principles of construction and some specific features of implementation of digital television systems according to DVB[1] standards are considered. In the case of enhanced-definition television or high-definition television, high-speed types of modulation are used. These include: quadrature amplitude modulation (QAM) used in DVB-T and DVB-C [2, 4]; and amplitude-phase shift keying (APSK) with circular signal constellation used in DVB-S2 [1, 3]. Receivers of QAM and APSK signals can be designed according to two basic schemes: multichannel type with decision making relating to the received symbol based on maximum likelihood (Fig. 1); and quadrature type (Fig. 2). The noise immunity characteristics are the same for both schemes. An important part of the receivers is the module generating reference oscillations: in-phase and quadrature components, shifted in phase by 90°. Any inaccurate operation of this circuit would cause the loss of orthogonality. This can result in errors while defining the transmitted symbols and, consequently, the reduced noise immunity of the information transmission system. The influence of errors in the scheme for generating quadrature reference oscillation on the reception of QAM signals is studied in [5–12].

[1] DVB. https://www.dvb.org/standards. Accessed May 22, 2023.

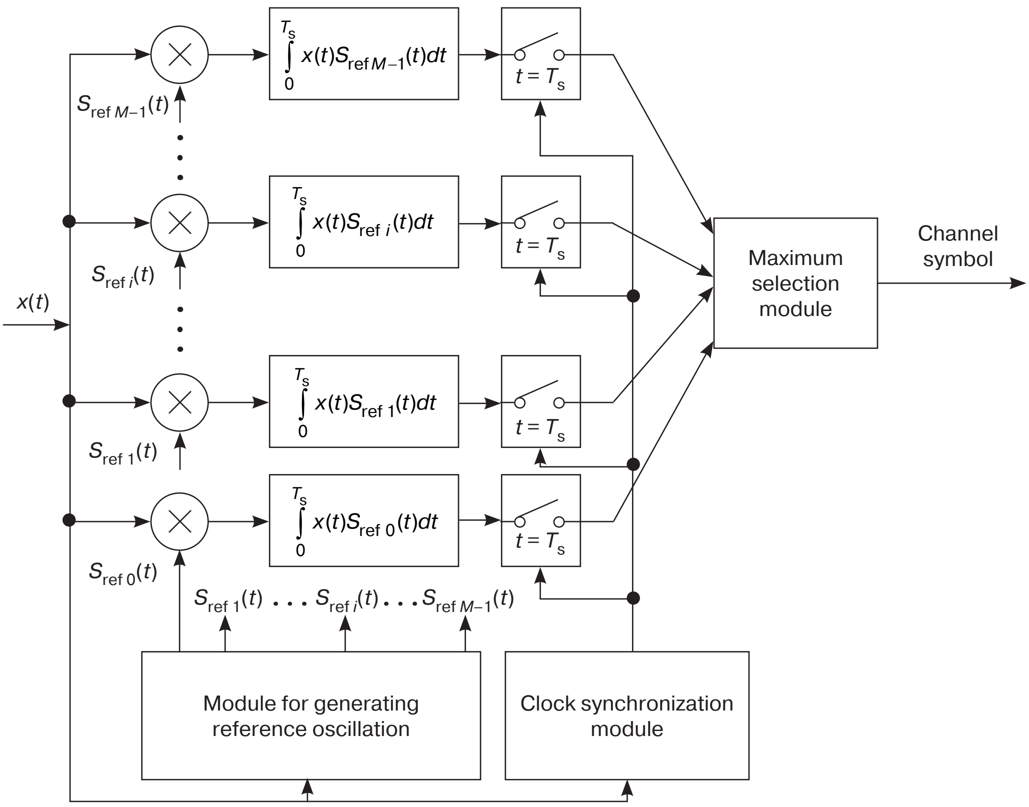

Fig. 1. Structural diagram of the multichannel coherent receiver

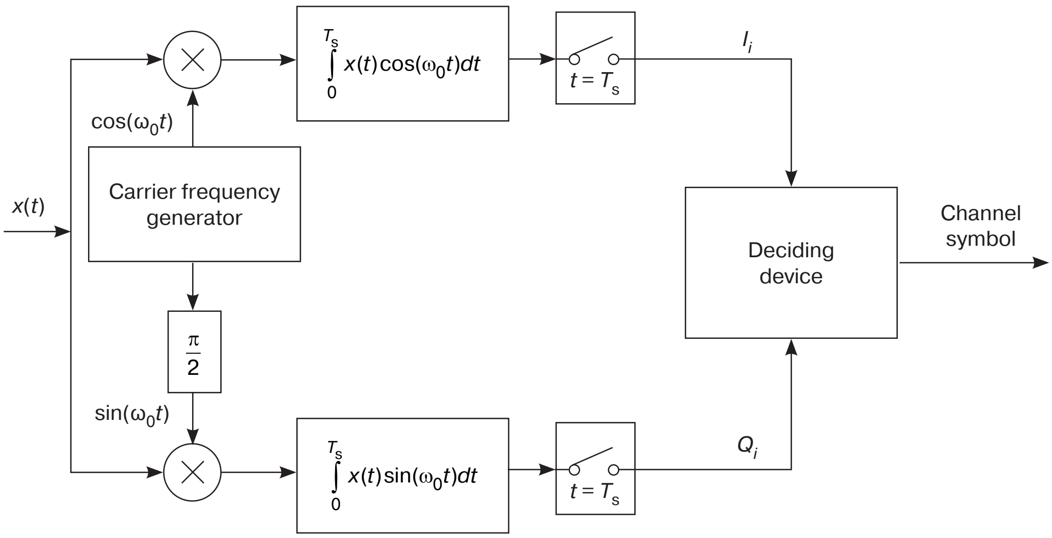

Fig. 2. Structural diagram of the quadrature demodulator

The aim of the paper is to evaluate the influence of amplitude and phase imbalance of quadrature reference oscillations when receiving APSK signals with circular signal constellation. The problem may be resolved in two ways: by the methods of statistical radio engineering using theoretical calculations of the bit error probability of a multichannel receiver; and by simulation modeling of a quadrature receiver.

METHODOLOGY FOR CALCULATING BIT ERROR PROBABILITY

Let us represent the APSK signal in the following quadrature form:

$$s_i(t) = Ar_i\cos(\omega_0 t + \varphi_i) = A(I_i\cos\omega_0 t - Q_i\sin\omega_0 t),$$
$$t \in \left(0, T_s\right], \ i = \overline{0, M-1}, \qquad (1)$$

where t is time; $I_i = r_i\cos\varphi_i$; $Q_i = r_i\sin\varphi_i$; A is the signal amplitude average; ω_0 is carrier frequency; r_i and φ_i are values determining the amplitude and phase of a signal element; T_s is the channel symbol duration; and M is signal positioning.

Let us assume that the signal reception occurs against the background of white Gaussian noise $n(t)$ with the following parameters:

$$< n(t) > = 0, \ < n(t_1)n(t_2) > = \frac{N_0}{2}\delta(t_2 - t_1),$$

where N_0 is the noise power spectral density, δ is delta function, t_1 and t_2 are time instants.

Then the signal-to-noise ratio is the following:

$$E_b/N_0 = E_s/(N_0\log_2 M) = A^2T_s/(2N_0\log_2 M),$$

where E_s is the average energy per symbol (assuming all symbols have the similar probability of occurrence), and E_b is the average bit energy.

The multichannel receiver correlators (Fig. 1) compute convolution integrals:

$$J_i = \frac{2}{N_0}\int_0^{T_s} x(t)s_{\text{ref}\,i}(t)dt, \ i = \overline{0, M-1} \qquad (2)$$

of the input process $x(t) = s_i(t) + n(t)$ with the reference signals $s_{\text{ref}\,i}(t)$, and ideally, $s_{\text{ref}\,i}(t) = A_{\text{ref}}\,(I_i\cos\omega_0 t - Q_i\sin\omega_0 t)$, with the amplitude of the reference signal $A_{\text{ref}} = A$.

We set the amplitude and phase imbalance values for quadrature reference oscillations through the amplitude coefficient a and the phase shift θ in one of the channels, as follows:

$$S_{\text{ref}\,i}(t) = A(I_i\cos\omega_0 t - aQ_i\sin(\omega_0 t + \theta)). \qquad (3)$$

In order to calculate the error probability, the methods described in [13, 14] are used. According to them, the error probability for receiving any mth channel symbol is equal to

$$P_{\text{es}\,m} = 1 - \prod_{\substack{i=0 \\ m\neq i}}^{M-1}\left(1 - Q\left(\frac{m_{mi}}{\sqrt{D_{mi}}}\right)\right), \ Q(x) = \frac{1}{\sqrt{2\pi}}\int_x^{\infty} e^{\frac{-t^2}{2}}dt, \qquad (4)$$

where m_{mi} are the mathematical expectations and D_{mi} are the dispersions of linear combinations of processes (2).

Calculating and averaging all $i \neq m; \ i, m = \overline{0, M-1}$ combinations enables us to find the error probability average for symbol reception and then the bit error probability when using Gray coding [15], as follows:

$$P_{\text{eb}} = P_{\text{es}}/\log_2 M.$$

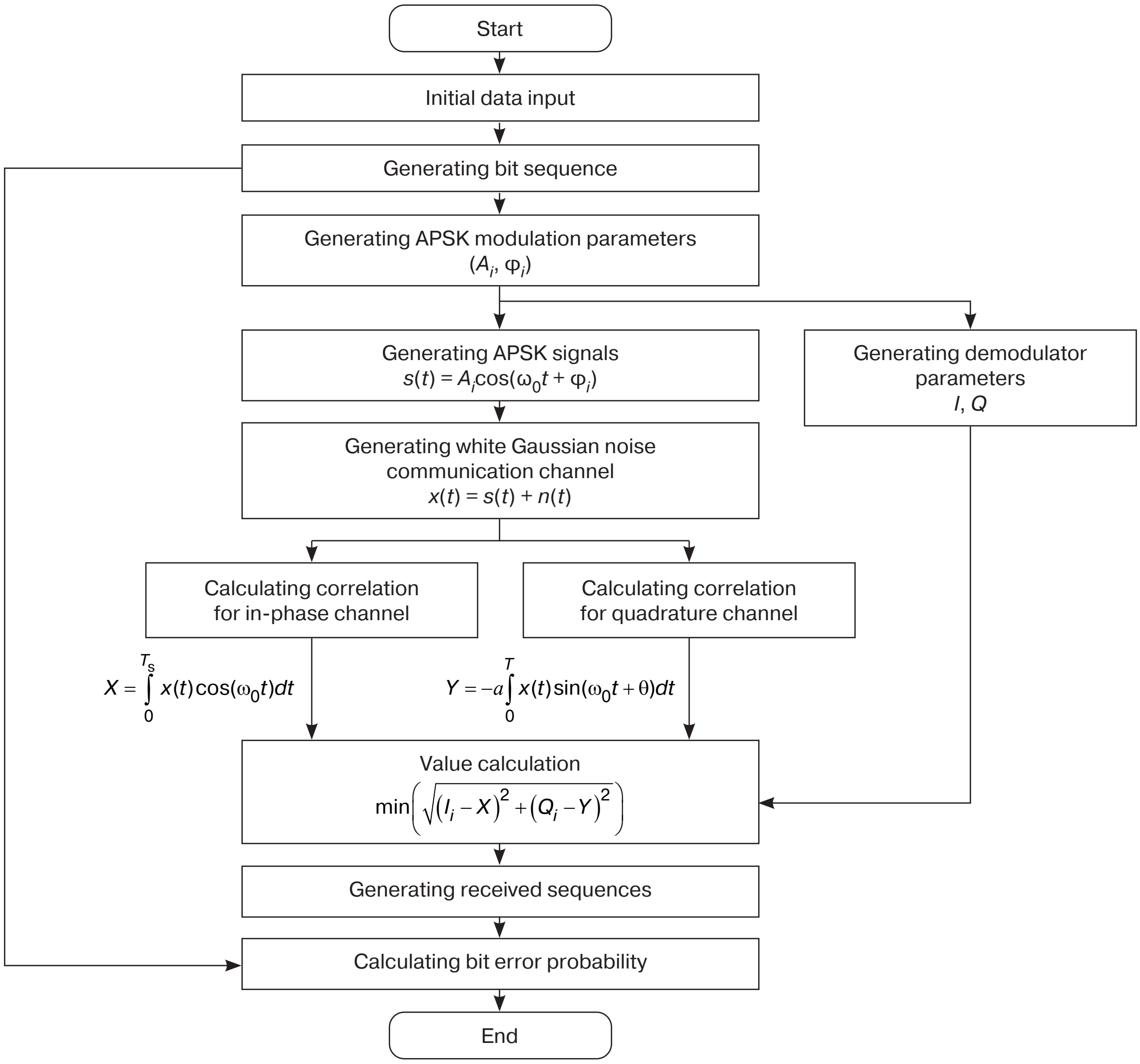

Fig. 3. Algorithm for simulation modeling of the APSK signal transmission system in a Gaussian noise channel

In (4), m_{mi} and D_{mi} with allowance for (1) and (3) are defined as follows:

$$m_{mi} = \frac{2E_s}{N_0}\Big(r_m{}^2\cos^2\varphi_m - r_m r_i\cos\varphi_m\cos\varphi_i - a r_m\sin(\theta - \varphi_m)\times (r_m\sin\varphi_m - r_i\sin\varphi_i) - \frac{r_m^2 - r_i^2}{2}\Big), \quad (5)$$

$$D_{mi} = \frac{2E_s}{N_0}\Big((r_m\cos\varphi_m - r_i\cos\varphi_i)^2 + a^2(r_m\sin\varphi_m - r_i\sin\varphi_i)^2 - 2a\sin\theta(r_m\cos\varphi_m - r_i\cos\varphi_i)\times (r_m\sin\varphi_m - r_i\sin\varphi_i)\Big). \quad (6)$$

In order to verify theoretical results, a simulation model of the APSK signal transmission system in a Gaussian noise channel. This includes quadrature converter modules with the possibility of introducing amplitude a, and developing phase θ imbalances. The modeling algorithm is shown in Fig. 3.

CALCULATION AND STIMULATION RESULTS

Influence of the amplitude imbalance of quadrature channels

The calculations assume that there is no phase imbalance, $\theta = 0$. In this case Eqs. (5) and (6) take the following form:

$$m_{mi} = \frac{2E_s}{N_0}\Big(r_m\cos\varphi_m(r_m\cos\varphi_m - r_i\cos\varphi_i) + a r_m\sin\varphi_m(r_m\sin\varphi_m - r_i\sin\varphi_i) - \frac{r_m^2 - r_i^2}{2}\Big),$$

$$D_{mi} = \frac{2E_s}{N_0}\left(\left(r_m \cos\varphi_m - r_i \cos\varphi_i\right)^2 + \right.$$
$$\left. + a^2\left(r_m \sin\varphi_m - r_i \sin\varphi_i\right)^2\right).$$

The dependencies of bit error probability on the amplitude imbalance at $E_b/N_0 = 13$ dB for 16-APSK and 32-APSK signals are shown in Fig. 4. The dependencies of the bit error probability on the signal-to-noise ratio at fixed values a are shown in Fig. 5. Note that the case $a = 1$ stands for the absence of imbalance.

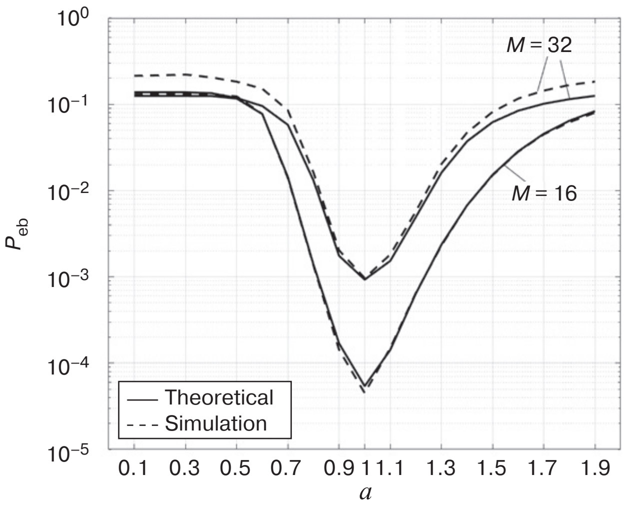

Fig. 4. Dependencies of the bit error probability on the amplitude imbalance of quadrature channels

It can be seen that in the case of both signals, low amplitude imbalance of quadrature channels ±10% affects the information reception quality insignificantly. This value may be considered acceptable. In particular, at $P_{eb} = 10^{-3}$ and $a = 1.1$, energy losses would not exceed 0.5 dB. At an amplitude imbalance of 20% ($a = 0.8$ and 1.2), the bit error probability increases by an order of magnitude. Greater imbalance ($a = 1.5$) is unacceptable and results in the reception failure. This is due to the fact that the bit error probability increases by several orders of magnitude while energy losses increase by 8–10 dB.

It should be also noted that the difference in the results for multichannel (theoretical calculation) and quadrature (simulation modeling) receivers is insignificant, thus indicating approximately the same stability of schemes against the amplitude imbalance of quadratures.

Influence of phase imbalance of quadrature channels

During the calculations it was assumed that there is no amplitude unbalance: $a = 1$. In this case, Eqs. (5) and (6) take the form:

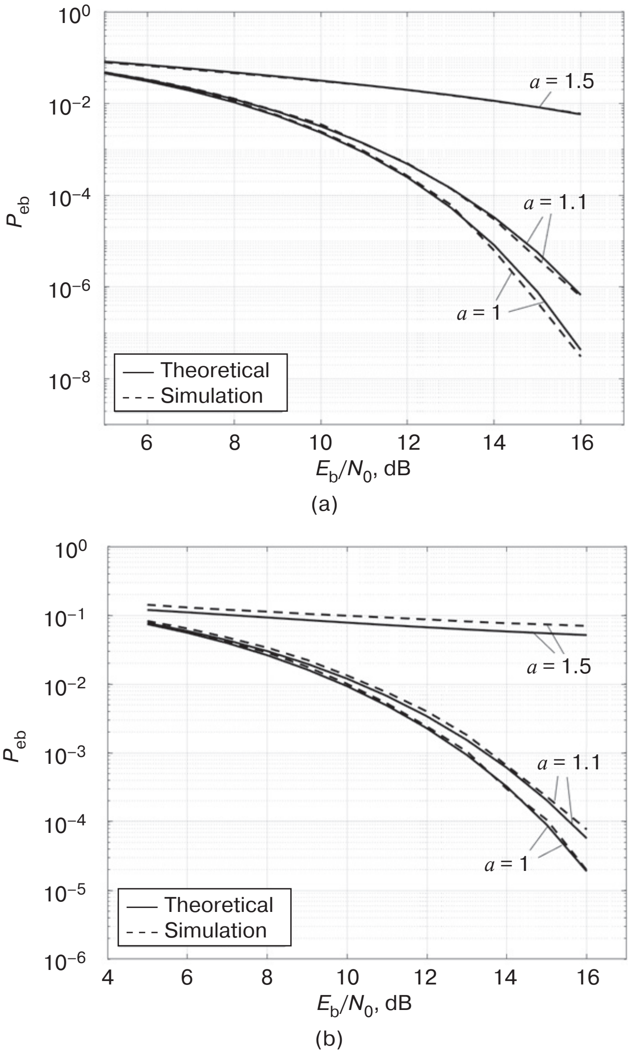

Fig. 5. Dependencies of the bit error probability on signal-to-noise ratio at amplitude imbalance of quadrature channels: (a) for 16-APSK, (b) for 32-APSK

$$m_{mi} = \frac{2E_s}{N_0}\left(r_m{}^2 \cos^2\varphi_m - \right.$$
$$- r_m r_i \cos\varphi_m \cos\varphi_i - r_m \sin(\theta - \varphi_m) \times$$
$$\left. \times (r_m \sin\varphi_m - r_i \sin\varphi_i) - \frac{r_m^2 - r_i^2}{2}\right),$$

$$D_{mi} = \frac{2E_s}{N_0}\left(\left(r_m \cos\varphi_m - r_i \cos\varphi_i\right)^2 + \right.$$
$$+ \left(r_m \sin\varphi_m - r_i \sin\varphi_i\right)^2 -$$
$$- 2\sin\theta\left(r_m \cos\varphi_m - r_i \cos\varphi_i\right) \times$$
$$\left. \times \left(r_m \sin\varphi_m - r_i \sin\varphi_i\right)\right).$$

The dependencies of the bit error probability on phase imbalance θ at ratio E_b/N_0 = 13 dB for 16-APSK and 32-APSK signals are shown in Fig. 6. The dependencies of the bit error probability on the signal-to-noise ratio at fixed values of phase imbalance are shown in Fig. 7.

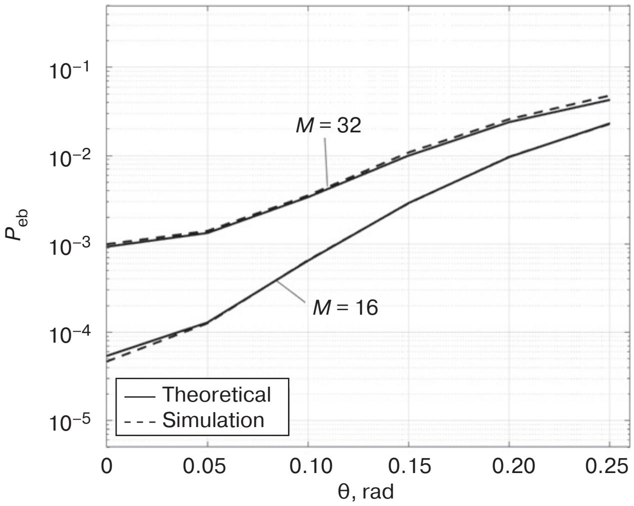

Fig. 6. Dependencies of the bit error probability on phase imbalance of quadrature channels

At phase imbalance θ = 0.1 rad (~5°) for $P_{eb} = 10^{-3}$, energy losses of 2 dB for M = 16 and 3 dB for M = 32 can be observed. With the imbalance increasing up to 0.15 rad (~8°), the losses are 4.5 dB or more. In the case of signals 16-APSK and 32-APSK, a phase imbalance of quadrature channels no more than 0.03–0.05 rad, i.e., 2°–3° can be considered acceptable. This can be judged by the graphs given in Fig. 5.

COMPARISON OF RESULTS FOR QAM AND APSK SIGNALS

The comparative dependencies of the probability P_{eb} on the amplitude imbalance coefficient a of quadrature channels for APSK and QAM signal receivers of the same positioning [2] are shown in Fig. 8. As can be seen, in the ideal case (a = 1) QAM signal has slightly better noise immunity. However, the steeper slope of graphs in the region 0.7 < a < 1.3 indicates a greater sensitivity of QAM receiver against the amplitude imbalance value.

It follows from Fig. 9 that the influence of phase imbalance of quadrature channels on the reception of APSK and QAM signals [5] is approximately equal.

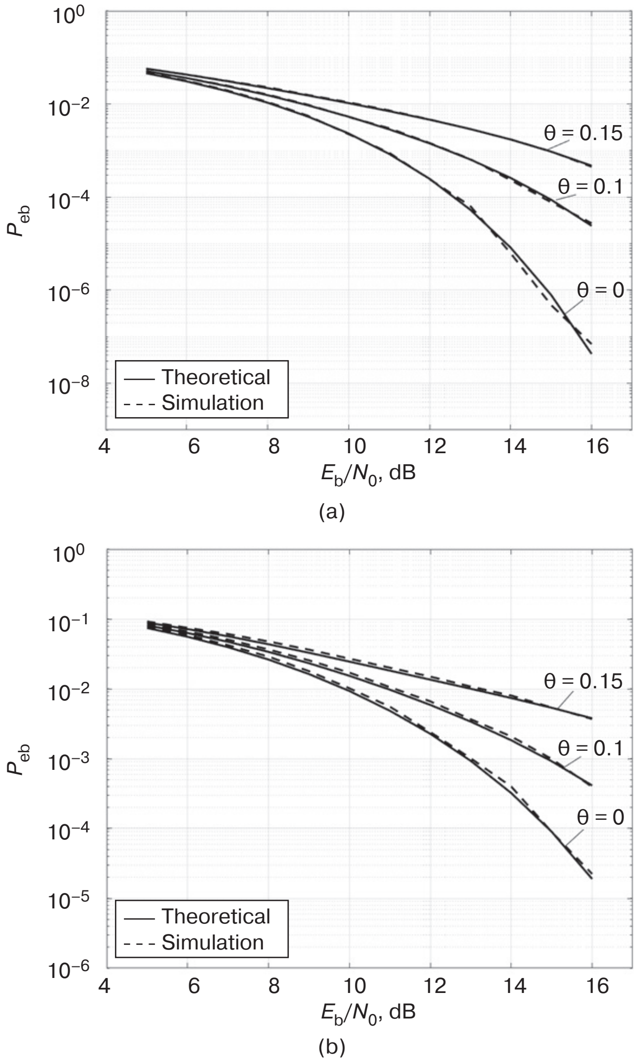

Fig. 7. Dependencies of the bit error probability on the signal-to-noise ratio at phase imbalance in quadrature channels: (a) for 16-APSK, (b) for 32-APSK

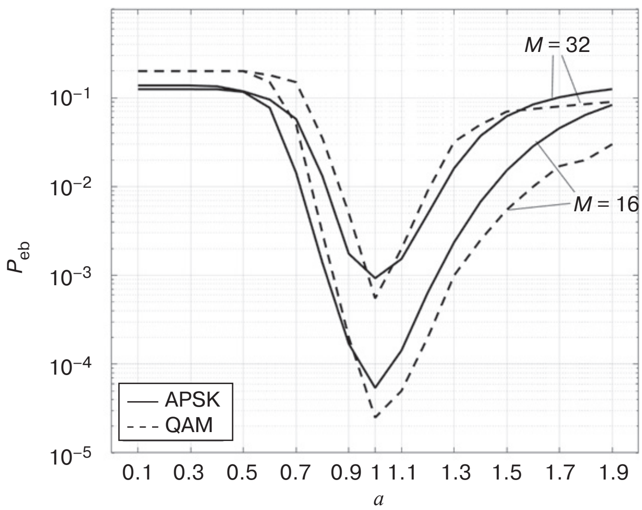

Fig. 8. Dependencies of the bit error probability on amplitude imbalance for APSK and QAM signals (E_b/N_0 = 13 dB)

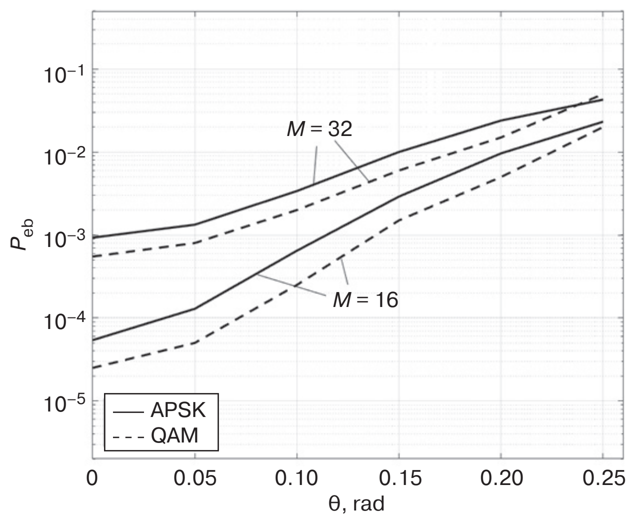

Fig. 9. Dependencies of the bit error probability on phase imbalance of quadrature channels for APSK and QAM signals (E_b/N_0 = 13 dB)

CONCLUSIONS

Thus, the results allow the following conclusions to be drawn:

1. The amplitude and phase imbalance of quadrature reference oscillations when receiving APSK signals, as well as QAM signals, may result in the significant decrease in noise immunity.
2. The acceptable value of amplitude imbalance for APSK receiver may be considered as ±10%.
3. The acceptable value of phase imbalance for APSK receiver may be considered as 2°–3°.
4. The amplitude imbalance of quadrature reference oscillations when receiving QAM signals affects more than that while receiving APSK signals. Phase imbalances are nearly the same.

Authors' contributions

G.V. Kulikov—the research idea, consultations on the issues of conducting all stages of the study.

X.Kh. Dang—making calculations, processing of results.

REFERENCES

1. Antiufrieva L., Ivchenko A., Dvorkovich A. Features of a coarse frequency synchronization for DVB-S2X system. In: *2020 International Conference Engineering and Telecommunication* (*En & T*). 2020. https://doi.org/10.1109/EnT50437.2020.9431306
2. Abramov S.S., Pavlov I.I., Abramova E.S., Pavlova M.S. *Formirovanie radiosignalov dlya tsifrovogo teleradioveshchaniya* (*Formation of Radio Signals for Digital Television and Radio Roadcasting*). 2nd ed. Novosibirsk: SibGUTI; 2019. 246 p. (in Russ.).
3. Maglitskii B.N., Sergeeva A.S., Sinyavskaya A.S. *Printsipy postroeniya sputnikovogo televideniya. Teoriya i praktika* (*Principles of Construction of Satellite Television. Theory and Practice.* Novosibirsk: SibGUTI; 2016. 95 p. (in Russ.).
4. Vershinin A.S., Erdyneev Zh.T. *Kosmicheskie i nazemnye sistemy radiosvyazi i seti teleradioveshchaniya* (*Space and Terrestrial Radio Communication Systems and Television and Radio Broadcasting Networks*). Tomsk: TUSUR; 2013. 184 p. (in Russ.). Available from URL: https://edu.tusur.ru/publications/3449. Accessed May 22, 2023.
5. Kulikov G.V., Lelyukh A.A. Influence of amplitude and phase imbalance of quadratures on noise immunity of coherent reception of signals with quadrature amplitude modulation. *Russ. Technol. J.* 2021;9(1):29–37 (in Russ.). https://doi.org/10.32362/2500-316X-2021-9-1-29-37
6. Babanin I.G., Mikhailova N.Yu., Nikolaenko A.I., Koptev D.S. Assessment procedure of influence of not idealities of parameters of the optimum demodulating device of the system of signal pick-up with different positioning and coefficient quadrature amplitude shift keying of irregularity of the signal constellation on equivalent power losses. *Radiotekhnika = Radioengineering*. 2019;83(10–2):60–69 (in Russ.).
7. Park J., Park S., Cho P.D., Lee H.-Ho. Effect of phase/quadrature error and I/Q gain imbalance for QAM symbol error probability. *IEICE Trans. Commun*. 2007;E90-B(11):3287–3289. https://doi.org/10.1093/ietcom/e90-b.11.3287
8. Yanushkovsky A.Y., Krivosheikin A.V. Noise-immune of receiving of phase-amplitude signals with imperfect quadrature channels. *Izvestiya vysshikh uchebnykh zavedenii. Priborostroenie = J. Instrument Engineering.* 2011;54(9):58–63 (in Russ.).
9. Gurevich V.E., Devyatkin D.V., Kharkov O.I. Analysis of radio access system with quadrature modulation real noise immunity while dephasing the reference oscillation. In: *Actual Problems of Infotelecommunication in Science and Education.* Collection of scientific papers: in 4 v. 2017. V. 1. P. 154–159 (in Russ.).
10. Khasyanova E.R., Sedov M.O. Experimental study of methods of estimation and compensation of errors of quadrature transformation of signals with M-QAM modulation. *Sistemy sinkhronizatsii, formirovaniya i obrabotki signalov = Systems of Signal Synchronization, Generation and Processing*. 2017;8(1):119–122 (in Russ.).
11. Pestryakov A.V., Poborchaya N.E., Khasyanova E.R. Influence carrier frequency offset on the performance of the errors of quadrature conversation compensation algorithm transformation. In: *26th International Crimean Conference "Microwave Technology and Telecommunications Technologies"* (*KrymiCo'2016*). Conference proceedings: in 13 v. 2016. V. 3. P. 413–417 (in Russ.).
12. Pestryakov A.V., Khasyanova E.R. Estimation and compensation of errors of quadrature transformation when receiving a signal with QAM-64 modulation using the method of statistical averaging. In: *Information Society Technologies. X International Industry Scientific and Technical Conference*: Proceedings. 2016. P. 196 (in Russ.).

13. Kulikov G.V., Usmanov R.R., Trofimov D.S. Noise immunity analysis of amplitude and phase-shift keying signals reception in presence of harmonic interference. *Naukoemkie tekhnologii = Science Intensive Technologies*. 2020;21(1):22–29 (in Russ.). Available from URL: http://radiotec.ru/ru/journal/Science_Intensive_Technologies/number/2020-1/article/19749. Accessed May 22, 2023.
14. Kulikov G.V., Khang D.X., Starikovskiy A.I. Noise immunity of signal reception with amplitude-phase shift keying in the background of frequency shift keying interference. *Voprosy radioelektroniki. Seriya: Tekhnika televideniya = Questions of Radio Electronics. Series: TV Technique*. 2022;4:44–51 (in Russ.).
15. Proakis J.G. *Digital communications*. 4th ed. NY: McGraw-Hill; 2001. 1002 p.

СПИСОК ЛИТЕРАТУРЫ

1. Antiufrieva L., Ivchenko A., Dvorkovich A. Features of a coarse frequency synchronization for DVB-S2X system. In: *2020 International Conference Engineering and Telecommunication* (*En & T*). 2020. https://doi.org/10.1109/EnT50437.2020.9431306
2. Абрамов С.С., Павлов И.И., Абрамова Е.С., Павлова М.С. *Формирование радиосигналов для цифрового телерадиовещания.* 2-е изд. Новосибирск: СибГУТИ; 2019. 246 с.
3. Маглицкий Б.Н., Сергеева А.С., Синявская А.С. *Принципы построения спутникового телевидения. Теория и практика.* Новосибирск: СибГУТИ; 2016. 95 с.
4. Вершинин А.С., Эрдынеев Ж.Т. *Космические и наземные системы радиосвязи и сети телерадиовещания.* Томск: ТУСУР; 2013. 184 с. URL: https://edu.tusur.ru/publications/3449. Дата обращения 22.05.2023.
5. Куликов Г.В., Лелюх А.А. Влияние амплитудного и фазового разбаланса квадратур на помехоустойчивость когерентного приема сигналов с квадратурной амплитудной модуляцией. *Russian Technological Journal*. 2021;9(1):29–37. https://doi.org/10.32362/2500-316X-2021-9-1-29-37
6. Бабанин И.Г., Михайлова Н.Ю., Николаенко А.И., Коптев Д.С. Процедура оценки влияния неидеальности параметров оптимального демодулирующего устройства системы приема сигналов с квадратурной амплитудной модуляцией различной позиционности и коэффициента неравномерности сигнального созвездия на эквивалентные энергетические потери. *Радиотехника*. 2019;83(10–16):60–69.
7. Park J., Park S., Cho P.D., Lee H.-Ho. Effect of phase/quadrature error and I/Q gain imbalance for QAM symbol error probability. *IEICE Trans. Commun*. 2007;E90-B(11):3287–3289. https://doi.org/10.1093/ietcom/e90-b.11.3287
8. Янушковский А.Ю., Кривошейкин А.В. Помехоустойчивость приема сигналов фазоамплитудной модуляции в условиях неидеальности квадратурных каналов. *Известия высших учебных заведений. Приборостроение.* 2011;54(9):58–63.
9. Гуревич В.Э., Девяткин Д.В., Харьков О.И. Исследование реальной помехоустойчивости системы радиодоступа с квадратурной модуляцией при дефазировании опорных колебаний. В сб.: *Актуальные проблемы инфотелекоммуникаций в науке и образовании*: Сборник научных статей: в 4 т. 2017. Т. 1. С. 154–159.
10. Хасьянова Е.Р., Седов М.О. Экспериментальное исследование методов оценки и компенсации погрешностей квадратурного преобразования сигналов с модуляцией М-КАМ. *Системы синхронизации, формирования и обработки сигналов*. 2017;8(1):119–122.
11. Пестряков А.В., Поборчая Н.Е., Хасьянова Е.Р. Оценка влияния сдвига несущей частоты на эффективность работы алгоритма компенсации погрешностей квадратурного преобразования. В сб.: *26-я Международная Крымская конференция «СВЧ-техника и телекоммуникационные технологии»* (*КрыМиКо'2016*): материалы конференции: в 13 т. 2016. Т. 3. С. 413–417.
12. Пестряков А.В., Хасьянова Е.Р. Оценка и компенсация погрешностей квадратурного преобразования при приеме сигнала с модуляцией КАМ-64 с применением метода статистического усреднения. В сб.: *Технологии информационного общества. X Международная отраслевая научно-техническая конференция*. 2016. С. 196.
13. Куликов Г.В., Усманов Р.Р., Трофимов Д.С. Анализ помехоустойчивости приема сигналов с многопозиционной амплитудно-фазовой манипуляцией в присутствии гармонической помехи. *Наукоемкие технологии*. 2020;21(1):22–29. URL: http://radiotec.ru/ru/journal/Science_Intensive_Technologies/number/2020-1/article/19749. Дата обращения 22.05.2023.
14. Куликов Г.В., Ханг Д.С., Стариковский А.И. Помехоустойчивость приема сигналов с амплитудно-фазовой манипуляцией на фоне частотно-манипулированной помехи. *Вопросы радиоэлектроники. Серия: Техника телевидения*. 2022;4:44–51.
15. Proakis J.G. *Digital communications.* 4th ed. NY: McGraw-Hill; 2001. 1002 p.

About the authors

Gennady V. Kulikov, Dr. Sci. (Eng.), Professor, Department of Radio Electronic Systems and Complexes, Institute of Radio Electronics and Informatics, MIREA – Russian Technological University (78, Vernadskogo pr., Moscow, 119454 Russia). E-mail: kulikov@mirea.ru. Scopus Author ID 36930533000, RSCI SPIN-code 2844-8073, http://orcid.org/0000-0001-7964-6653

Xuan Kh. Dang, Postgraduate Student, Department of Radio Electronic Systems and Complexes, Institute of Radio Electronics and Informatics, MIREA – Russian Technological University (78, Vernadskogo pr., Moscow, 119454 Russia). E-mail: dangxuankhang147@gmail.com. https://orcid.org/0000-0002-3372-7172

Об авторах

Куликов Геннадий Валентинович, д.т.н., профессор, профессор кафедры радиоэлектронных систем и комплексов Института радиоэлектроники и информатики ФГБОУ ВО «МИРЭА – Российский технологический университет» (119454, Россия, Москва, пр-т Вернадского, д. 78). E-mail: kulikov@mirea.ru. Scopus Author ID 36930533000, SPIN-код РИНЦ 2844-8073, http://orcid.org/0000-0001-7964-6653

Данг Суан Ханг, аспирант, кафедра радиоэлектронных систем и комплексов Института радиоэлектроники и информатики ФГБОУ ВО «МИРЭА – Российский технологический университет» (119454, Россия, Москва, пр-т Вернадского, д. 78). E-mail: dangxuankhang147@gmail.com. https://orcid.org/0000-0002-3372-7172

Translated from Russian into English by Kirill V. Nazarov
Edited for English language and spelling by Dr. David Mossop

Modern radio engineering and telecommunication systems

Современные радиотехнические и телекоммуникационные системы

UDC 621.314:681.586.7:004.942
https://doi.org/10.32362/2500-316X-2024-12-1-69-79

RESEARCH ARTICLE

Mathematical model of a DC/DC converter based on SEPIC topology

Aleksey I. Lavrenov @, Vladimir K. Bityukov

MIREA – Russian Technological University, Moscow, 119454 Russia
@ Corresponding author, e-mail: lavrenov@mirea.ru

Abstract

Objectives. A DC/DC converter based on SEPIC topology is a unipolar electronic device which converts an input positive voltage into a stabilized output voltage of the same polarity. It also has the ability to regulate polarity both below and above the input voltage. The aim of the paper is to analyze the DC/DC converter in its both operation phases, as well as to draw up equivalent circuits and obtain characterizing differential equations using Kirchhoff's rules for each phase. Each system of differential equations is reduced to Cauchy equations, in order to be further transformed into a limiting continuous mathematical model. Each system of equations is converted into a matrix form and subsequently combined into a single matrix system.

Methods. The construction of a limiting continuous mathematical model was accomplished using Kirchhoff's rules. *Multisim* software was used for the computer simulation, thus enabling the calculated results of direct currents and voltages to be compared to those of the simulation.

Results. Results show that the phase coordinates of the mathematical model tend towards the values of real currents and voltages of the converter at a switching frequency higher than 200 kHz. Fairly good agreement is established between the calculated values of currents and voltages and the values obtained by simulation (with varying fill factor and switching frequency).

Conclusions. The resulting limiting continuous mathematical model of the DC/DC converter based on SEPIC topology allows for an estimation of the dependence of the currents flowing through the inductor windings and the voltages across the capacitors on a number of parameters. The limiting continuous mathematical model of the DC/DC converter based on SEPIC topology is the basis for its circuit design and physical-and-mathematical analysis.

Keywords: DC/DC converter, buck-boost converter, equivalent circuit, SEPIC topology, limiting continuous mathematical model, Kirchhoff's rules, system of differential equations, Cauchy form, simulation

• **Submitted:** 09.04.2023 • **Revised:** 06.05.2023 • **Accepted:** 31.11.2023

For citation: Lavrenov A.I., Bityukov V.K. Mathematical model of a DC/DC converter based on SEPIC topology. *Russ. Technol. J.* 2024;12(1):69–79. https://doi.org/10.32362/2500-316X-2024-12-1-69-79

Financial disclosure: The authors have no a financial or property interest in any material or method mentioned.

The authors declare no conflicts of interest.

НАУЧНАЯ СТАТЬЯ

Математическая модель DC/DC-преобразователя, построенного по топологии SEPIC

А.И. Лавренов @**,**
В.К. Битюков

МИРЭА – Российский технологический университет, Москва, 119454 Россия
@ *Автор для переписки, e-mail: lavrenov@mirea.ru*

Резюме
Цели. DC/DC-преобразователь, построенный по топологии SEPIC, является униполярным электронным устройством, которое обеспечивает преобразование входного положительного напряжения в стабилизированное выходное напряжение той же полярности с возможностью его регулирования как ниже входного напряжения, так и выше. Цель статьи – выполнить анализ DC/DC-преобразователя в обеих фазах его работы. Для каждой из фаз необходимо составить эквивалентные схемы и получить характеризирующие дифференциальные уравнения с помощью правил Кирхгофа. Каждую систему дифференциальных уравнений нужно привести к виду Коши для дальнейшего преобразования в предельную непрерывную математическую модель, а каждую систему уравнений преобразовать в матричный вид и впоследствии объединить в единую матричную систему.
Методы. Задача построения предельной непрерывной математической модели решена с использованием правил Кирхгофа. Для компьютерного моделирования была применена программа *Multisim*. Это позволило сопоставить результаты расчета постоянных токов и напряжений и моделирования.
Результаты. Показано, что фазовые координаты математической модели стремятся к значениям реальных токов и напряжений преобразователя при частоте коммутации силового ключа более 200 кГц. Установлено достаточно хорошее соответствие расчетных значений токов и напряжений и их значений, полученных с помощью моделирования (при вариации коэффициента заполнения и частоты коммутации).
Выводы. Полученная предельная непрерывная математическая модель DC/DC-преобразователя, построенного по топологии SEPIC, позволяет оценить зависимость токов, протекающих через обмотки дросселей, и напряжения на конденсаторах от ряда параметров. Предельная непрерывная математическая модель DC/DC-преобразователя, построенного по топологии SEPIC, является базой его схемотехнического проектирования и физико-математического анализа.

Ключевые слова. DC/DC-преобразователь, понижающе-повышающий преобразователь, эквивалентная схема, топология SEPIC, предельная непрерывная математическая модель, правила Кирхгофа, система дифференциальных уравнений, форма Коши, моделирование

• **Поступила:** 09.04.2023 • **Доработана:** 06.05.2023 • **Принята к опубликованию:** 31.11.2023

Для цитирования: Лавренов А.И., Битюков В.К. Математическая модель DC/DC-преобразователя, построенного по топологии SEPIC. *Russ. Technol. J.* 2024;12(1):69–79. https://doi.org/10.32362/2500-316X-2024-12-1-69-79

Прозрачность финансовой деятельности: Авторы не имеют финансовой заинтересованности в представленных материалах или методах.

Авторы заявляют об отсутствии конфликта интересов.

INTRODUCTION

A feature of the construction of a modern radioelectronic device is the transition from mains power to autonomous power supply. This is characteristic of knowledge-intensive devices in many spheres of life such as communication devices, personal computers, measuring devices, and others. Autonomous devices are traditionally used in broad applications in aviation, medicine and space technology. The primary energy sources in these areas are lithium-ion batteries, rechargeable batteries, fuel cells, solar cells, and others [1–3]. Each of these power sources generates a voltage which is highly time-varying, hence the need for DC/DC converters in power supply devices [4]. Most DC/DC converters offered by electronic component manufacturers are either step-up, step-down, or polar-inverting. Only a small number combine the functions of increasing and decreasing output voltage relative to the input voltage and its stabilization [5, 6].

Efficient buck-boost DC/DC converters are devices built according to SEPIC, Cuck, and Zeta topologies [7]. The high efficiency rate of converters and the stability of their output voltage, as well as the need for small mass-size parameters predetermine the strict requirements for the design of such converters. An integrated approach to design may be achieved by applying the limiting continuous mathematical model (LCM) of DC/DC converter, circuit simulation, and experimental study.

The mathematical derivation and description of the technology of building LCM with periodic high-frequency structure change are presented in [8, 9]. In [10–12], examples of using this technology on basic step-up, step-down, and inverting converters, as well as the analysis of their LCMs are given. In [13, 14], the LCM of a buck-boost converter based on Cuck topology is indicated. The limiting continuous models under consideration here are systems whose phase trajectories are continuous, i.e. characteristic of real technical devices. The limiting nature of the system consists in the fact that when the period decreases, the accuracy of the phase trajectories of the system describes the properties of the modeled object to a greater extent.

The first developed and investigated LCM for Zeta DC/DC converter is proposed in [15, 16]. Analytical equations which determine and analyze Zeta converter ripples are presented in [17].

Unfortunately, a LCM for SEPIC converter has not yet been developed, so the aim of the paper is to develop and investigate this.

CIRCUIT ENGINEERING

The SEPIC, Cuck, and Zeta topologies of buck-boost DC/DC converters are accomplished almost using the same electronic component base. However, they have their own features due to differences in switching [18].

In the operation of SEPIC DC/DC converters (Fig. 1), as well as in other converters, there are two phases of operation traditionally determined by the state of the power transistor VT1 [19].

The first phase of the SEPIC converter operation is accomplished with transistor VT1 fully open. This is referred to as the accumulation phase. In this phase, energy is accumulated in the magnetic field of inductors L1 and L2, with inductor L1 accumulating energy in the form of an electromagnetic field from the input current flowing through the inductor winding, and inductor L2 accumulating energy from the voltage across capacitor C1. During this phase, capacitor C2 discharges to the load, thus forming the output voltage U_{out}.

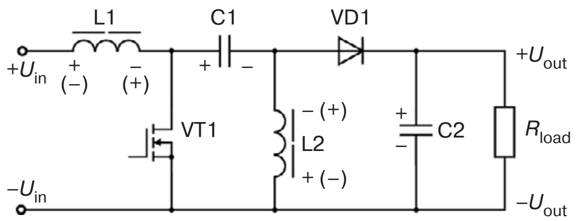

Fig. 1. Schematic circuit diagram of a buck-boost DC/DC converter based on SEPIC topology. U_{in} is the converter input voltage, R_{load} is the resistance. Here and in the following figures, the designations of circuit elements correspond to the designations adopted in GOST 2.710-81[1]

The second phase of the SEPIC converter operation is accomplished with the power transistor VT1 closed and is referred to as the discharge phase. The energy accumulated in the magnetic field of inductors L1 and L2 is used for charging capacitors C1 and C2.

MATHEMATICAL MODEL

Developing LCM for SEPIC converter requires describing each phase of the converter operation in terms of systems of differential equations in Cauchy form. It would be reasonable also to use Kirchhoff's rules to write these systems of equations. In order for the circuit equations of each phase of DC/DC converter operation to integrate alternating currents flowing through the windings of inductors L1 and L2, the inductors need to be represented in the form of series connected resistors R1 and R2 characterizing the ohmic resistance of the inductors and inductances L1 and L2.

The equivalent circuit of the first phase of the converter operation is shown in Fig. 2. Here the input power supply is labeled as E, while the inductors are represented as equivalent circuits. As can be seen from Fig. 2, all nodes of the circuit are connected to each other by conductors only, so they can be combined into one node.

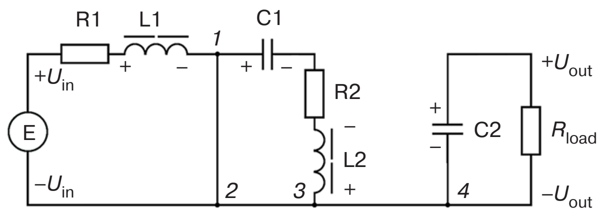

Fig. 2. Equivalent circuit of SEPIC converter operating in the energy accumulation phase

The equivalent circuit of the second phase of the converter operation is shown in Fig. 3, demonstrating

[1] GOST 2.710-81. *Interstate Standard. Unified system for design documentation. Alpha-numerical designations in electrical diagrams*. Moscow: Izd. Standartov; 1985 (in Russ.).

that nodes *1*, *3* and *2*, *4* are also connected to each other by conductors only. They can thus be combined into two nodes in pairs. It would be reasonable to combine the nodes in the circuits shown in Figs. 2 and 3, and designate contours on them (Figs. 4 and 5). Using the contours and nodes shown in Figs. 4 and 5, the equations of currents and voltages based on Kirchhoff's laws can be written.

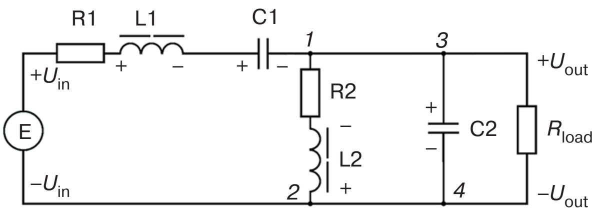

Fig. 3. Equivalent circuit of SEPIC converter operating in the energy transfer phase

First phase

The circuit shown in Fig. 4 has three branches and one node. Therefore, according to Kirchhoff's laws, the system of differential equations describing the first phase of DC/DC converter operation consists of three equations based on Kirchhoff's second law.

For circuits K1, K2, and K3 (Fig. 4), the following voltage equations can be written:

$$U_{\text{in}} = r_1 i_{\text{L1}} + L_1 \frac{di_{\text{L1}}}{dt}, \tag{1}$$

$$0 = -u_{\text{C1}} - r_2 i_{\text{L2}} - L_2 \frac{di_{\text{L2}}}{dt}, \tag{2}$$

$$0 = R_{\text{load}} i_{\text{load}} - u_{\text{C2}}, \tag{3}$$

where L_1 and L_2 are inductances of inductors; i_{L1} and i_{L2} are currents flowing through the windings of inductors L1 and L2; r_1 and r_2 are ohmic resistances of inductor windings L1 and L2; u_{C1} and u_{C2} are voltages on capacitors C1 and C2; and i_{load} is current flowing through the load with resistance R_{load}; U_{in} is the converter input voltage.

For the first phase, the currents flowing through capacitors C1 and C2 are defined by the following formulas:

$$i_{\text{L2}} = C_1 \frac{du_{\text{C1}}}{dt}, \tag{4}$$

$$i_{\text{load}} = C_2 \frac{du_{\text{C2}}}{dt}, \tag{5}$$

where C_1 and C_2 are capacitance of capacitors.

By expressing $\frac{di_{\text{L1}}}{dt}$ from Eq. (1), $\frac{di_{\text{L2}}}{dt}$ from Eq. (2), and $\frac{du_{\text{C1}}}{dt}$ from Eq. (4), the first three equations in Cauchy form are obtained. Substituting the load current from Eq. (5) into Eq. (3), we express $\frac{du_{\text{C2}}}{dt}$, thereby obtaining another equation in Cauchy form, as follows:

$$\begin{cases} \dfrac{di_{\text{L1}}}{dt} = \dfrac{U_{\text{in}}}{L_1} - \dfrac{r_1}{L_1} i_{\text{L1}}, \\ \dfrac{di_{\text{L2}}}{dt} = -\dfrac{1}{L_2} u_{\text{C1}} - \dfrac{r_2}{L_2} i_{\text{L2}}, \\ \dfrac{du_{\text{C1}}}{dt} = \dfrac{1}{C_1} i_{\text{L2}}, \\ \dfrac{du_{\text{C2}}}{dt} = \dfrac{1}{R_{\text{load}} C_2} u_{\text{C2}}. \end{cases} \tag{6}$$

Thus, Eqs. (6) form a system of differential equations in Cauchy form (6) describing the first phase of the SEPIC DC/DC converter operation.

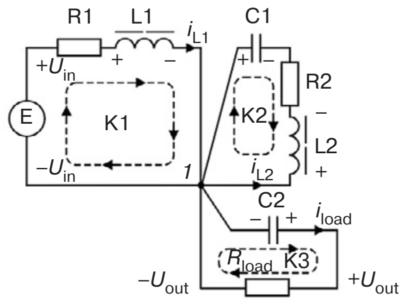

Fig. 4. Contours on the SEPIC converter circuit operating in the energy accumulation phase

Second phase

The circuit shown in Fig. 5 has four branches and two nodes. Therefore, according to Kirchhoff's rules, the system of differential equations describing the second phase of the converter consists of one equation based on Kirchhoff's first rule, and three equations based on the second rule. For node *1*, the following equation of currents can be written:

$$i_{\text{load}} = i_{\text{L1}} + i_{\text{L2}} - i_{\text{C2}}. \tag{7}$$

For circuits K1, K2, and K3, voltage equations in the following form can be written:

$$U_{\text{in}} = r_1 i_{\text{L1}} + L_1 \frac{di_{\text{L1}}}{dt} - u_{\text{C1}} - r_2 i_{\text{L2}} - L_2 \frac{di_{\text{L2}}}{dt}, \tag{8}$$

$$0 = -u_{\text{C2}} + r_2 i_{\text{L2}} + L_2 \frac{di_{\text{L2}}}{dt}, \tag{9}$$

$$0=-R_{\text{load}}i_{\text{load}}+u_{\text{C2}}. \tag{10}$$

For the second phase, equations for the currents flowing through capacitors C1 and C2 are determined by the following formulas:

$$-i_{\text{L1}}=C_1\frac{du_{\text{C1}}}{dt}, \tag{11}$$

$$-i_{\text{L2}}=C_2\frac{du_{\text{C2}}}{dt}. \tag{12}$$

Expressing $\frac{di_{\text{L2}}}{dt}$ from Eq. (9) and substituting it into Eq. (8), the first two equations in Cauchy form can be obtained. Expressing $\frac{du_{\text{C1}}}{dt}$ from Eq. (12) and substituting i_{load} from Eq. (7) into Eq. (10), two more equations in Cauchy form are obtained, as follows:

$$\begin{cases} \dfrac{di_{\text{L1}}}{dt}=\dfrac{U_{\text{in}}}{L_1}-\dfrac{r_1}{L_1}i_{\text{L1}}+\dfrac{1}{L_1}u_{\text{C1}}+\dfrac{1}{L_1}u_{\text{C2}}, \\ \dfrac{di_{\text{L2}}}{dt}=\dfrac{1}{L_2}u_{\text{C2}}-\dfrac{r_2}{L_2}i_{\text{L2}}, \\ \dfrac{du_{\text{C1}}}{dt}=-\dfrac{1}{C_1}i_{\text{L1}}, \\ \dfrac{du_{\text{C2}}}{dt}=-\dfrac{1}{C_2}i_{\text{L1}}-\dfrac{1}{C_2}i_{\text{L2}}+\dfrac{1}{R_{\text{load}}C_2}u_{\text{C2}}. \end{cases} \tag{13}$$

Thus, Eqs. (13) form a system of differential equations in Cauchy form which describe the second phase of the SEPIC DC/DC converter operation.

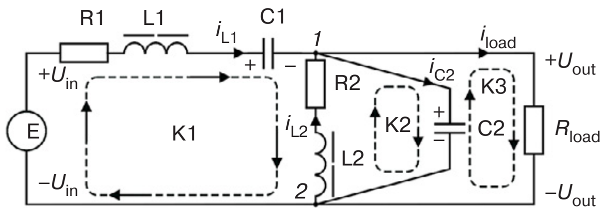

Fig. 5. Circuits on the SEPIC converter circuit operating in the energy transfer phase

TRANSFORMING SYSTEMS OF DIFFERENTIAL EQUATIONS IN CAUCHY FORM INTO MATRIX FORM TO OBTAIN A GENERALIZED MATRIX SYSTEM

For the convenient transformation of systems of differential Eqs. (6) and (13) into the generalized LCM, it would be reasonable to represent them in the form of coefficient matrices. These are multiplied by a matrix with variables in the form of currents and voltages: the so-called matrix $\mathbf{X}$ of the system phase coordinates. Therefore, each phase of the converter operation can be represented in the following form:

$$\mathbf{X}=\begin{bmatrix} i_{\text{L1}} \\ i_{\text{L2}} \\ u_{\text{C1}} \\ u_{\text{C2}} \end{bmatrix}, \quad \frac{d\mathbf{X}}{dt}=\mathbf{AX}+\mathbf{B}U, \tag{14}$$

where $\mathbf{A}$ is the coefficient matrix of phase coordinates, U is the external power supply, $\mathbf{B}$ is the coefficient matrix of the external source, and t is time.

After transformation of systems of differential Eqs. (6) and (13) into coefficient matrices $\mathbf{A}_1$, $\mathbf{B}_1$ and $\mathbf{A}_2$, $\mathbf{B}_2$, the following is obtained:

$$\mathbf{A}_1=\begin{bmatrix} -\dfrac{r_1}{L_1} & 0 & 0 & 0 \\ 0 & -\dfrac{r_2}{L_2} & -\dfrac{1}{L_2} & 0 \\ 0 & \dfrac{1}{C_1} & 0 & 0 \\ 0 & 0 & 0 & \dfrac{1}{R_{\text{load}}C_2} \end{bmatrix}, \tag{15}$$

$$\mathbf{A}_2=\begin{bmatrix} -\dfrac{r_1}{L_1} & 0 & \dfrac{1}{L_1} & \dfrac{1}{L_1} \\ 0 & -\dfrac{r_2}{L_2} & 0 & \dfrac{1}{L_2} \\ -\dfrac{1}{C_1} & 0 & 0 & 0 \\ -\dfrac{1}{C_2} & -\dfrac{1}{C_2} & 0 & \dfrac{1}{R_{\text{load}}C_2} \end{bmatrix}, \tag{16}$$

$$\mathbf{B}_1=\begin{bmatrix} \dfrac{1}{L_1} \\ 0 \\ 0 \\ 0 \end{bmatrix}, \tag{17}$$

$$\mathbf{B}_2=\begin{bmatrix} \dfrac{1}{L_1} \\ 0 \\ 0 \\ 0 \end{bmatrix}, \tag{18}$$

where $\mathbf{A}_1$ and $\mathbf{A}_2$ are the coefficient matrices of the phase coordinates of the first and second phase, respectively, while $\mathbf{B}_1$ and $\mathbf{B}_2$ are the coefficient matrices of the external source of the first and second phase, respectively.

The duration of the first phase of the converter operation is determined by fill factor D and is equal to DT, while the duration of the second phase is equal to $(1 - D)T$, where T is the switching period of the power switch VT1. Therefore, matrix $\mathbf{A}$ can be represented as $\mathbf{A}_1 D + \mathbf{A}_2(1 - D)$, while matrix $\mathbf{B}$ can be represented as $\mathbf{B}_1 D + \mathbf{B}_2(1 - D)$. It would thus be reasonable to combine matrices (15)–(18) into a generalized system, as follows:

$$\frac{d\mathbf{X}}{dt} = (\mathbf{A}_1 D + \mathbf{A}_2(1-D))\mathbf{X} +$$
$$+ (\mathbf{B}_1 D + \mathbf{B}_2(1-D))U = \mathbf{A}\mathbf{X} + \mathbf{B}U.$$

Then matrices $\mathbf{A}$ and $\mathbf{B}$ can be written in the following form:

$$\mathbf{A} = \begin{bmatrix} -\frac{r_1}{L_1} & 0 & \frac{1-D}{L_1} & \frac{1-D}{L_1} \\ 0 & -\frac{r_2}{L_2} & -\frac{D}{L_2} & \frac{1-D}{L_2} \\ -\frac{1-D}{C_1} & \frac{D}{C_1} & 0 & 0 \\ -\frac{1-D}{C_2} & -\frac{1-D}{C_2} & 0 & \frac{1}{R_{\text{load}} C_2} \end{bmatrix}, \quad (19)$$

$$\mathbf{B} = \begin{bmatrix} \frac{1}{L_1} \\ 0 \\ 0 \\ 0 \end{bmatrix}. \quad (20)$$

Thus, the system of equations (14), (19), and (20) is the LCM for the DC/DC converter based on SEPIC topology.

ANALYSIS OF THE LCM

It would be advisable to start LCM analysis by defining DC currents and voltages. The voltages and currents of a real device are the sum of constant and variable components. In order to simplify the circuit analysis, it would be advisable to study the considered device in a steady state when the transient process is over. In this case, constant values of currents and voltages do not depend on time. This allows the LCM for the steady state to be written in the following form:

$$\begin{cases} -\frac{r_1}{L_1} I_{\text{L1}} + \frac{1-D}{L_1} U_{\text{C1}} + \frac{1-D}{L_1} U_{\text{C2}} = -\frac{1}{L_1} U_{\text{in}}, \\ -\frac{r_2}{L_2} I_{\text{L2}} - \frac{D}{L_2} U_{\text{C1}} + \frac{1-D}{L_2} U_{\text{C2}} = 0, \\ -\frac{1-D}{C_1} I_{\text{L1}} + \frac{D}{C_1} I_{\text{L2}} = 0, \\ -\frac{1-D}{C_2} I_{\text{L1}} - \frac{1-D}{C_2} I_{\text{L2}} - \frac{1}{R_{\text{load}} C_2} U_{\text{C2}} = 0, \end{cases} \quad (21)$$

where I_{L1}, I_{L2} are constant currents flowing through the windings of inductors L1 and L2, respectively; U_{C1}, U_{C2} are constant voltages on capacitors C1 and C2, respectively. Solving the system of equations (21), the following formulas for determining the constant currents and voltages can be obtained:

$$I_{\text{L1}} = \\ = \frac{-U_{\text{in}} D^2}{\left(D^2 - 2D + 1\right) r_2 + D^2 r_1 + (2R_{\text{load}} D - R_{\text{load}} D^2 - R_{\text{load}})}, \quad (22)$$

$$I_{\text{L2}} = \\ = \frac{U_{\text{in}} D^2 - U_{\text{in}} D}{\left(D^2 - 2D + 1\right) r_2 + D^2 r_1 + (2R_{\text{load}} D - R_{\text{load}} D^2 - R_{\text{load}})}, \quad (23)$$

$$U_{\text{C1}} = \\ = \frac{\left(-U_{\text{in}} D + U_{\text{in}}\right) r_2 + \left(2R_{\text{load}} U_{\text{in}} D - R_{\text{load}} U_{\text{in}} D^2 - R_{\text{load}} U_{\text{in}}\right)}{\left(D^2 - 2D + 1\right) r_2 + D^2 r_1 + \left(2R_{\text{load}} D - R_{\text{load}} D^2 - R_{\text{load}}\right)}, \quad (24)$$

$$U_{\text{C2}} = \\ = -\frac{R_{\text{load}} U_{\text{in}} D^2 - R_{\text{load}} U_{\text{in}} D}{\left(D^2 - 2D + 1\right) r_2 + D^2 r_1 + \left(2R_{\text{load}} D - R_{\text{load}} D^2 - R_{\text{load}}\right)}. \quad (25)$$

These equations can be substantially simplified by assuming that ohmic resistances r_1 and r_2 of the inductor windings L1 and L2 are zero. Then Eqs. (22)–(25) can be written in the following form:

$$I_{\text{L1}} = \frac{U_{\text{in}} D^2}{\left(D-1\right)^2 R_{\text{load}}}, \quad (26)$$

$$I_{\text{L2}} = \frac{U_{\text{in}} D}{\left(1-D\right) R_{\text{load}}}, \quad (27)$$

$$U_{\text{C1}} = U_{\text{in}}, \quad (28)$$

$$U_{\text{C2}} = \frac{U_{\text{in}} D}{\left(1-D\right) R_{\text{load}}}. \quad (29)$$

Equations (22)–(25) are the basis for designing the DC/DC converter based on SEPIC topology and allow the calculation of constant currents I_{L1} and I_{L2} flowing

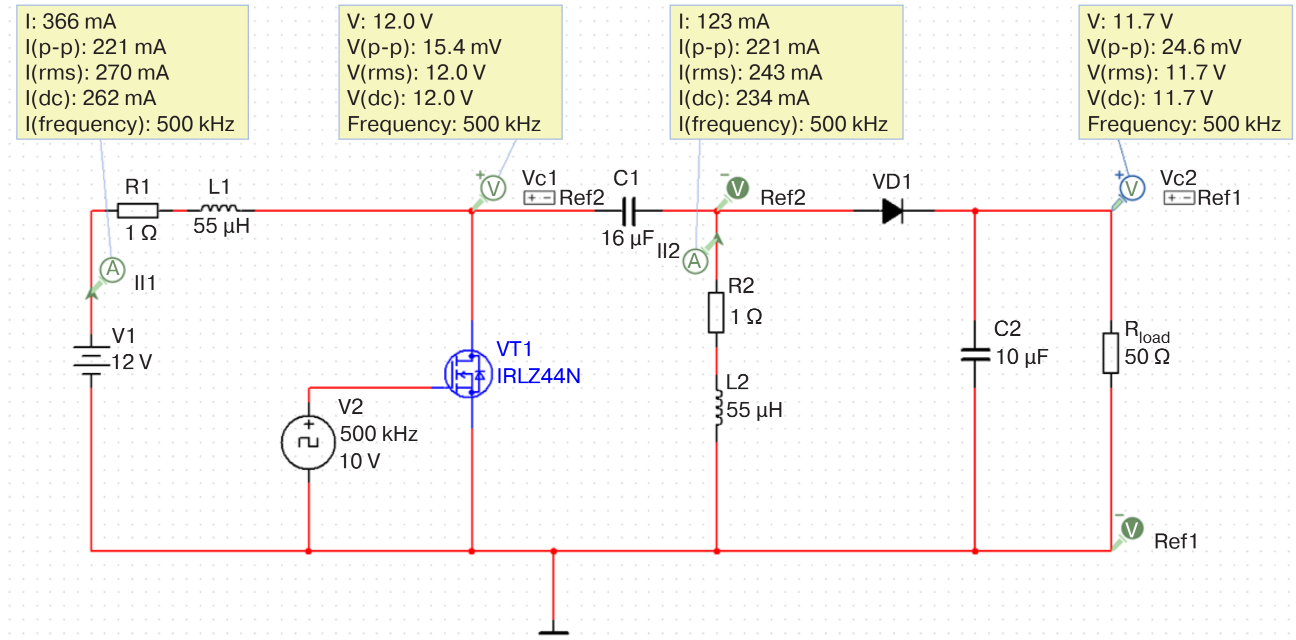

Fig. 6. Simulation circuit of the DC/DC converter based on SEPIC topology

through the windings of inductors L1 and L2, as well as voltages U_{C1} and U_{C2} on capacitors C1 and C2. Equations (26)–(29) are required for estimating the converter.

SIMULATION IN *MULTISIM*

The simulation circuit for the DC/DC converter based on SEPIC topology is shown in Fig. 6. Electronic elements are selected from *Multisim* database.[2] MOSFET IRLZ44N (International Rectifier, USA) is selected as power switch VT1. This transistor has been previously investigated in static and dynamic modes and has been compared with data from Datasheet [20, 21]. The analysis results show that the IRLZ44N transistor model in *Multisim* environment corresponds to the characteristics given in Datasheet.

The power supply is represented as the element of constant voltage V1. Modulation of the power switch VT1 is accomplished by pulse width modulation signal generator V2. The constant components of currents and voltages are measured by samples on the circuit in the DC mode. It should be noted that the measurements are carried out 3–5 ms after the start of simulation, thus enabling the currents and voltages in the steady state of the DC/DC converter under consideration to be measured.

The dependence plots of constant currents and voltages on fill factor D are shown in Figs. 7 and 8. There is an obvious correlation between calculated values obtained using LCM and the values obtained by simulation within the range of fill factor D changing from 0.3 to 0.7. It is worth noting that at fill factor D around 0.5, the best coincidence between calculated values and those obtained in simulation is observed.

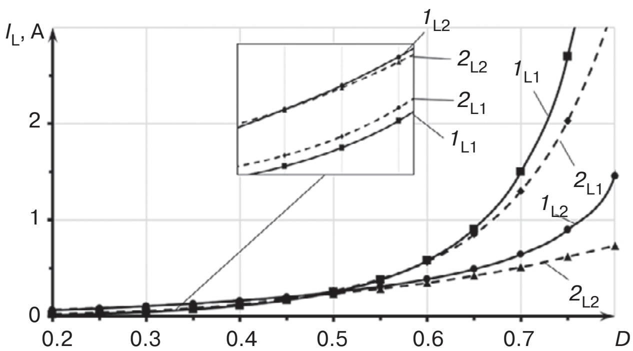

Fig. 7. Effect of the fill factor on currents flowing through the windings of inductors L1 and L2: 1_{L1} and 1_{L2} are calculation; 2_{L1} and 2_{L2} are simulation

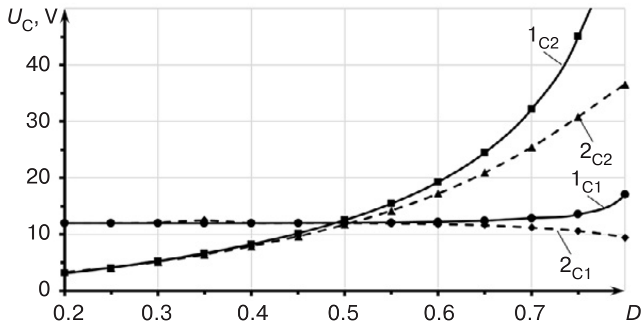

Fig. 8. Effect of fill factor on voltages on capacitors C1 and C2: 1_{C1} and 1_{C2} are calculation; 2_{C1} and 2_{C2} are simulation

[2] https://www.ni.com/en/support/downloads/software-products/download.multisim.html#452133. Accessed April 09, 2023.

At fill factor $D = 0.5$, the difference between calculated values and simulation results for currents flowing through inductor windings is 12 and 16 mA, with calculated value I_{L1} and I_{L2} equal to 250 mA. For capacitor C2 voltage, the difference between calculated values and simulation results is 0.8 V with a calculated value U_{C2} equal to 12.5 V. The calculated voltage value U_{C1} = 12.0 V coincides with the voltage obtained in simulation.

The difference between the calculated value and the value obtained in simulation for current I_{L1} at fill factor $D = 0.3$ is 11 mA, while at $D = 0.7$ it amounts to 0.2 A. The calculated current values I_{L1} are 45 mA and 1.5 A, respectively. Similarly, it may be noted that the difference of current I_{L2} is 2 mA at $D = 0.3$ and 135 mA at $D = 0.7$ for calculated current I_{L2} equal to 105 mA and 643 mA, respectively.

The difference between the calculated and simulated voltage values U_{C1} is 0.16 V at $D = 0.3$ and 1.65 V at $D = 0.7$, with the calculated value of DC voltage U_{C1} varying from 11.94 V at $D = 0.3$ to 12.85 V at $D = 0.7$. A similar dependence is also characteristic of the DC voltage U_{C2}. This difference is 0.13 V at calculated value U_{C2}, equal to 5.27 V, and 6.75 V at calculated value U_{C2} equal to 32.1 V for $D = 0.3$ and $D = 0.7$, respectively.

Similar dependences of calculated and simulated currents and voltages are characteristic of LCM for the DC/DC converter based on Zeta topology [15–17]. The dependences of currents I_{L1}, I_{L2} and voltages U_{C1}, U_{C2} on frequency also have a similarity: the calculated values begin to correspond to the values obtained in simulation at switching frequency f of the power switch VT1 above 200 kHz only. In addition, the graphs of calculated and simulation values intersect each other in the neighborhood of fill factor $D = 0.5$. When the fill factor increases or decreases, the difference between the values increases.

The graphs presented in Figs. 9 and 10 show that when switching frequency f of the power transistor increases, the values of DC currents and voltages described by LCM tend towards corresponding values of DC currents and voltages obtained in simulation (as described in [15–17]). This illustrates the limitation of the mathematical model for the DC/DC converter based on SEPIC topology.

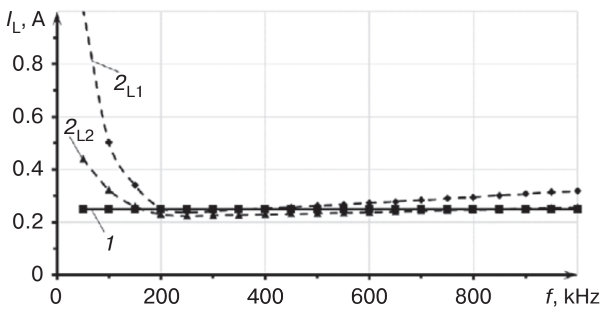

Fig. 9. Effect of switching frequency on currents flowing through the windings of the first and the second inductor at fill factor equal to 0.5: *1* is calculation; 2_{L1} and 2_{L2} are simulation

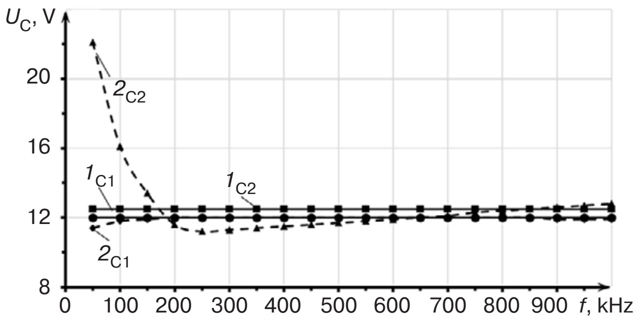

Fig. 10. Effect of switching frequency on voltages on the first and second capacitor at fill factor equal to 0.5: 1_{C1} and 1_{C2} are calculation; 2_{C1} and 2_{C2} are simulation

CONCLUSIONS

This is the first time that the LCM of the unipolar DC/DC converter based on SEPIC topology has been obtained. The analysis results of the equivalent circuits of the considered converter for both operation phases are given. Kirchhoff's rules were used to obtain differential equations for algebraic sums of currents and voltages in the device describing changes in the input power supply current, currents flowing through the windings of inductors L1 and L2, and voltages on capacitors C1 and C2.

The systems of differential equations in Cauchy form written for each phase of converter operation are transformed into coefficient matrices. This allows for the limit continuous mathematical model for DC/DC converter to be formulated. The mathematical model is used to obtain equations for calculating constant currents flowing through the inductor windings and the voltages on capacitors in the converter steady-state operation.

Calculation results using the obtained limit continuous mathematical model are compared with those obtained in the DC/DC converter simulation. Current values I_{L1} obtained in simulation differ from the calculated value in the range from 11 mA to 0.2 A. These correspond to the percentage value of 13–24%. Similarly, for current I_{L2}, the values range from 2 to 135 mA, that in percentage terms corresponds to a range of 2–20%. A similar pattern is characteristic of voltages U_{C1} and U_{C2}. The voltages deviate from the calculated value from 0.16 to 1.65 V for U_{C1} and from 0.13 to 6.74 V for U_{C2}. These ranges correspond to deviations of 1–13% for U_{C1} and 3–20% for U_{C2}. In addition, it is shown that at switching frequencies of the power switch VT1 greater than 200 kHz, there are small differences between calculated values and those obtained in simulation.

The LCM for the DC/DC converter based on SEPIC topology is the basis for its circuit design and physico-mathematical analysis.

Authors' contribution. All authors equally contributed to the research work.

REFERENCES

1. Vasyukov I.V., Pavlenko A.V., Batishchev D.V. Review and Analysis of Topologies of Converters of Power Supply Systems on Hydrogen Fuel Cells for Unmanned Aerial Vehicles of Kilowatt Power Class. *Izvestiya vysshikh uchebnykh zavedenii. Elektromekhanika = Russian Electromechanics*. 2022;65(2):19–26 (in Russ.). https://doi.org/10.17213/0136-3360-2022-2-19-26
2. Antchev H., Andonov A. Simple PV battery charger without MPPT based on SEPIC converter. *Electrotechnica & Electronica* (*E+E*). 2019;54(3–4):64–69. Available from URL: https://epluse.ceec.bg/wp-content/uploads/2019/08/20190304-04.pdf
3. Kushwaha R., Singh B. UPF-isolated zeta converter-based battery charger for electric vehicle. *IET Electrical Systems in Transportation*. 2019;9(3):103–112. https://doi.org/10.1049/iet-est.2018.5010
4. Sharov I.M., Demin O.A., Sudakov A.A., Yarlykov A.D. Development and research of an uninterruptible power supply system in networks with voltage up to 24 V. *Russ. Technol. J.* 2022;10(5):60–72 (in Russ.). https://doi.org/10.32362/2500-316X-2022-10-5-60-72
5. Murthy-Bellur D., Kazimierczuk M.K. Two-transistor Zeta-flyback DC-DC converter with reduced transistor voltage stress. *Electron. Lett*. 2010;46(10):719–720. https://doi.org/10.1049/el.2010.3494
6. Thirumeni M., Thangavelusamy D. Performance analysis of PI and SMC controlled zeta converter. *Int. J. Recent Technol. Eng*. 2019;8(3):8700–8706. http://www.doi.org/10.35940/ijrte.C5242.098319
7. Erickson R.W., Maksimović D. *Fundamentals of Power Electronics*. NY: Springer; 2020. 1084 p. https://doi.org/10.1007/978-3-030-43881-4
8. Korshunov A.I. Limiting continuous model of a system with high-frequency structure variation. *Izvestiya vysshikh uchebnykh zavedenii. Priborostroenie = J. Instrument Eng.* 2009;52(9):42−48 (in Russ.). Available from URL: https://pribor.ifmo.ru/file/article/4902.pdf
9. Korshunov A.I. Limiting Continuous Model of System with High-Frequency Variable Structure. *Silovaya elektronika.* 2021;5(92):48−51 (in Russ.).
10. Korshunov A.I. Methodology for constructing continuous models of pulsed DC voltage converters. *Komponenty i tekhnologii = Components & Technologies*. 2006;8(61):124−130 (in Russ.). Available from URL: https://kit-e.ru/powerel/metodika-postroeniya-nepreryvnyh-modelej-impulsnyh-preobrazovatelej-napryazheniya-postoyannogo-toka/
11. Korshunov A.I. Improving the quality of output voltage stabilisation of a pulsed DC converter. *Izvestiya vysshikh uchebnykh zavedenii. Priborostroenie = J. Instrument Eng.* 2013;56(3):48−57 (in Russ.). Available from URL: https://pribor.ifmo.ru/file/article/6176.pdf
12. Korshunov A.I. Two approaches to stability analysis of DC-DC converters with variable structure of power stage. *Prakticheskaya silovaya elektronika = Practical Power Electronics*. 2017;2(66):12−19 (in Russ.).
13. Korshunov A.I. Pulsed DC voltage converter based on Chuk scheme. *Silovaya elektronika = Power Electronics*. 2017;4(67):60−66 (in Russ.).
14. Korshunov A.I. Specifics of DC voltage stabilization by Chuk converter. *Prakticheskaya silovaya elektronika = Practical Power Electronics*. 2017;4(68):2−9 (in Russ.).
15. Bityukov V.K., Lavrenov A.I., Malitskiy D.A. Mathematical model of DC/DC converter based on Zeta topology (Part 1). *Proektirovanie i tekhnologiya elektronnykh sredstv = Design and Technology of Electronic Means*. 2022;4:53−57 (in Russ.).
16. Bityukov V.K., Lavrenov A.I., Malitskiy D.A. Mathematical model of DC/DC converter based on Zeta topology (Part 2). *Proektirovanie i tekhnologiya elektronnykh sredstv = Design and Technology of Electronic Means*. 2023;1:48−53 (in Russ.).
17. Bityukov V.K., Lavrenov A.I., Malitskiy D.A. Analysis of the DC/DC Zeta topology converter ripples by applying its limiting continuous mathematical model. *Russ. Technol. J.* 2023;11(4):36–48 (in Russ.). https://doi.org/10.32362/2500-316X-2023-11-4-36-48
18. Odinokov A.O., Kremzukov Yu.A. Selecting DC converter topology. SEPIC or Zeta. *Prakticheskaya silovaya elektronika = Practical Power Electronics*. 2022;4(88):44–47 (in Russ.).
19. Bityukov V.K., Simachkov D.S., Babenko V.P. *Skhemotekhnika elektropreobrazovatel'nykh ustroistv* (*Circuitry of Electrical Converter Devices*). Vologda: Infra-Inzheneriya; 2023. 384 p. (in Russ.). ISBN 978-5-9729-1439-5
20. Babenko V.P., Bityukov V.K. Simulation of Switching of High-Power FETs Using the Electronics Workbench Software. *J. Commun. Technol. Electron.* 2019;64(2):176–181. https://doi.org/10.1134/S1064226919020025
[Original Russian Text: Babenko V.P., Bityukov V.K. Simulation of Switching of High-Power FETs Using the Electronics Workbench Software. *Radiotekhnika i Elektronika.* 2019;64(2):199−205 (in Russ.). https://doi.org/10.1134/S0033849419020025]
21. Babenko V.P., Bityukov V.K., Kuznetsov V.V., Simachkov D.S. Simulation of static and dynamic losses in MOSFET keys. *Russ. Technol. J*. 2018;6(1):20−39 (in Russ.). Available from URL: https://doi.org/10.32362/2500-316X-2018-6-1-20-39

СПИСОК ЛИТЕРАТУРЫ

1. Васюков И.В., Павленко А.В., Батищев Д.В. Обзор и анализ топологий преобразователей систем электропитания на водородных топливных элементах для беспилотных летательных аппаратов киловаттного класса мощности. *Известия вузов. Электромеханика*. 2022;65(2):19–26. https://doi.org/10.17213/0136-3360-2022-2-19-26

2. Antchev H., Andonov A. Simple PV battery charger without MPPT based on SEPIC converter. *Electrotechnica & Electronica* (*E+E*). 2019;54(3–4):64–69. URL: https://epluse.ceec.bg/wp-content/uploads/2019/08/20190304-04.pdf
3. Kushwaha R., Singh B. UPF-isolated zeta converter-based battery charger for electric vehicle. *IET Electrical Systems in Transportation*. 2019;9(3):103–112. https://doi.org/10.1049/iet-est.2018.5010
4. Шаров И.М., Демин О.А., Судаков А.А., Ярлыков А.Д. Разработка и исследование системы бесперебойного питания в сетях с напряжением до 24 В. *Russ. Technol. J*. 2022;10(5):60–72. https://doi.org/10.32362/2500-316X-2022-10-5-60-72
5. Murthy-Bellur D., Kazimierczuk M.K. Two-transistor Zeta-flyback DC-DC converter with reduced transistor voltage stress. *Electron. Lett*. 2010;46(10):719–720. https://doi.org/10.1049/el.2010.3494
6. Thirumeni M., Thangavelusamy D. Performance analysis of PI and SMC controlled zeta converter. *Int. J. Recent Technol. Eng*. 2019;8(3):8700–8706. http://www.doi.org/10.35940/ijrte.C5242.098319
7. Erickson R.W., Maksimović D. *Fundamentals of Power Electronics*. NY: Springer; 2020. 1084 p. https://doi.org/10.1007/978-3-030-43881-4
8. Коршунов А.И. Предельная непрерывная модель системы с высокочастотным периодическим изменением структуры. *Известия вузов. Приборостроение*. 2009;52(9):42–48. URL: https://pribor.ifmo.ru/file/article/4902.pdf
9. Коршунов А.И. Предельная непрерывная модель системы с периодическим высокочастотным изменением структуры. *Силовая электроника*. 2021;5(92):48–51.
10. Коршунов А.И. Методика построения непрерывных моделей импульсных преобразователей напряжения постоянного тока. *Компоненты и технологии*. 2006;8(61):124–130. URL: https://kit-e.ru/powerel/metodika-postroeniya-nepreryvnyh-modelej-impulsnyh-preobrazovatelej-napryazheniya-postoyannogo-toka/
11. Коршунов А.И. Повышение качества стабилизации выходного напряжения импульсного преобразователя постоянного тока. *Известия вузов. Приборостроение*. 2013;56(3):48–57. URL: https://pribor.ifmo.ru/file/article/6176.pdf
12. Коршунов А.И. Два подхода к анализу устойчивости стабилизаторов напряжения постоянного тока с переменной структурой силовой части. *Практическая силовая электроника*. 2017;66:12–19.
13. Коршунов А.И. Импульсный преобразователь напряжения постоянного тока по схеме Чука. *Силовая электроника*. 2017;4(67):60–66.
14. Коршунов А.И. Особенности стабилизации напряжения постоянного тока с помощью преобразователя Чука. *Практическая силовая электроника*. 2017;4(68):2–9.
15. Битюков В.К., Лавренов А.И., Малицкий Д.А. Математическая модель DC/DC преобразователя, построенного по Zeta топологии (часть 1). *Проектирование и технология электронных средств*. 2022;4:53–57.
16. Битюков В.К., Лавренов А.И., Малицкий Д.А. Математическая модель DC/DC преобразователя, построенного по Zeta топологии (часть 2). *Проектирование и технология электронных средств*. 2023;1:48–53.
17. Битюков В.К., Лавренов А.И., Малицкий Д.А. Анализ пульсаций DC/DC преобразователя, построенного по Zeta топологии, с использованием его предельной непрерывной математической модели. *Russ. Technol. J.* 2023;11(4):36–48. https://doi.org/10.32362/2500-316X-2023-11-4-36-48
18. Одиноков А.О., Кремзуков Ю.А. Выбор топологии преобразователя постоянного напряжения. SEPIC или Zeta. *Практическая силовая электроника*. 2022;4(88):44–47.
19. Битюков В.К., Симачков Д.С., Бабенко В.П. *Схемотехника электропреобразовательных устройств*. Вологда: Инфра-Инженерия; 2023. 384 с. ISBN 978-5-9729-1439-5
20. Бабенко В.П., Битюков В.К. Имитационное моделирование процессов переключения силовых полевых транзисторов в программе Electronics Workbench. *Радиотехника и электроника*. 2019;64(2):199–205. https://doi.org/10.1134/S0033849419020025
21. Бабенко В.П., Битюков В.К., Кузнецов В.В., Симачков Д.С. Моделирование статических и динамических потерь в MOSFET ключах. *Российский технологический журнал.* 2018;6(1):20–39. https://doi.org/10.32362/2500-316X-2018-6-1-20-39

About the authors

Aleksey I. Lavrenov, Assistant, Department of Radio Wave Processes and Technology, Institute of Radio Electronics and Informatics, MIREA – Russian Technological University (78, Vernadskogo pr., Moscow, 119454 Russia). E-mail: lavrenov@mirea.ru. RSCI SPIN-code 6048-5027, https://orcid.org/0000-0001-5722-541X

Vladimir K. Bityukov, Dr. Sci. (Eng.), Professor, Department of Radio Wave Processes and Technologies, Institute of Radio Electronics and Informatics, MIREA – Russian Technological University (78, Vernadskogo pr., Moscow, 119454 Russia). E-mail: bitukov@mirea.ru. ResearcherID Y-8325-2018, Scopus Author ID 6603797260, RSCI SPIN-code 3834-5360, https://orcid.org/0000-0001-6448-8509

Об авторах

Лавренов Алексей Игоревич, ассистент, кафедра радиоволновых процессов и технологий Института радиоэлектроники и информатики ФГБОУ ВО «МИРЭА – Российский технологический университет» (119454, Россия, Москва, пр-т Вернадского, д. 78). E-mail: lavrenov@mirea.ru. SPIN-код РИНЦ 6048-5027, https://orcid.org/0000-0001-5722-541X

Битюков Владимир Ксенофонтович, д.т.н., профессор, профессор кафедры радиоволновых процессов и технологий Института радиоэлектроники и информатики ФГБОУ ВО «МИРЭА – Российский технологический университет» (119454, Россия, Москва, пр-т Вернадского, д. 78). E-mail: bitukov@mirea.ru. ResearcherID Y-8325-2018, Scopus Author ID 6603797260, SPIN-код РИНЦ 3834-5360, https://orcid.org/0000-0001-6448-8509

Translated from Russian into English by Kirill V. Nazarov
Edited for English language and spelling by Dr. David Mossop

Analytical instrument engineering and technology
Аналитическое приборостроение и технологии

UDC 62-519
https://doi.org/10.32362/2500-316X-2024-12-1-80-91

RESEARCH ARTICLE

Control system for noise-resistant electronic speed controller of a brushless electric motor for an unmanned aerial vehicle

Maksim V. Parinov @,
Aleksey N. Yurov,
Yaroslav V. Skitskiy

Voronezh State Technical University, Voronezh, 394006 Russia
@ Corresponding author, e-mail: parmax@mail.ru

Abstract
Objectives. The high demand for unmanned aircraft and their efficiency makes the production of their components a matter of relevance. One of these components is the speed controller of the brushless electric motor of the propeller motor group. At the current time, Russian industry, however, does not mass-produce them. In order to start production, control methods and algorithms for the hardware and software parts of devices of this type are needed. Criteria for selecting the main components also need to be formalized. The aim of this work is to develop a method for the software control of electric motors. This includes block diagrams and invariant algorithms and methods for the calculated selection of parameters of the main microcontroller of the electronic speed controller.
Methods. Methods of algorithmization, expert assessments, linear computational processes and experimental studies were used.
Results. The paper presents the theoretical basis for controlling the required motors. It proposes a block diagram of the implementation of the controller, and a technique for switching windings when controlling with a trapezoidal signal is proposed. Examples are given in the form of an oscillogram. Based on theoretical research, an invariant algorithmic apparatus was developed for building software for various types of microcontrollers. Block diagrams of all the main modules of the software are also presented. The main ones include: the event switching algorithm; and the main endless loop of the microcontroller. The requirements for microcontrollers to create the various types of speed controllers are formalized herein and presented in the form of a set of mathematical expressions. They enable the number of required peripheral devices and microcontroller ports to be calculated according to the requirements for the microcontroller, as well as the computing power of the core used.
Conclusions. Experimental studies show the reliability of the theoretical research presented herein. The results obtained can be used to select the optimal element base and develop software for speed controllers of electric motors of the propellers of unmanned aircraft.

Keywords: electric speed controller, algorithms, brushless direct current motor, unmanned aerial vehicle, noise-resistant solutions, software control, microcontroller

• **Submitted:** 30.11.2023 • **Revised:** 04.12.2023 • **Accepted:** 15.12.2023

For citation: Parinov M.V., Yurov A.N., Skitskiy Ya.V. Control system for noise-resistant electronic speed controller of a brushless electric motor for an unmanned aerial vehicle. *Russ. Technol. J*. 2024;12(1):80–91. https://doi.org/10.32362/2500-316X-2024-12-1-80-91

Financial disclosure: The authors have no a financial or property interest in any material or method mentioned.

The authors declare no conflicts of interest.

НАУЧНАЯ СТАТЬЯ

Система управления помехоустойчивым электронным регулятором оборотов бесщеточного электродвигателя беспилотного воздушного судна

М.В. Паринов @,
А.Н. Юров,
Я.В. Скитский

Воронежский государственный технический университет, Воронеж, 394006 Россия
@ Автор для переписки, e-mail: parmax@mail.ru

Резюме
Цели. Высокая востребованность и эффективность беспилотных воздушных судов делают актуальным производство их компонентов, одним из которых является регулятор скорости вращения бесщеточного электродвигателя винтомоторной группы. Однако российская промышленность в настоящее время не производит их серийно. Для запуска производства необходимо разработать методики и алгоритмы управления для аппаратной и программной частей устройств данного типа, а также формализовать критерии выбора основных компонентов. Целью работы является создание методики программного управления электродвигателем, включающее структурные схемы, инвариантные алгоритмы и методики расчетного выбора параметров основного микроконтроллера регулятора оборотов.
Методы. Использованы методы алгоритмизации, экспертных оценок, линейных вычислительных процессов и экспериментальных исследований.
Результаты. Представлены теоретические основы управления электродвигателями винтомоторной группы. Предложены структурная схема реализации регулятора, методики коммутации обмоток при управлении с трапецеидальным сигналом, представлены осциллограммы сигналов. На базе теоретических изысканий разработан инвариантный алгоритмический аппарат построения программного обеспечения для различных типов микроконтроллеров. Представлены блок-схемы основных модулей программного средства: алгоритмов событийной коммутации и основного бесконечного цикла микроконтроллера. Формализованы требования к микроконтроллерам для создания различных типов регуляторов оборотов, представленные в виде набора математических выражений. Они позволяют выполнить расчет количества необходимых периферийных устройств и портов микроконтроллера согласно требованиям к регулятору, а также вычислительной мощности используемого ядра.
Выводы. Экспериментальные исследования показали достоверность представленных теоретических изысканий. Полученные результаты могут быть использованы для подбора оптимальной элементной базы и разработки программного обеспечения для регуляторов скорости вращения электродвигателей винтомоторной группы беспилотных воздушных судов.

Ключевые слова: регулятор скорости вращения электродвигателя, алгоритмы, бесщеточный электродвигатель, беспилотное воздушное судно, помехоустойчивые решения, программное управление, микроконтроллер

• **Поступила:** 30.11.2023 • **Доработана:** 04.12.2023 • **Принята к опубликованию:** 15.12.2023

Для цитирования: Паринов М.В., Юров А.Н., Скитский Я.В. Система управления помехоустойчивым электронным регулятором оборотов бесщеточного электродвигателя беспилотного воздушного судна. *Russ. Technol. J.* 2024;12(1):80–91. https://doi.org/10.32362/2500-316X-2024-12-1-80-91

Прозрачность финансовой деятельности: Авторы не имеют финансовой заинтересованности в представленных материалах или методах.

Авторы заявляют об отсутствии конфликта интересов.

INTRODUCTION

At the present time, most light unmanned aerial vehicles (UAVs) use electric propeller group motors (EPGs) [1, 2]. The current trend is to switch to electric propulsion for larger aircraft (ACs).

Electric UAVs use brushless three-phase electric motors [3]. Their rotation speed is controlled by switching phases and changing the currents flowing in the windings. In order to synchronize the commutation process with the rotation of the rotor, the position of permanent magnets relative to the windings must be determined. This can be achieved by sensors built into the electric motor [4]. This approach gives good results, but it is complicated and expensive. Therefore, the most widely used approach is to use back electromotive force (EMF) measured on the currently unconnected phase, in order to establish commutation torque [5, 6].

The vast majority of lightweight brushless UAVs currently in use do not have built-in sensors. They are controlled by electric speed controllers (ESC). The generally accepted architecture of lightweight UAV [7] assumes typical interfaces for connection of standardized components. In particular, the main and obligatory components of ESC consist of a connection interface for the electric motor windings (3 phase lines), and a control interface (digital or using pulse width modulation (PWM)). The electronic controller usually has one or more telemetry signal outputs.

At the current time, the Russian market offers a wide range of ESCs, covering practically all existing needs. However, all the solutions known to the authors are foreign. Their software and technical documentation are not publicly available. Thus, due to the dependence on foreign supplies, the production of new devices with extended functionality is problematic. This contradicts the policy of technological sovereignty.

TASK ASSIGNMENT

In order to resolve this problem, a methodology needs to be designed which will ensure the development and manufacture of rotation speed controllers for EPG electric motors for light UAVs. This consists of two elements: hardware development methodology (circuit solution); and program control methodology. This article focuses on the second of these.

Development of the program control methodology requires the principles of the controller construction to be selected, and the basic principles and algorithms of future software to be developed. An additional task is to develop a methodology for selecting microcontroller parameters according to the given characteristics of the controller.

The main elements which affect the noise resistance of the device are as follows: control interface cabling; telemetry; data transmission protocols; choice of component base; and the printed circuit board design. Of these, only the digital interface protocols are relevant to this paper. Their selection significantly affects the noise immunity of the system [8]. However, when developing the ESC controller, we are limited to the typical list of protocols supported by classical flight controllers. The development of additional control and telemetry protocols is possible only in conjunction with a specialized flight controller.

The program control methodology for lightweight UAV rotational speed controllers can developed in two ways: full software implementation of control algorithms; and control using specialized controllers with a high degree of integration. The first option includes a hardware solution in which a microcontroller or programmable logic integrated circuit [9] directly controls the driver of phase switching field-effect transistors. The second option uses a bundle of a general-purpose microcontroller and a specialized controller for brushless motor control.[1,2]

The use of specialized brushless motor controllers allows software development for the controller to be significantly simplified. This is because all algorithms are implemented in this product. The circuit design is also simplified. However, the disadvantages of this approach include: increased cost; increased size of the controller; and a lack of the necessary controllers for brushless motors produced in Russia.

---

[1] A4960: Sensorless BLDC Motor Driver. https://www.allegromicro.com/en/products/motor-drivers/bldc-drivers/a4960. Accessed October 27, 2023.

[2] MOTIX™ BLDC Motor Control Ics. https://www.infineon.com/cms/en/product/power/motor-control-ics/bldc-motor-control-ics/. Accessed October 27, 2023.

Based on the results of the analysis, the following list of requirements to be met by the control system was compiled:

- sensorless control of three-phase brushless motors (based on the back EMF measurement);
- full software control mode without the use of specialized intermediate controllers;
- the need to maintain a PWM control signal;
- the need to maintain digital control protocols: Dshot[3], Proshot[4], Multishot[5];
- the need to maintain digital telemetry protocols: KISS[6], Dshot;
- the need to maintain analog output for the total current indication;
- the possibility for implementation based on Russian elements;
- the possibility for implementation of control devices for one or four electric motors.

THEORETICAL BASES FOR PROGRAM CONTROL OF UAV BRUSHLESS ELECTRIC MOTOR CONTROLLERS

The solution consists of three stages: development of algorithms and methods for controlling motor rotation; development of algorithms and methods for processing control commands; and development of algorithms and methods for forming the telemetry data. The second and third items are variable. Their implementation depends on specific protocols, the description of which is in the public domain.[7] Therefore, most of the attention will be paid to the first stage.

The general principles and models of program control of UAV electric motors based on electronic speed controllers are well known [10]. However, the focus here is narrower and more specific. In order to resolve it, it is necessary to consider the principles of controlling the used electric motors.

Brushless motors with concentrated windings and permanent magnet rotors are most common in light and medium-sized UAVs with EPG. They exceed 90% of the number of AC in the range up to 5 kg due to their weight, low cost and ease of use. These motors in Russian-language sources are often referred to as thyratron motors. In English-language literature the term brushless direct current (BLDC) motor is usually used [11].

UAV BLDC motors are usually supplied with trapezoidal voltage. This leads to certain disadvantages: torque ripple; generation of impulse noise; increased noise; and a slight reduction of the efficiency coefficient. These can be partially eliminated by using other control methods (e.g., using sinusoidal voltage). However, this approach is not justified due to the significant increase in UAV complexity and cost. Torque ripple and a certain reduction in efficiency are not critical for the EPG of lightweight UAVs. Propeller noise significantly exceeds electric motor noise. Impulse noise is suppressed by hardware filtering and specialized software methods.

The structural diagram of the hardware-software control system of UAV BLDC electric motor taking into account the data under consideration is shown in Fig. 1.

The microcontroller unit (MCU) generates a control signal to the drivers (DRV) of the field-effect transistors of the motor winding commutation. Control signals are generated through flight controller commands and feedback data. The feedback consists of a low-pass filter and a comparator. The low-pass filter filters out impulse noise during switching of motor steps and elimination of the PWM signal component. The comparator is used to determine the threshold level of the feedback EMF at which the subroutine of transition to the next step is started.

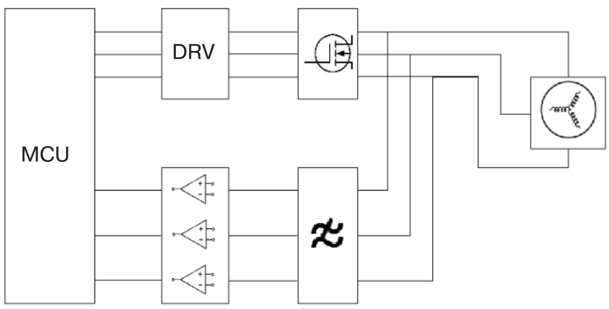

Fig. 1. Structural diagram of the hardware and software control system of the controller

Figure 2 shows a simplified view of the signals on the motor phases when the selected control methodology is used. The figure relates to a BLDC motor with one pair of poles, and shows one revolution. The solid line shows the ideal voltage change on each phase during one revolution. For example, phase A is energized with a positive polarity voltage for angle values up to 120°. Between 120° and 180°, phase A is disabled; while between 180° to 300°, the supplied power voltage has negative polarity.

The dashed line shows the back EMF, the shape of which is close to a trapezoid. When the supply voltage is

[3] DSHOT—the missing Handbook. https://brushlesswhoop.com/dshot-and-bidirectional-dshot/. Accessed October 27, 2023.

[4] Proshot—A new ESC protocol. https://oscarliang.com/proshot-esc-protocol/. Accessed October 27, 2023.

[5] What is Oneshot and Multishot in ESC. https://robu.in/what-is-oneshot-and-multishot-in-esc-difference-between-oneshot-and-multishot-esc-esc-calibration-protocol/. Accessed October 27, 2023.

[6] KISS ESC 32-bit series onewire telemetry protocol. https://www.rcgroups.com/forums/showatt.php?attachmentid=8524039&d=1450424877. Accessed October 27, 2023.

[7] Abdelrahman H. *Software Integration of Electronic Speed Controller* (*ESC*) *for an Unmanned Aerial Robot*: Bachelor Thesis. University of Twente. 2021. 23 p. https://essay.utwente.nl/87630/. Accessed October 27, 2023.

applied to the winding, the value of the back EMF is equal. When the winding is disconnected, it is formed as a result of generation. The design features of the motor require that the transition to the next step be performed at the moment when the back EMF crosses the zero mark [12].

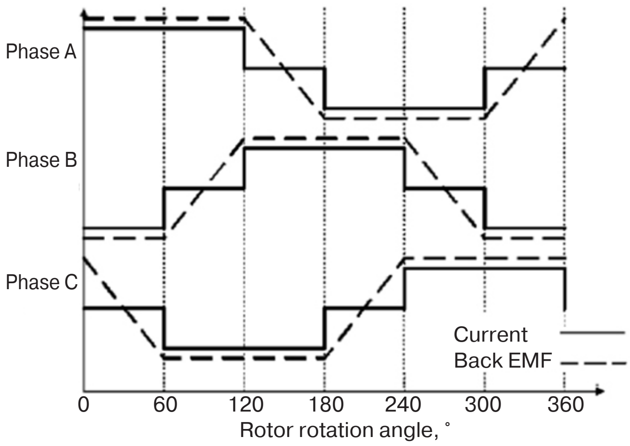

Fig. 2. Simplified view of signals on motor phases when using the selected control methodology

Thus, control based on back EMF allows for synchronous operation of the machine, while not determining rotation speed. The number of motor revolutions per minute is determined by the applied voltage and is calculated by the formula:

$$N = UK_{\mathrm{V}}k_{\mathrm{rm}}, \tag{1}$$

where U is the voltage on the windings, V; K_{V} is the speed factor, V^{-1} (shows the speed at which the motor will generate the back EMF of 1V); k_{rm} is the factor taking into account the peculiarities of the real electric machine (rm—real machine).

Thus, motor speed can be expressed through the switching frequency and the parameters of the electric machine:

$$N = \frac{n_{\mathrm{zc}}}{6n_{\mathrm{p}}}, \tag{2}$$

where n_{zc} is the number of zero crossings of the back EMF; n_{p} is the number of pole pairs of the electric motor.

However, transition to the next step is determined by back EMF. The number of revolutions is primarily dependent on voltage and motor design. Accordingly, the design determines the speed factor K_{V}.

The value of the resulting voltage on the windings is usually changed by means of PWM control. The design, which is currently under development, provides for a similar method of controlling rotation speed.

Figure 3 shows the oscillogram of the UAV BLDC motor during the operation. The signals in phases are close to the theoretical data as shown in Fig. 2. At the moment of active phase state, the PWM signal can be observed in the following figure.

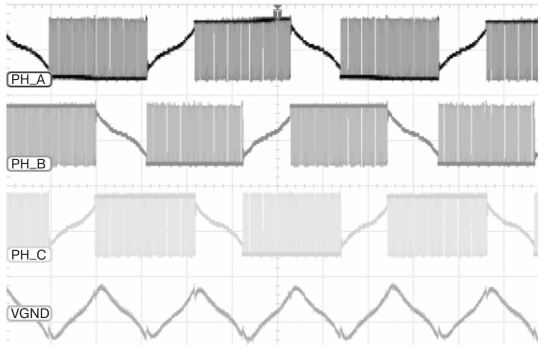

Fig. 3. Oscillograms of the AUV EPG operating BLDC motor. VGND is Virtual Ground

CONTROL SYSTEM ALGORITHMIZATION

Using theoretical research as a basis, we will formulate the methodology and control algorithms. A microcontroller was selected as a means of program control. Modern microcontrollers of sufficient power usually use architecture with hardware-level software abstraction [13, 14].

This approach provides a software tool structure which separates microcontroller hardware support from the core code that defines functionality.

Figure 4 shows the algorithm of the starting module of the control system proposed herein. After starting the program, device driver initialization functions are performed: I/O ports, timers, analog-to-digital converters (ADC), and others. Then the main block starts. This consists of an infinite loop of the microcontroller. In normal mode it is impossible to exit this block. Therefore, the error handler at the end of the block diagram can be executed only upon main block emergency termination. The driver initialization functions and the main block also have built-in error handlers. Their functionality is determined by the type of error and the place of its occurrence.

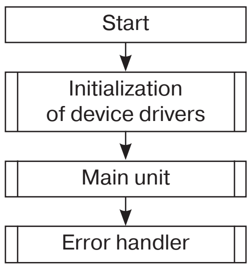

Fig. 4. Start module algorithm

Figure 5 shows the block diagram of the algorithm of the main module. It will be implemented as a separate file. The chosen architecture enhances security and emphasizes the abstraction of hardware from software implementation.

Fig. 5. Main module algorithm

Main module operation starts with device initialization and calibration. Here the ADC can be calibrated with subsequent start, start timers and direct memory access (DMA) controllers) in the specified mode. It configures the general-purpose ports and interrupts, as well as setting up and starting other devices. The sound and light signaling unit notifies the user of the successful start of the device operation. Next, the control protocol detection algorithm is started. The standards which are supported are set out in the Task Assignment section.

Before main cycle start, the settings are read out. The priority control protocol and rotation direction, as well as the normalization parameters of the control commands (if necessary) are stored in the flash memory.

The main cycle is an infinite microcontroller cycle. It executes the program code shown in Fig. 6. However, this functionality does not apply to the main motor control tasks. The main motor control tasks are not periodically time initiated, but related to hardware interrupts of the device.

The main cycle calculates the current speed and monitors the reverse command on a continuous basis. When a reverse command is received, it is displayed, and then memorized. The motor is stopped and the reverse flag for the switching function is set.

Also in the main cycle, the target speed is read by processing data from one of the control protocols

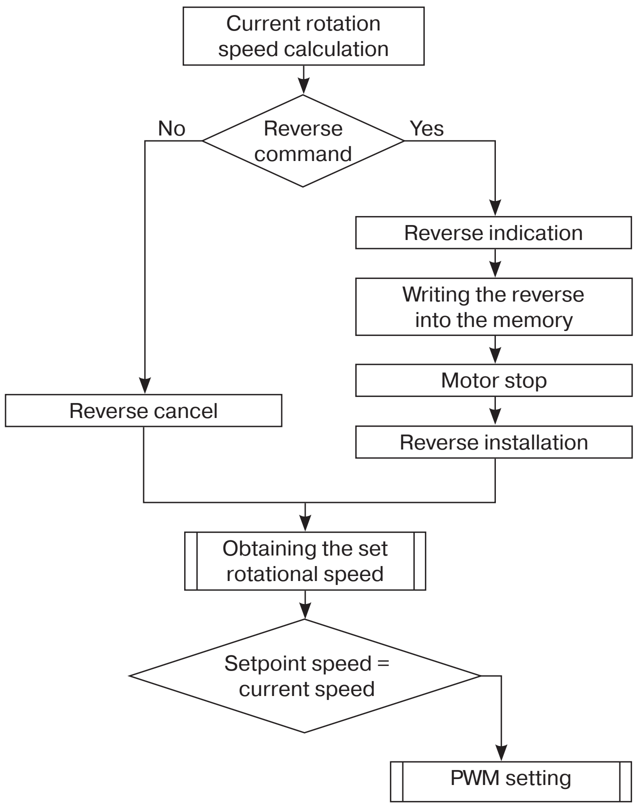

Fig. 6. Algorithm of the program main cycle

selected. If there is a difference between the current speed and the set speed, the phase voltage PWM control is set, in order to correct the speed.

The current speed is determined by measuring the frequency of interrupts. This corresponds to the zero crossing of the back EMF. The interrupt data processing functions initiate the winding switching program block.

Switching is performed according to the sequence shown in the table. The sequence of processes is shown in Fig. 2.

Table. Switching order of phases A, B, C

Step number	0	1	2	3	4	5
High level	A	B	B	C	C	A
Phase off	B	A	C	B	A	C
Low level	C	C	A	A	B	B

Block diagram of the switching algorithm is shown in Fig. 7. The phase for which one or another operation presented in the algorithm is performed differs at each switching step. The order of phase alternation is shown in the table and in Fig. 2.

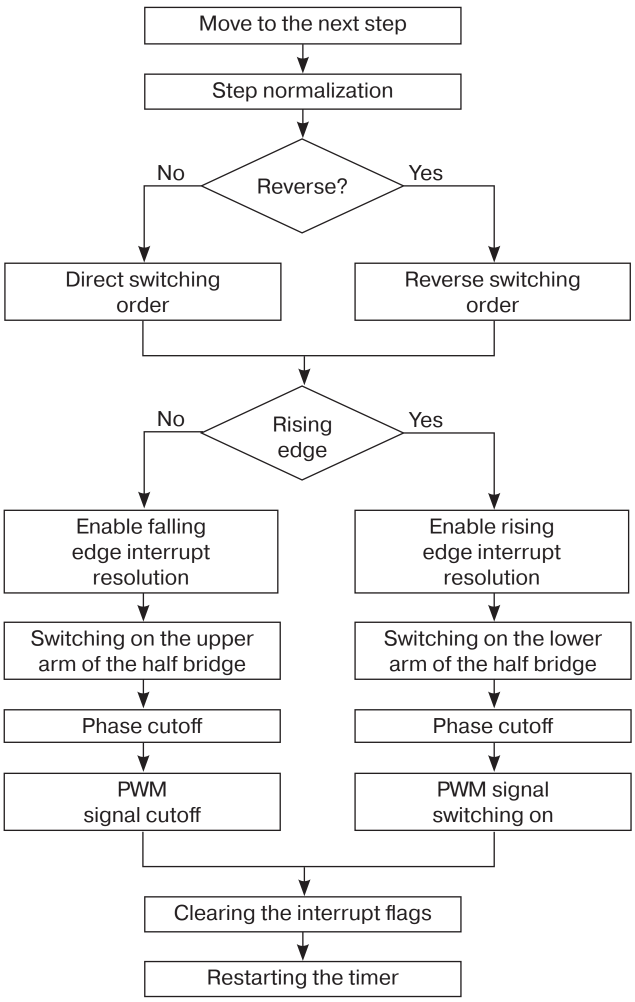

Fig. 7. Motor windings (phases) switching algorithm

The switching process is cyclic. It starts with switching to the next step. Step normalization is then performed (the step number is set to a value between 0 and 5). Switching is performed in forward or reverse sequence, depending on the state of the reverse flag.

The switching control function contains two branches which correspond to leading edge and trailing edge interrupts. When a rising edge interrupt is triggered, the corresponding interrupt is enabled. Then the lower key of the phase control half-bridge is turned on, the corresponding phase is switched off, and the DMA controller is turned on. This generates a PWM signal to control the motor phase voltage. In the event of a trailing edge interrupt, the sequence of operations is reversed.

When any of the branches of the branching operator are completed, the interrupt flags are cleared. Then the timer responsible for starting the motor is restarted.

The actual development has a significant number of additional program blocks, e.g., telemetry handling, error handling, and others. However, the scope of the current work does not allow them to be presented herein.

FORMALIZATION OF REQUIREMENTS TO THE APPLIED MICROCONTROLLERS

A microcontroller must be selected, in order to create the proposed control system. The development is invariant and therefore requires general criteria for the element base to be selected.

The microcontroller must have the required number of devices and ports, as well as to meet the performance requirements. Next, let us present a set of expressions describing the requirements for ports and devices.

The number of timer channels n_{tch} is determined by Eq. (3):

$$n_{\text{tch}} = 4n_{\text{mot}}, \tag{3}$$

where n_{mot} is the number of motors controlled by the controller.

Each motor needs to have 3 PWM signal outputs, in order to control the voltage on the winding. In modern microcontrollers, this functionality is allocated to timers. An additional timer channel is used to interpret the control protocols.

The number of general-purpose ports n_{Gpio} is defined by Eq. (4):

$$n_{\text{Gpio}} = 2 + 3n_{\text{mot}} + n_{\text{resGpio}}, \tag{4}$$

where n_{resGpio} is the number of redundant general purpose ports, index Gpio stands for General purpose input output.

Two general purpose ports are used to control the indicator and to set reverse. For each motor, 3 general purpose phase disconnect ports are required: one for each phase. A further intention is to allocate a number of ports for potential expansion of the functionality of the unit.

The number of interrupt lines n_{int} is calculated as one interrupt for each phase of each motor using Eq. (5):

$$n_{\mathrm{int}} = 3n_{\mathrm{mot}}. \tag{5}$$

At least two lines need to be considered for programming the microcontroller, two power supply lines, analog inputs for measuring battery current and voltage, and ADC output for analog telemetry output. Based on this, let us calculate the total number of microcontroller pins n_{pin}:

$$n_{\mathrm{pin}} = 9 + n_{\mathrm{tch}} + n_{\mathrm{Gpio}} + n_{\mathrm{int}} + n_{\mathrm{res}}, \tag{6}$$

where n_{res} is the number of additional redundant pins of the microcontroller.

Equation (6) can be represented by the number of motors:

$$n_{\mathrm{pin}} = 9 + 10n_{\mathrm{mot}} + n_{\mathrm{resCom}}, \tag{7}$$

with the total reserve n_{resCom}, including the reserve of general-purpose ports, taken into account as a reserve summand.

In order to select a satisfactory microcontroller, the performance parameters of the computational core and peripheral devices need to be correctly defined.

The minimum PWM frequency requirements for timers are defined by Eq. (8):

$$f_{\mathrm{pwm}} = 3Nn_{\mathrm{p}}k_{\mathrm{pwm}}, \tag{8}$$

where k_{pwm} is the coefficient determining the frequency parameters of PWM.

The constant factor 3 corresponds to three positive control pulses per revolution with one permanent magnet pole pair. k_{pwm} determines the number of PWM pulses per control pulse. The recommended value of $k_{\mathrm{pwm}} \geq 10$.

The value of f_{pwm} can be expressed through the parameters of the applied AC electric motors:

$$f_{\mathrm{pwm}} = 3UK_{\mathrm{V}}k_{\mathrm{rm}}n_{\mathrm{p}}k_{\mathrm{pwm}}. \tag{9}$$

Interrupt lines have requirements for minimum event response rates:

$$f_{\mathrm{int}} = 2Nn_{\mathrm{p}}. \tag{10}$$

The constant coefficient 2 is explained by two zero crossings of the back EMF per cycle at one pair of magnetic poles of the electric motor. Similarly to Eq. (9), Eq. (10) can be presented through the parameters of electric motors:

$$f_{\mathrm{int}} = 2UK_{\mathrm{V}}k_{\mathrm{rm}}n_{\mathrm{p}}. \tag{11}$$

Let us define the requirements for the microcontroller speed. In order to do this, the computing power required for individual modules needs to be summarized.

For program code executed in the body of an infinite loop of a microcontroller, the required computational performance P_{mc} is defined by Eq. (12):

$$P_{\mathrm{mc}} = f_{\mathrm{mc}}n_{\mathrm{mcInst}}, \tag{12}$$

where f_{mc} is the repetition rate of the infinite loop, n_{mcInst} is the average number of instructions per loop step.

The main volume of calculations is performed in interrupt handlers. Equations (13) and (14) allow the necessary computing power required for them to be calculated:

$$P_{\mathrm{int}} = 6n_{\mathrm{mot}}n_{\mathrm{p}}Nn_{\mathrm{intInst}}, \tag{13}$$

$$P_{\mathrm{int}} = 6n_{\mathrm{mot}}n_{\mathrm{p}}UK_{\mathrm{V}}k_{\mathrm{rm}}n_{\mathrm{intInst}}, \tag{14}$$

where n_{intInst} is the number of instructions to process the interrupt body (switch cycle).

The constant factor 6 is due to two interruptions for each of the three phases in one cycle for a motor with one pair of poles.

The sum of computing power for the applied microcontroller P_{Σ} is defined by Eq. (15):

$$P_{\Sigma} = f_{\mathrm{mc}}n_{\mathrm{mcInst}} + 6n_{\mathrm{mot}}n_{\mathrm{p}}UK_{\mathrm{V}}k_{\mathrm{rm}}n_{\mathrm{intInst}} + P_{\mathrm{add}} + P_{\mathrm{res}}, \tag{15}$$

where P_{add} is the computational power of additional modules, P_{res} is the reserve of computational power.

Computational power reserve should be at least 30% of the total value. For controllers with a small number of motors, this value is recommended to be increased.

EXPERIMENTAL STUDIES AND PRACTICAL RESULTS

Based on the methodology proposed herein, microcontrollers were selected to build controllers for one and four electric motors. For the first of them, the following minimum requirements were established: at least 22 pins, including 3 PWM lines and 3 interrupt lines. For the microcontroller of the four-motor controller, the corresponding parameters were: 55 pins, 12 PWM lines, and 12 interrupt lines.

The prototype software product developed pursuant to the algorithms considered herein, requires

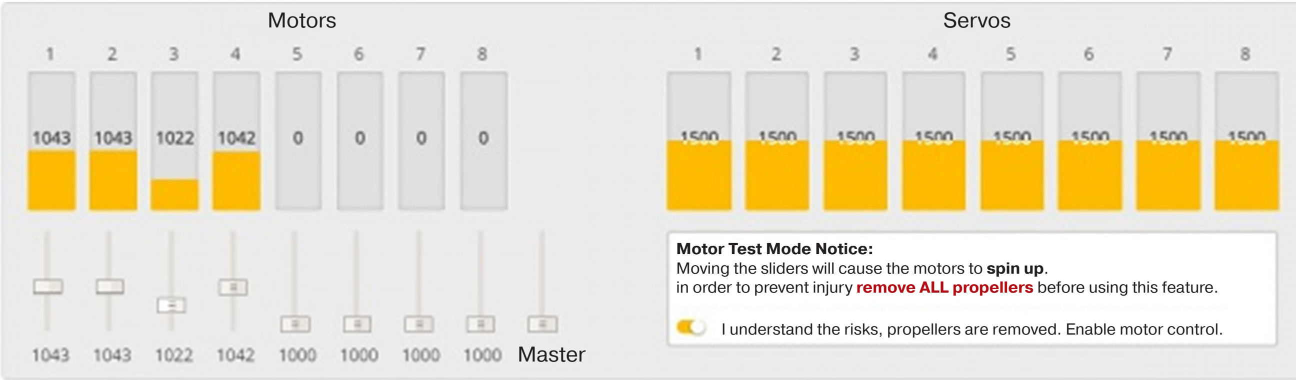

Fig. 8. Motor control in *BetaFlight*

a computational performance of not more than 20 DMIPS[8] for a single-motor controller and 75 DMIPS for a four-motor controller. The recommended microcontrollers need to have a performance rating of at least 30 and 100 DMIPS, respectively.

Other factors to be considered when selecting a microcontroller are its availability, as well as the inherent complexity of conducting development and electrical parameters. These factors are not considered in this paper. Given the complex combination of requirements, the STM32F103C8T6 microcontroller manufactured by STMicroelectronics, Switzerland, was used to build the first prototype of a single motor controller.

The maximum performance of this product is 90 DMIPS which exceeds the computing power requirements by several times. The requirements for peripherals and their number are similarly covered by the adopted device. With its low cost and wide availability, this choice can be considered optimal. However, STM32F103C8T6 pertains to the list of sanctioned products from non-friendly countries. Therefore, we considered alternative solutions.

The Russian 1921BK035[9] microcontroller produced by NIIET[10] was selected for the single-engine controller. The device is implemented on a 32-bit RISC core (reduced instruction set computer). It offers a performance rating of up to 100 DMIPS, and has all the necessary devices with the required parameters. This microcontroller theoretically allows us to produce a 2-motor controller.

It is proposed to build the four-motor speed controller on the basis of the K1921VK02T microcontroller from the same manufacturer. The device parameters significantly exceed those required (more than 200 DMIPS, 144 pins total).

The prototype controller assembled on STM32F103C8T6 was subjected to tests. For control purposes, digital protocols (Proshot, Dshot) and PWM signal operation were used. Control was performed by means of a *SpeedyBee F4 V3*[11] flight controller with *BetaFlight*[12] software installed. Rotation speed was set using the built-in configurator (Fig. 8). The Motors panel is used to control the rotation of the motors. The Servos panel is used to control the servos (not used in this work). The switch containing the information plate displayed in the lower right part of the figure authorizes the motors to turn on. The message asks you to confirm that the propellers have been removed and that you consent to the risks of enabling the motors.

A series of tests was used to rate the performance of the ESC controller. T-Motor Velox V2 V2207 1750KV BLDC motor (Feiying Technology, China) was used for load purposes. It is 5 inches in diameter and has an installed 4-inch pitch three-blade air propeller (Gemfan, China). It was powered by a 16.8V 4S battery (HRB, China).

Measurement of rotation speed was performed using a MEGEON™ 18005 (MEGEON, Russia) laser tachometer. Comparison of the results measured with the set values showed a difference of less than 5%.

During motor operation in cycles of 10 min, case heating did not exceed 70°C. The temperature of semiconductor components of the ESC controller was less than 80°C. The test object did not manifest any uncharacteristic sounds or other phenomena.

The phase signal oscillograms of the prototype controller are shown in Fig. 9. They indicate correct operation of the product. Insignificant delays of winding switching should, however, be noted. These delays will be eliminated in the future by making changes to the implementation of the commutation process algorithm.

[8] Dhrystone MIPS—standard for comparing microcontroller performance.

[9] 1921BK035: microcontroller with reduced overall dimensions with functions for electric drive control (in Russ.). https://niiet.ru/product/1921%D0%B2%D0%BA035. Accessed October 27, 2023.

[10] https://niiet.ru/ (in Russ.). Accessed October 13, 2023.

[11] SpeedyBee. https://www.speedybee.com/speedybee-f405-v3-bls-50a-30x30-fc-esc-stack/. Accessed October 13, 2023.

[12] Betaflight. https://www.betaflight.com. Accessed October 13, 2023.

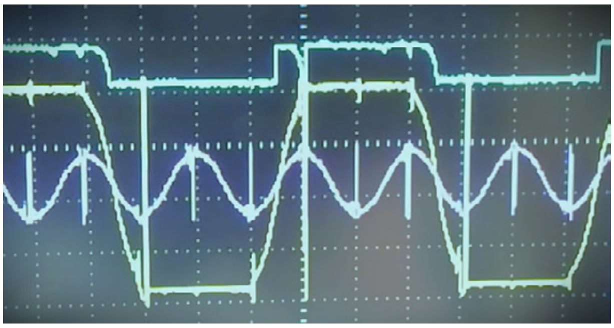

Fig. 9. Oscillograms obtained during the tests

CONCLUSIONS

In the development of in-house software for UAV BLDC motor controllers, invariant methods and algorithms are proposed to be used. They are based on the theoretical foundations of program control of this type of motor.

A methodology for defining the necessary microcontroller parameters for building a controller with the required characteristics was developed. This methodology prevents errors and optimizes microcontroller choice.

The results presented herein were tested. The methodology and algorithms formed the basis for the software development for a rotational controller prototype for a single UAV EPG engine. The test results provided a positive conclusion about the operability of the solution, and it was decided to continue its development. The main focus of further work will be to improve the software based on the algorithms considered in the article.

The testing process confirmed the suitability of the microcontroller selection method, according to the specified characteristics. The characteristics of peripheral devices fully correspond to operational ones. The calculated values of computing power differ from operational values by 10–15% upwards. Based on the results obtained, a positive conclusion can be made about the methodology presented in this paper.

ACKNOWLEDGMENTS

This work was financially supported by the Ministry of Science and Higher Education of the Russian Federation under the state assignment (project No. FZGM-2023-0011).

Authors' contribution. All authors equally contributed to the research work.

REFERENCES

1. Urazbakhtin R.R. Engines for unmanned aerial vehicles. *Mezhdunarodnyi nauchno-issledovatel'skii zhurnal = Int. Res. J.* 2017;2(56):142–144 (in Russ.). https://doi.org/10.23670/IRJ.2017.56.100
2. Yanturaev M.Yu., Mednov A.A. Electric motors of aircraft. In: *Elektrodvigateli letatel'nykh apparatov. Aktual'nye voprosy energetiki v APK: materialy vserossiiskoi (natsional'noi) nauchno-prakticheskoi konferentsii* (*Current Issues of Energy in the Agro-Industrial Complex: Materials of the All-Russian* (*National*) *Scientific and Practical Conference*). Blagoveshchensk: Dal'nevostochnyi gosudarstvennyi agrarnyi universitet; 2021. P. 106–113 (in Russ.).
3. Yuzawa N., Sakai K. A Permanent Magnet Motor Capable of Pole Changing for Variable Speed Drive. In: *International Conference on Electrical Machines and Systems* (*ICEMS*). 2013. P. 1127–1132. https://doi.org/10.1109/ICEMS.2013.6754392
4. Nikitin A.O., Petrova A.R., Petrov R.V. Magnetoelectric control system of the brushless motor revs for drones. *Vestnik Novgorodskogo gosudarstvennogo universiteta = Vestnik of Yaroslav the Wise Novgorod State University.* 2017;7(105):26–31 (in Russ.).
5. Penkin V.T., Sukhov D.V., Shevtsov D.A., Shishov D.M. Sensorless controller of BLDC motors with permanent magnets. *Prakticheskaya Silovaya Elektronika.* 2014;3(55):46–51 (in Russ.).
6. Wen J.-S., Wang C.-H., Chang Y.-D., Teng C.-C. Intelligent Control of High-Speed Sensorless Brushless DC Motor for Intelligent Automobiles. In: *2008 IEEE International Conference on Systems, Man and Cybernetics* (*IEEE/SMC*). 2008. P. 3394–3398. https://doi.org/10.1109/ICSMC.2008.4811822
7. Shtaev D.V. Analysis of control technology of unmanned aerial vehicles. *Territoriya novykh vozmozhnostei. Vestnik Vladivostokskogo gosudarstvennogo universiteta ekonomiki i servisa = The Territory of New Opportunities. The Herald of Vladivostok State University of Economics and Service*. 2019;2(11):113–119 (in Russ.). Available from URL: https://cyberleninka.ru/article/n/analiz-tehnologii-upravleniya-bespilotnymi-letatelnymi-apparatami
8. Bashkirov A.V., Ostroumov I.V., Sviridova I.V. Fundamentals of Error-Correcting Coding, Key Advantages, and Disadvantages of Decoding Algorithms. *Vestnik Voronezhskogo gosudarstvennogo tekhnicheskogo universiteta = Bulletin of Voronezh State Technical University*. 2012;8(2):20–22 (in Russ.).
9. Il'ushin S.A., Sharonov A.A., Kiselev V.V. Development of the control unit of the BLDC motor on the base of the programmable logic device. *Informacionno-izmeritel'nye i upravlyayushchie sistemy = J. Information-Measuring and Control Systems.* 2015;12(9):51–55 (in Russ.).
10. Sleptsov V.V., Afonin V.L., Ablaeva A.E., Dinh B. Development of an information measuring and control system for a quadrocopter. *Russ. Technol. J.* 2021;9(6):26–36 (in Russ.). https://doi.org/10.32362/2500-316X-2021-9-6-26-36
11. Kalachev Yu.N. *SimlnTech: modelirovanie v elektroprivode* (*SimInTech: Modeling in Electric Drives*). Moscow: DMK Press; 2019. 98 p. (in Russ.). ISBN 978-5-97060-766-4

12. Janpan I., Chaisricharoen R., Boonyanant P. Control of the Brushless DC Motor in Combine Mode. *Procedia Engineering.* 2012;32:279–285. https://doi.org/10.1016/j.proeng.2012.01.1268
13. Yiu J. *The Definitive Guide to ARM® Cortex®-M3 and Cortex®-M4 Processors*. London: Newnes; 2013. 864 p.
14. Pakdel M. *Advanced Programming with STM32 Microcontrollers.* Limbricht: Elektor; 2020. 216 p.

СПИСОК ЛИТЕРАТУРЫ

1. Уразбахтин Р.Р. Двигатели для беспилотных летательных аппаратов. *Международный научно-исследовательский журнал*. 2017;2(56):142–144. https://doi.org/10.23670/IRJ.2017.56.100
2. Янтураев М.Ю., Меднов А.А. Электродвигатели летательных аппаратов. В сб.: *Актуальные вопросы энергетики в АПК*: *материалы всероссийской (национальной) научно-практической конференции*. Благовещенск: Дальневосточный государственный аграрный университет; 2021. С. 106–113.
3. Yuzawa N., Sakai K. A Permanent Magnet Motor Capable of Pole Changing for Variable Speed Drive. In: *International Conference on Electrical Machines and Systems* (*ICEMS*). 2013. P. 1127–1132. https://doi.org/10.1109/ICEMS.2013.6754392
4. Никитин А.О., Петрова А.Р., Петров Р.В. Магнитоэлектрическая система управления оборотами бесколлекторного электродвигателя для беспилотных летательных аппаратов. *Вестник Новгородского государственного университета*. 2017;7(105):26–31.
5. Пенкин В.Т., Сухов Д.В., Шевцов Д.А., Шишов Д.М. Бездатчиковый регулятор бесколлекторного двигателя постоянного тока с постоянными магнитами на роторе. *Практическая силовая электроника*. 2014;3(55):46–51.
6. Wen J.-S., Wang C.-H., Chang Y.-D., Teng C.-C. Intelligent Control of High-Speed Sensorless Brushless DC Motor for Intelligent Automobiles. In: *2008 IEEE International Conference on Systems, Man and Cybernetics* (*IEEE/SMC*). 2008. P. 3394–3398. https://doi.org/10.1109/ICSMC.2008.4811822
7. Штаев Д.В. Анализ технологии управления беспилотными летательными аппаратами. *Территория новых возможностей. Вестник Владивостокского государственного университета экономики и сервиса*. 2019;11(2):113–119. URL: https://cyberleninka.ru/article/n/analiz-tehnologii-upravleniya-bespilotnymi-letatelnymi-apparatami
8. Башкиров А.В., Остроумов И.В., Свиридова И.В. Основы помехоустойчивого кодирования, основные преимущества и недостатки алгоритмов декодирования. *Вестник Воронежского государственного технического университета.* 2012;8(2):20–22.
9. Ильюшин С.А., Шаронов А.А., Киселев В.В. Разработка блока управления электродвигателем типа BLDC на базе ПЛИС. *Информационно-измерительные и управляющие системы*. 2015;13(9):51–55.
10. Слепцов В.В., Афонин В.Л., Аблаева А.Е., Динь Б.Ф. Разработка информационно-измерительной и управляющей системы квадрокоптера. *Russian Technological Journal*. 2021;9(6):26–36. https://doi.org/10.32362/2500-316X-2021-9-6-26-36
11. Калачёв Ю.Н. *SimlnTech: моделирование в электроприводе*. М.: ДМК Пресс; 2019. 98 с. ISBN 978-5-97060-766-4
12. Janpan I., Chaisricharoen R., Boonyanant P. Control of the Brushless DC Motor in Combine Mode. *Procedia Engineering.* 2012;32:279–285. https://doi.org/10.1016/j.proeng.2012.01.1268
13. Yiu J. *The Definitive Guide to ARM® Cortex®-M3 and Cortex®-M4 Processors*. London: Newnes; 2013. 864 p.
14. Pakdel M. *Advanced Programming with STM32 Microcontrollers.* Limbricht: Elektor; 2020. 216 p.

About the authors

Maksim V. Parinov, Cand. Sci. (Eng.), Associate Professor, Department of Computer-assisted Intelligent Design Technologies, Voronezh State Technical University (84, 20-letiya Oktyabrya ul., Voronezh, 394006 Russia). E-mail: parmax@mail.ru. RSCI SPIN-code 6411-5587, https://orcid.org/0000-0002-7427-5475

Aleksey N. Yurov, Cand. Sci. (Eng.), Associate Professor, Department of Computer-assisted Intelligent Design Technologies, Voronezh State Technical University (84, 20-letiya Oktyabrya ul., Voronezh, 394006 Russia). E-mail: yurovalex@mail.ru. RSCI SPIN-code 5828-0075, https://orcid.org/0009-0007-9320-7519

Yaroslav V. Skitskiy, Postgraduate Student, Department of Radio Apparatus Design and Engineering, Voronezh State Technical University (84, 20-letiya Oktyabrya ul., Voronezh, 394006 Russia). E-mail: nauchrab@mail.ru. https://orcid.org/0000-0001-5547-1940

Об авторах

Паринов Максим Викторович, к.т.н., доцент, кафедра компьютерных интеллектуальных технологий проектирования ФГБОУ ВО «Воронежский государственный технический университет» (34006, Россия, Воронеж, ул. 20-летия Октября, д. 84). E-mail: parmax@mail.ru. SPIN-код РИНЦ 6411-5587, https://orcid.org/0000-0002-7427-5475

Юров Алексей Николаевич, к.т.н., доцент, кафедра компьютерных интеллектуальных технологий проектирования ФГБОУ ВО «Воронежский государственный технический университет» (34006, Россия, Воронеж, ул. 20-летия Октября, д. 84). E-mail: yurovalex@mail.ru. SPIN-код РИНЦ 5828-0075, https://orcid.org/0009-0007-9320-7519

Скитский Ярослав Витальевич, аспирант, кафедра конструирования и проектирования радиоаппаратуры ФГБОУ ВО «Воронежский государственный технический университет» (34006, Россия, Воронеж, ул. 20-летия Октября, д. 84). E-mail: nauchrab@mail.ru. https://orcid.org/0000-0001-5547-1940

Translated from Russian into English by Lyudmila O. Bychkova
Edited for English language and spelling by Dr. David Mossop

Russian Technological Journal. 2024;12(1):92–100 ISSN 2500-316X (Online)

UDC 537.86, 621.37
https://doi.org/10.32362/2500-316X-2024-12-1-92-100

RESEARCH ARTICLE

Local spatial analysis of EEG signals using the Laplacian montage

Andrey A. Slezkin [1,2,@],
Svetlana P. Stepina [3],
Namik G. Gusein-zade [2,4]

[1] *Institute of Higher Nervous Activity and Neurophysiology, Russian Academy of Sciences, Moscow, 117485 Russia*
[2] *MIREA – Russian Technological University, Moscow, 119454 Russia*
[3] *Patrice Lumumba Peoples' Friendship University of Russia (RUDN university), Moscow, 117198 Russia*
[4] *Prokhorov General Physics Institute, Russian Academy of Sciences, Moscow, 119991 Russia*
[@] *Corresponding author, e-mail: com2274@yandex.ru*

Abstract
Objectives. One pressing problem when recording brain activity signals by electroencephalography (EEG) is the need to reduce the effect of interference (artifacts). This study presents a method for resolving this problem using the Laplace differential operator. The aim is to determine the number of electrodes included in the Laplacian montage, as well as to clarify the requirements for the geometric shape of their placement, in order to ensure the best quality of EEG signal processing.
Methods. The Laplacian montage method is based on the use of individual electrodes to determine the second derivative of the signal, proportional to the electric current at the corresponding point on the surface of the head. This approach allows the potential of neural activity of the source located in a small area limited by the electrode complex to be evaluated. By using a small number of equidistant electrodes placed around the target electrode, the Laplacian montage can produce a significantly higher quality signal from the area under the electrode complex.
Results. Among all the methods for constructing the Laplacian montage discussed in the article, a complex consisting of 16 + 1 electrodes was shown to be preferable. The choice of the 16 + 1 scheme was determined by the best compromise between the quality of EEG signal processing and the complexity of manufacturing the electrode complex with given geometric parameters. The quality assessment was carried out by simulating the interference signal which allowed the correctness of the choice of installation design to be evaluated.
Conclusions. The use of the Laplacian montage method can significantly reduce the effect of artifacts. The proposed montage scheme ensures a good suppression of interference signals, the sources of which are located far beyond the projection of the electrode complex. However, not all interference arising from sources deep inside the brain, can be effectively suppressed using the Laplacian montage scheme alone.

Keywords: electroencephalography, EEG signals, artifact, reference montage, Laplacian montage, electrode placement scheme, electrode complex

• **Submitted:** 26.05.2023 • **Revised:** 13.09.2023 • **Accepted:** 05.12.2023

For citation: Slezkin A.A., Stepina S.P., Gusein-zade N.G. Local spatial analysis of EEG signals using the Laplacian montage. *Russ. Technol. J.* 2024;12(1):92–100. https://doi.org/10.32362/2500-316X-2024-12-1-92-100

Financial disclosure: The authors have no a financial or property interest in any material or method mentioned.

The authors declare no conflicts of interest.

НАУЧНАЯ СТАТЬЯ

Локальный пространственный анализ ЭЭГ-сигналов с помощью лапласиановского монтажа

А.А. Слезкин [1, 2, @],
С.П. Степина [3],
Н.Г. Гусейн-заде [2, 4]

[1] *Институт высшей нервной деятельности и нейрофизиологии, Российская академия наук, Москва, 117485 Россия*
[2] *МИРЭА – Российский технологический университет, Москва, 119454 Россия*
[3] *Российский университет дружбы народов, Москва, 117198 Россия*
[4] *Институт общей физики им. А.М. Прохорова, Российская академия наук, Москва, 119991 Россия*
[@] *Автор для переписки, e-mail: com2274@yandex.ru*

Резюме
Цели. Одной из актуальных задач, возникающих при регистрации сигналов мозговой активности с помощью электроэнцефалографии (ЭЭГ), является уменьшение влияния помех (артефактов). В данном исследовании рассматривается один из способов решения данной задачи с помощью дифференциального оператора Лапласа. Цель работы – определение количества электродов, входящих в лапласиановский монтаж, а также выяснение требований к геометрической форме их расположения для обеспечения наилучшего качества обработки сигналов ЭЭГ.
Методы. Метод лапласиановского монтажа основывается на использовании отдельных электродов для определения второй производной сигнала, которая пропорциональна электрическому току в соответствующей точке поверхности головы. Этот подход позволяет оценить потенциал нейронной активности источника, находящегося в малой области, ограниченной комплексом электродов. При использовании небольшого количества равноудаленных электродов вокруг целевого электрода при лапласиановском монтаже удается получить значительно более качественный сигнал из области, находящейся под электродным комплексом.
Результаты. Для всех рассмотренных в статье способов построения лапласиановского монтажа, было показано, что комплекс, состоящий из 16 + 1 отдельных электродов, является наиболее предпочтительным для использования. Выбор схемы 16 + 1 обусловлен наилучшим компромиссом между качеством обработки сигналов ЭЭГ и сложностью изготовления электродного комплекса при заданных геометрических параметрах. Оценка качества проводилась моделированием сигнала помехи, с помощью чего удалось оценить правильность выбора схемы построения монтажа.
Выводы. Установлено, что применение метода лапласиановского монтажа способно значительно уменьшить влияние артефактов. С помощью предложенной схемы монтажа обеспечивается высокий уровень подавления помеховых сигналов, источники которых находятся далеко за пределами проекции электродного комплекса. Однако не все помехи, источники которых лежат в глубине мозга, могут быть эффективно подавлены с помощью одной лишь схемы лапласиановского монтажа. Необходимо использовать различные цифровые методы обработки сигналов, учитывающие их статистические свойства.

Ключевые слова: электроэнцефалография, ЭЭГ-сигналы, артефакт, референтный монтаж, лапласиановский монтаж, схема наложения электродов, электродный комплекс

• **Поступила:** 26.05.2023 • **Доработана:** 13.09.2023 • **Принята к опубликованию:** 05.12.2023

Для цитирования: Слезкин А.А., Степина С.П., Гусейн-заде Н.Г. Локальный пространственный анализ ЭЭГ-сигналов с помощью лапласиановского монтажа. *Russ. Technol. J.* 2024;12(1):92–100. https://doi.org/10.32362/2500-316X-2024-12-1-92-100

Прозрачность финансовой деятельности: Авторы не имеют финансовой заинтересованности в представленных материалах или методах.

Авторы заявляют об отсутствии конфликта интересов.

INTRODUCTION

Electroencephalography (EEG) is one of the most common methods for studying the electrical activity of the brain which helps to determine the functional state of the brain. When registering electrical potentials on the surface of the head, the useful signal is often noisy due to artifacts of various nature. In order to obtain adequate information about the functioning of brain structures, various radiophysical methods are used. These consist of hardware and are based on approaches known from signal processing theory and statistical radiophysics.

Hardware methods for improving the quality of the EEG signal are primarily based on the use of new types of electrodes, as well as electrode montage and arrangement schemes. A lead montage is a system of connections between electrodes, the most common of which are described in the review [1]. The number of electrodes included in the montage can vary from 2 to 20 depending on the purpose of recording. The use of different types of montage in EEG studies allows more accurate data on the electrical activity of the brain to be obtained, as well as specific electrical events which may be important for the diagnosis and treatment of various diseases [2]. There are variants of montage, some of which will be described below.

Monopolar montage in which the potential difference between one electrode and a reference point (usually located behind the ear) is recorded. ***Bipolar montage*** records the potential difference between two electrodes located on neighboring areas of the head. In the case of ***monophasic montage***, only positive or only negative half-waves of the EEG signal are recorded. This type of montage is used to detect specific electrical events such as misalignment or synchronization between different areas of the brain.

Reference montage uses an additional electrode located away from the brain regions of interest. The total electrical activity recorded with this additional electrode helps to account for the effects of artifacts arising, for example, from eye movements or muscle activity (particularly facial muscles).

The purpose of using the reference montage is to record the EEG signal without the influence of interfering sources and noise, i.e., in relation to an electrically neutral electrode. However, due to the conductivity of biological tissues, it is impossible to place on the surface of the head a reference electrode which retains electrical neutrality. In theory, this condition is met at an infinite distance from the source. In the 1950s. [3], a method known as the ***common average reference montage*** was developed. In this method, electrode potentials are measured relative to a common average reference, i.e., the potential obtained by averaging the values recorded from all electrodes. With random signals at all electrodes, the average potential, i.e., the potential of the common reference electrode, would be zero. However, the activity of neuronal ensembles is spatially distributed quite widely, and the signals at the electrodes are not independent. In order to address this problem, ***local averaged reference montage*** was developed, in which a small number of electrodes near the target electrode are used to compute a complex reference. There are several types of averaged reference montage—Laplacian, Lemos, and Hjorth montages [4, 5].

LAPLACIAN REFERENCE MONTAGE

In the present work, the Laplacian local averaged reference montage will be used. This is based on the fact that the second spatial derivative of EEG signals is proportional to the electric current in the corresponding point of the head surface. This allows the value of the underlying neural activity source potential to be estimated.

The potential field gradient at any given electrode is calculated by measuring the difference between the voltage at the electrode of interest and the voltage of each of its nearest neighbors. If the potential field gradient at an electrode is calculated, there is no need for a common reference comparison electrode.

The currently used modification of the Laplacian montage for surface potentials was developed under the assumption of homogeneous cortical conductivity [2]. In this method, the second spatial derivative of the potential field is defined by the electric current perpendicular to the cortical surface.

There are a number of limitations associated with the Laplacian montage. The accuracy with which this montage represents the signal strongly depends on the interelectrode distance. In the first Laplacian scheme, no additional electrodes were used, and only the standard EEG electrode arrangement scheme was used. In this method, data from the nearest 8 grid electrodes was used to obtain the value of the local averaged reference electrode (for lead C4, for example) (Fig. 1). The general idea of the montage is based on the fact that the target electrode, at which the resulting signal is determined, is assigned a weight of +1. The other electrodes are assigned weights based on their distances from the target electrode location, such that each weight is proportional to the inverse of the distance squared and scaled such that the sum of these weights equals −1. Thus, the sum of all weights is zero, which makes the differential operation indifferent to the choice of the reference electrode location [4].

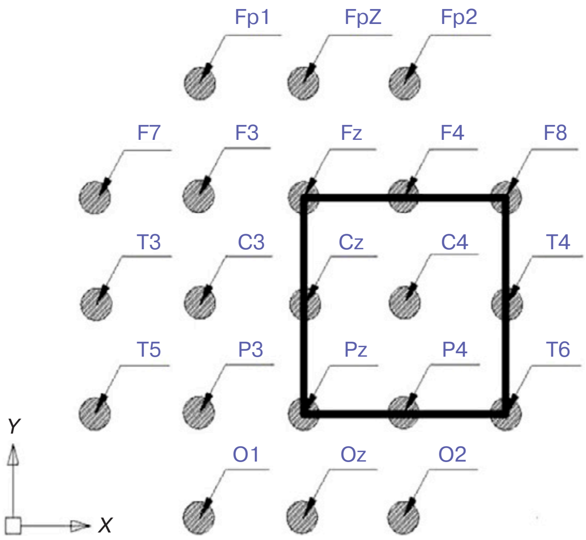

Fig. 1. Display of the EEG 10–20 electrode placement scheme on the plane

The following formula [1] is used to obtain the electrode C4 value using a locally averaged reference electrode:

$$C4 = (Fz + F4 + F8 + Cz + T4 + Pz + P4 + T6)/8. \quad (1)$$

This scheme works relatively well for medial and central electrodes in standard EEG circuits. However, the fulfillment of these assumptions is rather problematic with regard to peripheral electrodes. In this case, weighting coefficients are introduced for edge electrodes, for example, the formula [2] is taken for T3:

$$T3 = (2 \cdot F7 + 2 \cdot T5 + C3)/5. \quad (2)$$

This Laplacian scheme, as can be seen, uses data from electrodes located at different distances from the center electrode which may require the selection of weights for them and introduces distortions in the resulting signal.

Another way of constructing a Laplacian montage is to use solid electrically conductive concentric rings as electrodes (Fig. 2), as presented in [6, 7].

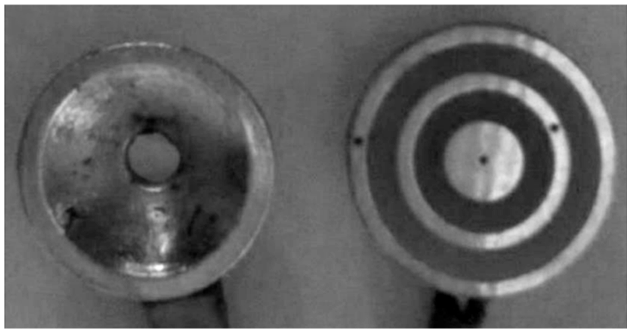

(a) (b)

Fig. 2. Conventional electrode (a) and tripolar electrode (b) consisting of three concentric rings (photo from [2])

This method has its advantages and disadvantages in use. For example, with best signal accuracy, it is quite difficult to ensure a uniform fit of the ring to the scalp. This ring montage cannot be converted to a different signal processing scheme, as opposed to a montage based on individual electrodes.

In addition, an EEG signal whose source is not a point, but a scalp, scattered (diffuse) electric charge will also be distorted when processed by Laplacian. Laplacian is best suited for working with relatively focal sources, i.e., concentrated in a small area compared to the size of the electrode complex included in the montage [8].

Our choice in favor of the ring shape of the electrode complex consisting of individual electrodes was determined by consideration of the computational problems of the Laplacian method associated with different electrode configurations and interelectrode distances [9], as well as the problem of ensuring uniform adherence of electrodes to the scalp. For such a shape, the finite difference method is the simplest way of signal processing. As will be shown below, when using a small number of equidistant electrodes around the target electrode in the Laplacian montage, a much better signal from the area under the electrode complex may be obtained.

(16 + 1)-ELECTRODE LAPLACIAN MONTAGE SCHEME

In the scheme (Fig. 3) of the (16 + 1)-electrode Laplacian Montage, as proposed by the authors, the distance from the circle on which the peripheral electrodes of the complex are located to the central electrode was 25 mm. This corresponds approximately to the average interelectrode distance for the 10–20 EEG overlay scheme. A diameter of 50 mm was determined

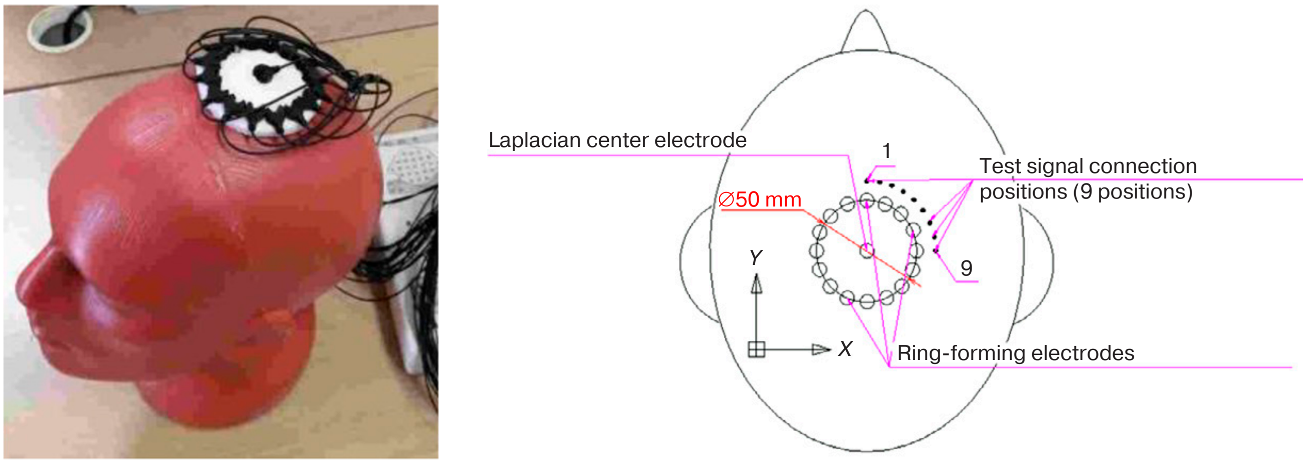

(a) (b)

Fig. 3. Montage scheme of the (16 + 1)-electrode complex: (a) picture of a dummy head with a set of electrodes, implementing the Laplacian montage; (b) sketch of the electrode complex (top view)

based on the area under the electrode complex required to analyze the cortical structures of interest. Taking into account the size of a single electrode, the total number of electrodes placed on a circle of this diameter was $N = 16$.

The most convenient location of the (16 + 1)-electrode complex to study the properties and to illustrate the operation of the Laplacian assembly is the sensorimotor area of the cerebral cortex. The location of the electrode complex is a relatively flat surface in this region of the head and corresponds to the lead Cz in the standard scheme of electrode placement 10–20.

For such Laplacian montage, the value of the resulting S_{lap} signal with respect to the local averaged reference electrode is calculated using the following formula:

$$S_{\text{lap}} = \frac{1}{N}\sum_{i=1}^{N}(S_0 - S_i), \qquad (3)$$

where S_0 is the signal at the central electrode of the Laplacian; S_i are the signals at the electrodes included in the ring complex; N is the number of electrodes included in the ring complex.

EXPERIMENTAL SCHEME

In order to understand the processes of information acquisition and processing performed by the brain, the initial shape of the signal arising in the source of interest in the brain's neural activity needs to be known. However, the presence of many activity centers in the human brain does not allow the shape of the signal to be described with a given accuracy. In order to clarify the result of the multi-electrode complex, an interfering test signal was used which was transmitted to different points of the scalp surface (Fig. 3), after which the potentials of this signal on all electrodes of the complex was measured. The source of the test signal in the experiment was a generator of sinusoidal oscillations with an amplitude of 50 mV and a frequency of 130 Hz. The Laplacian method for (4 + 1), (8 + 1), and (16 + 1)-electrode ring montages was used to process the potentials. In EEG measurement, this test signal is an interfering signal. The application of the Laplacian should reduce, and ideally completely suppress, this interfering signal. We will evaluate the effectiveness of a particular montage by comparing the power attenuation coefficients of the signal source external to the perimeter of the electrode complex. Thus, we can experimentally determine the number of N electrodes included in the $(N + 1)$-electrode mounting scheme at which the interfering signal is effectively suppressed, and the mounting is not hindered.

A generator signal was sequentially applied to the scalp (9 positions) located at a distance of 40 mm from the central electrode of the complex (Fig. 3). These 9 points are located at a distance of 1/8 quarter of the circumference length from each other. In the monopolar withdrawal mode, the amplitude of the signal recorded at the center electrode was 40 mV in all cases. The signals obtained by the Laplacian method for all three types of mounting considered (4 + 1, 8 + 1, and 16 + 1) are shown in Fig. 4 and have different amplitudes, different from zero.

The ratio of signal powers at the central electrode to the signal power obtained using the Laplacian was calculated by the formula:

$$R_{\text{m}} = \frac{\sum_{t=0}^{T} x_{S_0\_\text{pos}}(t)^2}{\sum_{t=0}^{T} x_{\text{lap}\_\text{m}\_\text{pos}}(t)^2}, \qquad (4)$$

where R_m is the power ratio for the Laplacian of type m; m is the type of Laplacian (4 + 1, 8 + 1, or 16 + 1); $x_{\text{lap\_m\_pos}}$ is the amplitude of signal samples after processing by the Laplacian of type m for the electrode position of the test signal generator pos; $x_{S_0\_\mathrm{pos}}$ is the amplitude of signal samples at the center electrode of the Laplacian for the position of the test signal generator electrode pos; T is the total signal recording time.

Figure 5 shows that increasing the number of electrodes in the ring from 4 to 16 contributes to better attenuation of interference signals. However, the characteristics obtained with (8 + 1) and (16 + 1)-electrode montages are already very close. A further increase in the number of electrodes in the ring complex to more than 16 can be considered inexpedient, since it will not lead to a significant improvement of the signal. However, it will unnecessarily complicate the montage scheme [10].

APPLICATION OF THE (16 + 1)-ELECTRODE MONTAGE AND DISCUSSION ON THE RESULTS

The main objective of the proposed Laplacian montage is to suppress EEG artifacts which may distort the structure of the electroencephalographic signal. Such interference includes, for example, oculographic and myographic artifacts associated with eye movements and muscle work at the moment of EEG recording. Figure 6 shows the effect of such interferences on the signal recorded on the lead (electrode) Cz in the standard scheme 10–20.

When using a multi-electrode (16 + 1) Laplacian montage in this case, oculographic interference (from

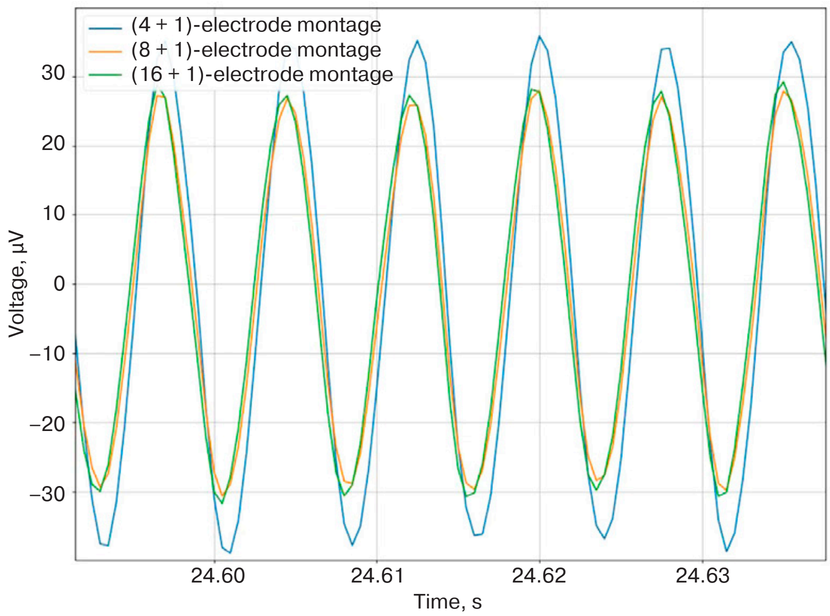

Fig. 4. Fragment of the result of test signal processing by Laplacian montages

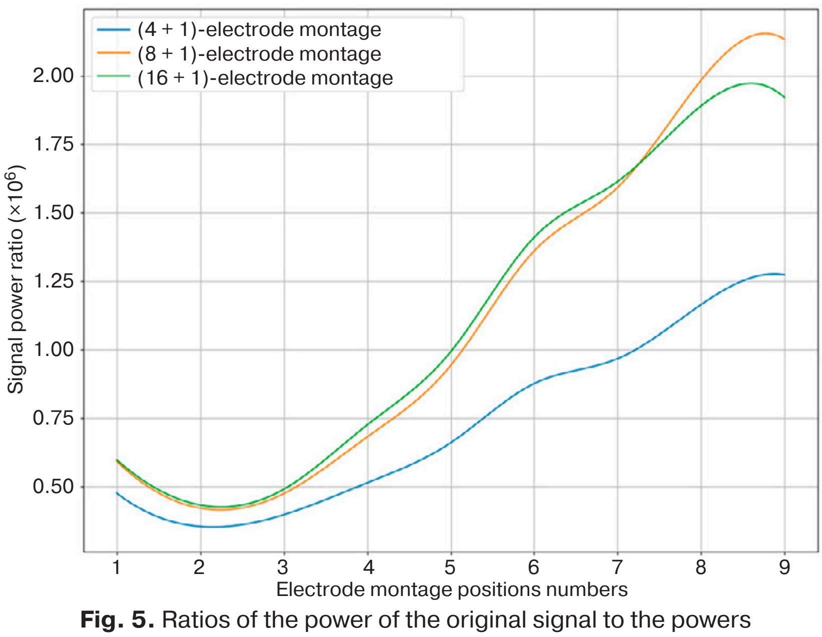

Fig. 5. Ratios of the power of the original signal to the powers of the signals obtained by Laplacian montage

eye blinking) has been almost completely leveled out (Fig. 7a).

The disadvantages of Laplacian montage of any configuration include the fact that it processes signals of neural activity sources located not only on the surface of the head, but also inside the brain volume. Consequently, if a source of interference/artifacts falls within the projection of the electrode complex, it is difficult to reduce it by Laplacian, as can be seen in Fig. 7b. In this case, the ring electrode complex is installed in the temporal region (lead T3). Therefore, the source of oculographic artifacts/interference (from eye blinking) falls in the projection of the Laplacian. In this case, inversion occurs in addition to a slight attenuation of the signal. It is not possible to eliminate interference in such a case. This is also true for another type of artifacts: myographic artifacts. They have a diffuse nature, and in the event of hitting the projection of the electrode complex, they cannot be completely suppressed either.

In order to counteract this phenomenon, other processing methods [11, 12] need to be used, including those not related to the types of electrode mounting [13]. A range of digital signal processing methods need to be used which take into account their statistical properties [14–16]. Since the artifact signal and the signal of interest related to neural activity are of different nature, they are uncorrelated. This allows statistical filtering methods to be used, such as Wiener filter and similar methods in order to separate them.

CONCLUSIONS

The studies confirmed the assumption that the applied Laplacian assembly provides good suppression of interference signals whose sources are far beyond the projection of the electrode complex. However, not all interference signals from sources deep in the brain, can be effectively suppressed with the help of the Laplacian montage scheme alone.

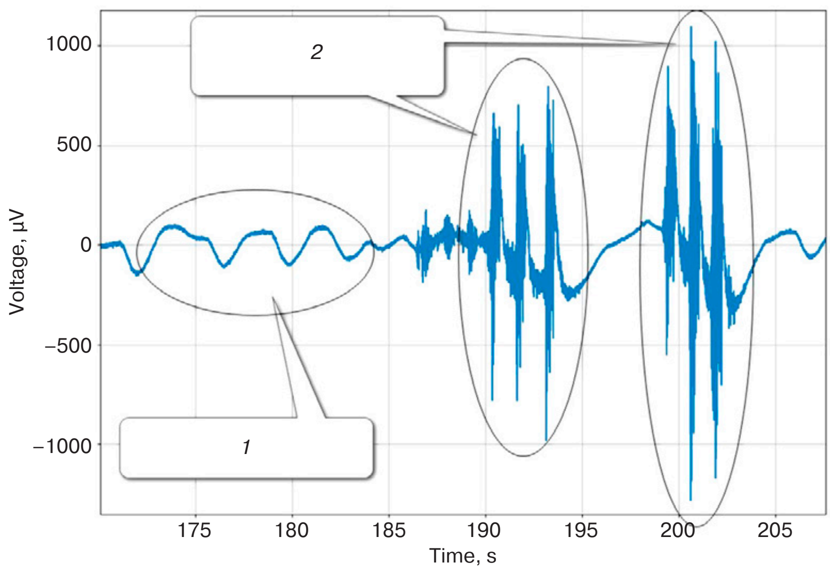

Fig. 6. Impact of the oculographic artifacts of blinking (*1*) and myographic artifacts of jaw muscle movements (*2*) on the EEG signal

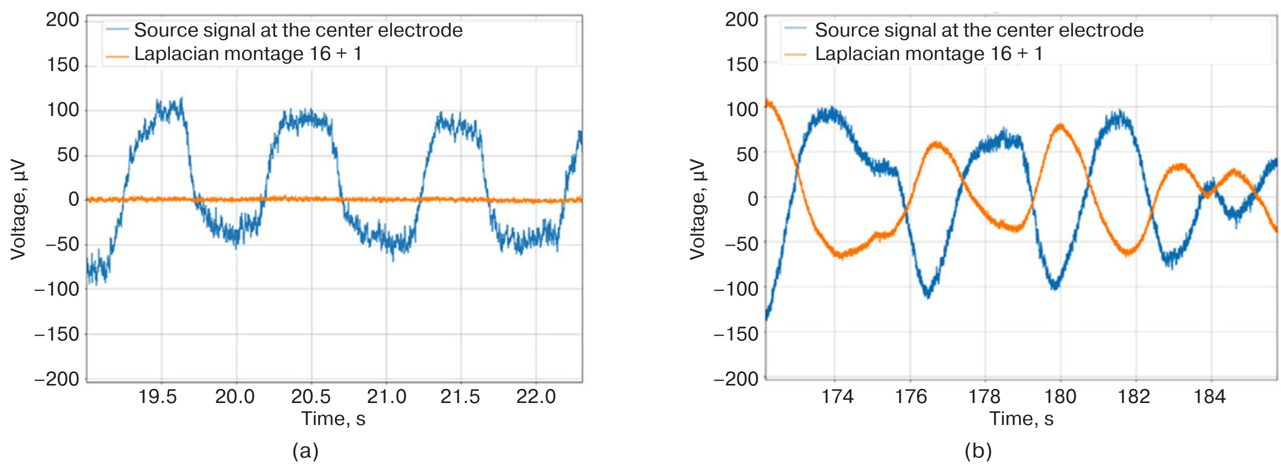

Fig. 7. Fragment of the signal noisy with oculographic artifacts and its corresponding fragment after Laplacian processing (16 + 1): (a) obtained in the parietal region Cz; (b) obtained in the temporal region (T3)

For all the methods of construction of the Laplacian montage considered in the article, in which the 4 + 1, 8 + 1, and 16 + 1 separate electrodes were used, the complex consisting of 16 + 1 electrodes is preferable. A further increase in the number of electrodes in the ring is inexpedient, since it will not lead to a significant improvement of the obtained signal but will unnecessarily complicate the mounting scheme. The choice of the 16 + 1 scheme is conditioned by the best compromise between the quality of EEG signal processing and the complexity of electrode complex manufacturing at the given geometrical parameters.

The use of the Laplacian montage method can significantly improve the quality of EEG signals and, therefore, increase accuracy when detecting various pathologies.

Authors' contributions

A.A. Slezkin—setting the problem, developing the design of the experiment, conducting the experiment, analyzing the results obtained, and formulating conclusions.

S.P. Stepina—conducting the experiment and writing the text of the article.

N.G. Gusein-zade—setting the problem, analyzing the results obtained, and formulating conclusions.

REFERENCES

1. Acharya J.N., Acharya V.J. Overview of EEG Montages and Principles of Localization. *J. Clin. Neurophysiol*. 2019;36(5): 325–329. https://doi.org/10.1097/wnp.0000000000000538
2. Tsuchimoto S., Shibusawa S., Iwama S., Hayashi M., Okuyama K., Mizuguchi N., Kato K., Ushiba J. Use of common average reference and large-Laplacian spatial-filters enhances EEG signal-to-noise ratios in intrinsic sensorimotor activity. *J. Neurosci. Methods*. 2021;353:109089. https://doi.org/10.1016/j.jneumeth.2021.109089
3. Gordon R., Rzempoluck E.J. Introduction to Laplacian Montages. *Am. J. Electroneurodiagnostic Technol*. 2004;44(2): 98–102. http://doi.org/10.1080/1086508X.2004.11079469
4. Hjorth B. An on-line transformation off EEG scalp potentials into orthogonal source derivations. *Electroencephalogr. Clin. Neurophysiol*. 1975;39(5):526–530. https://doi.org/10.1016/0013-4694(75)90056-5
5. Alzahrani S.I., Anderson C.W. A Comparison of Conventional and Tri-Polar EEG Electrodes for Decoding Real and Imaginary Finger Movements from One Hand. *Int. J. Neural. Syst*. 2021;31(9):2150036. https://doi.org/10.1142/s0129065721500362
6. Makeyev O., Ding Q., Besio W.G. Improving the accuracy of Laplacian estimation with novel multipolar concentric ring electrodes. *Measurement* (*Lond*). 2016;80:44–52. https://doi.org/10.1016/j.measurement.2015.11.017
7. Makeyev O. Solving the general inter-ring distances optimization problem for concentric ring electrodes to improve Laplacian estimation. *BioMed. Eng. OnLine.* 2018;17(1):117. https://doi.org/10.1186/s12938-018-0549-6
8. Dickey A.S., Alwaki A., Kheder A., Willie J.T., Drane D.L., Pedersen N.P. The Referential Montage Inadequately Localizes Corticocortical Evoked Potentials in Stereoelectroencephalography. *J. Clin. Neurophysiol*. 2022;39(5):412–418. https://doi.org/10.1097/wnp.0000000000000792
9. Carvalhaes C., de Barros J.A. The surface Laplacian technique in EEG: Theory and methods. *Int. J. Psychophysiol*. 2015;97(3):174–188. https://doi.org/10.1016/j.ijpsycho.2015.04.023
10. Greischar L.L., Burghy C.A., van Reekum C.M., Jackson D.C., Pizzagalli D.A., Mueller C., Davidson R.J. Effects of electrode density and electrolyte spreading in dense array electroencephalographic recording. *Clin. Neurophysiol*. 2004;115(3): 710–720. https://doi.org/10.1016/j.clinph.2003.10.028
11. Smith E.E., Bel-Bahar T.S., Kayser J. A systematic data-driven approach to analyze sensor-level EEG connectivity: Identifying robust phase-synchronized network components using surface Laplacian with spectral-spatial PCA. *Psychophysiology.* 2022;59(10):e14080. https://doi.org/10.1111/psyp.14080
12. Bufacchi R.J., Magri C., Novembre G., Iannetti G.D. Local spatial analysis: an easy-to-use adaptive spatial EEG filter. *J. Neurophysiol*. 2021;125(2):509–521. https://doi.org/10.1152/jn.00560.2019
13. Martin-Chinea K., Gomez-Gonzalez J.F., Acosta L. A New PLV-Spatial Filtering to Improve the Classification Performance in BCI Systems. *IEEE Trans. Neural. Syst. Rehabil. Eng*. 2022;30:2275–2282. https://doi.org/10.1109/tnsre.2022.3198021
14. Liu Q., Yang L., Zhang Z., Yang H., Zhang Y., Wu J. The Feature, Performance, and Prospect of Advanced Electrodes for Electroencephalogram. *Biosensors* (*Basel*). 2023;13(1):101. https://doi.org/10.3390/bios13010101
15. Ponomarev V.A., Pronina M.V., Kropotov Y.D. Dynamics of the EEG spectral density in the θ, α, and β bands in the visual *Go*/*NoGo* task. *Hum. Physiol.* 2017;43(4):366–376. https://doi.org/10.1134/S0362119717040132
[Original Russian Text: Ponomarev V.A., Pronina M.V., Kropotov Y.D. Dynamics of the EEG spectral density in the Theta, Alpha and Beta bands in the visual Go/NoGo task. *Fiziologiya cheloveka.* 2017;43(4):13–24 (in Russ.). https://doi.org/10.7868/S0131164617040130]
16. Poller B.V., Shchetinin Y.I., Orlov I.S. Adaptive digital filtering of signals in the systems of analysis of the electroencephalogram. *Nauchnyi vestnik Novosibirskogo gosudarstvennogo tekhnicheskogo universiteta = Scientific Bulletin of NSTU.* 2013;1(50):31–38 (in Russ.). https://elibrary.ru/PWURSR

About the authors

Andrey A. Slezkin, Engineer, Laboratory of General and Clinical Neurophysiology, Institute of Higher Nervous Activity and Neurophysiology of the Russian Academy of Sciences (5A, Butlerova ul., Moscow, 117485 Russia); Postgraduate Student, Department of Modeling of Radiophysical Processes, Institute of Radio Electronics and Informatics, MIREA – Russian Technological University (78, Vernadskogo pr., Moscow, 119454 Russia). E-mail: com2274@yandex.ru. http://orcid.org/0000-0003-1230-8347

Svetlana P. Stepina, Cand. Sci. (Phys.-Math.), Associate Professor, Scientific Educational Institute of Physical Research and Technology, Patrice Lumumba Peoples' Friendship University of Russia (RUDN University) (6, Miklukho-Maklaya ul., Moscow, 117198 Russia). E-mail: stepina_sp@pfur.ru. Scopus Author ID 8937542900, ResearcherID E-7025-2018, http://orcid.org/0000-0002-3900-0329

Namik G. Gusein-zade, Dr. Sci. (Phys.-Math.), Professor, Head of Department of Modeling of Radiophysical Processes, Institute of Radio Electronics and Informatics, MIREA – Russian Technological University (78, Vernadskogo pr., Moscow, 119454 Russia); Chief Researcher of Theoretical Department, Prokhorov General Physics Institute of the Russian Academy of Sciences (38, Vavilova ul., Moscow, 119991 Russia). E-mail: ngus@mail.ru. Scopus Author ID 6506825772, ResearcherID S-7407-2016, http://orcid.org/0000-0001-8000-1107

Об авторах

Слезкин Андрей Александрович, инженер, лаборатория общей и клинической нейрофизиологии ФГБУН «Институт высшей нервной деятельности и нейрофизиологии Российской академии наук» (117485, Москва, ул. Бутлерова, д. 5); аспирант, кафедра моделирования радиофизических процессов Института радиоэлектроники и информатики ФГБОУ ВО «МИРЭА – Российский технологический университет» (119454, Россия, Москва, пр-т Вернадского, д. 78). E-mail: com2274@yandex.ru. http://orcid.org/0000-0003-1230-8347

Степина Светлана Петровна, к.ф.-м.н., доцент, Научно-образовательный институт физических исследований и технологий ФГАОУ ВО «Российский университет дружбы народов им. Патриса Лумумбы» (РУДН) (117198, Россия, Москва, ул. Миклухо-Маклая, д. 6). E-mail: stepina_sp@pfur.ru. Scopus Author ID 8937542900, ResearcherID E-7025-2018, http://orcid.org/0000-0002-3900-0329

Гусейн-заде Намик Гусейнага оглы, д.ф.-м.н., профессор, заведующий кафедрой моделирования радиофизических процессов Института радиоэлектроники и информатики ФГБОУ ВО «МИРЭА – Российский технологический университет» (119454, Россия, Москва, пр-т Вернадского, д. 78); главный научный сотрудник теоретического отдела ФГБУН ФИЦ «Институт общей физики им. А.М. Прохорова Российской академии наук» (119991, Россия, Москва, ул. Вавилова, д. 38). E-mail: ngus@mail.ru. Scopus Author ID 6506825772, ResearcherID S-7407-2016, http://orcid.org/0000-0001-8000-1107

Translated from Russian into English by Lyudmila O. Bychkova
Edited for English language and spelling by Dr. David Mossop

Mathematical modeling

Математическое моделирование

UDC 330.4
https://doi.org/10.32362/2500-316X-2024-12-1-101-110

RESEARCH ARTICLE

Implementation of bagging in time series forecasting

Ian V. Gramovich,
Danila Yu. Musatov,
Denis A. Petrusevich @

MIREA – Russian Technological University, Moscow, 119454 Russia
@ Corresponding author, e-mail: petrusevich@mirea.ru, petrdenis@mail.ru

Abstract
Objectives. The purpose of the article is to build different models of bagging, to compare the accuracy of their forecasts for the test period against standard models, and to draw conclusions about the possibility of further use of the bagging technique in time series modeling.
Methods. This study examines the application of bagging to the random component of a time series formed after removing the trend and seasonal part. A bootstrapped series combining into a new random component is constructed. Based on the component thus obtained, a new model of the series is built. According to many authors, this approach allows the accuracy of the time series model to be improved by better estimating the distribution.
Results. The theoretical part summarizes the characteristics of the different bagging models. The difference between them comes down to the bias estimate obtained, since the measurements making up the bootstraps are not random. We present a computational experiment in which time series models are constructed using the index of monetary income of the population, the macroeconomic statistics of the Russian Federation, and the stock price of Sberbank. Forecasts for the test period obtained by standard, neural network and bagging-based models for some time series are compared in the computational experiment. In the simplest implementation, bagging showed results comparable to ARIMA and ETS standard models, while and slightly inferior to neural network models for seasonal series. In the case of non-seasonal series, the ARIMA and ETS standard models gave the best results, while bagging models gave close results. Both groups of models significantly surpassed the result of neural network models.
Conclusions. When using bagging, the best results are obtained when modeling seasonal time series. The quality of forecasts of seigniorage models is somewhat inferior to the quality of forecasts of neural network models, but is at the same level as that of standard ARIMA and ETS models. Bagging-based models should be used for time series modeling. Different functions over the values of the series when constructing bootstraps should be studied in future work.

Keywords: dynamic series, macroeconomic statistics, ARIMA, nonoverlapping block bootstrap (NBB), moving block bootstrap (MBB), stationary bagging (SB)

• **Submitted:** 21.06.2023 • **Revised:** 19.07.2023 • **Accepted:** 14.12.2023

For citation: Gramovich Ia.V., Musatov D.Yu., Petrusevich D.A. Implementation of bagging in time series forecasting. *Russ. Technol. J.* 2024;12(1):101–110. https://doi.org/10.32362/2500-316X-2024-12-1-101-110

Financial disclosure: The authors have no a financial or property interest in any material or method mentioned.

The authors declare no conflicts of interest.

НАУЧНАЯ СТАТЬЯ

Применение беггинга в прогнозировании временных рядов

Я.В. Грамович,
Д.Ю. Мусатов,
Д.А. Петрусевич @

МИРЭА – Российский технологический университет, Москва, 119454 Россия
@ *Автор для переписки, e-mail: petrusevich@mirea.ru, petrdenis@mail.ru*

Резюме

Цели. Цель работы состоит в построении различных моделей беггинга, сопоставлении точности их прогнозов на тестовый период со стандартными моделями и получении выводов о возможности дальнейшего использования техники беггинга при моделировании временных рядов.

Методы. Исследуется применение беггинга к случайной составляющей временного ряда, формируемой после удаления тренда и сезонной части. Строится серия псевдовыборок, совмещающихся в новую случайную составляющую. На основе полученной компоненты строится новая модель ряда. По мнению многих авторов такой подход позволяет повысить точность модели временного ряда, лучшим образом оценив распределение.

Результаты. В теоретической части приведены характеристики различных моделей беггинга. Разница между ними сводится к оценке смещения, получаемой из-за того, что измерения, которые составляют псевдовыборки, не являются случайными. Представлен вычислительный эксперимент, в котором модели временных рядов строятся по индексу денежных доходов населения макроэкономической статистики Российской Федерации и по курсу акций Сбербанка. Прогнозы на тестовый период, полученные стандартными, нейросетевыми моделями и моделями на основе беггинга для некоторых временных рядов, сравниваются в вычислительном эксперименте. В самой простой реализации беггинг показал результаты, сравнимые со стандартными моделями ARIMA и ETS и несколько уступающие нейросетевым моделям для сезонных рядов; для несезонных рядов лучшие результаты дали стандартные модели ARIMA и ETS, модели беггинга дали близкие результаты. Обе группы моделей существенно превзошли результат нейросетевых моделей.

Выводы. При использовании беггинга лучшие результаты получены при моделировании сезонных временных рядов. Качество прогнозов моделей беггинга несколько уступает качеству прогнозов нейросетевых моделей, но оказывается на том же уровне, что у стандартных моделей ARIMA и ETS. Модели на основе беггинга следует использовать для моделирования временных рядов, различные функции над значениями ряда при построении псевдовыборок должны быть исследованы в дальнейшей работе.

Ключевые слова: динамические ряды, макроэкономическая статистика, ARIMA, псевдовыборка неперекрывающихся блоков, псевдовыборка перекрывающихся блоков, стационарный беггинг

• **Поступила:** 21.06.2023 • **Доработана:** 19.07.2023 • **Принята к опубликованию:** 14.12.2023

Для цитирования: Грамович Я.В., Мусатов Д.Ю., Петрусевич Д.А. Применение беггинга в прогнозировании временных рядов. *Russ. Technol. J.* 2024;12(1):101–110. https://doi.org/10.32362/2500-316X-2024-12-1-101-110

Прозрачность финансовой деятельности: Авторы не имеют финансовой заинтересованности в представленных материалах или методах.

Авторы заявляют об отсутствии конфликта интересов.

INTRODUCTION

This work considers the application of bagging [1–5] in time series modeling. The use of bagging in time series modeling can be considered as an expression of the general idea of building a more accurate model based on several available models. The approach of making a weighted combination of forecasts of several time series models and averaging several forecasts is discussed in [6, 7]. The main difference between bagging and combining forecasts of time series models is that it combines only noise components. The main objective in both approaches is to improve the quality of forecasts on the basis of building a combination of forecasts of several time series models.

The approach under consideration is relevant due to the expediency of improving the accuracy of time series forecasting based on the best estimate of the distribution of the random component. The article contains new research results expressed in the experimental realization of models built on the basis of bagging of time series and comparison of forecasting results against results obtained using alternative ARIMA[1] and neural network models. The aim of the work is to build different bagging models, to compare the accuracy of their forecasts for the test period with standard models and to draw conclusions about the possibility of further use of the bagging method in time series modeling.

The time series is represented as a combination of three parts: seasonal component S_t, trend T_t, and noise R_t in additive or multiplicative form (index t stands for time):

$$y_t = S_t + T_t + R_t, \tag{1}$$

$$y_t = S_t \times T_t \times R_t. \tag{2}$$

Bagging is applied to the noise component R_t. This strategy was originally successfully applied in the classification task, where it involves building an ensemble model by training independent classifiers on different samples [8]. The predictions obtained by each model are then averaged, in order to obtain the final result (the weighted averaging can be applied depending on how accurate the predictions of each model participating in the ensemble are on the test sample). In this way, the forecasting accuracy is improved.

In addition to the idea of combining models, bagging is based on bootstrap. This approach consists in replacing the unknown distribution of data (characterizing the time process under consideration) with an empirical distribution constructed by the researcher. When using bootstrap in classification tasks, the data have no temporal dimension, so they can be mixed randomly. Things get more complicated when such ideas are applied to time series. In this case, the different sample values must follow each other according to the time dimension, even if chosen randomly. Here, the idea is transformed into constructing a set of bootstraps based on the original time series data. Several times in fact, (the number of patterns is specified by the user), based on a certain principle, values are selected from the series data to represent a new time sequence. Since there are usually many values of the time series, it is possible to build a set of new time series based on the original one, randomly selecting new values for each bootstrap. It is assumed that the characteristics of the time series under study will be close to the parameters of the resulting bootstraps.

CONSIDERED BAGGING METHODS

The approaches to obtaining bootstraps from the time series values are as follows:

1. Construction of bootstraps from nonoverlapping blocks (nonoverlapping block bootstrap, block bootstrap, circular bootstrap, NBB) [9, 10]. The time series data is divided into a given number of nonoverlapping blocks. The block length is a customizable parameter. When constructing bootstraps, each block can fall into any of them with some probability. For example, let us build blocks with the length of 3 elements from a row with 12 values: $X = \{X_1, \ldots, X_{12}\}$:

   $(X_1, X_2, X_3), (X_4, X_5, X_6), (X_7, X_8, X_9), (X_{10}, X_{11}, X_{12})$.

   When compiling a bootstrap, any blocks can be selected from them with return. If the length of the bootstrap is 12, you can take 4 blocks, e.g.:

   $(X_4, X_5, X_6), (X_1, X_2, X_3), (X_{10}, X_{11}, X_{12}), (X_4, X_5, X_6)$.

   Note that blocks can be repeated. The measurements in the bootstrap do not have to follow the same temporal order as the original data, so the stationarity of the original time series does not have to be preserved.
2. Constructing a bootstrap from overlapping blocks (moving block bootstrap, MBB) [11–13]. The blocks into which the time series data are divided can overlap. The block length is a customizable parameter. When constructing bootstraps, each block can fall into any block with some probability. In general, this case differs from the first, in that the blocks can overlap. The example from the previous paragraph can be transformed as follows:

[1] ARIMA is an autoregressive integrated moving average model or Box–Jenkins model.

$$(X_1, X_2, X_3), (X_3, X_4, X_5), (X_5, X_6, X_7), (X_7, X_8, X_9),$$
$$(X_9, X_{10}, X_{11}), (X_{10}, X_{11}, X_{12}).$$

Note that the beginning of each block (except for the first one) overlaps with the end of the previous block. The number of overlapping elements is, of course, adjustable. In general, further construction of the bootstrap follows point 1, so stationarity of the initial series, if any, does not guarantee stationarity of the bootstraps.

3. Constructing a stationary bootstrap [14]. This differs from the first two cases in that the researchers set the idea of preserving the stationarity property for the extracted bootstraps, provided that the original time series X is stationary. The length of the blocks is not fixed. Instead, a certain block termination probability p is given. The first element of the block X_i is selected randomly. Then each subsequent element either falls into the block with probability $1 - p$, or the block is terminated and a new one begins. The block lengths L_1, L_2, ... are subject to geometric distribution, so the probability of obtaining a block of length l:

$$p(L_j = l) = (1 - p)^{l-1} p.$$

The length L_j and initial position X_i of a block are set. We thus obtain the set of blocks $B_j(i, L_j) = \{X_1^*, X_2^*, ..., X_{L_j}^*\}$. Here the asterisk denotes that the values selected from the series do not have to form a continuous interval, but that the elements are selected following the initial element X_i of the bootstrap: $X_1^* = X_i$. Figure 1 schematically represents the process of selecting elements of the time series into the bootstrap when applying stationary bagging: X_i is the sequence of values of the time series, X_i^* is the bootstrap selected by bagging). Each subsequent element must be later than the previously selected element (X_{i+1}^* is always later than the moment corresponding to the element of the row X_i^*). That said, there may be gaps between them.

$$\begin{array}{cccc} X_1X_2\ldots & X_iX_{i+1} & X_{i+2}\ldots & X_{i+k}\ldots X_n \\ & \downarrow & \downarrow & \downarrow \\ & X_1^* & X_2^* & X_{L_j}^* \end{array}$$

Fig. 1. Example of selecting time series elements X into the bootstrap X^* when applying the stationary bagging (element X_{i+1}^* always comes later than the previously selected X_i^*)

The work [15] studies the selection of the optimal block length and concludes that the length should be proportional to the cube root of the length of the time series.

The present work also considers the fourth method which in many respects repeats stationary bagging. The main difference is the prohibition to use blocks (values in the next block could refer to an earlier time interval than the previous one). Instead, a single block is actually used, where each previous value refers to an earlier measurement than the next. Interpolation is used when it is necessary to align the length of the bootstrap with the length of the row.

In [16] the author compares methods by the bias of the expectation (which appears due to the fact that independent quantities cannot be extracted from the time process), while in [15] a simpler bias estimation for the mathematical expectation E and the dispersion V is suggested:

$$B(\hat{E}(b)) = \frac{A_1}{b} + \overline{o}\left(\frac{1}{b}\right),$$
$$B(\hat{V}(b)) = \frac{A_2}{b} + \overline{o}\left(\frac{1}{b}\right). \tag{3}$$

Here b is the block length in the bagging scheme. A_1, A_2 are constants, the calculation details of which are given in [16]. Thus, when considering first-order estimates, the different approaches to bagging remain theoretically identical.

The MBB (overlapping blocks) method has smaller second order moments compared to NBB (non-overlapping blocks) and stationary bagging [15, 16]. The estimates for each method are given in formulas (4)–(6):

$$V_{\text{NBB}}(\hat{E}(b)) = \frac{4\pi^2 g_1(0)}{3n^3} b + \overline{o}\left(\frac{b}{n^3}\right),$$
$$V_{\text{NBB}}(\hat{V}(b)) = \frac{4\pi^2 g_2(0)}{3n^3} b + \overline{o}\left(\frac{b}{n^3}\right), \tag{4}$$

$$V_{\text{MBB}}(\hat{E}(b)) = \frac{2\pi^2 g_1(0)}{n^3} b + \overline{o}\left(\frac{b}{n^3}\right),$$
$$V_{\text{MBB}}(\hat{V}(b)) = \frac{2\pi^2 g_2(0)}{n^3} b + \overline{o}\left(\frac{b}{n^3}\right), \tag{5}$$

$$V_{\text{SB}}(\hat{E}(b)) = \frac{4\pi^2 g_1(0) + 2\pi G_1}{n^3} b + \overline{o}\left(\frac{b}{n^3}\right),$$
$$V_{\text{SB}}(\hat{V}(b)) = \frac{4\pi^2 g_2(0) + 2\pi G_2}{n^3} b + \overline{o}\left(\frac{b}{n^3}\right), \tag{6}$$

where g_1, g_2, G_1, G_2 are functions, the type and properties of which are described in [15, 16]. Here n is the number of time series elements. The method based on overlapping MBB blocks has lower second order moments than NBB.

Table 1. Comparison of the groups of models involved in the calculation experiment

Group of models	Learning algorithm (principle of model fitting to series values)	Additional model comparison indicators
Standard (ARIMA, ETS)	Principle of maximum plausibility	Akaike, Bayes (Schwartz) information criteria
Neural networks (LSTM, GRU, RNN, fully-connected neural networks) [19]	Error back propagation algorithm (with added batch normalization, dropout)/ gradient descent	Absent
Models based on bagging	After dividing by the trend-seasonality residual using STL processing the residual and rebuilding the model with the new residual	Absent

The bias estimation for stationary bagging differs significantly in the type of expression from the other two cases, so the comparison is difficult. The variance for stationary bagging is believed to be higher. At the same time, it has certain advantages. In [14] the properties of stationary bagging are studied. Here it is shown that the bootstrap is a Markovian chain, the order of which depends on how many matching blocks fall into the bootstrap.

Various statistical packages mainly implement the MBB algorithm as theoretically superior to other basic bagging strategies. Modifications of bagging for time series are widely used for modeling and forecasting of time processes [2–5, 17].

The algorithm for processing of time series values to apply one of the bootstrap strategies is presented in [17, 18]. Its block diagram is shown in Fig. 2.

In this way, the standard models ARIMA and exponential time smoothing (ETS), neural network models (long-short term memory (LSTM), gated recurrent unit (GRU), recurrent neural network (RNN), fully-connected multilayer perseptron) are presented in the computational experiment. Their comparison is presented in Table 1.

The purpose of the work is to compare the forecast accuracy of models built using different bagging approaches: with each other; and with other models often used for time series modeling and forecasting.

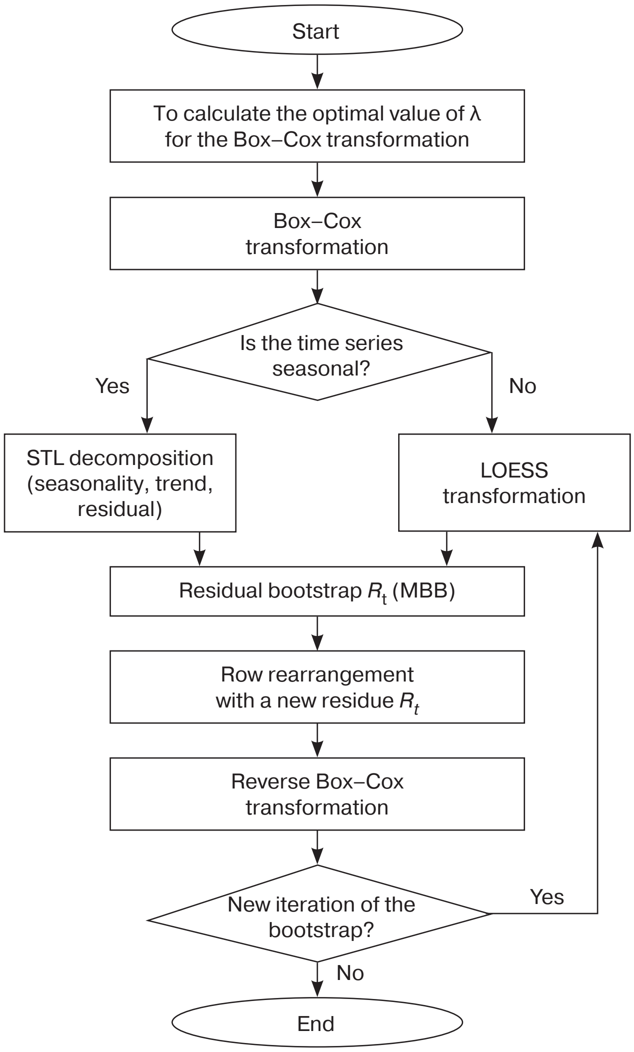

Fig. 2. Illustration of an example of selecting time series elements X into the bootstrap X^* when using stationary bagging (element X^*_{i+1} always comes later than the previously selected X^*_i).
λ is the parameter for the Box–Cox transformation; LOESS—locally estimated scatterplot smoothing; STL (seasonal and trend decomposition using LOESS)—method of time series decomposition into trend, seasonality, and residuals

CALCULATION EXPERIMENT

The computational experiment considers several time series models: real personal income (HHI)[2]; and real agricultural production (AGR)[3] according to macroeconomic statistics of the Russian Federation; as

[2] Unified archive of economic and sociological data. Dynamic series of macroeconomic statistics of the Russian Federation. Index of money incomes of the population. http://sophist.hse.ru/hse/1/tables/HHI_M_I.htm (in Russ.). Accessed September 01, 2023.

[3] Unified archive of economic and sociological data. Dynamic series of macroeconomic statistics of the Russian Federation. Index of real agricultural production. http://sophist.hse.ru/hse/1/tables/AGR_M_I.htm (in Russ.). Accessed September 01, 2023.

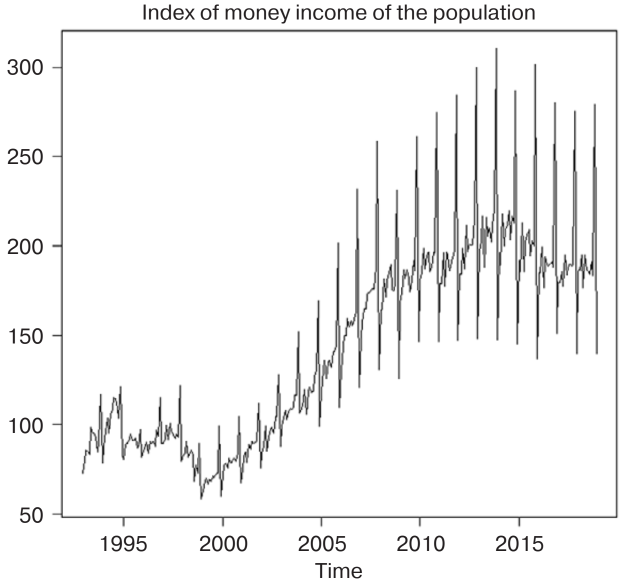

Fig. 3. Time series of the index of money income of the population (in %) according to macroeconomic statistics of the Russian Federation for 1993–2019

well as Sberbank shares on the Moscow stock exchange[4]. This article does not address economic issues. The data is used for modeling and forecasting. All data except the last year is used for training purposes. The test period for which the forecast is made is the last year of the time series. It should be emphasized that the beginning of the global economic crisis in 2008 and the beginning of the crisis relating to the shift in power in Ukraine in 2014 are excluded from consideration. This is because the behavior of indicators at this time undergoes significant change (changes in the mathematical expectation, variance of the series, heteroscedasticity appears). The data of the previous and the next year are glued together with respect to the crisis year. The graph for the series of real monetary income of the population (the ratio of the average per capita money income in the current month to the same indicator for the corresponding month of the last year) and its autocorrelation function (ACF) and partial autocorrelation function (PACF) [1] are presented in Figs. 3 and 4. The graphs for the series of real agricultural production are presented in Figs. 5 and 6.

Mean absolute error (MAE) and root mean square error (RMSE) estimates are measured as similarity metrics [1]. The results of processing the index of money income of the population are presented in Table 2 (the best models according to various criteria are marked in bold, accuracy is 0.01). In addition to models based on bagging and standard ARIMA and ETS models [20], models based on neural networks GRU, LSTM, RNN [21–24] are also presented in the experiment.

Table 2. Monetary income index models according to macroeconomic statistics of the Russian Federation and their forecasts for the test period

Time series model	MAE	RMSE
NBB	4.67	5.53
MBB	4.78	5.57
Stationary bagging	**4.10**	**4.91**
LOESS method	**3.49**	**4.57**
ARIMA	5.86	7.01
ETS	6.57	8.47
RNN	**3.88**	**4.45**
LSTM model	5.91	6.63
GRU model	**3.94**	**4.36**

4 Sberbank (SBER) stock price. https://www.moex.com/ru/issue.aspx?board=TQBR&code=SBER (in Russ.). Accessed September 01, 2023.

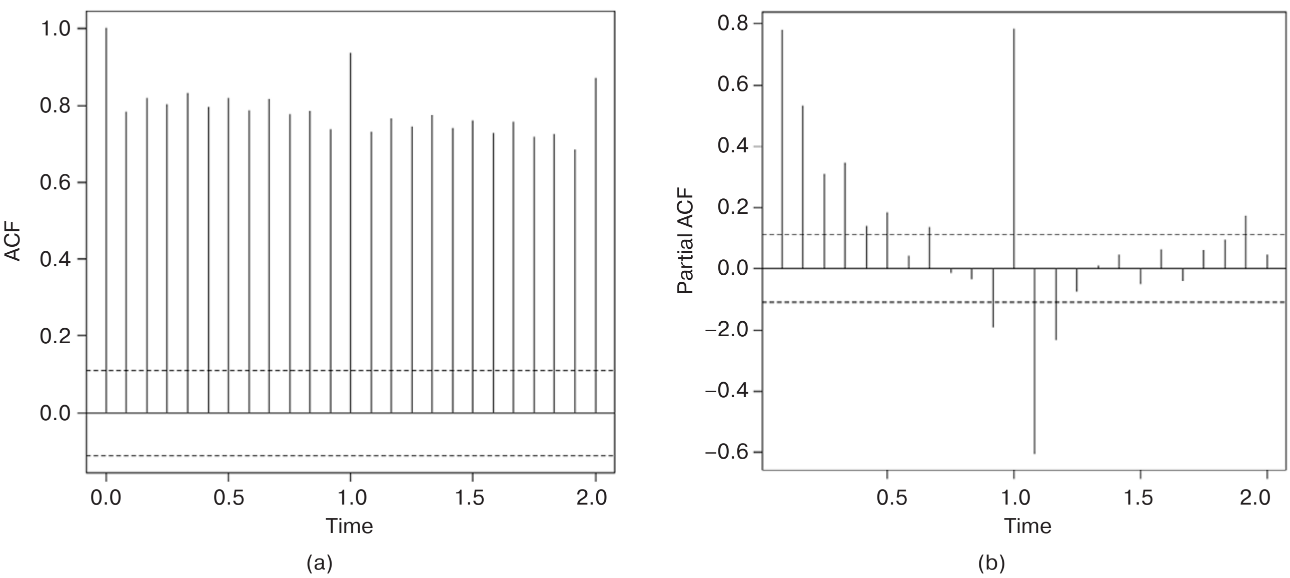

Fig. 4. Diagrams of ACF (a) and PACF (b) functions for the time series of money incomes of the population according to macroeconomic statistics of the Russian Federation

Bagging-based time series models show better results than the ARIMA and ETS standard series models. Among them, the best forecast was given by the model based on stationary bagging. At the same time, the forecast quality of the model based on stationary bagging is inferior to certain neural network models (RNN and GRU) and LOESS method (STL series decomposition).

Experiment 2 considers the index of real agricultural production in Russia for the period 2000–2020. Figures 5 and 6 show the plots of series and functions of ACF and PACF. All the models considered were adjusted for the training period 2000–2020 (the crisis years 2008 and 2014 were removed from it, the data were glued together). The results of their forecasts for the test period (2021) are compared in Table 3.

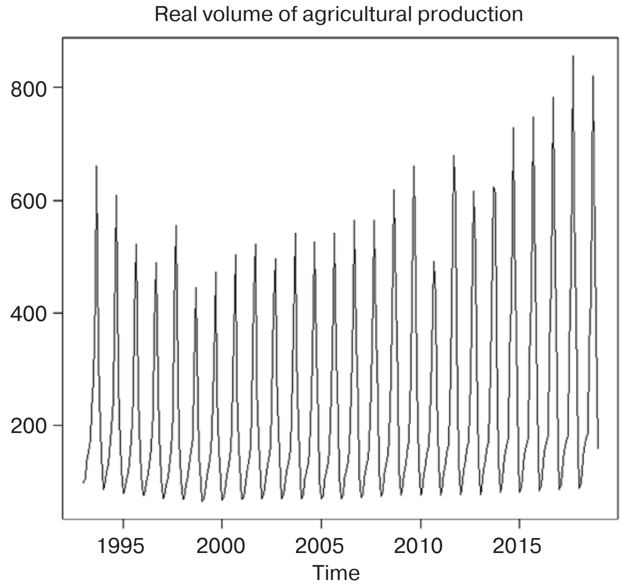

Fig. 5. Time series of real volume of agricultural production (in %) according to macroeconomic statistics of the Russian Federation

Table 3. Models of the index of real volume of agricultural production according to macroeconomic statistics of the Russian Federation and their forecasts for the test period

Time series model	MAE	RMSE
NBB	15.01	22.47
MBB	16.63	25.80
Stationary bagging	17.11	25.59
ARIMA	13.24	18.51
ETS	17.22	25,40
LSTM model	**8.78**	**15.41**
GRU model	**10.11**	**16.34**
RNN	**10.51**	**16.17**

In this experiment, the NBB approach (based on non-intersecting blocks) showed the best result among the bagging-based models. It showed approximately equal characteristics in terms of forecast quality for the test period with the ARIMA and ETS standard models. At the same time, the neural network models LSTM, GRU and RNN outperformed the standard and bagging-based models in terms of forecasting (the former—significantly, the latter two—insignificantly).

Let us separately consider a series of exchange rate of exchange-traded shares: those of Sberbank of the Russian Federation. This series has heteroscedasticity. Since the stock rate is non-seasonal, only two approaches are possible for each neural network system: to make a forecast for the entire test period at once (integral); or to make step-by-step forecasts, declaring each new step as a part of the training sample to move to the next point in time. The plots of the ACF and PACF functions are shown in Fig. 7.

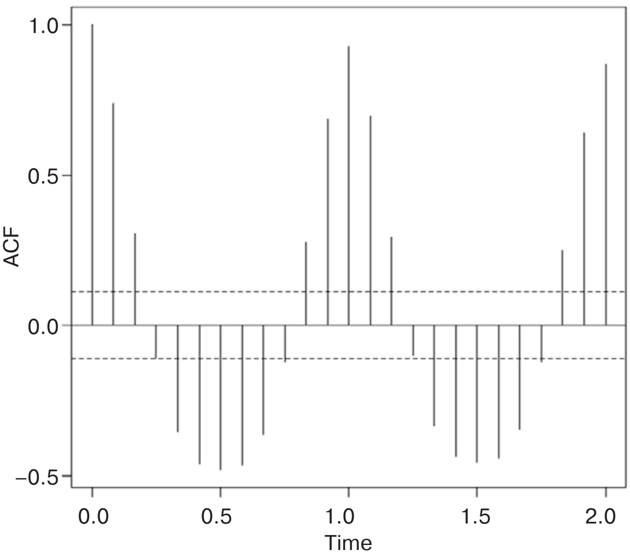

(a)

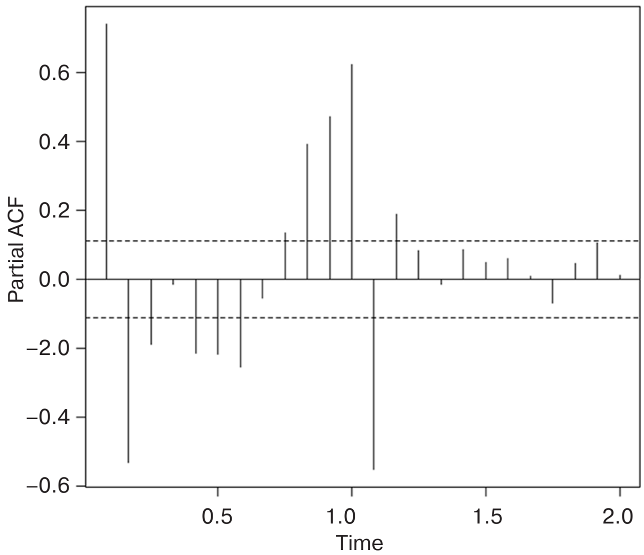

(b)

Fig. 6. Diagrams of ACF (a) and PACF (b) functions for the time series of real volume of agricultural production according to macroeconomic statistics of the Russian Federation

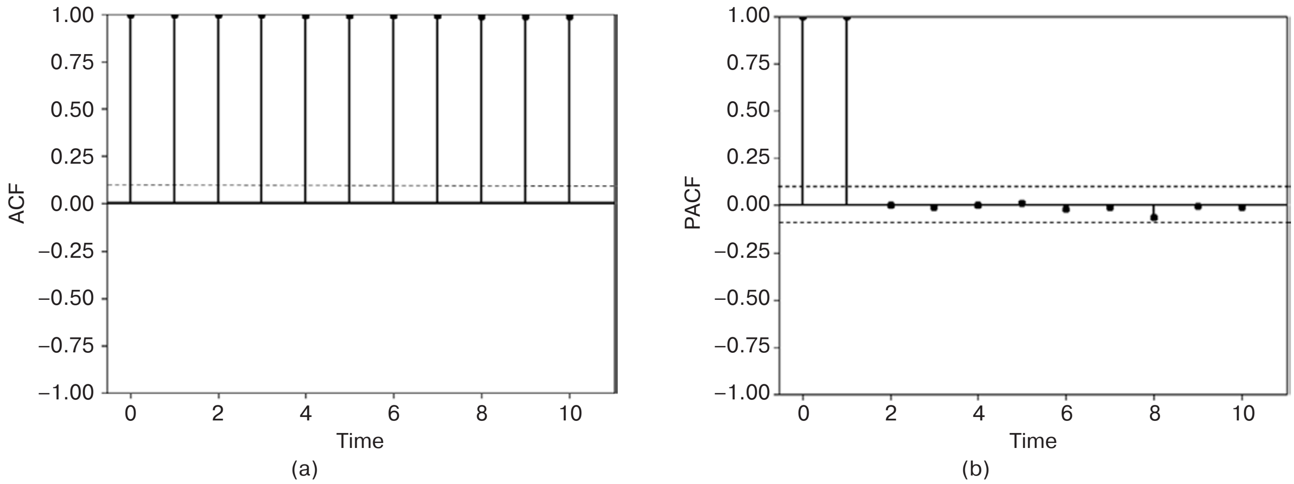

Fig. 7. Diagrams of the ACF (a) and PACF (b) functions for the time series of Sberbank of the Russian Federation stock price

Table 4. Stock price time series models for Sberbank of the Russian Federation

Time series model	MAE	RMSE
NBB	23.78	25.53
MBB	24.60	26.39
Stationary bagging	20.94	22,61
ARIMA	11.23	42.11
ETS	**4.95**	**20.68**
RNN network	80.53	86.39
LSTM model	76.95	81.40
GRU model	24.66	85.05

The best results are shown by classical methods of series modeling: ETS and ARIMA models. Stationary bagging shows slightly worse results, although significantly outperforming all neural network models. It should be noted that the standard ARIMA and ETS models describe the time series statistically better in the absence of seasonality. The main idea of bagging is to determine the properties of the noise component of the series. Obviously, it makes sense to do this for series with seasonal or cyclical patterns. Modeling noise for non-seasonal series does not lead to better forecasting (standard models gave better forecasts than models based on bagging application).

CONCLUSIONS

The work presents an analysis of different approaches to time series bagging and examples of their application to non-seasonal and seasonal time series. In computational experiments, the results of models applying bagging are compared with the forecasts of standard models (ARIMA and ETS), and models based on neural networks (RNN, LSTM, GRU).

When processing a non-seasonal time series, modeling of the noise component did not improve the modeling of the whole series and its forecast. In this experiment, the best results among all three groups of models were obtained by ARIMA and ETS standard models. It should be noted that neural network models, often used in modeling processes of a different nature, gave forecasts of worse quality compared to ARIMA and ETS models (Table 4).

When modeling seasonal time series, the best results were shown by neural network models, actively used in time series modeling, and the LOESS method. Bagging-based models outperformed the standard ARIMA and ETS models. Bagging was better able to model the residual of the series (which is obtained by removing the trend and seasonal component of the series). Thus, work on various bootstrap schemes should be continued and their accuracy improved. In addition, it may be possible to improve the accuracy of modeling and forecasting by working separately on the trend, seasonality, and residual. At the same time, it is not possible to determine which bootstrap type will best model the residual of a given series. Each type is best suited for a different set of seasonal time series. In this work, the different bootstrap approaches are implemented in the simplest form. Based on the experimental results, the work should be continued by editing the differing bootstrap features and combining the various approaches to model trend, noise and residual.

Authors' contribution. All authors equally contributed to the research work.

REFERENCES

1. Hyndman R.J., Athanasopoulos G. *Forecasting: Principles and Practice.* 2nd ed. Publisher OTexts; 2018. 382 p. ISBN 978-0-9875-0711-2
2. Özen K., Yildirim D. Application of bagging in day-ahead electricity price forecasting and factor augmentation. *Energy Econ*. 2021;103(2):105573. http://doi.org/10.1016/j.eneco.2021.105573
3. Meira E., Oliveira F.L.C., de Menezes L.M. Forecasting natural gas consumption using Bagging and modified regularization techniques. *Energy Econ*. 2022;106(3):105760. http://doi.org/10.1016/j.eneco.2021.105760
4. Kim D., Baek J-G. Bagging ensemble-based novel data generation method for univariate time series forecasting. *Expert Syst. Appl*. 2022;203(1):117366. http://doi.org/10.1016/j.eswa.2022.117366
5. Liu X., Liu A., Chen J.L., Li G. Impact of decomposition on time series bagging forecasting performance. *Tourism Manag.* 2023;97(2):104725. https://doi.org/10.1016/j.tourman.2023.104725
6. Beletskaya N., Petrusevich D. Linear Combinations of Time Series Models with Minimal Forecast Variance. *J. Commun. Technol. Electron.* 2023;67(1):144–158. http://doi.org/10.1134/S1064226922130022
7. Musatov D., Petrusevich D. Modeling of forecasts variance reduction at multiple time series prediction averaging with ARMA(1, q) functions. In: *Proceedings of MIP Computing-V 2022*: *V International Scientific Workshop on Modeling, Information Processing and Computing*. 2022;3091:1–11. https://doi.org/10.47813/dnit-mip5/2022-3091-1-11
8. Golov V.A., Petrusevich D.A. Data analysis methods in astronomic objects classification (Sloan Digital Sky Survey DR14). *Russ. Technol. J*. 2021;9(3):66–77 (in Russ.). https://doi.org/10.32362/2500-316X-2021-9-3-66-77
9. Carlstein E. The use of subseries methods for estimating the variance of a general statistic from a stationary time series. *Ann. Statist*. 1986;14(3):1171–1179. https://doi.org/10.1214/aos/1176350057
10. Carlstein E., Do K-A., Hall P., Hesterberg T., Künsch H.R. *Matched-Block Bootstrap for Dependent Data*. Research Report 74. Seminar für Statistik. ETH Zentrum. Zürich, Switzerland; 1995. 25 p.
11. Künsch H.R. The jackknife and the bootstrap for general stationary observations. *Ann. Statist*. 1989;17(3):1217–1261. https://doi.org/10.1214/aos/1176347265
12. Götze F., Künsch H.R. Second-order correctness of the blockwise bootstrap for stationary observations. *Ann. Statist*. 1996;24(5):1914–1933. http://doi.org/10.1214/aos/1069362303
13. Bühlman P., Künsch H.P. Block length selection in the bootstrap for time series. *Comput. Stat. Data Anal*. 1999;31(3):295–310. https://doi.org/10.1016/S0167-9473(99)00014-6
14. Politis D.N., Romano J.P. The stationary bootstrap. *J. Am. Stat. Assoc*. 1994;89(428):1303–1313. https://doi.org/10.1080/01621459.1994.10476870
15. Politis D.N., White H. Automatic Block-Length Selection for the Dependent Bootstrap. *Econometric Rev*. 2004;23(1):53–70. https://doi.org/10.1081/ETC-120028836
16. Lahiri S.N. Theoretical comparison of block bootstrap methods. *Ann. Statist*. 1999;27(1):386–404. https://doi.org/10.1214/aos/1018031117
17. Bergmeir C., Hyndman R. J., Benitez J.M. Bagging exponential smoothing methods using STL decomposition and Box–Cox transformation. *Int. J. Forecast.* 2016;32(2):303–312. https://doi.org/10.1016/j.ijforecast.2015.07.002
18. Petropoulos F., Hyndman R.J., Bergmeir C. Exploring the sources of uncertainty: Why does bagging for time series forecasting work? *Eur. J. Oper. Res*. 2018;268(2):545–554. http://doi.org/10.1016/j.ejor.2018.01.045
19. Haykin S. *Neural Networks and Learning Machines*. Pearson Education; 2011. 936 p. ISBN 978-0-1330-0255-3
20. Box G., Jenkins G. *Time Series Analysis: Forecast and Management*. John Wiley & Sons; 2015. 712 p. ISBN 978-1-1185-6749-18
21. Rasjid Z.E., Setiawan R., Effendi A. A Comparison: Prediction of Death and Infected COVID-19 Cases in Indonesia Using Time Series Smoothing and LSTM Neural Network. *Procedia Comput. Sci*. 2021;179(5):982–988. http://doi.org/10.1016/j.procs.2021.01.102
22. Liu X., Lin Z., Feng Z. Short-term offshore wind speed forecast by seasonal ARIMA – A comparison against GRU and LSTM. *Energy*. 2021;227:120492. http://doi.org/10.1016/j.energy.2021.120492
23. Shahid F., Zameer A., Muneeb M. Predictions for COVID-19 with deep learning models of LSTM, GRU and Bi-LSTM. *Chaos, Solitons & Fractals*. 2020;140:110212. https://doi.org/10.1016/j.chaos.2020.110212
24. Amalou I., Mouhni N., Abdali A. Multivariate time series prediction by RNN architectures for energy consumption forecasting. *Energy Rep*. 2022;8:1084–1091. https://doi.org/10.1016/j.egyr.2022.07.139

About the authors

Ian V. Gramovich, Student, Institute of Artificial Intelligence, MIREA – Russian Technological University (78, Vernadskogo pr., Moscow, 119454 Russia). https://orcid.org/0009-0000-2908-7611

Danila Yu. Musatov, Student, Institute of Artificial Intelligence, MIREA – Russian Technological University (78, Vernadskogo pr., Moscow, 119454 Russia). Scopus Author ID 57469172700, https://orcid.org/0000-0003-0673-5393

Denis A. Petrusevich, Cand. Sci. (Phys.-Math.), Associate Professor, Higher Mathematics Department, Institute of Artificial Intelligence, MIREA – Russian Technological University (78, Vernadskogo pr., Moscow, 119454 Russia). E-mail: petrusevich@mirea.ru, petrdenis@mail.ru. Scopus Author ID 55900513600, ResearcherID AAA-6661-2020, RSCI SPIN-code 7999-6345, https://orcid.org/0000-0001-5325-6198

Об авторах

Грамович Ян Вадимович, студент, ФГБОУ ВО «МИРЭА – Российский технологический университет» (119454, Россия, Москва, пр-т Вернадского, д. 78). https://orcid.org/0009-0000-2908-7611

Мусатов Данила Юрьевич, студент, ФГБОУ ВО «МИРЭА – Российский технологический университет» (119454, Россия, Москва, пр-т Вернадского, д. 78). Scopus Author ID 57469172700, https://orcid.org/0000-0003-0673-5393

Петрусевич Денис Андреевич, к.ф.-м.н., доцент, кафедра высшей математики Института искусственного интеллекта ФГБОУ ВО «МИРЭА – Российский технологический университет» (119454, Россия, Москва, пр-т Вернадского, д. 78). E-mail: petrusevich@mirea.ru, petrdenis@mail.ru. Scopus Author ID 55900513600, ResearcherID AAA-6661-2020, SPIN-код РИНЦ 7999-6345, https://orcid.org/0000-0001-5325-6198

Translated from Russian into English by Lyudmila O. Bychkova
Edited for English language and spelling by Dr. David Mossop

Russian Technological Journal. 2024;12(1):111–122 ISSN 2500-316X (Online)

Mathematical modeling

Математическое моделирование

UDC 519.857
https://doi.org/10.32362/2500-316X-2024-12-1-111-122

RESEARCH ARTICLE

The use of complex structure splines in roadway design

Valery I. Struchenkov @,
Dmitry A. Karpov

MIREA – Russian Technological University, Moscow, 119454 Russia
@ *Corresponding author, e-mail: str1942@mail.ru*

Abstract
Objectives. The aim of the work is to develop the theory of spline-approximation of a sequence of points on a plane for using compound splines with a complex structure. In contrast to a simple spline (e.g., polynomial), a compound spline contains repeating bundles of several elements. Such problems typically arise in the design of traces for railroads and highways. The plan (projection on the horizontal plane) of such a trace is a curve consisting of a repeating bundle of elements "line + clothoid + circle + clothoid ...," which ensures continuity not only of curve and tangent but also of curvature. The number of spline elements, which is unknown, should be determined in the process of solving the design problem. An algorithm for solving the problem with respect to the spline, which consists of arcs conjugated by straight lines, was implemented and published in an earlier work. The approximating spline in the general case is a multivalued function, whose ordinates may be limited. Another significant factor that complicates the problem is the presence of clothoids that are not expressed analytically (in a formula). The algorithm for determining the number of elements of a spline with clothoids and constructing an initial approximation was also published earlier. The present work considers the next stage of solving the spline approximation problem: optimization using a nonlinear programming spline obtained at the first stage by means of the dynamic programming method.
Methods. A new mathematical model in the form of a modified Lagrange function is used together with a special nonlinear programming algorithm to optimize spline parameters. In this case, it is possible to calculate the derivatives of the objective function by the spline parameters in the absence of its analytical expression through these parameters.
Results. A mathematical model and algorithm for optimization of compound spline parameters comprising arcs of circles conjugated by clothoids and lines have been developed.
Conclusions. The previously proposed two-step scheme for designing paths of linear structures is also suitable for the utilization of compound splines with clothoids.

Keywords: trace plan, spline, nonlinear programming, clothoid, objective function, constraints

• **Submitted:** 18.05.2023 • **Revised:** 29.07.2023 • **Accepted:** 08.12.2023

For citation: Struchenkov V.I., Karpov D.A. The use of complex structure splines in roadway design. *Russ. Technol. J.* 2024;12(1):111–122. https://doi.org/10.32362/2500-316X-2024-12-1-111-122

Financial disclosure: The authors have no a financial or property interest in any material or method mentioned.

The authors declare no conflicts of interest.

НАУЧНАЯ СТАТЬЯ

Использование сплайнов сложной структуры в проектировании дорожных трасс

В.И. Струченков @,
Д.А. Карпов

МИРЭА – Российский технологический университет, Москва, 119454 Россия
@ *Автор для переписки, e-mail: str1942@mail.ru*

Резюме

Цели. Цель работы состоит в развитии теории сплайн-аппроксимации последовательности точек на плоскости на случай использования составных сплайнов сложной структуры. В отличие от простого, например, полиномиального сплайна, составной сплайн содержит повторяющиеся связки нескольких элементов. Такая задача возникает в проектировании трасс железных и автомобильных дорог. План (проекция на горизонтальную плоскость) такой трассы – это кривая, состоящая из повторяющейся связки элементов «прямая + + клотоида + окружность + клотоида ...», что обеспечивает непрерывность не только кривой и касательной, но и кривизны. Число элементов сплайна неизвестно и должно определяться в процессе решения проектной задачи. Алгоритм решения задачи применительно к сплайну, состоящему из дуг окружностей, сопрягаемых прямыми, реализован и опубликован ранее. Аппроксимирующий сплайн в общем случае – многозначная функция. На координаты точек ее графика могут накладываться ограничения. Еще одним существенным фактором, усложняющим задачу, является наличие клотоид, которые не выражаются аналитически (формулой). Алгоритм определения числа элементов сплайна с клотоидами и построения начального приближения опубликован ранее. В настоящей статье рассматривается следующий этап решения задачи – оптимизация с применением нелинейного программирования сплайна, полученного на первом этапе по методу динамического программирования.

Методы. Для оптимизации параметров сплайна используется новая математическая модель в виде модифицированной функции Лагранжа и специальный алгоритм нелинейного программирования. При этом удается вычислять аналитически производные целевой функции по параметрам сплайна при отсутствии ее аналитического выражения через эти параметры.

Результаты. Разработаны математическая модель и алгоритм оптимизации параметров составного сплайна, состоящего из дуг окружностей, сопрягаемых клотоидами и прямыми.

Выводы. Предложенная ранее двухэтапная схема проектирования плана трасс линейных сооружений пригодна и при использовании составных сплайнов с клотоидами.

Ключевые слова: план трассы, сплайн, нелинейное программирование, клотоида, целевая функция, ограничения

• **Поступила:** 18.05.2023 • **Доработана:** 29.07.2023 • **Принята к опубликованию:** 08.12.2023

Для цитирования: Струченков В.И., Карпов Д.А. Использование сплайнов сложной структуры в проектировании дорожных трасс. *Russ. Technol. J.* 2024;12(1):111–122. https://doi.org/10.32362/2500-316X-2024-12-1-111-122

Прозрачность финансовой деятельности: Авторы не имеют финансовой заинтересованности в представленных материалах или методах.

Авторы заявляют об отсутствии конфликта интересов.

INTRODUCTION

The method of approximating a given sequence of points in the plane using a special kind of spline implies a two-stage scheme for obtaining a solution [1]. Here, the first stage consists in obtaining the number of spline elements and approximate parameter values using the dynamic programming method. At the second stage, optimization of the parameters of obtained spline used as an initial approximation is performed using nonlinear programming. The first stage was considered in [1]. In the present article, representing the culmination of a series of articles [1–3] devoted to spline approximation methods, the second stage is considered in relation to the use of a spline with clothoids for conjugating straight lines with circles. The solution to this problem with respect to a spline consisting of arcs of circles conjugated by straight lines was presented in [3]. The results of this earlier work are referred to in the present article, which develops the model and algorithm [3] for the more complex case of a spline with clothoids.

A spline consists of a repeated conjunction "line segment + clothoid arc + circle arc + clothoid arc...." In what follows, the word "arc" will be omitted for brevity unless ambiguity arises. At this stage, the initial point and the direction of the tangent in it, as well as the lengths of all curves and lines conjugating them, are known. This allows us to apply continuous optimization methods—in particular, methods of nonlinear programming of the gradient type—despite the desired spline in the general case representing a multivalued function.

The problem is considered in relation to the design of route plans for railroads and highways, where—unlike other linear structures, such as pipelines—clothoids are a necessary means of ensuring curvature continuity to ensure traffic comfort and safety.[1,2]

In this connection, the accepted approach is noted to differ significantly from the method of selecting elements in interactive mode used in design practice, as well as from various semi-automatic methods of searching curve boundaries on the basis of curvature and angle diagrams, and from the new heuristic method of searching curve boundaries [4] with the subsequent application of genetic optimization algorithms [5–14].

Consequently, the use of adequate mathematical models and mathematically correct algorithms seems to represent a more promising approach.

[1] SP 34.13330.2012. *Automobile roads*. Updated edition of SNiP 2.05.02-85* (with Amendments No. 1, 2). Code of Regulations. June 30, 2012. https://docs.cntd.ru/document/1200095524 (in Russ.). Accessed December, 20, 2023.

[2] SP 119.13330.2017. *Railway with 1520 mm track*. Updated edition of SNiP 32-01-95 (with Amendment No. 1). https://docs.cntd.ru/document/550965737 (in Russ.). Accessed December, 20, 2023.

1. TASK STATEMENT AND ITS FORMALIZATION

The task statement and its formalization do not differ significantly from that presented in [3] when solving the problem without clothoids. However, the presence of clothoids creates significant difficulties in the realization of gradient calculation concepts for the application of nonlinear programming.

A clothoid represents a plane curve (Fig. 1) whose curvature σ depends linearly on its length l. Thus, for a piece of clothoid with an arbitrary initial point A, curvature at this point σ_A, and the end point B with curvature σ_B, we have the formula:

$$\sigma_B = \sigma_A + kL, \tag{1}$$

where L is the length of the clothoid piece and k is its parameter.

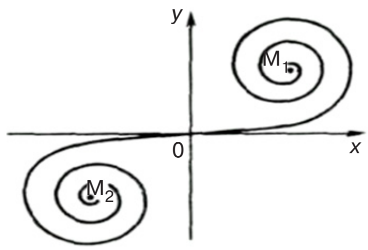

Fig. 1. Clothoid

This linear dependence is the basis for all subsequent actions in calculating derivatives in order to apply mathematical programming.

The task is as follows: to find a spline of a given form, which satisfies all constraints and best approximates a given sequence of points in the plane (Fig. 2).

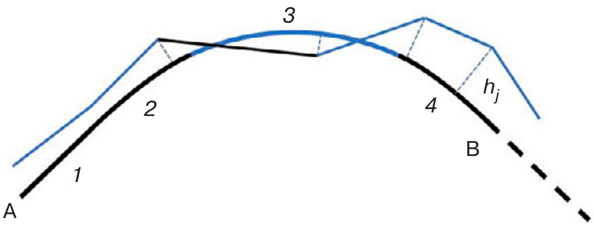

Fig. 2. One spline bundle: *1*—straight line, *2* and *4*—clothoids, *3*—circle

The preset initial point A and direction of the tangent to the desired spline at this point do not change during the optimization process.

Approximation quality is estimated by the sum of squares of deviations h_j (Fig. 2) of the given points from the spline. In other words, h_j represents the displacement of a given point to its designed position, calculated along the normal to the original broken line [3], i.e., along the direction to the center of the circle connecting three adjacent points. If three points lie on the same line, h_j are calculated along the normal to this line.

Offsets of the initial points to the design position are considered to be positive if they are carried out in the direction of the external normal.

Now it is necessary to obtain

$$\min F(\mathbf{h}) = 1/2\sum_{1}^{n} h_j^2. \tag{2}$$

Here $\mathbf{h}(h_1, h_2, \ldots, h_n)$ is the vector of variables; n is their number. A weighted sum of squares can be specified instead of a simple sum.

Since each variable is constrained separately, the system of constraints on the main variables contains simple inequalities. This system is practically the same as in [3]. Only the constraint on the length of the clothoid is added; instead of a variable radius, a variable curvature is considered. The constraints on the individual displacements hm are the same as in [3].

It is not possible to express the conditions of presence and position of lines, clothoids and circles through the variables h_j. We consider these variables as intermediate variables, while the main variables are the lengths of lines, clothoids and circles, as well as the curvatures of circles.

In formal terms, the mathematical programming problem is the same as in [3]. However, since the presence of clothoids significantly complicates the task, it requires a separate consideration.

2. TASK FEATURES

A spline is completely defined by the main variables, taking into account the initial point and the direction of the tangent in it. However, we lack analytical expressions of dependencies (formulas) of intermediate variables on the main variables. The constraints on the main variables are not expressed through the intermediate variables. Moreover, there is no analytical dependence of the objective function (2) on the main variables.

A clothoid cannot be generally represented in a Cartesian coordinate system by a function $y(x)$.

If the origin of the coordinate system coincides with the point of zero curvature of the clothoid, and the OX axis is a tangent at this point (Fig. 1), then the parametric representation of the x and y coordinates as functions of the length l counted from the point of zero curvature in the form of degree series is used in this case:

$$\begin{aligned} x(l) &\approx l\left(1-\frac{l^4k^2}{40}+\frac{l^8k^4}{3456}-\ldots\right), \\ y(l) &\approx \frac{l^3k}{6}\left(1-\frac{l^4k^2}{56}+\frac{l^8k^4}{7040}-\ldots\right). \end{aligned} \tag{3}$$

For expanding the series, formulas for the clothoid in an arbitrary coordinate system are obtained, taking into account the coordinates of the initial point, the angle of the tangent in it to the OX axis, and the curvature [15].

Due to the noted features of the problem, the idea of solving it as a nonlinear programming task using gradient methods [16–18] seems unfeasible. However, the task of spline approximation using circles conjugated by straight lines was solved in this way [3] despite the lack of analytical expressions of differentiable functions. After obtaining formulas for derivatives of intermediate variables h_j on the main variables, we were able to easily calculate the derivatives of the objective function on the main variables [3].

3. INTEGRAL REPRESENTATION OF THE CLOTHOID AND ITS APPLICATION

Since, for any smooth curve, $\sigma = d\varphi/dl$, where σ is the curvature, φ and l are the respective current values of the tangent angle with the OX axis and length, we derive from (1):

$$\varphi_B = \varphi_A + \sigma_A L + kL^2/2 = \varphi_A + L(\sigma_A + \sigma_B)/2. \tag{4}$$

Between the arc length increment of any smooth curve and the coordinate increment, there are the relations $dx = \cos\varphi\ dl$ and $dy = \sin\varphi\ dl$, from which, using (4) to denote the integration variable by t, we derive a representation of the clothoid in parametric form:

$$\begin{aligned} x(l) &= x_A + \int_0^l \cos(\varphi_A + \sigma_A t + kt^2/2)dt, \\ y(l) &= y_A + \int_0^l \sin(\varphi_A + \sigma_A t + kt^2/2)dt. \end{aligned} \tag{5}$$

Here x_A, y_A are the coordinates of the initial point and l is the length of the piece of clothoid from the initial point A to the current point with coordinates $x(l)$, $y(l)$.

Further, we will rely on the parametric representation of the clothoid (5).

Let us consider what transformations occur with the spline when changing one and only one main variable. An understanding of these transformations will be used to generate formulas for calculating partial derivatives of intermediate variables (h_j) from element lengths and curvatures, i.e., by basic variables.

When changing the length of a line by ΔL, the right part of the spline is shifted in the direction of this line. When changing the length of the circle arc, a shift in the direction of the tangent at the end point of the arc plus rotation is centered at this point by $\Delta\varphi = \sigma\Delta L$. When the length of the clothoid changes, the following occurs:

1. The clothoid parameter is varied in such a way that the curvature at the end point does not change when the length changes, since we calculate partial derivatives.
2. The coordinates of the right end (point B) of the clothoid and the angle of the tangent in it with the *OX* axis change. According to (5)

$$x_{\mathrm{B}} = x_{\mathrm{A}} + \int_0^L \cos(\varphi_{\mathrm{A}} + \sigma_{\mathrm{A}} t + kt^2/2)dt,$$
$$y_{\mathrm{B}} = y_{\mathrm{A}} + \int_0^L \sin(\varphi_{\mathrm{A}} + \sigma_{\mathrm{A}} t + kt^2/2)dt, \tag{6}$$

$$\frac{\partial x_{\mathrm{B}}}{\partial L} = \cos\varphi_{\mathrm{B}} + \frac{\partial x_{\mathrm{B}}}{\partial k}\cdot\frac{\partial k}{\partial L} = \cos\varphi_{\mathrm{B}} - \frac{\partial x_{\mathrm{B}}}{\partial k}\cdot\frac{(\sigma_{\mathrm{B}} - \sigma_{\mathrm{A}})}{L^2}, \tag{7}$$

$$\frac{\partial y_{\mathrm{B}}}{\partial L} = \sin\varphi_{\mathrm{B}} + \frac{\partial y_{\mathrm{B}}}{\partial k}\cdot\frac{\partial k}{\partial L} = \sin\varphi_{\mathrm{B}} - \frac{\partial y_{\mathrm{B}}}{\partial k}\cdot\frac{(\sigma_{\mathrm{B}} - \sigma_{\mathrm{A}})}{L^2}. \tag{8}$$

The relation derived from (1) is used here: $\partial k/\partial L = -(\sigma_{\mathrm{B}} - \sigma_{\mathrm{A}})/L^2$.

$$\frac{\partial \varphi_{\mathrm{B}}}{\partial L} = \sigma_{\mathrm{A}} + kL + \frac{\partial k}{\partial L}\cdot\frac{L^2}{2} = \sigma_{\mathrm{A}} + kL - \frac{(\sigma_{\mathrm{B}} - \sigma_{\mathrm{A}})}{2} = \frac{(\sigma_{\mathrm{A}} + \sigma_{\mathrm{B}})}{2}. \tag{9}$$

Thus, on the right side of the clothoid there is a shift and rotation centered at point B, while inside the clothoid we need to take into account only the effect of changing the parameter k.

When changing the curvature of the circle, the parameters of the adjacent clothoids on the left and right change along with the coordinates of the end point of the circle arc and the angle of the tangent in it with the *OX* axis. All this leads to shifts and rotations of the spline part following the end point of the right clothoid. In addition, the coordinates of the internal points of the circle arc, as well as those of the left and right clothoids, also change.

We proceed to derive the formulas that will be used to account for the change in the clothoid parameter.

We will need four integrals:

$$I_1 = \int_0^L \sin\left(\varphi_{\mathrm{A}} + \sigma_{\mathrm{A}} t + k\frac{t^2}{2}\right) t\,dt,$$
$$I_2 = \int_0^L \cos\left(\varphi_{\mathrm{A}} + \sigma_{\mathrm{A}} t + k\frac{t^2}{2}\right) t\,dt,$$
$$I_3 = \int_0^L \sin\left(\varphi_{\mathrm{A}} + \sigma_{\mathrm{A}} t + k\frac{t^2}{2}\right) t^2 dt,$$
$$I_4 = \int_0^L \cos\left(\varphi_{\mathrm{A}} + \sigma_{\mathrm{A}} t + k\frac{t^2}{2}\right) t^2 dt,$$

$$I_1 = \frac{1}{k}\int_0^L \sin\left(\varphi_{\mathrm{A}} + \sigma_{\mathrm{A}} t + k\frac{t^2}{2}\right)(kt + \sigma_{\mathrm{A}} - \sigma_{\mathrm{A}})dt = \frac{1}{k}\int_0^L \sin\left(\varphi_{\mathrm{A}} + \sigma_{\mathrm{A}} t + k\frac{t^2}{2}\right) d\left(\varphi_{\mathrm{A}} + \sigma_{\mathrm{A}} t + k\frac{t^2}{2}\right) - \frac{\sigma_{\mathrm{A}}}{k}\int_0^L \sin\left(\varphi_{\mathrm{A}} + \sigma_{\mathrm{A}} t + k\frac{t^2}{2}\right)dt = -\frac{1}{k}(\cos\varphi_{\mathrm{B}} - \cos\varphi_{\mathrm{A}}) - \frac{\sigma_{\mathrm{A}}}{k}(y_{\mathrm{B}} - y_{\mathrm{A}}), \tag{10}$$

$$I_2 = \frac{1}{k}\int_0^L \cos\left(\varphi_{\mathrm{A}} + \sigma_{\mathrm{A}} t + k\frac{t^2}{2}\right)(kt + \sigma_{\mathrm{A}} - \sigma_{\mathrm{A}})dt = \frac{1}{k}\int_0^L \cos\left(\varphi_{\mathrm{A}} + \sigma_{\mathrm{A}} t + k\frac{t^2}{2}\right) d\left(\varphi_{\mathrm{A}} + \sigma_{\mathrm{A}} t + k\frac{t^2}{2}\right) - \frac{\sigma_{\mathrm{A}}}{k}\int_0^L \cos\left(\varphi_{\mathrm{A}} + \sigma_{\mathrm{A}} t + k\frac{t^2}{2}\right)dt = \frac{1}{k}(\sin\varphi_{\mathrm{B}} - \sin\varphi_{\mathrm{A}}) - \frac{\sigma_{\mathrm{A}}}{k}(x_{\mathrm{B}} - x_{\mathrm{A}}), \tag{11}$$

$$I_3 = \frac{1}{k}\int_0^L \sin\left(\varphi_{\mathrm{A}} + \sigma_{\mathrm{A}} t + k\frac{t^2}{2}\right) t(kt + \sigma_{\mathrm{A}} - \sigma_{\mathrm{A}})dt = -\frac{1}{k}\int_0^L t\,d\cos\left(\varphi_{\mathrm{A}} + \sigma_{\mathrm{A}} t + k\frac{t^2}{2}\right) - \frac{\sigma_{\mathrm{A}}}{k} I_1 = -\frac{1}{k}\big(L\cos\varphi_{\mathrm{B}} - (x_{\mathrm{B}} - x_{\mathrm{A}})\big) + \frac{\sigma_{\mathrm{A}}}{k^2}\big((\cos\varphi_{\mathrm{B}} - \cos\varphi_{\mathrm{A}}) + \sigma_{\mathrm{A}}(y_{\mathrm{B}} - y_{\mathrm{A}})\big), \tag{12}$$

$$I_4 = \frac{1}{k}\int_0^L \cos\left(\varphi_{\mathrm{A}} + \sigma_{\mathrm{A}} t + k\frac{t^2}{2}\right) t(kt + \sigma_{\mathrm{A}} - \sigma_{\mathrm{A}})dt = \frac{1}{k}\int_0^L t\,d\sin\left(\varphi_{\mathrm{A}} + \sigma_{\mathrm{A}} t + k\frac{t^2}{2}\right) - \frac{\sigma_{\mathrm{A}}}{k} I_2 = \frac{1}{k}\big(L\sin\varphi_{\mathrm{B}} - (y_{\mathrm{B}} - y_{\mathrm{A}})\big) - \frac{\sigma_{\mathrm{A}}}{k^2}\big((\sin\varphi_{\mathrm{B}} - \sin\varphi_{\mathrm{A}}) - \sigma_{\mathrm{A}}(x_{\mathrm{B}} - x_{\mathrm{A}})\big). \tag{13}$$

It follows from (5) that

$$\frac{\partial x_B}{\partial k} = -\frac{1}{2}I_3 = \frac{1}{2k}\left(L\cos\varphi_B - (x_B - x_A)\right) - \\ -\frac{\sigma_A}{2k^2}\left((\cos\varphi_B - \cos\varphi_A) + \sigma_A(y_B - y_A)\right), \quad (14)$$

$$\frac{\partial y_B}{\partial k} = \frac{1}{2}I_4 = \frac{1}{2k}\left(L\sin\varphi_B - (y_B - y_A)\right) - \\ -\frac{\sigma_A}{2k^2}\left((\sin\varphi_B - \sin\varphi_A) + \sigma_A(x_B - x_A)\right). \quad (15)$$

For the left clothoid, the curvature at the initial point and the length do not change with the changes in the curvature of the circle. Denoting, as before, the curvature of the circle by σ, taking into account (1) and (5) and fixing σ_A, we obtain:

$$\frac{\partial x_B}{\partial \sigma} = \frac{\partial x_B}{\partial k}\cdot\frac{1}{L}, \quad (16)$$

$$\frac{\partial y_B}{\partial \sigma} = \frac{\partial y_B}{\partial k}\cdot\frac{1}{L}. \quad (17)$$

Let us consider the effect of changing the curvature of the circle σ on the right clothoid. For its initial and end points, as well as its length, we keep the designations A, B, and L, respectively.

$$x_B = \int_0^L \cos\left(\varphi_A + \sigma t + \frac{\sigma_B - \sigma}{L}\cdot\frac{t^2}{2}\right)dt,$$

$$\frac{\partial x_B}{\partial \sigma} = -\int_0^L \sin\left(\varphi_A + \sigma t + \frac{\sigma_B - \sigma}{L}\cdot\frac{t^2}{2}\right)\left(t - \frac{t^2}{2L}\right)dt = \\ = -I_1 + \frac{1}{2L}I_3, \quad (18)$$

$$y_B = \int_0^L \sin\left(\varphi_A + \sigma t + \frac{\sigma_B - \sigma}{L}\cdot\frac{t^2}{2}\right)dt,$$

$$\frac{\partial y_B}{\partial \sigma} = \int_0^L \cos\left(\varphi_A + \sigma t + \frac{\sigma_B - \sigma}{L}\cdot\frac{t^2}{2}\right)\left(t - \frac{t^2}{2L}\right)dt = \\ = I_2 - \frac{1}{2L}I_4. \quad (19)$$

When substituting in (18) and (19) instead of I_1, I_2, I_3, I_4 their values from (10)–(13) for the right clothoid, it should be taken into account that $\sigma_A = \sigma$ and $k = (\sigma_B - \sigma)/L$.

Formulas (18) and (19) can be used in computing the derivatives of the coordinates of any interior point C of the right clothoid along the curvature of the circle by substituting in (10)–(13) x_C and y_C instead of x_B and y_B, φ_C instead of φ_B, and, instead of L, the length of the clothoid from the initial point A to this point C. However, in formulas (18) and (19), L is the length of the entire right clothoid from point A to point B.

Then it follows from (1) and (2) that:

$$\frac{\partial \varphi_B}{\partial \sigma} = \frac{L}{2}. \quad (20)$$

Here σ is the curvature of the circle, φ_B is the angle with the OX axis at the end point of the clothoid, and L is its length.

Formula (20) is applicable to both left and right clothoids.

Now we have everything necessary to proceed to the computation of partial derivatives of displacements on normals (intermediate variables) on basic variables.

4. CALCULATION OF DERIVATIVE DISPLACEMENTS ALONG NORMALS

Thus, it has been found that, even in the presence of clothoids, all spline transformations are reduced to shifts and rotations when changing one main variable. Let us consider how to successively calculate the derivatives of displacements by normals on the main variables without having the corresponding analytical relationships.

4.1. Derivatives by the straight-line length

When changing the length of the line by δl the subsequent part of the spline is shifted in the direction of the changed line. This direction is determined by the angle α of the line with the axis OX (Fig. 3). For the shift along the jth normal, the formula is valid

$$\frac{\partial h_j}{\partial l} = \frac{\sin(\alpha - \beta)}{\sin(\gamma_j - \beta)}, \quad (21)$$

where β is the angle with the OX axis of the tangent (line AB in Fig. 3) to the spline element (in a special case it is a line) at the point of intersection with the jth normal); γ_j is the angle of the normal (C_0C_1 in Fig. 3) with the OX axis.

In Fig. 3, point C is the initial position of the intersection point of the normal and the spline, which corresponds to the value of the intermediate variable h_j. At the shift in the direction determined by the angle α at δl, AB moves to A_1B_1, point C moves to C_2, and C_1 becomes the point of intersection of the normal with the spline. The displacement h_j gets the increment $\delta h_j = CC_1$.

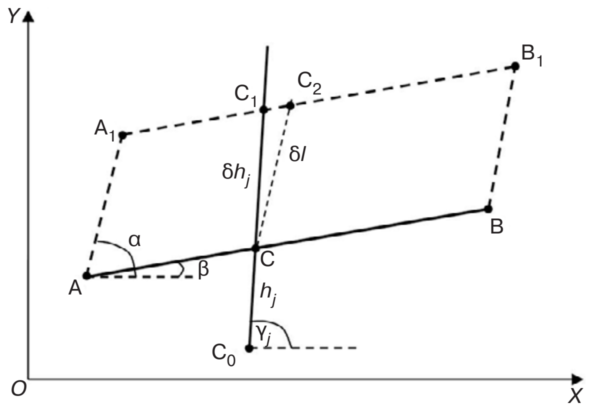

Fig. 3. To the calculation of partial derivatives at the shift

Formula (21) is derived from the sine theorem when applied to the triangle C_1CC_2. It is valid for all normals intersecting the spline to the right of the end of the varying line.

4.2. Derivatives by the arc length of a circle

When the arc length of the circle is changed by δL, the whole subsequent part of the spline (starting from the end point of arc B) is shifted by δL in the direction of the tangent to the circle at B. This direction is determined by the angle α of the tangent with the OX axis. Additionally, the right side of the spline is rotated by the angle $\delta\alpha = \sigma\delta L$ around the point B, where σ is the curvature of the circle. The shift is accounted for in the same way as for the change in the length of a straight line. In [3], the formula (13) for calculating the derivative of the length of the circle of the displacement along the jth normal is given and justified, which, in the notations we have adopted, will be as follows:

$$\frac{\partial h_j}{\partial L} = \frac{\sin(\alpha-\beta)+\left[(x_C-x_B)\cos\beta+(y_C-y_B)\sin\beta\right]\sigma}{\sin(\gamma_j-\beta)}. \tag{22}$$

Here L is the length of the circle arc, α is the angle of the tangent to it at the end point B, x_C, y_C are the coordinates of the point of intersection of the spline with the jth normal, β is the angle of the tangent to the spline at this point C with the OX axis, γ_j is the angle of the normal with the OX axis. This formula takes into account both shift and rotation. It is valid for any normal intersecting the spline to the right of the end point of the circle arc.

4.3. Derivatives by the arc length of the clothoid

When the length of the clothoid changes, the subsequent part of the spline is shifted and rotated with the center at the end point of the clothoid arc B.

The respective increments of displacements along the jth normal to the right of the clothoid are represented in the form:

$$\partial h_j = \partial h_j^{\mathrm{s}} + \partial h_j^{\mathrm{r}}, \tag{23}$$

where $\partial h_j^{\mathrm{s}}$ is the increment of displacement along the jth normal at the shift; $\partial h_j^{\mathrm{r}}$ is the increment of displacement along the jth normal at the rotation.

The change in the coordinates of the end point B occurs due to the tangent shift by ∂L and the change in the parameter k, which additionally leads to a change in the coordinates of the intersection points of the normals with the clothoid.

For the calculation of $\partial h_j^{\mathrm{s}}$, we use formulas (7) and (8), which give the increments of coordinates ∂x_B and ∂y_B of the end point of the clothoid arc caused by the increment ∂L. The same increments will be given by the shift to the coordinates of all subsequent points. It is notable that the first summands in these formulas correspond to the shift along the tangent at point B by ∂L, while the second summands correspond to the shift due to the change in the parameter of the clothoid while maintaining the curvature at its initial and end points. If we denote the increment h_j^{s} caused by a shift along the OX axis by ∂x_B via ∂h_{jx}, and along the OY axis by ∂y_B via ∂h_{jy}, then

In order to calculate ∂h_{jx} in formula (21), we replace ∂l by ∂x_B , and α by 0. We obtain $\dfrac{\partial h_{jx}}{\partial x_B} = -\dfrac{\sin\beta}{\sin(\gamma_j-\beta)}$.

Similarly for ∂h_{jy} when $\alpha = \pi/2$: $\dfrac{\partial h_{jy}}{\partial y_B} = \dfrac{\cos\beta}{\sin(\gamma_j-\beta)}$.

Hence it follows:

$$\partial h_j^{\mathrm{s}} = -\frac{\sin\beta}{\sin(\gamma_j-\beta)}\partial x_B + \frac{\cos\beta}{\sin(\gamma_j-\beta)}\partial y_B. \tag{24}$$

Further:

$$\frac{\partial h_j^{\mathrm{s}}}{\partial L} = -\frac{\sin\beta}{\sin(\gamma_j-\beta)}\cdot\frac{\partial x_B}{\partial L} + \frac{\cos\beta}{\sin(\gamma_j-\beta)}\cdot\frac{\partial y_B}{\partial L}. \tag{25}$$

Derivatives $\dfrac{\partial x_B}{\partial L}$ and $\dfrac{\partial y_B}{\partial L}$ are calculated by formulas (7) and (8), in which, instead of $\dfrac{\partial x_B}{\partial k}$ and $\dfrac{\partial y_B}{\partial k}$, we should substitute their expressions from (14) and (15), respectively.

For intersections with normals inside the clothoid in (22), instead of (6) and (7), we should use expressions $\dfrac{\partial x_C}{\partial L} = -\dfrac{\partial x_C}{\partial k}\cdot\dfrac{(\sigma_B-\sigma_A)}{L^2}$ and $\dfrac{\partial y_C}{\partial L} = -\dfrac{\partial y_C}{\partial k}\cdot\dfrac{(\sigma_B-\sigma_A)}{L^2}$, while the derivatives $\frac{\partial x_C}{\partial k}$ and $\frac{\partial y_C}{\partial k}$ should be calculated by formulas (13) and (14), substituting x_C, y_C instead of x_B, y_B, and φ_C instead of φ_B and L, representing the length of the clothoid from the initial point A to the end point B.

For the calculation of ∂h_j^r, it is necessary to take into account the rotation of the subsequent part of the spline around the end point of the clothoid B by the angle $\partial\varphi_B$. In [3], the formula for calculating the derivatives of displacements along the jth normal by the rotation angle is derived, which in our notations will be as follows:

$$\frac{\partial h_j^r}{\partial \varphi_B} = \frac{(x_C - x_B)\cos\beta + (y_C - y_B)\sin\beta}{\sin(\gamma_j - \beta)}.$$

Taking into account that, by formula (9) $\partial\varphi_B/\partial L = (\sigma_A + \sigma_B)/2$, we obtain:

$$\frac{\partial h_j^r}{\partial L} = \frac{(x_C - x_B)\cos\beta + (y_C - y_B)\sin\beta}{\sin(\gamma_j - \beta)}(\sigma_A + \sigma_B)/2. \quad (26)$$

Here x_C, y_C are the coordinates of the point of intersection of the spline with the jth normal; β is the angle of the tangent to the spline at this point C with the OX axis; γ_j is the angle of the normal with the OX axis; σ_A and σ_B are the curvature at the initial and end points of the clothoid.

According to (23), the sum of the right parts of (25) and (26) gives the derivative for the subsequent part of the spline.

4.4. Derivatives by curvature

As already mentioned, the most complex transformation of the spline takes place when changing the curvature σ of one circle and maintaining the values of all other main variables: the parameter of the left clothoid is changed, which results in shifts inside it; the right part of the spline is shifted and rotated up to its end; within the circle arc, there are shifts along the normals intersecting it; additionally, there are shifts and rotations of the spline part beyond the end point of the circle arc; finally, the parameter of the right clothoid is changed, which provides shifts and rotations of the spline part beyond the end point of this clothoid, as well as shifts inside it.

We will calculate the derivatives of displacements by normals along the curvature sequentially by sections.

Within the limits of the left clothoid and up to the end of the spline

For the point C of intersection of the jth normal with the clothoid, we designate its coordinates as x_C, y_C, the length from the origin of the arc of the clothoid (point A) to the point C as L_C, the angle of the tangent at the point C as φ_C, and the parameter of the left clothoid as k_1. Let us use formulas (14) and (15):

$$\frac{\partial x_C}{\partial k_1} = \frac{1}{2k_1}\left(L_C\cos\varphi_C - (x_C - x_A)\right) - \frac{\sigma_A}{2k_1^2}\left((\cos\varphi_C - \cos\varphi_A) + \sigma_A(y_C - y_A)\right), \quad (27)$$

$$\frac{\partial y_C}{\partial k_1} = \frac{1}{2k_1}\left(L_C\sin\varphi_C - (y_C - y_A)\right) - \frac{\sigma_A}{2k_1^2}\left((\sin\varphi_B - \sin\varphi_A) + \sigma_A(x_C - x_A)\right). \quad (28)$$

According to (16) and (17), $\frac{\partial x_C}{\partial\sigma} = \frac{\partial x_C}{\partial k_1}\cdot\frac{1}{L}$ and $\frac{\partial y_C}{\partial\sigma} = \frac{\partial y_C}{\partial k_1}\cdot\frac{1}{L}$, where L is the length of the clothoid AB.

According to (24), the coordinate increment gives the normal displacement increment by $\partial h_j^s = -\frac{\sin\beta}{\sin(\gamma_j - \beta)}\partial x_C + \frac{\cos\beta}{\sin(\gamma_j - \beta)}\partial y_C$. For the corresponding derivative on the curvature of the circle of the jth normal displacement within the left clothoid, we obtain:

$$\frac{\partial h_j^s}{\partial\sigma} = \left(-\frac{\sin\beta}{\sin(\gamma_j - \beta)}\cdot\frac{\partial x_C}{\partial k_1} + \frac{\cos\beta}{\sin(\gamma_j - \beta)}\cdot\frac{\partial y_C}{\partial k_1}\right)\Big/ L. \quad (29)$$

Here, as before, β is the angle with the OX axis of the tangent to the spline at the point C of intersection with the normal, while γ_j is the angle of the normal with the OX axis. In (29), it is necessary to substitute both $\frac{\partial x_C}{\partial k_1}$ and from (27) and (28).

For the normals intersecting the spline to the right of the left clothoid, formulas (27) and (28) are applied to the end point B and the is result substituted into formula (29), in which the angles β and γ_j refer to the corresponding normal. For the same normals, the derivative $\frac{\partial h_j^r}{\partial\sigma}$ due to the rotation of the tangent at point B of the clothoid is calculated using (26) and $\frac{\partial\varphi_B}{\partial\sigma} = \frac{L}{2}$, which is derived from (4). As a result, for an arbitrary point C of the intersection of the normal with the spline to the right of the left clothoid, we obtain:

$$\frac{\partial h_j^r}{\partial\sigma} = \frac{(x_C - x_B)\cos\beta + (y_C - y_B)\sin\beta}{\sin(\gamma_j - \beta)}\cdot\frac{L}{2}. \quad (30)$$

Summarizing (29) and (30) gives

$$\frac{\partial h_j}{\partial \sigma} = \frac{\partial h_j^{\mathrm{s}}}{\partial \sigma} + \frac{\partial h_j^{\mathrm{r}}}{\partial \sigma}. \quad (31)$$

Within the circle and to the end of the spline

Additionally, there are changes in coordinates of intersection points with normals within the circle arc due to changes in its curvature.

Formula (17), obtained in [1] for calculating the partial derivatives of the displacements h_j along normals within the circle by radius R, has the following form $\frac{\delta h_j}{\delta R} = \frac{\cos(\beta - \alpha) - 1}{\sin(\gamma - \beta)}$. In it, there are the angles with the OX axis: α and β are the angles of the tangents to the arc of the circle at its initial and end points, while γ_j is the angle of the jth normal. In our designations for the curvature derivative of the displacements along the normals inside the circle, we obtain:

$$\frac{\partial h_j^{\mathrm{s1}}}{\partial \sigma} = \frac{1 - \cos(\beta - \varphi_{\mathrm{B}})}{\sin(\gamma_j - \beta)\sigma^2}. \quad (32)$$

As a result, for the derivatives of displacements along the normals intersecting the arc of the circle, we obtain:

$$\frac{\partial h_j}{\partial \sigma} = \frac{\partial h_j^{\mathrm{s}}}{\partial \sigma} + \frac{\partial h_j^{\mathrm{r}}}{\partial \sigma} + \frac{\partial h_j^{\mathrm{s1}}}{\partial \sigma}. \quad (33)$$

Due to the change of curvature σ, there is an additional shift of the whole subsequent part of the spline from the end of the circle arc (point B), as well as its rotation centered at this point.

According to formulas (14) and (15) from [1], when passing from radius to curvature, we obtain:

$$\frac{\partial x_{\mathrm{B}}}{\partial \sigma} = -\frac{\sin\beta - \sin\alpha - (\beta - \alpha)\cos\beta}{\sigma^2}, \quad (34)$$

$$\frac{\partial y_{\mathrm{B}}}{\partial \sigma} = -\frac{\cos\alpha - \cos\beta - (\beta - \alpha)\sin\beta}{\sigma^2}. \quad (35)$$

Here, α and β are the angles with the OX axis of the tangents to the arc of the circle at its initial and end points, respectively.

We obtain for the derivatives of displacements h_j^{s2} along the normals resulting from the shift at the end point of the circle using formula (24), which allows us to switch from displacements along x and y coordinates to displacements along the normal:

$$\frac{\partial h_j^{\mathrm{s2}}}{\partial \sigma} = -\frac{\sin\beta_1}{\sin(\gamma_j - \beta_1)} \cdot \frac{\partial x_{\mathrm{B}}}{\partial \sigma} + \frac{\cos\beta_1}{\sin(\gamma_j - \beta_1)} \cdot \frac{\partial y_{\mathrm{B}}}{\partial \sigma}. \quad (36)$$

Here, β_1 is the angle with the OX axis of the tangent to the spline at the point of its intersection by the jth normal; γ_j is the angle of this normal with the OX axis.

Following substitution $\frac{\partial x_{\mathrm{B}}}{\partial \sigma}$ and $\frac{\partial y_{\mathrm{B}}}{\partial \sigma}$ from (34) and (35) into (36) and simplifications, we obtain:

$$\frac{\partial h_j^{\mathrm{s2}}}{\partial \sigma} = -\frac{\cos(\beta_1 - \alpha) - \cos(\beta_1 - \beta) + (\beta - \alpha)\sin(\beta_1 - \beta)}{\sin(\gamma_j - \beta_1)\sigma^2}. \quad (37)$$

The consequences of the tangent rotation at the end point of the circle when its curvature changes will be taken into account in the same way as was done above for the tangent rotation at the end of the left clothoid. According to (26)

$$\frac{\partial h_j^{\mathrm{r2}}}{\partial \varphi_{\mathrm{B}}} = \frac{(x_{\mathrm{C}} - x_{\mathrm{B}})\cos\beta + (y_{\mathrm{C}} - y_{\mathrm{B}})\sin\beta}{\sin(\gamma_j - \beta)}.$$

Here x_{C}, y_{C} are the coordinates of the point of intersection of the spline with the jth normal; β is the angle of the tangent to the spline at this point C with the OX axis; γ_j is the angle of the normal with the OX axis; φ_{B} is the angle of the tangent to the arc of the circle at its end point.

Taking into account that, for a circle $\frac{\partial \varphi_{\mathrm{B}}}{\partial \sigma} = L$, where L is the length of the circle arc, we obtain:

$$\frac{\partial h_j^{\mathrm{r2}}}{\partial \sigma} = \frac{(x_{\mathrm{C}} - x_{\mathrm{B}})\cos\beta + (y_{\mathrm{C}} - y_{\mathrm{B}})\sin\beta}{\sin(\gamma_j - \beta)} L. \quad (38)$$

Formulas (37) and (38) are true for all points of intersection of normals with the spline not only within the right clothoid, but also up to the end of the spline. The effect of a change in the circle curvature on the right clothoid is taken into account in the same way.

5. CALCULATION OF THE OBJECTIVE FUNCTION GRADIENT

The initial approximation for the optimization algorithm is a spline obtained by a separate program implementing the dynamic programming method [1]. Using this spline, the offsets of given survey points along the normals to the design position are determined (Fig. 2). These are the current values of intermediate variables h_j. In order to determine them, the elements of the spline starting from the initial straight line are sequentially considered. For each element (line, clothoid, circle) the number of the first normal intersecting it is memorized.

Formula (9) from [1] is used for determining the intersection points of normals with the circle. The iterative algorithm [19] is used to find intersections with the clothoid. Then, for each basic variable x_i (lengths of elements and curvatures of circles), the number of the first normal j_i is sequentially determined, the displacement along which is affected by the change of the corresponding basic variable. For the lengths of straight lines and circles, this is the number of the first normal that intersects the next element. For the length of a clothoid, it is the number of the first normal intersecting it; for the curvature of a circle, it is the number of the first normal intersecting the left clothoid. The number of the final normal for all elements is the number of the last normal n.

The derivatives of the initial objective function (2) by main variables are calculated by the formula:

$$\frac{\partial F(\mathbf{h}(\mathbf{x}))}{\partial x_i} = \sum_{j=j_i}^{n} h_j \frac{\partial h_j}{\partial x_j}. \qquad (39)$$

Here $\mathbf{x}$ and $\mathbf{h}$ are the vectors of basic and intermediate variables, respectively.

The same modified Lagrange function [20–22] and the same algorithm [23, 24] as for the spline consisting of line segments and arcs of circles [3] are used to optimize the spline parameters. For this purpose, the derivative of the penalty function [3] is added to the right part of (39) when calculating the gradient.

CONCLUSIONS

The main result of this research is the development of mathematical models and algorithms for approximation of functions given by a discrete sequence of points by compound splines of complex structure, including splines with clothoids. A successful choice of variables allowed us to solve the task of approximating multivalued functions. Such problems are typical of those arising in the design of railroad and highway traces.

The unique approach of obtaining formulas for calculating partial derivatives in the absence of analytical expressions of differentiable functions can also be used in solving other problems.

Performed calculations using the experimental programs have shown that, although the presence of clothoids significantly increases counting time, this does not become critical when using commonly available modern personal computers. Unfortunately, the developed algorithms and programs have yet to find practical application due to the lack of interest in improving the quality of design solutions at the same time as reducing costs in the construction and reconstruction of the roads and railways.

Authors' contribution. All authors equally contributed to the present work.

REFERENCES

1. Karpov D.A., Struchenkov V.I. Two-stage spline-approximation in linear structure routing. *Russ. Technol. J.* 2021;9(5):45−56 (in Russ.). https://doi.org/10.32362/2500-316X-2021-9-5-45-56
2. Karpov D.A., Struchenkov V.I. Spline approximation of multivalued function in leaner structures routing. *Russ. Technol. J.* 2022;10(4):65–74 (in Russ.). https://doi.org/10.32362/2500-316X-2022-10-4-65-74
3. Karpov D.A., Struchenkov V.I. Optimization of spline parameters in approximation of multi-valued function *Russ. Technol. J.* 2023;11(2):72–83 (in Russ.). https://doi.org/10.32362/2500-316X-2023-11-2-72-83
4. Li W., Pu H., Schonfeld P., et al. A Method for Automatically Recreating the Horizontal Alignment Geometry of Existing Railways. *Comput. Aided Civ. Infrastruct. Eng.* 2019;34(1):71–94. https://doi.org/10.1111/mice.12392
5. Jha M.K., McCall C., Schonfeld P. Using GIS, genetic algorithms, and visualization in highway development. *Comput. Aided Civ. Infrastruct. Eng.* 2001;16(6):399–414. https://doi.org/10.1111/0885-9507.00242
6. Jha M.K., Schonfeld P. A highway alignment optimization model using geographic information systems. *Transp. Res. Part A. Policy Pract*. 2004;8(6):455–481. https://doi.org/10.1016/j.tra.2004.04.001
7. Jong J.C., Jha M.K., Schonfeld P. Preliminary highway design with genetic algorithms and geographic information systems. *Comput. Aided Civ. Infrastruct. Eng.* 2000;15(4):261–271. https://doi.org/10.1111/0885-9507.00190
8. Kang M.W., Schonfeld P., Yang N. Prescreening and repairing in a genetic algorithm for highway alignment optimization. *Comput. Aided Civ. Infrastruct. Eng.* 2009;24(2):109–119. https://doi.org/10.1111/j.1467-8667.2008.00574.x
9. Pushak Y., Hare W., Lucet Y. Multiple-path selection for new highway alignments using discrete algorithms. *Eur. J. Oper. Res*. 2016;248(2):415–427. https://doi.org/10.1016/j.ejor.2015.07.039
10. Sarma K.C., Adeli H. Bilevel parallel genetic algorithms for optimization of large steel structures. *Comput. Aided Civ. Infrastruct. Eng.* 2001;16(5):295–304. https://doi.org/10.1111/0885-9507.00234
11. Shafahi Y., Bagherian M. A customized particle swarm method to solve highway alignment optimization problem. *Comput. Aided Civ. Infrastruct. Eng.* 2013;28(1):52–67. https://doi.org/10.1111/j.1467-8667.2012.00769.x
12. Bosurgi G., D'Andrea A. A polynomial parametric curve (PPC-curve) for the design of horizontal geometry of highways. *Comput. Aided Civ. Infrastruct. Eng.* 2012;27(4):303–312. https://doi.org/10.1111/j.1467-8667.2011.00750.x
13. Cerf R. The quasispecies regime for the simple genetic algorithm with roulette wheel Selection. Cornell University. *Adv. Appl. Probability*. 2017;49(3):903–926. https://doi.org/10.1017/apr.2017.26

14. Oudshoorn M., Koppenberg T., Yorke-Smith N. Optimization of annual planned rail maintenance. *Comput. Aided Civ. Infrastruct. Eng.* 2021;37(6):669–687. https://doi.org/10.1111/mice.12764
15. Struchenkov V.I. New algorithm for perelement calculation of line structures routes. *Informacionnye tekhnologii = Information Technologies*. 2015;21(4):271–276 (in Russ.).
16. Borodakii Yu.V., Zagrebaev A.M., Kritsyna N.A., Kulyabichev Yu.P., Shumilov Yu.Yu. *Nelineinoe programmirovanie v sovremennykh zadachakh optimizatsii* (*Nonlinear Programming in Modern Optimization Problem*). Moscow: NIYAU MEPhI; 2008. 244 p. (in Russ.).
17. Polyakov V.M., Agalarov Z.S. *Metody optimizatsii* (*Optimization Methods)*. Moscow: Dashkov i K; 2022. 86 p. (in Russ.). ISBN 978-5-3940-5003-9
18. Gasnikov A.V. *Sovremennye chislennye metody optimizatsii. Metod universal'nogo gradientnogo spuska* (*Modern Numerical Optimization Methods. Universal Gradient Method Descent*). Moscow: MTsNMO; 2021.272 p. (in Russ.). ISBN 978-5-4439-1614-9
19. Struchenkov V.I. *Metody optimizatsii trass v SAPR lineinykh sooruzhenii* (*Methods for Route Optimization in CAD of Linear Structures*). Moscow: SOLON-Press; 2020. 272 p. (in Russ.). ISBN 978-5-9135-9139-5
20. Kochenderfer M.D., Wheeler T.A. *Algoritmy optimizatsii* (*Algorithms for Optimization*). Moscow: Vil'yams; 2020. 528 p. (in Russ.).
[Kochenderfer M.D., Wheeler T.A. *Algorithms for Optimization*. London: The MIT Press; 2019. 520 p.]
21. Audet C., Hare W. *Derivative-Free and Blackbox Optimization.* Springer Series in Operations Research and Financial Engineering. Springer; 2017. 302 p. https://doi.org/10.1007/978-3-319-68913-5
22. Chernorutskii I.G. Metody optimizatsii. Komp'yuternye tekhnologii (*Methods of Optimization*. *Computer Technologies*). St. Petersburg: BHV-Petersburg; 2011. 329 p. (in Russ.).
23. Gill Ph.E., Murray W., Wright M.H. *Prakticheskaya optimizatsiya* (*Practical Optimization*): transl. from Engl. Moscow: Mir; 1985. 509 p. (in Russ.).
[Gill Ph.E., Murray W., Wright M.H. *Practical Optimization*. London: Academic Press; 1981. 402 p.]
24. Larichev O.I., Gorvits G.G. *Metody poiska lokal'nykh ekstremumov ovrazhnykh funktsii* (*Methods for Finding Local Extrema of Ravine Functions*). Moscow: Nauka; 1990. 96 p. (in Russ.).

СПИСОК ЛИТЕРАТУРЫ

1. Карпов Д.А., Струченков В.И. Двухэтапная сплайн-аппроксимация в компьютерном проектировании трасс линейных сооружений. *Russ. Technol. J.* 2021;9(5):45–56. https://doi.org/10.32362/2500-316X-2021-9-5-45-56
2. Карпов Д.А., Струченков В.И. Сплайн-аппроксимация многозначных функций в проектировании трасс линейных сооружений. *Russ. Technol. J.* 2022;10(4):65–74. https://doi.org/10.32362/2500-316X-2022-10-4-65-74
3. Карпов Д.А., Струченков В.И. Оптимизация параметров сплайна при аппроксимации многозначных функций. *Russ. Technol. J.* 2023;11(2);72–83. https://doi.org/10.32362/2500-316X-2023-11-2-72-83
4. Li W., Pu H., Schonfeld P., et al. A Method for Automatically Recreating the Horizontal Alignment Geometry of Existing Railways. *Comput. Aided Civ. Infrastruct. Eng.* 2019;34(1):71–94. https://doi.org/10.1111/mice.12392
5. Jha M.K., McCall C., Schonfeld P. Using GIS, genetic algorithms, and visualization in highway development. *Comput. Aided Civ. Infrastruct. Eng.* 2001;16(6):399–414. https://doi.org/10.1111/0885-9507.00242
6. Jha M.K., Schonfeld P. A highway alignment optimization model using geographic information systems. *Transp. Res. Part A. Policy Pract*. 2004;8(6):455–481. https://doi.org/10.1016/j.tra.2004.04.001
7. Jong J.C., Jha M.K., Schonfeld P. Preliminary highway design with genetic algorithms and geographic information systems. *Comput. Aided Civ. Infrastruct. Eng.* 2000;15(4):261–271. https://doi.org/10.1111/0885-9507.00190
8. Kang M.W., Schonfeld P., Yang N. Prescreening and repairing in a genetic algorithm for highway alignment optimization. *Comput. Aided Civ. Infrastruct. Eng.* 2009;24(2):109–119. https://doi.org/10.1111/j.1467-8667.2008.00574.x
9. Pushak Y., Hare W., Lucet Y. Multiple-path selection for new highway alignments using discrete algorithms. *Eur. J. Oper. Res*. 2016;248(2):415–427. https://doi.org/10.1016/j.ejor.2015.07.039
10. Sarma K.C., Adeli H. Bilevel parallel genetic algorithms for optimization of large steel structures. *Comput. Aided Civ. Infrastruct. Eng.* 2001;16(5):295–304. https://doi.org/10.1111/0885-9507.00234
11. Shafahi Y., Bagherian M. A customized particle swarm method to solve highway alignment optimization problem. *Comput. Aided Civ. Infrastruct. Eng.* 2013;28(1):52–67. https://doi.org/10.1111/j.1467-8667.2012.00769.x
12. Bosurgi G., D'Andrea A. A polynomial parametric curve (PPC-curve) for the design of horizontal geometry of highways. *Comput. Aided Civ. Infrastruct. Eng.* 2012;27(4):303–312. https://doi.org/10.1111/j.1467-8667.2011.00750.x
13. Cerf R. The quasispecies regime for the simple genetic algorithm with roulette wheel Selection. Cornell University. *Adv. Appl. Probability*. 2017;49(3):903–926. https://doi.org/10.1017/apr.2017.26
14. Oudshoorn M., Koppenberg T., Yorke-Smith N. Optimization of annual planned rail maintenance. *Comput. Aided Civ. Infrastruct. Eng.* 2021;37(6):669–687. https://doi.org/10.1111/mice.12764
15. Струченков В.И. Новый алгоритм поэлементного расчета трасс в САПР линейных сооружений. *Информационные технологии.* 2015;21(4):271–276.
16. Бородакий Ю.В., Загребаев А.М., Крицына Н.А., Кулябичев Ю.П., Шумилов Ю.Ю. *Нелинейное программирование в современных задачах оптимизации*. М.: НИЯУ МИФИ; 2011. 244 с. ISBN 987-5-7262-1451-1

17. Поляков В.М., Агаларов З.С. *Методы оптимизации*. М.: Дашков и К; 2022. 86 с. ISBN 978-5-3940-5003-9
18. Гасников А.В. *Современные численные методы оптимизации. Метод универсального градиентного спуска*. М.: МЦНМО; 2021. 272 с. ISBN 978-5-4439-1614-9
19. Струченков В.И. *Методы оптимизации трасс в САПР линейных сооружений*. М.: СОЛОН-Пресс; 2020. 272 с. ISBN 978-5-9135-9139-5
20. Кохендерфер М. Д., Уилер Т.А. *Алгоритмы оптимизации*. М.: Вильямс; 2020. 528 с.
21. Audet C., Hare W. *Derivative-Free and Blackbox Optimization.* Springer Series in Operations Research and Financial Engineering. Springer; 2017. 302 p. https://doi.org/10.1007/978-3-319-68913-5
22. Черноруцкий И.Г. *Методы оптимизации. Компьютерные технологии*. СПб.: БХВ-Петербург; 2011. 329 с.
23. Гилл Ф., Мюррей У., Райт М. *Практическая оптимизация*: пер. с англ. М.: Мир; 1985. 509 с.
24. Ларичев О.И., Горвиц Г.Г. *Методы поиска локальных экстремумов овражных функций*. М.: Наука; 1990. 96 с.

About the authors

Valery I. Struchenkov, Dr. Sci. (Eng.), Professor, Department of Geographic Information Systems, Institute of Radio Electronics and Informatics, MIREA – Russian Technological University (78, Vernadskogo pr., Moscow, 119454 Russia). E-mail: str1942@mail.ru. Scopus Author ID 36451166800, RSCI SPIN-code 4581-4698, https://orcid.org/0000-0002-9801-7454

Dmitry A. Karpov, Cand. Sci. (Eng.), Head of the Department of Geographic Information Systems, Institute of Radio Electronics and Informatics, MIREA – Russian Technological University (78, Vernadskogo pr., Moscow, 119454 Russia). E-mail: karpov@mirea.ru. Scopus Author ID 57211584863, RSCI SPIN-code 2619-7100, https://orcid.org/0000-0003-3734-7182

Об авторах

Струченков Валерий Иванович, д.т.н., профессор, кафедра геоинформационных систем Института радиоэлектроники и информатики ФГБОУ ВО «МИРЭА – Российский технологический университет» (119454, Россия, Москва, пр-т Вернадского, д. 78). E-mail: str1942@mail.ru. Scopus Author ID 36451166800, SPIN-код РИНЦ 4581-4698, https://orcid.org/0000-0002-9801-7454

Карпов Дмитрий Анатольевич, к.т.н., заведующий кафедрой геоинформационных систем Института радиоэлектроники и информатики ФГБОУ ВО «МИРЭА – Российский технологический университет» (119454, Россия, Москва, пр-т Вернадского, д. 78). E-mail: karpov@mirea.ru. Scopus Author ID 57211584863, SPIN-код РИНЦ 2619-7100, https://orcid.org/0000-0003-3734-7182

Translated from Russian into English by Lyudmila O. Bychkova
Edited for English language and spelling by Thomas A. Beavitt

Product quality management. Standardization

Управление качеством продукции. Стандартизация

UDC 681.2.083:535.2:543.063
https://doi.org/10.32362/2500-316X-2024-12-1-123-132

RESEARCH ARTICLE

Quality control of instruments for measuring the characteristics of bactericidal UV radiation

Olga A. Minaeva [1,@], Alexander V. Ragutkin [1], Sergei I. Anevsky [1], Roman V. Minaev [2], Thanh T. Minh [1], Inna A. Romanova [1]

[1] *MIREA – Russian Technological University, Moscow, 119454 Russia*
[2] *Elektrosteklo, Moscow, 119571 Russia*
[@] *Corresponding author, e-mail: minaeva_o@mirea.ru*

Abstract

Objectives. Quality control of instruments for measuring bactericidal irradiance of ultraviolet (UV) radiation is based on studying the main metrological characteristics. These characteristics include: angular and spectral sensitivity; linearity range; and absolute calibration in irradiance units. Deviations of the angular sensitivity of measuring instruments from the ideal cosine characteristic can significantly impact error estimation. They can also lead to the distortion of measurement results and a significant difference in instrument readings. The aim of this work is to enhance accuracy in resolving metrological problems of determining irradiance of bactericidal radiation.

Methods. An effective method of resolving this problem is to introduce correction coefficients for the angular sensitivity of radiometers, spectroradiometers and dosimeters. The values are calculated based on the results of measurements on the goniometer when testing measuring instruments. An important role is played by computer models and digital twins of measuring instruments based on the results of studies of the metrological characteristics of radiometers by means of software. This includes modeling the measuring task.

Results. The study of angular dependence of bactericidal UV radiometer sensitivity complemented by an analysis of measurement results obtained by other authors allows determining the value of the angular sensitivity correction coefficients by the deviation of the angular sensitivity of the irradiance measuring instruments of bactericidal radiation from the standard cosine dependence.

Conclusions. Deviations of the angular dependence of bactericidal radiation UV radiometer sensitivity from the cosine characteristic lead to a significant underestimation of the irradiance measurements results from extended emitters. An effective solution is the use of digital angular sensitivity correction coefficients to measure the irradiance of bactericidal radiation determined during tests. When assessing the quality of radiometers, spectroradiometers and dosimeters for bactericidal radiation, incomplete control of the main metrological characteristics of the measuring instruments creates risks of serious errors in the measurement results of bactericidal irradiance.

Keywords: angular sensitivity correction, radiometers, spectroradiometers, spectral sensitivity, bactericidal installation

• **Submitted:** 01.11.2023 • **Revised:** 03.11.2023 • **Accepted:** 11.12.2023

For citation: Minaeva O.A., Ragutkin A.V., Anevsky S.I., Minaev R.V., Minh Th.T., Romanova I.A. Quality control of instruments for measuring the characteristics of bactericidal UV radiation. *Russ. Technol. J.* 2024;12(1):123–132. https://doi.org/10.32362/2500-316X-2024-12-1-123-132

Financial disclosure: The authors have no a financial or property interest in any material or method mentioned.

The authors declare no conflicts of interest.

НАУЧНАЯ СТАТЬЯ

Контроль качества средств измерений характеристик бактерицидного УФ-излучения

О.А. Минаева [1, @], А.В. Рагуткин [1], С.И. Аневский [1], Р.В. Минаев [2], Т.Ч. Минь [1], И.А. Романова [1]

[1] *МИРЭА – Российский технологический университет, Москва, 119454 Россия*
[2] *Электростекло, Москва, 119571 Россия*
[@] *Автор для переписки, e-mail: minaeva_o@mirea.ru*

Резюме
Цели. Контроль качества средств измерений бактерицидной освещенности ультрафиолетового (УФ) излучения основан на исследовании основных метрологических характеристик, включающих угловую и спектральную чувствительность, диапазон линейности, абсолютную калибровку в единицах энергетической освещенности. Наибольшее влияние на предел допускаемой погрешности оказывают отклонения угловой чувствительности средств измерений от идеальной косинусной характеристики, приводящие к искажению результатов измерений и существенной разнице в показаниях приборов. Целью работы является повышение точности средств измерений при решении метрологических задач определения энергетической освещенности бактерицидного излучения.
Методы. Эффективным методом решения проблемы является введение коэффициентов коррекции угловой чувствительности радиометров, спектрорадиометров и дозиметров, значения которых рассчитываются по результатам измерений чувствительности на гониометре при испытаниях средств измерений. Большую роль играет использование компьютерных моделей и цифровых двойников средств измерений на основе результатов исследований метрологических характеристик радиометров с использованием программного обеспечения, включающего моделирование измерительной задачи.
Результаты. Исследование угловой зависимости чувствительности бактерицидных УФ-радиометров на гониометре и анализ результатов измерений, полученных другими авторами, позволяют по отклонению угловой чувствительности средств измерений энергетической освещенности бактерицидного излучения от стандартной косинусной зависимости определить значение коэффициентов коррекции угловой чувствительности.
Выводы. Отклонения угловой зависимости чувствительности УФ-радиометров бактерицидного излучения от косинусной характеристики приводят к существенному занижению результатов измерений энергетической освещенности от протяженных излучателей. Эффективным решением проблемы является использование коэффициентов цифровой угловой коррекции чувствительности средств измерений энергетической освещенности бактерицидного излучения, определяемых при испытаниях. При оценке качества радиометров, спектрорадиометров и дозиметров бактерицидного излучения неполный контроль основных метрологических характеристик средств измерений создает риски серьезных ошибок в результатах измерений энергетической бактерицидной освещенности.

Ключевые слова: коррекция угловой чувствительности, радиометры, спектрорадиометры, спектральная чувствительность, бактерицидные установки

• **Поступила:** 01.11.2023 • **Доработана:** 03.11.2023 • **Принята к опубликованию:** 11.12.2023

Для цитирования: Минаева О.А., Рагуткин А.В., Аневский С.И., Минаев Р.В., Минь Т.Ч., Романова И.А. Контроль качества средств измерений характеристик бактерицидного УФ-излучения. *Russ. Technol. J.* 2024;12(1):123–132. https://doi.org/10.32362/2500-316X-2024-12-1-123-132

Прозрачность финансовой деятельности: Авторы не имеют финансовой заинтересованности в представленных материалах или методах.

Авторы заявляют об отсутствии конфликта интересов.

INTRODUCTION

The use of bactericidal irradiation facilities in medicine, photobiology, photochemistry, and pharmacology, especially during the COVID-19 pandemic, has shown the need for increased requirements for the quality control of ultraviolet irradiators, as well as means of measuring energetic and effective bactericidal irradiance.[1]

Tubular low-pressure mercury lamps are used in bactericidal complexes as the sources of ultraviolet (UV) radiation. More than 60% of the radiation flux falls on the resonance line with a wavelength of 253.7 nm, located in the range of maximum bactericidal action of UV radiation from 230 to 300 nm [1]. The advantages of using low-pressure mercury lamps are associated with the position of the maximum bactericidal action of UV radiation on destructively modified DNA and RNA damage corresponding to a wavelength of 265 nm. Currently, along with low-pressure mercury lamps, bactericidal UV irradiators based on xenon pulse emitters, LEDs, and high-pressure mercury lamps are increasingly being used [2].

CHARACTERISTICS OF BACTERICIDAL RADIATION MEASURING INSTRUMENTS

In order to ensure the quality of bactericidal irradiation facilities, the main radiometric characteristics need to be monitored. This includes: the spectral density of the radiation flux of bactericidal radiation; energy illuminance; exposure dose; photobiological hazard; and the rate of decrease of the bactericidal radiation flux. Radiometers, spectroradiometers and dosimeters are used as measuring instruments to control one of the main characteristics of UV emitters: energy effective bactericidal illumination [3–5].[2] Problems relating to the formation of metrological characteristics of measuring instruments of bactericidal effective illuminance are related to the legislative and technical documents. These documents are also based on the research of national metrological institutes and contain requirements for the quality assurance of measurements.[3, 4, 5, 6]

An integrated approach to quality management of measuring instruments for measuring the characteristics of the bactericidal UV radiation includes:

- optimization of quality control methods for UV radiometers during the lifetime of measuring instruments with the use of digital technologies during verification and calibration;
- risk and opportunity management in the measurement of bactericidal irradiance through the characterization of measuring instruments related to the practical measurement task;
- development of methods for statistical quality control and consumer evaluation of bactericidal irradiance measuring instruments;
- application of computer models for assessing the quality of measuring instruments when confirming conformity to existing technical regulations and standards.

[1] Clark M., Zuber R., Ribnitzky M. *Far UV-C Germicidal Sources: Measurement Challenges and Solutions. UV Solutions*. 2022. https://uvsolutionsmag.com/articles/2022/far-uv-c-germicidal-sources-measurement-challenges-and-solutions/. Accessed November 01, 2023.

[2] Miller C.C. *UVC Measurement Methods & UVC Documentary Standard Development.* National Institute of Standards and Technology. Washington, DC: U.S. Department of Energy; 2022. https://www.energy.gov/sites/default/files/2022-02/ssl-rd22_miller_guv.pdf. Accessed November 01, 2023.

[3] GOST R 8.760-2011. *State system for ensuring the uniformity of measurements. Measurement of energy and the effective characteristics ultraviolet radiation germicidal irradiators. Procedure of measurements*. Moscow: Standartinform; 2019 (in Russ.). https://docs.cntd.ru/document/1200095426. Accessed November 01, 2023.

[4] RMG 70-2003. GSOEI. *Characteristics of ultraviolet radiation of bactericidal irradiators. Methodology for performing measurements*. Moscow: IPK Izdatelstvo standartov; 2004 (in Russ.). https://docs.cntd.ru/document/1200037656. Accessed November 01, 2023.

[5] R 50.2.018-2001. GSOEI. *Measuring instruments of ultraviolet radiation characteristics of bactericidal irradiators. Methods of verification*. Moscow: Gosstandart; 2001 (in Russ.). https://docs.cntd.ru/document/1200029414. Accessed November 01, 2023.

[6] *Ultraviolet air disinfection*. Techn. Report CIE Central Bureau. Vienna. Austria: 2003.

Non-compliance with the requirements of standards and recommendations during practical measurements can lead to differences in the readings of devices of different types, as well as to a loss of accuracy and reliability of measurement results. The technical committees on standardization of the Federal Agency for Technical Regulation and Metrology are responsible for the development of standards and recommendations covering methods of quality control of measuring instruments of bactericidal radiation characteristics.[7] The main metrological characteristics determining the quality of measuring instruments of bactericidal radiation include: angular dependence of radiometer sensitivity; spectral dependence of sensitivity; linearity range; as well as absolute calibration in units of energy illumination. These can be compared to the state primary standards related to the approved state verification schemes.

When assessing the quality of radiometers, spectroradiometers, and dosimeters for bactericidal radiation, the incomplete control of basic metrological characteristics of measuring instruments can create risks of serious errors in the results of measurements of energetic bactericidal irradiance. The deviation of relative spectral sensitivity of radiometers from the relative bactericidal efficiency of UV radiation can significantly impact the accuracy of measuring instruments for bactericidal radiation characteristics. In works on quality assessment of measuring instruments for bactericidal radiation characteristics in the national metrological institutes, special attention is paid to one of the most important characteristics: the angular dependence of sensitivity. Deviation from the ideal cosine characteristic is the primary cause of errors in measurement results [6–8].

METHOD FOR MEASURING THE ANGLE DEFINITION OF THE BACTERICIDAL UV RADIATION RADIOMETERS SENSITIVITY

Resolving matters relating to the correction of the angular dependence of the sensitivity of measuring instruments is especially important when controlling the energy illumination from several radiation sources. It is also significant when evaluating the bactericidal efficiency of extended UV emitters and dimensional panels. When UV radiation falling on the receiving surface of the radiometer deviates from the normal, the radiometer signal decreases. This is because the projection area of the photodetector in the direction of the incident flux decreases in accordance with the cosine relationship. The problems of ensuring accuracy and reliability of the results of practical measurements of energy illumination of bactericidal radiation are associated with the fact that commercially available radiometers have angular dependence of sensitivity. This can differ significantly from the ideal cosine dependence of sensitivity. Various types of goniometers are used to control the angular sensitivity of radiometers, spectroradiometers and UV dosimeters [9].

The required angular correction of the sensitivity of short-wave UV radiation receivers in radiometers, spectroradiometers and dosimeters is a technically difficult task, requiring the development of special devices. Figure 1 shows the angular dependence of the sensitivity of various types of germicidal UV radiometers No. 1, No. 2, and No. 3, as well as the ideal cosine dependence of the sensitivity cos φ [7, 10].

As shown in the diagrams, the decrease in sensitivity of radiometer No. 2 reaches 50% at an angle of incidence of radiation φ on the receiving surface of the radiometer of 30°. At an angle of incidence of 45°, the decrease in sensitivity reaches 75%. The sensitivity of radiometer No. 1 is completely absent at angles of incidence exceeding 75°. This limits its application in water treatment systems at short distances from the radiator. In the area of large angles of incidence of radiation (with a sharp decrease in the levels of radiometer signals proportional to sensitivity) the influence of scattered radiation on the results of measurements of the relative angular sensitivity of the radiometer increases significantly.

A general view of the goniometer for measuring the dependence of the radiometer sensitivity on the angle of incidence of UV radiation is shown in Fig. 2.

Deviation $f(\varphi)$ of the angular sensitivity of the UV radiometer $S(\varphi)$ from the standard function cos φ, expressed in percent, is determined by the expression:

$$f(\varphi) = 100\% \, [\cos\varphi - S(\varphi)]/\cos\varphi. \quad (1)$$

Figure 3 shows the results of measurements of deviations $f(\varphi)$ of angular sensitivity of bactericidal radiation radiometers No. 1, No. 2, and No. 3 from the standard cosine characteristic.

Deviations of the angular dependence of the sensitivity from the cosine characteristic are presented in Fig. 3. The deviations of angular dependence of sensitivity from the cosine characteristic indicate a significant underestimation of the results of measurements of energy illuminance from extended emitters when using commercially available UV radiometers of bactericidal radiation. In order to exclude systematic error, coefficients of angular correction of sensitivity must be used which enable the distortion of the results of measurements of energy bactericidal irradiance to be compensated.

[7] https://www.rst.gov.ru/portal/gost (in Russ.). Accessed November 01, 2023.

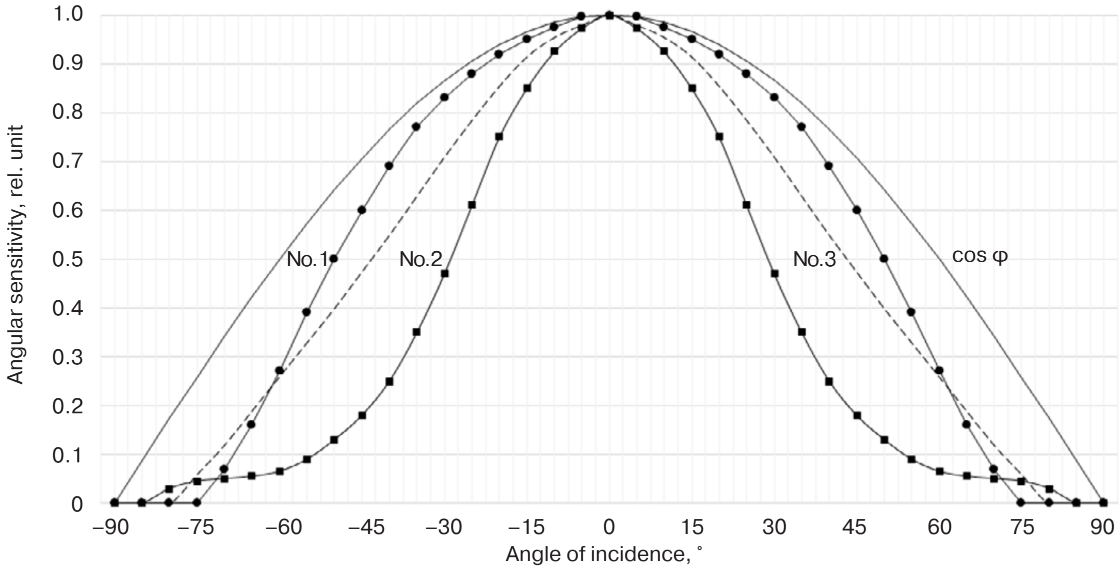

Fig. 1. Angular dependence of sensitivity of different types of bactericidal UV radiometers and ideal cosine dependence of sensitivity

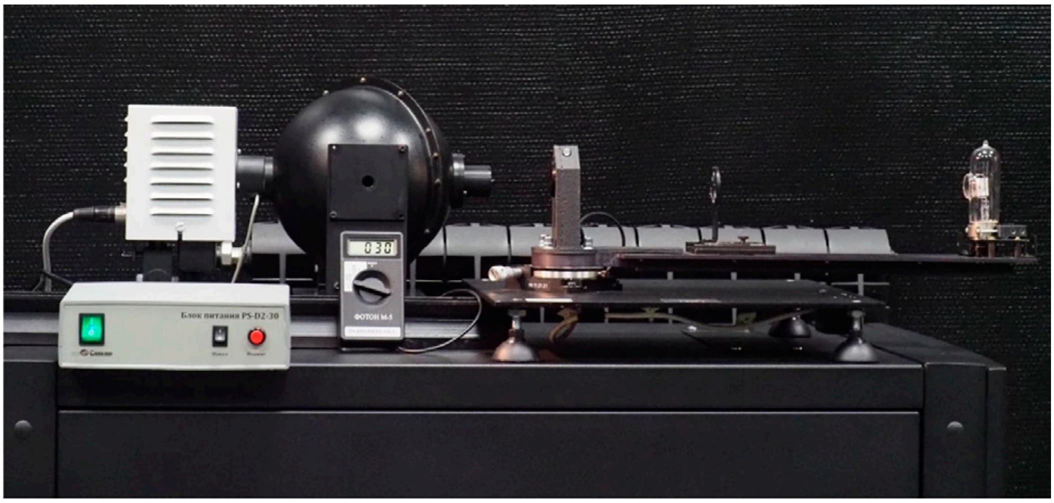

Fig. 2. General view of a goniometer designed for measuring angular sensitivity of bactericidal UV radiation radiometers

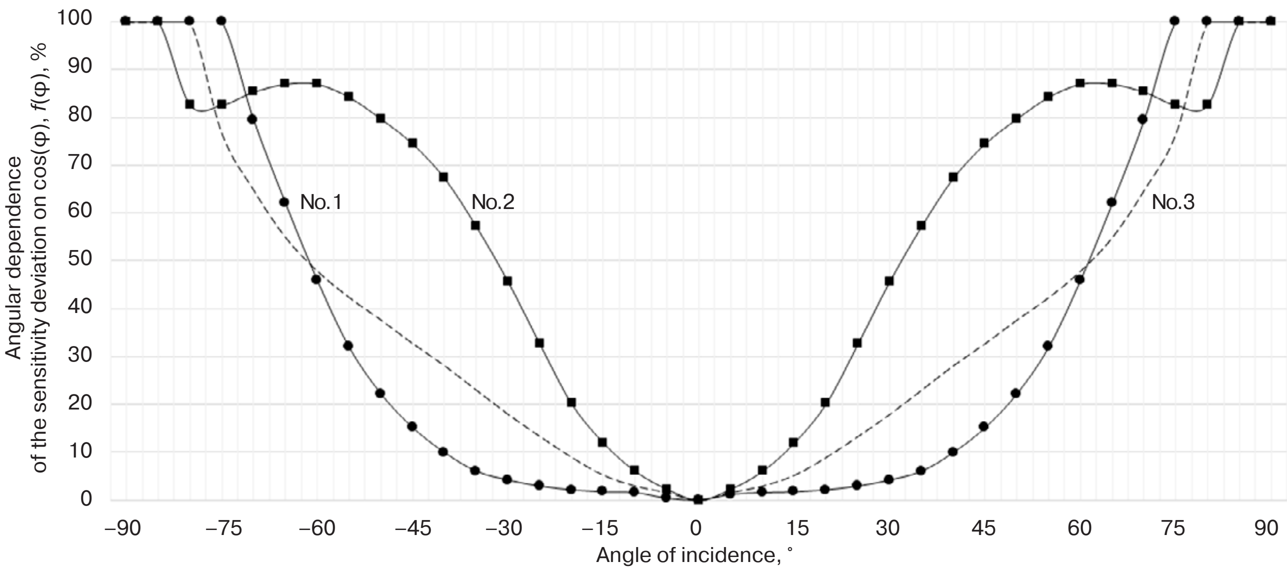

Fig. 3. Deviation $f(\varphi)$ of the bactericidal radiation radiometers angular sensitivity from the standard cosine characteristic

DETERMINATION OF THE COEFFICIENTS OF ANGULAR CORRECTION OF THE UV RADIOMETER SENSITIVITY

The radiometer signal is determined by integrating the energy brightness spectral density (EBSD) over the area of the radiator within the working solid angle, taking into account the spectral and angular dependence of the radiometer sensitivity. The equation describing the signal of a radiometer (spectroradiometer, dosimeter) of bactericidal UV radiation can be represented in the following form:

$$i = N \int_{\Omega_0} \int_{\varphi} \int_{\lambda} \int_{\delta_0} L(\lambda, \delta, \Omega) S(\lambda, \varphi) d\delta\, d\lambda\, d\varphi\, d\Omega, \quad (2)$$

where λ is the wavelength; δ is the radiating area of the UV radiation source; Ω is the solid angle; $L(\lambda, \delta, \Omega)$ is the EBSD of the bactericidal UV radiation source; $S(\lambda, \varphi)$ is the spectral and angular dependence of the radiometer (spectroradiometer, dosimeter) sensitivity); N is the dimension coefficient; δ_0 is the total area of the radiating region of the bactericidal UV radiation source; Ω_0 is the total solid angle determined by the angular dimensions of the bactericidal UV radiation source.

The sensitivity angular correction coefficient $K(\varphi)$ of the radiometers is presented in Fig. 1. This is determined by the results of measurements of the angular dependence of sensitivity. It is intended for the maximum correction of the results of measurements of energy illumination of bactericidal UV radiation arising due to technically imperfect design of diffuse diffusers in the measuring instruments.

The angular correction coefficient of radiometer sensitivity is equal to the ratio of the signal of an ideal radiometer $i_{id}(\varphi)$, This has a standard cosine dependence of sensitivity to the signal of a real radiometer $i_r(\varphi)$:

$$K(\varphi) = i_{id}(\varphi)/i_r(\varphi). \quad (3)$$

In most cases, the relative EBSD of radiation sources and the relative spectral sensitivity of radiometers do not depend on the direction of radiation of the source, or the angle of incidence of radiation on the photodetector. In this case, the angular sensitivity correction coefficient is determined by the angular dependence of the radiometer sensitivity $S(\varphi)$ and the angular dependence of the source EBSD $L(\delta, \Omega)$ according to the expression:

$$K(\varphi) = \frac{\int_{\varphi} \int_{\Omega_0} \int_{\delta_0} L(\delta, \Omega) \cos\varphi d\delta\, d\Omega\, d\varphi}{\int_{\varphi} \int_{\Omega_0} \int_{\delta_0} L(\delta, \Omega) S(\varphi) d\delta\, d\Omega\, d\varphi}. \quad (4)$$

When the radiometer is used to measure the energy illumination produced by a small-diameter tubular bactericidal emitter, the sensitivity angle correction coefficient $K(\varphi)$ is determined by the following formula:

$$K(\varphi) = \frac{\int_{\varphi} \int_{\delta_0} L(\delta, \varphi) \cos\varphi d\delta\, d\varphi}{\int_{\varphi} \int_{\delta_0} L(\delta, \varphi) S(\varphi) d\delta\, d\varphi}. \quad (5)$$

The use of the angular sensitivity correction coefficient taking into account geometric conditions of measurements enables the systematic error of correction of angular sensitivity of radiometer (spectroradiometer, dosimeter) to be radically reduced. This thus compensates for the technical shortcomings of measuring instruments, and excludes any significant variations of measurement results of energy illumination of bactericidal UV radiation by different measuring instruments.

Table presents the results of calculating the values of the angular correction coefficients of sensitivity of UV radiometers No. 1, No. 2, and No. 3 obtained in accordance with expression (5) for low-pressure mercury lamps. The results depend on the maximum angle of deviation of the incident radiation flux from the normal from 10° to 70° to the receiving surface of the radiometer.

Table. Values of angle correction coefficients of UV radiometers sensitivity

UV radiometers	Maximum deflection angle, °						
	10	20	30	40	50	60	70
Radiometer No. 1	1.01	1.03	1.04	1.05	1.08	1.16	1.26
Radiometer No. 2	1.07	1.13	1.31	1.50	1.70	1.08	2.00
Radiometer No. 3	1.03	1.06	1.13	1.18	1.23	1.31	1.39

The data presented in Table shows that the results of measurements of energy illuminance of bactericidal radiation of mercury tube lamps by radiometers of different types will differ significantly from each other.

These results indicate that, in order to meet the requirements of the normative documents[8] for an angular sensitivity correction error of 4%, the coefficients $K(\varphi)$ for radiometer No. 1 at angles of incidence exceeding 40° need to be used. For radiometer No. 2—at angles of incidence exceeding 0°, and for radiometer No. 3—at

[8] Miller C.C. *UVC Measurement Methods & UVC Documentary Standard Development*. National Institute of Standards and Technology. Washington, DC: U.S. Department of Energy; 2022. https://www.energy.gov/sites/default/files/2022-02/ssl-rd22_miller_guv.pdf. Accessed November 01, 2023.

angles of incidence exceeding 10°. Radiometer No. 1 is characterized by the smallest error of angular correction of sensitivity from those presented in Table. For radiometer No. 2, the coefficients of angular correction of sensitivity at any angles of deviation of the incident radiation from normal must be used.

It is difficult to ensure the accuracy of measurements when the emitters are located in the center of the room and the energy illuminance of bactericidal radiation needs to be measured in the corners of the room. This is also the case when the emitters are located in the corners of the room and the energy illuminance is measured in the center [8]. The influence of the quality of the radiometer's angular response on the measurement results is less in the case when the radiometer is directed to the center of the extended emitter. Here the main contribution to the measurement results is made by UV radiation incident at angles close to the normal with respect to the radiometer's receiving surface. The radiation falling on the radiometer receiving surface at large angles to the normal is also lateral to the peripheral radiating region of the radiometer and its contribution is relatively small.

The application of interlaboratory comparisons of measuring instruments of the characteristics of the bactericidal radiation produced by tubular mercury lamps allows discrepancies in the measurement results to be identified. Discrepancies can be significantly reduced by using the coefficients of angular correction of sensitivity.[9]

When creating digital doubles of measuring instruments for energy illuminance of bactericidal UV radiation, the use of sensitivity angular correction coefficients in the list of basic metrological characteristics of the radiometer allows the accuracy and reliability of measurement results to be achieved without the development of complex quartz diffusers.

Evaluation of random and systematic errors of measurement results after introduction of angular correction coefficients of radiometer sensitivity is carried out in accordance with GOST R 8.736-2011[10]. The tolerance limit of error of bactericidal radiation radiometers is established in accordance with the requirements of national and international standards. This limit is estimated based on the results of studies of the error components of the main metrological characteristics of UV radiometers (spectroradiometers, dosimeters). They include: angular and spectral dependence of sensitivity; deviation from linearity of sensitivity in the operating dynamic range; and absolute calibration in units of energy illuminance. The limit of tolerance of measuring instruments of energy bactericidal irradiance is 10%. This takes into account the systematic error of angular correction of sensitivity which is not more than 4%.

In order to estimate the random error of the angular sensitivity of the radiometer, measurements on the goniometer are repeated after rotating the radiometer relative to the optical axis. The unexcluded systematic error in the angular correction of the radiometer is estimated by taking the following into account: the angular resolution of the goniometer; the nonlinearity of the sensitivity; the sensitivity threshold of the radiation receiver; the instability of the energy brightness of the transmitter; and the level of scattered radiation.

For spectroradiometers, the problem of providing angular correction of sensitivity is associated with a small angle of view due to the use of diffraction gratings. This makes it difficult to use spectroradiometers in monitoring the characteristics of bactericidal irradiation facilities without an integrating sphere [11, 12].

The most effective step in ensuring quality by reducing the systematic error of means used to measure the characteristics of bactericidal UV radiation is to introduce coefficients of angular and spectral correction of sensitivity These must take into account the complexities of applied measurement tasks when using digital models and digital twins in the future.

CONCLUSIONS

Analysis of the problem of quality control of bactericidal irradiators shows the need to ensure angular correction of sensitivity of radiometers, spectroradiometers and dosimeters. This is associated with a significant revision of methods and means of measuring the energy illuminance of UV radiation, in order to meet the requirements of existing regulatory documents.

An efficient solution to this problem is the use of correction coefficients of angular sensitivity of radiometers, determined during the type approval tests of measuring instruments.

The most progressive method in the future of increasing accuracy when resolving metrological problems of energy illumination of bactericidal radiation will be the use of computer models and digital doubles of measuring instruments. These will be based on the results of studies of basic metrological characteristics of radiometers, spectroradiometers and dosimeters with the use of software for modeling measurement conditions.

[9] Krames M. *The rise of UV-C LEDs*. LEDs & SSL Magazine. July 24, 2020. https://www.ledsmagazine.com/leds-ssl-design/article/14178371/technology-roadmap-shows-uvc-leds-are-onthe-rise. Accessed November 01, 2023.

[10] GOST R 8.736-2011. *State system for ensuring the uniformity of measurements. Multiple Direct measurements. Methods of measurement results processing. Main positions*. Moscow: Standartinform; 2013 (in Russ.). https://docs.cntd.ru/document/1200089016. Accessed November 01, 2023.

The experience of national metrological institutes in Russia and abroad shows the need to enhance accuracy and eliminate the gross errors in measuring energy illumination created by bactericidal facilities based on the use of correction factors of angular and spectral sensitivity of UV radiometers.

Authors' contribution. All authors equally contributed to the research work.

REFERENCES

1. Kostyuchenko S.V., Tkachev A.A., Frolikova T.N. UV technologies for disinfection of water, air and surfaces: principles and possibilities. *Epidemiologiya i Vaktsinoprofilaktika = Epidemiology and Vaccination Prevention*. 2020;19(5):112–119 (in Russ.). https://doi.org/10.31631/2073-3046-2020-19-5-112-119
2. Kostyuchenko S.V., Volkov S.V., Tkachev A.A., Strelkov A.K., Smirnov A.D., Baranov V.L. Modern trends and peculiarties of UV disinfection usage in water treatment. *Vodosnabzhenie i sanitarnaya tekhnika = Water Supply and Sanitary Equipment*. 2022;7:4–11 (in Russ.). https://doi.org/10.35776/VST.2022.07.01
3. Blatchley E.R. III, Brenner D.J., Claus H., Cowan T.E., Linden K.G., Liu Y., Mao T., et al. Far UV-C radiation: An emerging tool for pandemic control. *Critical Reviews in Environmental Science and Technology*. 2023;53(6):733–753. https://doi.org/10.1080/10643389.2022.2084315
4. Endo T., Gemma A., Mitsuyoshi R., et al. Discussion on effect of material on UV reflection and its disinfection with focus on Japanese Stucco for interior wall. *Sci. Rep.* 2021;11(1):21840. https://doi.org/10.1038/s41598-021-01315-1
5. Neu D.T., Mead K.R., McClelland T.L., Lindsley W.G., Martin S.B., Heil G., See M., Feng H.A. Surface Dosimetry of Ultraviolet Germicidal Irradiation Using a Colorimetric Technique. *Ann. Work Expo. Health*. 2021;65(5):605–611. https://doi.org/10.1093/annweh/wxaa147
6. Zong Y., Brown S.W., Johnson B.C., Lykke K.R., Ohno Y. Simple spectral stray light correction method for array spectroradiometers. *Appl. Opt.* 2006;45(6):1111–1119. https://doi.org/10.1364/AO.45.001111
7. Larason T.C., Cromer C.L. Sources of Error in UV Radiation Measurements. *J. Res. Nat. Inst. Stand. Technol*. 2001;106(4): 649–656. https://doi.org/10.6028/jres.106.030
8. Vijeta Kapri R.K., Saha S., Jaiswal V.K., Sharma P. Theoretical Simulation for Evaluating Error in Irradiance Measurement Using Optical Detectors Having Different Cosine Responses. *MAPAN – Journal of Metrology Society of India*. 2021;36(3): 473–480. https://doi.org/10.1007/s12647-021-00486-6
9. Marquez J.M.A., Bohórquez M.A.M., Garcia J.M., Nieto F.J.A. A New Automatic System for Angular Measurement and Calibration in Radiometric Instruments. *Sensors.* 2010;10(4):3703–3717. https://doi.org/10.3390/s100403703
10. Anevskii S.I., Zolotarevskii Yu.M., Ivanov V.S., Krutikov V.N., Minaeva O.A., Minaev R.V. Spectroradiometry of ultraviolet radiation. *Meas. Tech.* 2016;28(11):1216–1222. http://doi.org/10.1007/s11018-016-0873-9
[Original Russian Text: Anevskii S.I., Zolotarevskii Yu.M., Ivanov V.S., Krutikov V.N., Minaeva O.A., Minaev R.V. Spectroradiometry of ultraviolet radiation. *Izmeritel'naya Tekhnika*. 2015;11:26–30 (in Russ.).]
11. Mekaoui S., Zibordi G. Cosine error for a class of hyperspectral irradiance sensors. *Metrologia*. 2013;50(187):187–199. http://doi.org/10.1088/0026-1394/50/3/187
12. Nevas S., Wübbeler G., Sperling A., Elster C., Teuber A. Simultaneous correction of bandpass and stray-light effects in array spectroradiometer data. *Metrologia*. 2012;49(2):S43–S47. http://doi.org/10.1088/0026-1394/49/2/S43

СПИСОК ЛИТЕРАТУРЫ

1. Костюченко С.В., Ткачев А.А., Фроликова Т.Н. УФ-технологии для обеззараживания воды, воздуха и поверхностей: принципы и возможности. *Эпидемиология и Вакцинопрофилактика*. 2020;19(5):112–119. https://doi.org/10.31631/2073-3046-2020-19-5-112-119
2. Костюченко С.В., Волков С.В., Ткачев А.А., Стрелков А.К., Смирнов А.Д., Баранов В.Л. Современные тенденции и особенности применения УФ-обеззараживания в водоподготовке. *Водоснабжение и санитарная техника*. 2022;7:4–11. https://doi.org/10.35776/VST.2022.07.01
3. Blatchley E.R. III, Brenner D.J., Claus H., Cowan T.E., Linden K.G., Liu Y., Mao T., et al. Far UV-C radiation: An emerging tool for pandemic control. *Critical Reviews in Environmental Science and Technology*. 2023;53(6):733–753. https://doi.org/10.1080/10643389.2022.2084315
4. Endo T., Gemma A., Mitsuyoshi R., et al. Discussion on effect of material on UV reflection and its disinfection with focus on Japanese Stucco for interior wall. *Sci. Rep.* 2021;11(1):21840. https://doi.org/10.1038/s41598-021-01315-1
5. Neu D.T., Mead K.R., McClelland T.L., Lindsley W.G., Martin S.B., Heil G., See M., Feng H.A. Surface Dosimetry of Ultraviolet Germicidal Irradiation Using a Colorimetric Technique. *Ann. Work Expo. Health*. 2021;65(5):605–611. https://doi.org/10.1093/annweh/wxaa147
6. Zong Y., Brown S.W., Johnson B.C., Lykke K.R., Ohno Y. Simple spectral stray light correction method for array spectroradiometers. *Appl. Opt.* 2006;45(6):1111–1119. https://doi.org/10.1364/AO.45.001111
7. Larason T.C., Cromer C.L. Sources of Error in UV Radiation Measurements. *J. Res. Nat. Inst. Stand. Technol*. 2001;106(4): 649–656. https://doi.org/10.6028/jres.106.030

8. Vijeta Kapri R.K., Saha S., Jaiswal V.K., Sharma P. Theoretical Simulation for Evaluating Error in Irradiance Measurement Using Optical Detectors Having Different Cosine Responses. *MAPAN – Journal of Metrology Society of India*. 2021;36(3): 473–480. https://doi.org/10.1007/s12647-021-00486-6
9. Marquez J.M.A., Bohórquez M.A.M., Garcia J.M., Nieto F.J.A. A New Automatic System for Angular Measurement and Calibration in Radiometric Instruments. *Sensors.* 2010;10(4):3703–3717. https://doi.org/10.3390/s100403703
10. Аневский С.И., Золотаревский Ю.М., Иванов В.С., Крутиков В.Н., Минаева О.А., Минаев Р.В. Спектрорадиометрия ультрафиолетового излучения. *Измерительная техника.* 2015;11:26–30.
11. Mekaoui S., Zibordi G. Cosine error for a class of hyperspectral irradiance sensors. *Metrologia*. 2013;50(187):187–199. http://doi.org/10.1088/0026-1394/50/3/187
12. Nevas S., Wübbeler G., Sperling A., Elster C., Teuber A. Simultaneous correction of bandpass and stray-light effects in array spectroradiometer data. *Metrologia*. 2012;49(2):S43–S47. http://doi.org/10.1088/0026-1394/49/2/S43

About the authors

Olga A. Minaeva, Dr. Sci. (Eng.), Head of the Department of Metrology and Standardization, Institute for Advanced Technologies and Industrial Programming, MIREA – Russian Technological University (78, Vernadskogo pr., Moscow, 119454 Russia). E-mail: minaeva_o@mirea.ru. Scopus Author ID 6603019847, RSCI SPIN-code 5081-1976, https://orcid.org/0000-0001-9465-3210

Alexander V. Ragutkin, Cand. Sci. (Eng.), Rector's Advisor, MIREA – Russian Technological University (78, Vernadskogo pr., Moscow, 119454 Russia). E-mail: ragutkin@mirea.ru. Scopus Author ID 56871217700, ResearcherID AAE-4437-2022, RSCI SPIN-code 7531-7376, https://orcid.org/0000-0001-8256-1941

Sergei I. Anevsky, Dr. Sci. (Eng.), Professor, Department of Metrology and Standardization, Institute for Advanced Technologies and Industrial Programming, MIREA – Russian Technological University (78, Vernadskogo pr., Moscow, 119454 Russia). E-mail: anevskij@mirea.ru. https://orcid.org/0000-0001-9197-0034

Roman V. Minaev, Cand. Sci. (Eng.), Head of the Research Department, Elektrosteklo (5, 26 Bakinskikh Komissarov ul., Moscow, 119571 Russia). E-mail: minaev@elektrosteklo.ru. Scopus Author ID 22235214600, https://orcid.org/0009-0009-6335-5531

Thanh T. Minh, Postgraduate Student, Department of Metrology and Standardization, Institute for Advanced Technologies and Industrial Programming, MIREA – Russian Technological University (78, Vernadskogo pr., Moscow, 119454 Russia). E-mail: trunghnt321@mail.ru. https://orcid.org/0009-0005-4976-6271

Inna A. Romanova, Senior Lecturer, Department of Metrology and Standardization, Institute for Advanced Technologies and Industrial Programming, MIREA – Russian Technological University (78, Vernadskogo pr., Moscow, 119454 Russia). E-mail: romanova_i@mirea.ru. RSCI SPIN-code 7864-7200, https://orcid.org/0000-0002-1642-2801

Об авторах

Минаева Ольга Александровна, д.т.н., заведующий кафедрой метрологии и стандартизации Института перспективных технологий и индустриального программирования ФГБОУ ВО «МИРЭА – Российский технологический университет» (119454, Россия, Москва, пр-т Вернадского, д. 78). E-mail: minaeva_o@mirea.ru. Scopus Author ID 6603019847, SPIN-код РИНЦ 5081-1976, https://orcid.org/0000-0001-9465-3210

Рагуткин Александр Викторович, к.т.н., советник ректора, ФГБОУ ВО «МИРЭА – Российский технологический университет» (119454, Россия, Москва, пр-т Вернадского, д. 78). E-mail: ragutkin@mirea.ru. Scopus Author ID 56871217700, ResearcherID AAE-4437-2022, SPIN-код РИНЦ 7531-7376, https://orcid.org/0000-0001-8256-1941

Аневский Сергей Иосифович, д.т.н., профессор, кафедра метрологии и стандартизации Института перспективных технологий и индустриального программирования ФГБОУ ВО «МИРЭА – Российский технологический университет» (119454, Россия, Москва, пр-т Вернадского, д. 78). E-mail: anevskij@mirea.ru. https://orcid.org/0000-0001-9197-0034

Минаев Роман Владимирович, к.т.н., начальник научно-исследовательского отдела ООО «Электростекло» (119571, Россия, Москва, ул. 26-ти Бакинских Комиссаров, д. 5). E-mail: minaev@elektrosteklo.ru. Scopus Author ID 22235214600, https://orcid.org/0009-0009-6335-5531

Минь Тхань Чунг, аспирант, кафедра метрологии и стандартизации Института перспективных технологий и индустриального программирования ФГБОУ ВО «МИРЭА – Российский технологический университет» (119454, Россия, Москва, пр-т Вернадского, д. 78). E-mail: trunghnt321@mail.ru. https://orcid.org/0009-0005-4976-6271

Романова Инна Алексеевна, старший преподаватель, кафедра метрологии и стандартизации Института перспективных технологий и индустриального программирования ФГБОУ ВО «МИРЭА – Российский технологический университет» (119454, Россия, Москва, пр-т Вернадского, д. 78). E-mail: romanova_i@mirea.ru. SPIN-код РИНЦ 7864-7200, https://orcid.org/0000-0002-1642-2801

Translated from Russian into English by Lyudmila O. Bychkova
Edited for English language and spelling by Dr. David Mossop

MIREA – Russian Technological University.
78, Vernadskogo pr., Moscow, 119454 Russian Federation.
Publication date January 31, 2024.
Not for sale.

МИРЭА – Российский технологический университет.
119454, РФ, г. Москва, пр-т Вернадского, д. 78.
Дата опубликования 31.01.2024 г.
Не для продажи.